

**A Multiscale/Multiphysics Model for Concrete  
Promovieren (IKM 2014)**

Der Fakultät für Maschinenbau  
der Gottfried Wilhelm Leibniz Universität Hannover  
zur Erlangung des akademischen Grades

Doktor-Ingenieurin

vorgelegte

Dissertation

von

M.Sc. Tao Wu

geboren am 31.07.1984 in Guixi

---

**To whom it may concern.**

---

## Zusammenfassung

In dieser Arbeit wird ein multiskalen-multiphysikalisches Modell zur Analyse von Materialversagen in Beton vorgestellt, das durch Alkali-Kieselsäure-Reaktion (AKR) sowie durch schwache Eigenschaften der Übergangszone (ITZ) hervorgerufen werden. Die Mesostruktur des Betons besteht aus Zuschlägen, die statistisch verteilt und in homogenisierten Zementstein eingebettet sind, sowie Grenzflächenelemente mit der Stärke Null, die die Übergangszone zwischen Zuschlägen und Zementstein repräsentieren. Eine Skala tiefer wird die Mikroskala von Beton durch die Mikrostruktur von Zementstein dargestellt, welche durch dreidimensionale CT-Aufnahmen gewonnen wurde. Sie beinhaltet Bestandteile von Hydratisationsprodukten, unhydratisierten Klinkern und Mikroporen.

Ein dreidimensionales, diffusions-thermisch-chemisch-mechanisches Modell wird für die Mesoskala von Beton entwickelt, welches die durch AKR hervorgerufene Schädigung in der Mikroskala beschreibt. Die Auswertung der durch AKR hervorgerufenen Schädigung als Funktion des Ausmaßes der chemischen Reaktion wird auf die Mikroskala im Zementstein initialisiert. Die Temperatur und die relative Feuchtigkeit beeinflussen das chemische Ausmaß. Eine Korrelation zwischen der effektiven Schädigung durch AKR und dem chemischen Ausmaß wird durch Homogenisierung erreicht. Somit wird eine Beziehung zwischen der Schädigung in der Mikroskala und dem Versagen in der Makroskala hergestellt.

Thermische Homogenisierung und Diffusionshomogenisierung mit statistischen Tests werden auf Zementstein angewendet, um die effektive Wärmeleitfähigkeit als Funktion der relativen Luftfeuchtigkeit und der effektiven Diffusivität in Abhängigkeit der Temperatur zu erhalten. Die sich ergebenden effektiven Eigenschaften können in die nächste Größenskala hochskaliert werden. Die Möglichkeit, derartige Effekte abzubilden, ist von maßgebender Bedeutung bei der Modellierung von chemischen Reaktionen in Beton, die durch Temperatur und Luftfeuchtigkeit beeinflusst werden, wie AKR.

Risse innerhalb der Übergangszone zwischen Zuschlägen und Zementstein werden, basierend auf einem kohäsiven Modell, mittels eines diskreten Rissansatzes abgebildet. Ausserdem wird ein Zugkraft-Separationsgesetz für die kohäsive Zone entwickelt, welches eine mikromechanisch begründete Wärme-Fluss-Separationsbeziehung und eine Diffusionsfluss-Separationsbeziehung kombiniert. Damit kann der Temperatur- und der Feuchtigkeitssprung im kohäsiven Riss beschrieben werden.

Schließlich werden numerische Beispiele vorgestellt, bei denen die Kombination aus induzierter Schädigung durch AKR, die nichtlineare effektive Wärmeleitfähigkeit als Funktion der relativen Luftfeuchtigkeit und die effektive Diffusivität als Funktion der Temperatur, sowie ein diffusions-thermisch-chemisch-mechanisches kohäsives Modell in der Übergangszone zwischen Zuschlägen und Zementstein berücksichtigt wird.

**Schlagnworte:** Multiskale, Multiphysics, Beton, Alkali-Kieselsäure-Reaktion, Übergangszone

# Abstract

This thesis presents a reliable multiscale multiphysics model to analyze failure induced by alkali-silica reaction (ASR) as well as by weak properties of interfacial transition zone (ITZ) in the concrete. The mesostructure of concrete consists of aggregates with a random distribution embedded in a homogenized hardened cement paste (HCP) as well as the interface elements with zero-thickness as a representation of the ITZ. One scale lower, the microscale of concrete is represented by the microstructure of HCP obtained from three-dimensional computer-tomography (CT) scans, including hydration products, unhydrated residual clinker and micropores.

A three-dimensional diffusion-thermal-chemical-mechanical model is developed at the mesoscale of concrete, which reflects the deterioration induced by ASR at the microscale. The analysis of the ASR induced deterioration as a function of the extent of the chemical reaction is initialized at the microscale of HCP. The temperature and relative humidity determine the chemical extent. A correlation between the effective damage due to ASR and chemical extent is obtained through computational homogenization, enabling to build the bridge between microscale damage and macroscale failure.

Computational thermal homogenization and diffusion homogenization with statistical tests are applied to HCP for obtaining the effective thermal conductivity as a function of relative humidity and effective diffusivity affected by temperature. The resulting effective properties of HCP can be upscaled to the next length-scale and the ability to capture such effects is of significant importance in modeling temperature and humidity mediated chemical reaction in concrete, such as ASR.

The cohesive zone model (CZM) is used to model the debonding at the ITZ between HCP and aggregates. Furthermore, the traction-separation law in CZM combined with micromechanically motivated thermal flux-separation relation and diffusion flux-separation relation is developed, thus enabling to describe the temperature jump and humidity jump across the cohesive crack.

At the end numerical examples are illustrated combining the ASR induced damage, effective thermal conductivity and effective diffusivity of HCP affected by humidity and temperature respectively, as well as the mechanical-thermal-diffusion analysis at the ITZ between aggregates and HCP.

**Keywords:** Multiscale, Multiphysics, Concrete, Alkali-Silica Reaction, Interfacial Transition Zone

## Danksagung/Acknowledgements

To be constructed



# Contents

<b>1</b>	<b>Introduction</b>	<b>1</b>
1.1	Motivation . . . . .	1
1.2	Background and state of the art . . . . .	2
1.3	Structure . . . . .	3
<b>2</b>	<b>Continuum mechanics</b>	<b>7</b>
2.1	Kinematics . . . . .	7
2.1.1	Deformation . . . . .	8
2.1.2	Strains . . . . .	9
2.2	Stresses . . . . .	10
2.3	Balance equations . . . . .	10
2.3.1	Balance of mass . . . . .	10
2.3.2	Balance of linear and angular momentum . . . . .	11
2.3.3	Balance of energy . . . . .	12
2.3.4	Second fundamental theorem of thermodynamics . . . . .	13
2.4	Constitutive equations of bulk phase . . . . .	14
2.4.1	Continuum damage model . . . . .	14
2.4.2	Visco-plasticity . . . . .	16
2.5	Constitutive equations of interface phase . . . . .	17
2.5.1	Introduction to cohesive zone model (CZM) . . . . .	18
2.5.2	Adopted CZM in this work . . . . .	20
2.5.3	Thermal conduction across the interface . . . . .	24
2.5.4	Humidity diffusion across the interface . . . . .	27
2.6	Weak forms of balance equations . . . . .	28
2.6.1	Weak form of balance of linear momentum . . . . .	28
2.6.2	Weak form of balance of energy . . . . .	29
2.6.3	Weak form of balance of mass . . . . .	30
<b>3</b>	<b>Fundamentals of computational aspect</b>	<b>33</b>
3.1	Finite elements . . . . .	33
3.1.1	Isoparametric concept . . . . .	34
3.1.2	Solution strategies . . . . .	35
3.1.3	Numerical integration . . . . .	37
3.1.4	Coupling . . . . .	38
3.2	Discretized weak forms of balance equations of bulk phase . . . . .	38

---

3.2.1	Mechanical problem . . . . .	38
3.2.2	Thermal problem . . . . .	42
3.2.3	Diffusion problem . . . . .	43
3.3	Discretized weak forms of balance equations of interface phase . . . . .	43
3.3.1	Review of numerical fracture mechanics for concrete . . . . .	44
3.3.2	Numerical implementation of CZM . . . . .	44
3.3.3	Thermal conduction across the interface in the FEM . . . . .	49
3.3.4	Diffusion across the interface in the FEM . . . . .	52
<b>4</b>	<b>Alkali-Silica Reaction</b>	<b>55</b>
4.1	Chemical mechanism of ASR . . . . .	56
4.1.1	Review of theoretical models of ASR . . . . .	58
4.1.2	Review of numerical models of ASR . . . . .	59
4.2	Kinetics of ASR . . . . .	62
4.2.1	Chemical reaction kinetics . . . . .	62
4.2.2	Influence of temperature on chemical extent . . . . .	63
4.2.3	Influence of relative humidity on chemical extent . . . . .	63
4.2.4	Fundamentals and assumptions . . . . .	66
<b>5</b>	<b>Multiscale representation of concrete</b>	<b>69</b>
5.1	Mesoscale of concrete . . . . .	70
5.1.1	Representation of mesoscale . . . . .	71
5.1.2	Take-and-place approach . . . . .	72
5.1.3	Discretization technique . . . . .	72
5.2	Interfacial transition zone between aggregates and HCP . . . . .	74
5.2.1	Zero-thickness interface element . . . . .	75
5.2.2	Numerical example of unit cell . . . . .	76
5.3	Microscale of hardened cement paste . . . . .	80
5.3.1	Representation of hardened cement paste . . . . .	81
5.3.2	Constitutive equation of each component in HCP . . . . .	82
5.3.3	Solid phase . . . . .	82
5.3.4	Gel in micropores of HCP . . . . .	82
5.3.5	ASR induced damage in HCP . . . . .	83
<b>6</b>	<b>Computational homogenization to ASR damage</b>	<b>85</b>
6.1	Introduction . . . . .	85
6.2	Analytical homogenization . . . . .	86
6.3	Computational homogenization . . . . .	87
6.3.1	Computational thermal homogenization . . . . .	88
6.3.2	Window method . . . . .	94
6.3.3	Computational diffusion homogenization . . . . .	100
6.3.4	Computational mechanical homogenization . . . . .	102

---

<b>7</b>	<b>Computational simulation of effects of the ITZ</b>	<b>111</b>
7.1	Numerical results in uniaxial tension . . . . .	112
7.1.1	Damage distribution . . . . .	113
7.1.2	Influence of parameters in CZM . . . . .	114
7.1.3	Influence of specimen size . . . . .	116
7.1.4	Influence of random distribution of aggregates . . . . .	117
7.1.5	Debonding interface damage in uniaxial tension . . . . .	118
7.1.6	Parameter identification . . . . .	119
7.2	Numerical results in uniaxial compression . . . . .	119
7.3	Mechanical-thermal-diffusion coupling for the ITZ . . . . .	123
7.3.1	Staggered method . . . . .	123
7.3.2	Numerical thermal results . . . . .	125
7.3.3	Numerical diffusion results . . . . .	125
<b>8</b>	<b>Multiscale Multiphysics Simulation Results</b>	<b>129</b>
8.1	Introduction . . . . .	129
8.2	Numerical example . . . . .	130
<b>9</b>	<b>Conclusions and outlook</b>	<b>135</b>
<b>A</b>	<b>Homogenization</b>	<b>139</b>
A.1	Mechanical homogenization . . . . .	139
A.1.1	Average strain theorem . . . . .	139
A.1.2	Average stress theorem . . . . .	140
A.2	Thermal homogenization . . . . .	141
A.2.1	Average temperature gradient theorem . . . . .	141
A.2.2	Average thermal flux theorem . . . . .	141
A.3	Diffusion homogenization . . . . .	142
A.3.1	Average humidity gradient theorem . . . . .	142
A.3.2	Average diffusion flux theorem . . . . .	143
	<b>Bibliography</b>	<b>143</b>



# Chapter 1

## Introduction

### 1.1 Motivation

The many fields of applicability of concrete stem from its wide spectrum of material properties and stable characteristics. The durability issue of concrete structures is of great concern, as they are subjected to various environmental attacks, such as alkali-silica reaction (ASR) (ULM ET AL. (2000)), thermal loading (TOUMI & RESHEIDAT (2010)), severe mechanical overloading (DENARIÉ ET AL. (2006)) or frost (HAIN & WRIGGERS (2008a)).

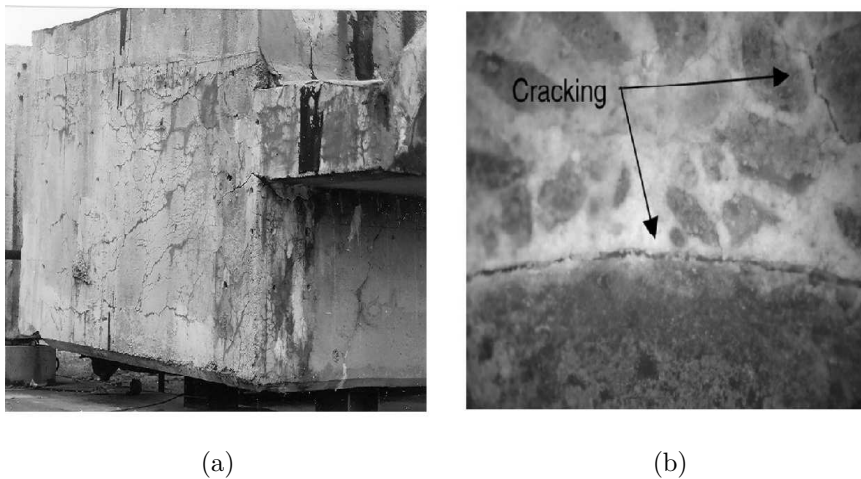


**Figure 1.1:** (a) ASR-induced cracks viewed on the end face of a 20-year-old reinforced concrete bridge beam from GRACE company in the U.S. and (b) cracks at interfacial transition zone (ITZ) between cement paste and aggregates during freezing and thawing cycles (SICAT ET AL. (2014)).

Figure 1.1(a) illustrates ASR-induced cracks viewed on the end face of a 20-year-old reinforced (Portland cement only) concrete bridge beam from GRACE company in the

U.S., where reactive aggregates were obtained from river gravels. Figure 1.1(b) displays the existence of cracks at the ITZ between aggregates and cement paste during freezing and thawing cycles, which could be explained by the weak property of the ITZ due to higher porosity. The variation of the underlying microstructure of concrete leads to the macroscale failure, which justifies the need of a deeper insight at the material level. However, the difficulty and high cost of conventional experiments to be conducted at the material level of concrete suggests an alternative approach. The increase of computational capability motivates the development of a multiscale modeling approach to investigate the correlation between the macroscale failure and the variation of the microstructure. The multiscale model established in this work is applied to describe failures induced by ASR and weak properties of the ITZ.

## 1.2 Background and state of the art

Homogenization is an efficient approach to link micro- and macroscale. Rough bounds of effective elastic material properties were introduced by VOIGT (1889) and REUSS (1929), and other tight bounds can be found in ZOHDI & WRIGGERS (2005). The limitation that analytical estimates are only valid for simple microstructural geometries, justifies the need of developing computational homogenization approaches, providing arbitrarily refinable bounds. For linear elasticity, computational homogenization is well-established, see TORQUATO (2002), ZOHDI & WRIGGERS (2005) and references therein. In the nonlinear elastic regime, the existing problems of the non-uniqueness of the solution at finite deformations and the non-invertibility of the stress-strain relation lead to the need of more efforts on the investigations, e.g. isotropic damage with finite deformation (LÖHNERT (2004)), anisotropic finite elastoplasticity (MIEHE & SCHOTTE (2007)) and crystal plasticity (LEHMANN (2013)). Clearly, the computational cost of homogenization for nonlinear problem is high. Computational homogenization was also applied to the thermal problem. Contributions on first-order thermal homogenization to determine the effective thermal conductivity can be found e.g. in ASAKUMA ET AL. (2004), LASCHET ET AL. (2009), ZHANG ET AL. (2011a) and references therein. Additionally, a second-order thermal homogenization framework with higher-order fluxes was proposed by TEMIZER & WRIGGERS (2010b) to capture absolute size effects when the size of the representative volume element (RVE) is not sufficiently small compared to a representative macrostructural length scale. Applying diffusion homogenization to estimate the effective diffusivity is also of significant concern, see RIM ET AL. (2007), KRABBENHØFT ET AL. (2008) and NILENIUS ET AL. (In press). Furthermore, TEMIZER & WRIGGERS (2011) developed a homogenization framework for the finite thermoelasticity analysis of heterogeneous media, based on the appropriate identifications of the macroscopic density, internal energy, entropy and thermal dissipation.

During the last decade, a considerable amount of work has been developed to describe the ASR induced failure at different length scales of the concrete in a numerical manner. HUANG & PIETRUSZCZAK (1996) established the simple correlation between the expansion strain due to ASR and mechanical degradation at the macroscale of

concrete. ULM ET AL. (2000), BANGERT ET AL. (2004) and COMI ET AL. (2012) analyzed ASR at the macroscale of concrete in the framework of BIOT's theory, taking into account the influences of temperature and relative humidity on the extent of reaction. Various analytical models based on empirical equations were also developed to explain ASR at the mesoscale of concrete, see BAŽANT & STEFFENS (2000) and MULTON ET AL. (2009). Later on, COMBY-PEYROT ET AL. (2009) introduced a three-dimensional mesoscopic model, where the damage in the cement matrix was caused by the ASR induced isotropic dilatation of reactive aggregates. DUNANT & SCRIVENER (2010) and DUNANT (2009) proposed a two-dimensional finite element/extended finite element framework to qualitatively depict the ASR induced deterioration at the mesoscale of concrete. ALNAGGAR ET AL. (2013) adopted the framework of Lattice Discrete Particle Model (LDPM) to capture the ASR induced crack patterns at the mesoscale of concrete, where the expansion of the gel occurred at the level of each individual aggregate particle.

The ITZ plays a significant role in the behavior of concrete. The microstructure of the ITZ with high porosity was investigated through experiments, see MONTEIRO ET AL. (1985) and MASO (1996). Later on, its significant role was considered numerically. For instance, in order to obtain the better estimation of the elastic modulus of concrete, not only the cement paste and aggregates, but also the ITZ have already been considered in the numerical simulations, see RAMESH ET AL. (1996) and NADEAU (2003) and LEE & PARK (2008). Cohesive zone model (CZM) was widely utilized to describe the debonding at the ITZ as well as the resulting influences on the macroscale behavior of concrete, see CAROL ET AL. (2001), HÄFNER ET AL. (2006), ECKARDT & KÖNKE (2008), SNOZZI ET AL. (2011) and SNOZZI ET AL. (2012), in terms of various types of load, e.g. static tension and compression as well as dynamic tension and compression. Apart from the mechanical problem, the thermal conduction across the ITZ also gains attention. WILLAM ET AL. (2004) employed a traction-separation law in CZM combined with a thermal flux-separation relation to model the thermal resistance at the crack interface, where the thermal interface damage was defined as a function of separation. As compared to a few contributions on the thermal problem for the ITZ, more investigations concerning the influence of cracking or debonding on the diffusivity of concrete were conducted through not only analytical but also numerical approaches. GÉRARD & MARCHAND (2000) and LUNDGREN (2002) addressed analytical models to describe how cracks affect the diffusion properties of concrete based on the assumption of the simple size distribution and geometry of the crack. Numerical work can be found e.g. in KAMALI-BERNARD & BERNARD (2009), BENTZ ET AL. (2013) and references therein.

## 1.3 Structure

The aim of this thesis is to develop a reliable multiscale multiphysics model to analyze failures induced by ASR as well as by weak properties of the ITZ between hardened cement paste (HCP) and aggregates, see Figure 1.2 for the framework, which can be split into three blocks.

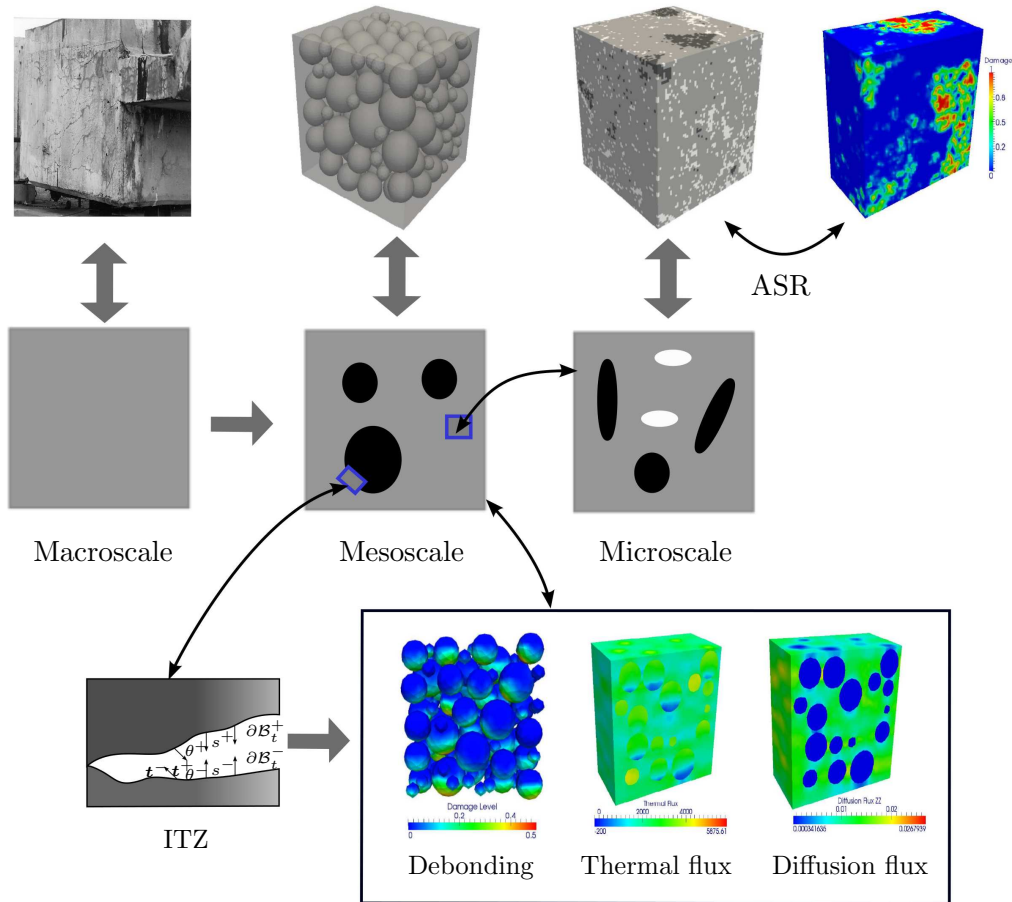


**Figure 1.2:** Framework of multiscale multiphysics modeling of concrete.

- At the mesoscale, the transient temperature and relative humidity in the HCP determine the ASR chemical extent at the material point. The resulting chemical extent is utilized to calculate the damage induced by ASR at the microscale through the correlation between the effective damage of HCP and chemical extent. A staggered method is employed at the mesoscale of concrete to solve the coupled problems, yet the chemical damage quantity is upscaled from the microscale during the process.
- Debonding at the ITZ between HCP and aggregates is modeled by CZM, which subsequently leads to the temperature jump and the humidity jump across the interface crack.
- By using computational thermal homogenization and diffusion homogenization, the effective thermal conductivity of HCP as a function of humidity and effective diffusivity of HCP affected by temperature are obtained. Such effects could be incorporated into the modeling of ASR.

Chapter 2 provides an introduction to the fundamentals of continuum mechanics and constitutive laws for the bulk phase, e.g. damage and visco-plasticity, and for the interface phase, e.g. CZM as well as thermal conduction and humidity diffusion across the cohesive interface. Also, the weak forms of the mechanical, thermal and diffusion problems are addressed, including the components related to interface and bulk phases.

Chapter 3 explains the theory of the Finite Element Method (FEM) and the discretized weak forms of the mechanical, thermal and diffusion problems.

One of important aims of this thesis is to model the ASR-induced failure. Chapter 4 illustrates the chemical mechanism of ASR as well as the analytical expression of chemical extent as functions of temperature and relative humidity, thus establishing the basis of diffusion-thermal-chemical-mechanical coupling.

Constructing the geometry representation at the material level of concrete determines the accuracy and reliability of multiscale numerical simulations. The approaches followed for generating the mesostructure of concrete, the zero-thickness interface elements representing the ITZ as well as the microstructure of HCP are explained in Chapter 5.

Chapter 6 focuses on the introduction to computational mechanical, thermal and diffusion homogenization. Moreover, two-step homogenization is utilized to obtain the microscale expansion coefficient of the gel as a reaction product of ASR. This chapter is concluded with one example to explain the effective damage of HCP induced by ASR as a function of the chemical extent.

In Chapter 7, CZM is employed to model the debonding at the ITZ and various parameters are tested to investigate their influences on the macroscale behavior of concrete. These parameters are tensile strength, fracture energy, specimen size as well as random distribution of aggregates. Additionally, a mechanical-thermal-diffusion cohesive model is established based on a staggered method to depict the evolution of thermal conduction and humidity diffusion, as the cracks occur.

Numerical examples are illustrated in Chapter 8, combining ASR induced damage, effective thermal conductivity and diffusivity of HCP affected by humidity and temperature respectively, as well as failure at the ITZ.

The conclusions of this thesis and an outlook on future work are addressed in Chapter 9.



# Chapter 2

## Continuum mechanics

This chapter outlines the fundamentals of continuum mechanics for the material body. Here, the basic equations of kinematics, balance equations, constitutive equations as well as variational principles are presented. More details about continuum mechanics can be found, e.g. in TRUESDELL & NOLL (1965), MASE & MASE (1999), HOLZAPFEL (2000), HAUPT (2002), REDDY (2008), GURTIN ET AL. (2010) and references therein.

### 2.1 Kinematics

Kinematics deals with the description of the motion and deformation of a body  $\mathfrak{B}$  in time, see Figure 2.1. This section provides the introduction to motion, deformation, as well as strain tensor.

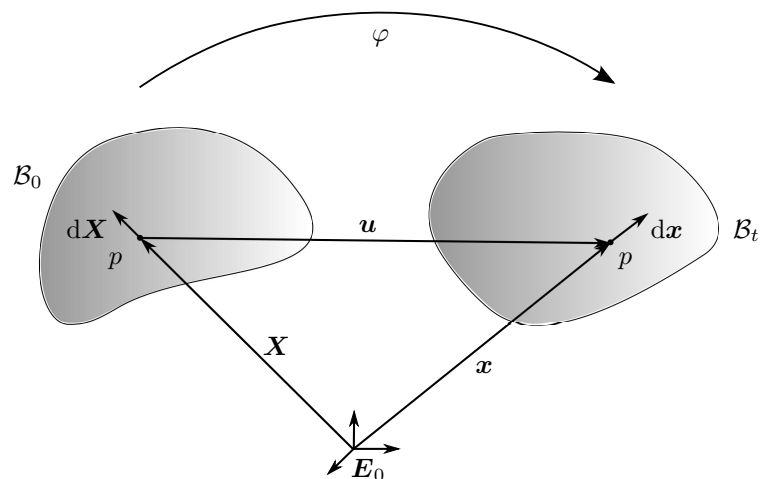


**Figure 2.1:** Initial configuration  $\mathcal{B}_0$  and current configuration  $\mathcal{B}_t$ .

### 2.1.1 Deformation

In the context of continuum theory, a material body  $\mathfrak{B}$  is assumed to be a set of continuously distributed material points  $p$  in EUCLIDEAN space  $\mathbb{R}^3$ . According to the assumption of the coherence of material points during the deformation, the kinematic process can be described by a continuous and one-to-one mapping of each material point  $p$  from the material body  $\mathfrak{B}$  to a region  $\mathcal{B}$  through a bijective function  $\chi$

$$\chi := \mathfrak{B} \mapsto \mathcal{B} \quad . \quad (2.1.1)$$

The position vector of an arbitrary material point  $p$  at time  $t_0 = 0$  is defined by

$$\mathbf{X} = \chi_0(p) \quad , \quad \mathbf{X} \in \mathcal{B}_0 \quad , \quad (2.1.2)$$

where  $\mathcal{B}_0$  is referred to as the *initial* configuration. At an arbitrary time  $t > t_0$ , the position vector of a material point  $p$  is

$$\mathbf{x} = \chi_t(p) \quad , \quad \mathbf{x} \in \mathcal{B}_t \quad , \quad (2.1.3)$$

where  $\mathcal{B}_t$  referred to as the *current* configuration deforms due to either internal or external load. The mapping between  $\mathbf{x}$  and  $\mathbf{X}$  is unique

$$\mathbf{X} = \chi_0(\chi_t^{-1}(\mathbf{x})) := \varphi^{-1}(\mathbf{x}) \quad , \quad \mathbf{x} = \chi_t(\chi_0^{-1}(\mathbf{X})) := \varphi(\mathbf{X}) \quad . \quad (2.1.4)$$

As displayed in Figure 2.1, the displacement vector  $\mathbf{u}$  describes the motion of the point  $p$  from the initial to the current configuration

$$\mathbf{u} = \mathbf{x} - \mathbf{X} \quad . \quad (2.1.5)$$

The deformation gradient  $\mathbf{F}$  characterizes a mapping of an infinitesimal line element in the initial configuration  $d\mathbf{X}$  to the current configuration  $d\mathbf{x}$

$$d\mathbf{x} = \mathbf{F} \cdot d\mathbf{X} \quad , \quad (2.1.6)$$

with the definition

$$\mathbf{F} = \frac{\partial \mathbf{x}}{\partial \mathbf{X}} = \mathbf{1} + \frac{\partial \mathbf{u}}{\partial \mathbf{X}} = \mathbf{1} + \mathbf{H} \quad , \quad (2.1.7)$$

where  $\mathbf{H}$  is the displacement gradient and the deformation gradient  $\mathbf{F}$  is an unsymmetric two-point tensor

$$\mathbf{F} = F_{ij} \mathbf{e}_i \otimes \mathbf{E}_j \quad , \quad (2.1.8)$$

where  $F_{ij}$  are the components of  $\mathbf{F}$ .  $\mathbf{E}_j$  and  $\mathbf{e}_i$  are base vectors in the initial and current configuration respectively. Thus,  $\mathbf{F}$  is able to transform tensors between the initial and current configuration. The determinant of the deformation gradient  $\mathbf{F}$

$$J = \det(\mathbf{F}) > 0 \quad , \quad (2.1.9)$$

is named the JACOBIAN  $J$ . Following Equation (2.1.6), NANSON's formula is adopted to transform an infinitesimal surface element from the initial to current configuration

$$\mathbf{n} da = J \mathbf{F}^{-T} \cdot \mathbf{N} dA \quad , \quad (2.1.10)$$

where  $dA$  and  $da$  are infinitesimal surface elements in the initial and current configuration respectively. In addition,  $\mathbf{N}$  and  $\mathbf{n}$  are the outward unit normal vectors to the surface element in the initial and current configuration. With the aid of the JACOBIAN  $J$ , the transformation of an infinitesimal volume element between the initial configuration  $dV$  and the current configuration  $dv$  is given by

$$dv = J dV \quad . \quad (2.1.11)$$

### 2.1.2 Strains

The limitation that the deformation gradient  $\mathbf{F}$  can only describe the deformation of an infinitesimal volume element as well as rigid body rotations, enforces the development of alternatives, such as GREEN-LAGRANGE strain tensor  $\mathbf{E}$  in the initial configuration and EULER-ALMANSI strain tensor  $\mathbf{e}$  in the current configuration, which are described by interpreting strains as infinitesimal length changes

$$\begin{aligned} \|\mathbf{d}\mathbf{x}\|_2^2 - \|\mathbf{d}\mathbf{X}\|_2^2 &= \mathbf{d}\mathbf{x} \cdot \mathbf{d}\mathbf{x} - \mathbf{d}\mathbf{X} \cdot \mathbf{d}\mathbf{X} \\ &= \mathbf{d}\mathbf{X} \cdot \mathbf{F}^T \cdot \mathbf{F} \cdot \mathbf{d}\mathbf{X} - \mathbf{d}\mathbf{X} \cdot \mathbf{d}\mathbf{X} \\ &= \mathbf{d}\mathbf{X} \cdot (\mathbf{F}^T \cdot \mathbf{F} - \mathbf{1}) \cdot \mathbf{d}\mathbf{X} \\ &= \mathbf{d}\mathbf{X} \cdot 2\mathbf{E} \cdot \mathbf{d}\mathbf{X} \quad . \end{aligned} \quad (2.1.12)$$

$$\begin{aligned} \|\mathbf{d}\mathbf{x}\|_2^2 - \|\mathbf{d}\mathbf{X}\|_2^2 &= \mathbf{d}\mathbf{x} \cdot \mathbf{d}\mathbf{x} - \mathbf{d}\mathbf{X} \cdot \mathbf{d}\mathbf{X} \\ &= \mathbf{d}\mathbf{x} \cdot \mathbf{d}\mathbf{x} - \mathbf{d}\mathbf{x} \cdot \mathbf{F}^{-T} \cdot \mathbf{F}^{-1} \cdot \mathbf{d}\mathbf{x} \\ &= \mathbf{d}\mathbf{x} \cdot (\mathbf{1} - \mathbf{F}^{-T} \cdot \mathbf{F}^{-1}) \cdot \mathbf{d}\mathbf{x} \\ &= \mathbf{d}\mathbf{x} \cdot 2\mathbf{e} \cdot \mathbf{d}\mathbf{x} \quad . \end{aligned} \quad (2.1.13)$$

The GREEN-LAGRANGE strain tensor  $\mathbf{E}$  is expressed as a function of displacement gradient  $\mathbf{H}$  by

$$\mathbf{E} = \frac{1}{2}(\mathbf{H} + \mathbf{H}^T + \mathbf{H}^T \cdot \mathbf{H}) \quad . \quad (2.1.14)$$

For small deformation, it can also be written as

$$\mathbf{E} \approx \frac{1}{2}(\mathbf{H} + \mathbf{H}^T) \quad . \quad (2.1.15)$$

Analogously, the symmetric strain tensor  $\boldsymbol{\epsilon}$  for small deformation in the current configuration is given by

$$\boldsymbol{\epsilon} = \frac{1}{2}(\text{grad } \mathbf{u} + \text{grad}^T \mathbf{u}) \quad . \quad (2.1.16)$$

In order to depict the irrelevant deformation like viscosity or plasticity, the material velocity gradient is defined by

$$\dot{\mathbf{F}} = \frac{\partial \dot{\mathbf{x}}}{\partial \mathbf{X}} \quad . \quad (2.1.17)$$

The spatial strain velocity  $\mathbf{d}$

$$\mathbf{d} = \frac{1}{2}(\dot{\mathbf{F}} \cdot \mathbf{F}^{-1} + \mathbf{F}^{-T} \cdot \dot{\mathbf{F}}^T) \quad , \quad (2.1.18)$$

is also required.

## 2.2 Stresses

Let the body  $\mathfrak{B}$  deform under an external load, such that it occupies the space  $\mathcal{B}_t$  in the current configuration, and then assume that it is cut by a plane surface, see Figure 2.2. The traction  $\mathbf{t}$  is defined as surface force  $\mathbf{f}_s$  per unit area  $ds$ , i.e.  $d\mathbf{f}_s = \mathbf{t}ds$ . The tractions on the corresponding surface elements in the counterpart of the body cut by a plane are of the same magnitude, yet with opposite directions, following the NEWTON's third law, see,  $\mathbf{t}(\mathbf{x}, -\mathbf{n}) = -\mathbf{t}(\mathbf{x}, \mathbf{n})$ . According to the CAUCHY's stress

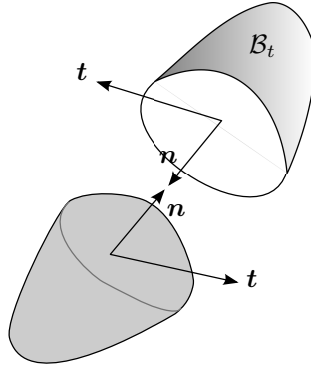


**Figure 2.2:** Surface traction vectors on surfaces resulting from a cut through a body.

theorem, the surface traction  $\mathbf{t}$  can be defined by

$$\mathbf{t} = \boldsymbol{\sigma} \cdot \mathbf{n} \quad , \quad (2.2.1)$$

where  $\boldsymbol{\sigma}$  is the CAUCHY's stress tensor with the symmetric property  $\boldsymbol{\sigma} = \boldsymbol{\sigma}^T$  resulting from the balance law of angular momentum in non-polar media.

## 2.3 Balance equations

The balance equations of continuum mechanics, developed from physical observations, are valid independent of the material body under consideration. This section outlines the balance of mass, balance of linear and angular momentum, balance of energy as well as the second fundamental theorem of thermodynamics.

### 2.3.1 Balance of mass

The mass  $m$  as a physical parameter exists in each material body  $\mathfrak{B}$ . In a closed system, the mass change of the body in time is assumed to be preserved, independent of the motion and deformation

$$\frac{d}{dt}m = 0 \quad . \quad (2.3.1)$$

Evaluating the volume integral of the mass density  $\rho$  over the domain in the initial or current configuration yields the mass of the body with the aid of Equation (2.1.11)

$$m = \int_{\mathcal{B}_t} \rho \, dv = \int_{\mathcal{B}_0} J\rho \, dV = \int_{\mathcal{B}_0} \rho_0 \, dV \quad , \quad (2.3.2)$$

where  $V$  and  $v$  denote the volume elements in the initial and current configuration respectively. The relationship of the initial mass density  $\rho_0$  and the current mass density  $\rho$  is given by

$$\rho_0 = J\rho \quad . \quad (2.3.3)$$

Inserting Equation (2.3.3) into (2.3.1) yields the integral form of mass balance

$$\frac{d}{dt}m = \int_{\mathcal{B}_0} \frac{d}{dt}(J\rho) \, dV = \int_{\mathcal{B}_0} (\dot{\rho} + \rho \operatorname{div} \dot{\mathbf{x}})J \, dV = \int_{\mathcal{B}_t} (\dot{\rho} + \rho \operatorname{div} \dot{\mathbf{x}}) \, dv = 0. \quad (2.3.4)$$

As Equation (2.3.4) has to hold for any arbitrary volume, the local form is written as

$$\dot{\rho} + \rho \operatorname{div} \dot{\mathbf{x}} = 0 \quad . \quad (2.3.5)$$

### 2.3.2 Balance of linear and angular momentum

The linear momentum  $\mathbf{I}$  of the body is defined by

$$\mathbf{I} = \int_{\mathcal{B}_t} \rho \dot{\mathbf{x}} \, dv \quad . \quad (2.3.6)$$

The time derivative of linear momentum  $\mathbf{I}$  equals the sum of all external and internal forces

$$\frac{d}{dt}\mathbf{I} = \int_{\mathcal{B}_t} \rho \mathbf{b} \, dv + \int_{\partial\mathcal{B}_t} \mathbf{t} \, da \quad , \quad (2.3.7)$$

where  $\mathbf{f} = \rho \mathbf{b}$  is the volume force vector. Employing the combination of the CAUCHY's stress theorem, the balance of mass in Equation (2.3.4) as well as the change of linear momentum in Equation (2.3.7), yields the change of linear momentum in integral form

$$\int_{\mathcal{B}_t} (\operatorname{div} \boldsymbol{\sigma} + \mathbf{f}) \, dv = 0 \quad . \quad (2.3.8)$$

Thus, the local form of the balance of linear momentum is given by

$$\operatorname{div} \boldsymbol{\sigma} + \mathbf{f} = 0 \quad . \quad (2.3.9)$$

The angular momentum  $\mathbf{L}$  of a body is defined by

$$\mathbf{L} = \int_{\mathcal{B}_t} \rho (\mathbf{x} - \mathbf{x}_0) \times \dot{\mathbf{x}} \, dv \quad . \quad (2.3.10)$$

Here, the time derivative of angular momentum  $\mathbf{L}$  equals the sum of all momentums of forces acting on the body in the current configuration

$$\frac{d}{dt}\mathbf{L} = \int_{\mathcal{B}_t} \rho ((\mathbf{x} - \mathbf{x}_0) \times \mathbf{b}) \, dv + \int_{\partial\mathcal{B}_t} ((\mathbf{x} - \mathbf{x}_0) \times \mathbf{t}) \, da \quad . \quad (2.3.11)$$

### 2.3.3 Balance of energy

In a closed system, the energy  $W$  of a body is preserved in the context of the first law of thermodynamics.  $W$  is the sum of the internal energy  $U$  and the kinetic energy  $K$

$$W = U + K \quad . \quad (2.3.12)$$

The internal energy  $U$  is written as

$$U = \int_{\mathcal{B}_t} \rho u \, dv \quad , \quad (2.3.13)$$

where  $u$  is the specific internal energy. The kinetic energy  $K$  is defined by

$$K = \frac{1}{2} \int_{\mathcal{B}_t} \rho \dot{\mathbf{x}} \cdot \dot{\mathbf{x}} \, dv \quad . \quad (2.3.14)$$

The change of the energy  $W$  in time is determined by the sum of the external power input  $P$  and the thermal power supply  $Q$

$$\dot{W} = P + Q \quad . \quad (2.3.15)$$

The body forces  $\rho \mathbf{b}$  and the surface tractions  $\mathbf{t}$  contribute to the external power input  $P$

$$P = \int_{\mathcal{B}_t} \rho \mathbf{b} \cdot \dot{\mathbf{x}} \, dv + \int_{\partial \mathcal{B}_t} \mathbf{t} \cdot \dot{\mathbf{x}} \, da \quad . \quad (2.3.16)$$

The thermal power supply  $Q$  is given by

$$Q = \int_{\mathcal{B}_t} \rho r \, dv - \int_{\partial \mathcal{B}_t} \mathbf{q} \cdot \mathbf{n} \, da \quad , \quad (2.3.17)$$

which is contributed by a distributed internal heat source of strength  $r$  and heat flux  $\mathbf{q}$  through the surface of the body. With the combinations of Equations (2.3.13), (2.3.14), (2.3.15), (2.3.16) and (2.3.17), the balance of energy in integral form is given by

$$\frac{d}{dt} \int_{\mathcal{B}_t} \rho \left( u + \frac{1}{2} \dot{\mathbf{x}} \cdot \dot{\mathbf{x}} \right) \, dv = \int_{\mathcal{B}_t} \rho (r + \mathbf{b} \cdot \dot{\mathbf{x}}) \, dv + \int_{\partial \mathcal{B}_t} (\mathbf{t} \cdot \dot{\mathbf{x}} - \mathbf{q} \cdot \mathbf{n}) \, da \quad . \quad (2.3.18)$$

According to the symmetric part of the velocity gradient in Equation (2.1.18), the local balance of linear momentum in Equation (2.3.9) and the CAUCHY's stress theorem, the integral form of the balance of energy can also be written as

$$\int_{\mathcal{B}_t} \rho \dot{u} \, dv = \int_{\mathcal{B}_t} (\boldsymbol{\sigma} : \mathbf{d} + \rho r - \operatorname{div} \mathbf{q}) \, dv \quad , \quad (2.3.19)$$

leading to the local form of the balance of energy in the current configuration

$$\rho \dot{u} - \boldsymbol{\sigma} : \mathbf{d} + \operatorname{div} \mathbf{q} - \rho r = 0 \quad . \quad (2.3.20)$$

### 2.3.4 Second fundamental theorem of thermodynamics

In a closed system, the theorem of the balance of energy indicates that no energy can be created. The second fundamental theorem of thermodynamics addresses the direction of a thermomechanical process with the aid of entropy  $L$ , which is formulated by

$$L = \int_{\mathcal{B}_t} \rho l \, dv \quad , \quad (2.3.21)$$

where  $l$  is a specific density of entropy. According to the second fundamental theorem of thermodynamics, the change of entropy of a body in time is not less than the entropy input due to internal heat source  $\rho r$  and the entropy input due to heat flux  $\mathbf{q}$  through the surface of the body

$$\frac{d}{dt} \int_{\mathcal{B}_t} \rho l \, dv \geq \int_{\mathcal{B}_t} \rho \frac{r}{\theta} \, dv - \int_{\partial \mathcal{B}_t} \frac{\mathbf{q} \cdot \mathbf{n}}{\theta} \, da \quad . \quad (2.3.22)$$

Using the divergence theorem, the global form of the fundamental theorem can be written as

$$\int_{\mathcal{B}_t} \rho \dot{l} \, dv \geq \int_{\mathcal{B}_t} \left( \rho \frac{r}{\theta} - \frac{(\theta \operatorname{div} \mathbf{q} - \mathbf{q} \cdot \operatorname{grad} \theta)}{\theta^2} \right) \, dv \quad , \quad (2.3.23)$$

leading to the local form

$$\rho \theta \dot{l} \geq \rho r - \operatorname{div} \mathbf{q} + \frac{\mathbf{q}}{\theta} \cdot \operatorname{grad} \theta \quad . \quad (2.3.24)$$

Considering Equation (2.3.20), it yields

$$0 \leq \rho \frac{d}{dt} [\theta l - u] - \rho \dot{\theta} l + \boldsymbol{\sigma} : \mathbf{d} - \frac{\mathbf{q}}{\theta} \cdot \operatorname{grad} \theta \quad . \quad (2.3.25)$$

The term in brackets is denoted as free energy  $\psi$  or HELMHOLTZ free energy

$$\rho \psi := u - \theta l \quad . \quad (2.3.26)$$

The time total differentiation of  $\psi = \psi(\theta, \operatorname{grad} \theta, \boldsymbol{\epsilon})$  leads to

$$\dot{\psi} = \frac{\partial \psi}{\partial \theta} \dot{\theta} + \frac{\partial \psi}{\partial \operatorname{grad} \theta} \cdot \overline{\operatorname{grad} \theta} + \frac{\partial \psi}{\partial \boldsymbol{\epsilon}} : \dot{\boldsymbol{\epsilon}} \quad . \quad (2.3.27)$$

Incorporating Equation (2.3.25), it yields

$$0 \leq \left( \boldsymbol{\sigma} - \rho \frac{\partial \psi}{\partial \boldsymbol{\epsilon}} \right) : \dot{\boldsymbol{\epsilon}} - \rho \dot{\theta} \left( \frac{\partial \psi}{\partial \theta} + l \right) - \rho \frac{\partial \psi}{\partial \operatorname{grad} \theta} \cdot \overline{\operatorname{grad} \theta} - \frac{\mathbf{q}}{\theta} \cdot \operatorname{grad} \theta \quad , \quad (2.3.28)$$

where  $\dot{\boldsymbol{\epsilon}}$  and  $\mathbf{d}$  are equal in the small deformation. As standard arguments of continuum mechanics state for arbitrary rates of each term, the stress  $\boldsymbol{\sigma}$  and entropy  $l$  are given by

$$\boldsymbol{\sigma} := \rho \frac{\partial \psi}{\partial \boldsymbol{\epsilon}} \quad , \quad l := - \frac{\partial \psi}{\partial \theta} \quad . \quad (2.3.29)$$

Hence, the HELMHOLTZ free energy has to be independent of the temperature gradient

$$\frac{\partial \psi}{\partial \text{grad} \theta} = 0 \quad , \quad (2.3.30)$$

leading to

$$\psi = \psi(\theta, \boldsymbol{\epsilon}) \quad . \quad (2.3.31)$$

Simplifying Equation (2.3.25) yields the CLAUSIUS-DUHEM inequality

$$0 \leq \boldsymbol{\sigma} : \dot{\boldsymbol{\epsilon}} - \rho(\dot{\psi} + l\dot{\theta}) - \frac{\mathbf{q}}{\theta} \cdot \text{grad} \theta \quad , \quad (2.3.32)$$

with the dissipation  $\mathcal{D} := \boldsymbol{\sigma} : \dot{\boldsymbol{\epsilon}} - \rho(\dot{\psi} + l\dot{\theta})$ .

## 2.4 Constitutive equations of bulk phase

Apart from the kinetics and balance equations mentioned above, the so-called constitutive law describing the physical behavior is also required to solve the boundary value problem (BVP). In order to avoid developing a non-physical constitutive law, the following principles should be fulfilled, e.g. principles of causality, determinism, objectivity, material symmetry, local action and among others. For getting the thorough review of each principle, the reader is referred e.g. to NOLL (1955), CIARLET (1994) and TRUESDELL & NOLL (2004).

Even though concrete exhibits heterogeneity at different length-scales, it could be generally classified into *bulk* phase and *interface* phase. This section concentrates on the constitutive equations for the bulk phase, e.g. damage and visco-plasticity.

### 2.4.1 Continuum damage model

Continuum damage mechanics is a prevailing approach to describe the deterioration of the material. In the context of continuum damage mechanics, the damage variable is employed to phenomenologically predict the initiation and propagation of microcracks, as well as the ultimately induced macroscale failure of the material, relying on the assumption that the material is continuum, as explained in ZHANG & CAI (2010). The significance of continuum damage mechanics is underlined due to its intrinsic simplicity, consistency within the framework of the thermodynamics of irreversible processes, as well as low computational cost from the numerical point of view.

Over the past 30 years, a large number of continuum damage models were developed for concrete, which can be generally classified into two categories: *isotropic* and *anisotropic*. The isotropic damage model assumes the orientation of microcracks with uniform distributions in all directions, see e.g. MAZARS (1986), MAZARS & PIJAUDIER-CABOT (1989), KARIHALOO & FU (1990) and COMI & PEREGO (2001). However, in the concept of anisotropic damage model, opening microcracks are predominantly oriented, orthogonal to the direction of the maximum tensile stress, thereby leading to the existence of the anisotropy, see e.g. HALM & DRAGON (1998), FICHANT

ET AL. (1999), BADEL ET AL. (2007) and KIM & AL-RUB (2011).

In this work, the isotropic MAZARS damage model is defined for HCP, see MAZARS & PIJAUDIER-CABOT (1989) for more details. Incorporating the isotropic mechanical damage  $D^u$ , the relationship of strain-stress for the elastodamaging material is given by

$$\boldsymbol{\sigma} = (1 - D^u) \mathbb{C}_0 \boldsymbol{\epsilon} \quad , \quad (2.4.1)$$

where  $\mathbb{C}_0$  is the elastic material tensor. The mechanical damage variable  $D^u$  ( $0 \leq D^u \leq 1$ ) indicates 0 for the virgin material and states 1 for the completely damaged material. The free energy or elastic energy per unit mass of the material is expressed by

$$\rho \psi = \frac{1}{2} (1 - D^u) \boldsymbol{\epsilon} \mathbb{C}_0 \boldsymbol{\epsilon} \quad . \quad (2.4.2)$$

The damage energy release rate  $Y$  is written as

$$Y = -\rho \frac{\partial \psi}{\partial D^u} = \frac{1}{2} \boldsymbol{\epsilon} \mathbb{C}_0 \boldsymbol{\epsilon} \quad , \quad (2.4.3)$$

with the rate of the dissipated energy  $\dot{\phi}$

$$\dot{\phi} = -\rho \frac{\partial \psi}{\partial D^u} \dot{D}^u \quad . \quad (2.4.4)$$

Here, the equivalent strain  $\tilde{\epsilon}$  is expressed by

$$\tilde{\epsilon}(\boldsymbol{\epsilon}) = \sqrt{\sum_{i=1}^3 (\langle \epsilon_i \rangle_+)^2} \quad , \quad (2.4.5)$$

where  $\epsilon_i$  are principal strains and  $\langle \bullet \rangle_+$  is the MACAULEY bracket. The loading function of the mechanical damage is given by

$$f_m(\tilde{\epsilon}, \kappa_b) = \tilde{\epsilon} - \kappa_b \quad , \quad (2.4.6)$$

where  $\kappa_b$  is the threshold of damage growth, determined by the maximum value of the equivalent strain during the loading history, yet it is initialized with  $\kappa_0 = \frac{f_t}{E}$ , as a function of the peak stress  $f_t$  and YOUNG's modulus  $E$  under uniaxial tensile load.

MEHTA & MONTEIRO (2001) indicated that the concrete exhibits high compressive strength, yet relatively lower tensile strength, such that it behaves distinctively in tension and compression. For this reason, the mechanical damage is split into two parts

$$D^u = D_t^u + D_c^u \quad , \quad (2.4.7)$$

where  $D_t^u$  and  $D_c^u$  are mechanical damage variables induced by tensile and compressive loads respectively. The weighting coefficients  $\alpha_t$  and  $\alpha_c$  are determined by

$$\alpha_t = \sum_{i=1}^3 \left( \frac{\langle \epsilon_{ti} \rangle \langle \epsilon_i \rangle}{\tilde{\epsilon}^2} \right) \quad , \quad \alpha_c = \sum_{i=1}^3 \left( \frac{\langle \epsilon_{ci} \rangle \langle \epsilon_i \rangle}{\tilde{\epsilon}^2} \right) \quad . \quad (2.4.8)$$

In uniaxial tension  $\alpha_t = 1$  and  $\alpha_c = 0$ . In uniaxial compression  $\alpha_t = 0$  and  $\alpha_c = 1$ . Principal strains  $\epsilon_t$  and  $\epsilon_c$  are defined as functions of positive stress  $\sigma_t$  and negative stress  $\sigma_c$  by

$$\epsilon_t = (1 - D^u)\mathbb{C}_0^{-1}\sigma_t \quad , \quad \epsilon_c = (1 - D^u)\mathbb{C}_0^{-1}\sigma_c \quad . \quad (2.4.9)$$

The evolution equations of mechanical damage variables in tension and compression are written as

$$\begin{aligned} D_t^u &= 1 - \frac{\kappa_0(1 - A_t)}{\kappa} - \frac{A_t}{\exp[B_t(\kappa_b - \kappa_0)]} \\ D_c^u &= 1 - \frac{\kappa_0(1 - A_c)}{\kappa} - \frac{A_c}{\exp[B_c(\kappa_b - \kappa_0)]} \quad , \end{aligned} \quad (2.4.10)$$

which are defined in the strain space as a function of  $\kappa_b$ . Moreover,  $A_t, A_c, B_t, B_c$  and  $\kappa_0$  are material parameters to be determined. Thus, the mechanical damage can also be defined as a function of  $\kappa_b$  by

$$D^u = D_t^u + D_c^u = g(\kappa_b) \quad , \quad (2.4.11)$$

representing the failure surface function  $S^u$ . Loading function  $f_m$  controls whether the damage is increased or not

$$\text{If } f_m(\tilde{\epsilon}, \kappa_b) \text{ and } \dot{f}(\tilde{\epsilon}, \kappa_b) = 0, \text{ then } . \quad (2.4.12)$$

$$\begin{cases} D^u = g(\kappa_b) \\ \kappa_b = \tilde{\epsilon} \end{cases} \quad \text{with } \dot{D}^u \geq 0, \quad \text{else } \begin{cases} \dot{D}^u = 0 \\ \dot{\kappa}_b = 0 \end{cases} . \quad (2.4.13)$$

## 2.4.2 Visco-plasticity

Continuum mechanics model is able to predict the stiffness reduction of the material, yet fails to describe the irreversible deformations. Therefore, in the present work, a visco-plastic model of the classical PERZYNA-type combined with isotropic MAZARS damage is defined for the HCP based on HAIN (2007) and HAIN & WRIGGERS (2008b). Neglecting the thermal strain and the expansion strain due to ASR, the energy dissipation  $\mathcal{D}$  can be written as

$$\mathcal{D} : \quad \sigma : \dot{\epsilon}^{\text{pl}} + Y\dot{D}^u \geq 0 \quad , \quad (2.4.14)$$

where  $Y = -\rho \frac{\partial \psi}{\partial D^u} = \frac{1}{2}\epsilon^{\text{el}} : \mathbb{C}_0 : \epsilon^{\text{el}}$  is an elastic energy rate as functions of an elastic material tensor  $\mathbb{C}_0$  and the elastic strain  $\epsilon^{\text{el}}$ . According to the DRUCKER's postulate and the PENALTY-LAGRANGE approach, an unconstrained optimization is given by

$$\mathcal{P} : \quad -\sigma : \dot{\epsilon}^{\text{pl}} - Y\dot{D}^u + \frac{1}{\eta}\phi(f_y) + \chi S^u \rightarrow \text{stationary} \quad , \quad (2.4.15)$$

where  $\frac{1}{\eta}$  denotes the penalty-parameter of the viscosity,  $\epsilon^{\text{pl}}$  is the plastic strain,  $\phi(f_y)$  is the penalty function and  $\chi$  states the LAGRANGE multiplier. In addition, the yield surface  $f_y \leq 0$  is defined in the stress space and the failure surface  $S^u \leq 0$  is defined in the strain space. Assuming that the elastic energy rate  $Y$ , the rate of mechanical

damage  $\dot{D}^u$  and the failure surface  $S^u$  are independent of the stress, the partial differentiation of  $\mathcal{P}$  with respect to  $\boldsymbol{\sigma}$  yields the evolution equation of the plastic strain  $\boldsymbol{\epsilon}^{\text{pl}}$

$$\begin{aligned} \frac{\partial \mathcal{P}}{\partial \boldsymbol{\sigma}} \stackrel{!}{=} 0 \rightarrow -\dot{\boldsymbol{\epsilon}}^{\text{pl}} - \frac{\partial Y}{\partial \boldsymbol{\sigma}} \dot{D}^u - Y \frac{\partial \dot{D}^u}{\partial \boldsymbol{\sigma}} + \frac{1}{\eta} \frac{\partial \phi(f_y)}{\partial f_y} \frac{\partial f_y}{\partial \boldsymbol{\sigma}} + \dot{\chi} \frac{\partial S^u}{\partial \boldsymbol{\sigma}} = 0 \\ \dot{\boldsymbol{\epsilon}}^{\text{pl}} = \frac{1}{\eta} \phi^+ \frac{f_y}{\partial \boldsymbol{\sigma}} \quad , \end{aligned} \quad (2.4.16)$$

where  $\phi^+$  is the derivative of the penalty function  $\phi(f_y)$

$$\phi^+ := \frac{\partial \phi(f_y)}{\partial f_y} \rightarrow \phi(f_y) = \begin{cases} 0 & ; f_y < 0 \\ \frac{1}{m+1} f_y^{m+1} & ; f_y > 0 \end{cases} \quad (2.4.17)$$

where  $m$  is assumed to be 1. Here, the VON-MISES-type yield surface is chosen

$$f_y := \|\text{dev} \boldsymbol{\sigma}\| - \sqrt{\frac{2}{3}} k_f < 0 \quad , \quad (2.4.18)$$

where  $\text{dev} \boldsymbol{\sigma}$  is the deviatoric part of the stress tensor and  $k_f$  is the material property of the model.

The evolution equation of the damage  $D^u$  is obtained through the partial differentiation of  $\mathcal{P}$  with respect to the elastic energy rate  $Y$

$$\begin{aligned} \frac{\partial \mathcal{P}}{\partial Y} \stackrel{!}{=} 0 \rightarrow 0 = -\dot{D}^u - \frac{1}{\eta} \frac{\partial \phi(f_y)}{\partial f_y} \frac{\partial f_y}{\partial Y} + \dot{\chi} \frac{\partial S^u}{\partial Y} \\ \dot{D}^u = \dot{\chi} \frac{\partial S^u}{\partial Y} \quad . \end{aligned} \quad (2.4.19)$$

which is independent from the strain since the penalty function  $\phi(f_y)$  is defined in the stress space. In terms of the failure surface  $S^u$ , one can refer to Equation (2.4.11). Applying the implicit time integration of BACKWARD-EULER to Equations (2.4.16) and (2.4.19) yields the evolution equations for inelastic strain and damage

$$\boldsymbol{\epsilon}_{n+1}^{\text{pl}} = \boldsymbol{\epsilon}_n^{\text{pl}} + \frac{\Delta t}{\eta} \phi^+ \frac{\partial f_y}{\partial \boldsymbol{\sigma}} \quad . \quad (2.4.20)$$

$$D_{n+1}^u = D_n^u + \Delta \chi \frac{\partial S^u}{\partial Y} \quad . \quad (2.4.21)$$

## 2.5 Constitutive equations of interface phase

As illustrated in Figure 2.3, an interface layer exists in the body  $\mathcal{B}_t$  subjected to various boundary conditions, e.g. displacement  $\bar{\mathbf{u}}$ , traction  $\bar{\mathbf{t}}$ , temperature  $\bar{\theta}$ , thermal flux  $\bar{q}_n$ , humidity  $\bar{s}$  and diffusion flux  $\bar{j}_n$ . The external force could result in the cracking or debonding at the interface layer, such that the body is split into two parts:  $\mathcal{B}_t^+$  and  $\mathcal{B}_t^-$ . Later on, it poses the problem how the interface crack affects the thermal conduction

and the humidity diffusion.

The aim of this section is to address the constitutive equations for the interface phase of concrete, namely for the ITZ between the HCP and aggregates. With an intention of modeling the debonding at the interface phase, CZM is used, which is characterized by a phenomenological traction-separation law. Also, the investigations of the influence of the interface crack on the thermal conduction as well as the humidity diffusion are conducted. The established traction-separation law of CZM is combined with micromechanically motivated thermal flux-separation relation and diffusion flux-separation relation, thereby enabling to account for the evolving thermal conduction and humidity diffusion.

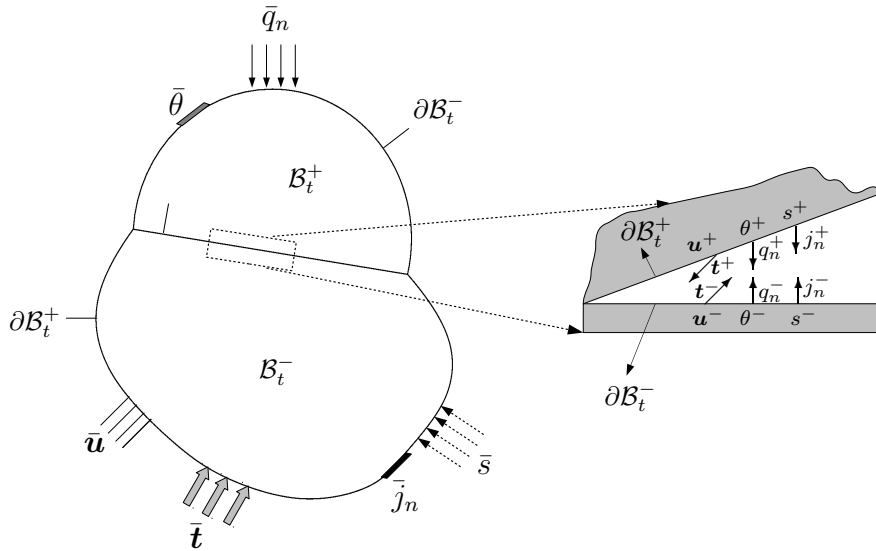


**Figure 2.3:** An interface exists in a body subjected to various boundary conditions leading to: displacement jump, temperature jump and humidity jump across the interface crack.

### 2.5.1 Introduction to cohesive zone model (CZM)

The CZM first developed by DUGDALE (1960) has already been widely applied to adequately predict the failure in various materials, e.g. concrete (ELICES ET AL. (2009)), ceramics (CHANDRA ET AL. (2002)) and composites (LI ET AL. (2005)), which successes in circumventing the problems existing in linear elastic fracture mechanics (LFEM), like stress singularity. Theoretically, CZM describes the failure of the material by means of a phenomenological model rather than an exact physical characterization of the fracture process zone with distributed microcracks, see Figure 2.4(a), where  $a_0$  and  $a_d$  indicate the length of the real crack and the fictitious crack respectively, as well as  $w_d$  states the width of the real crack. Furthermore, the real crack is not capable of bearing stress transmission, however, the assumed “fictitious

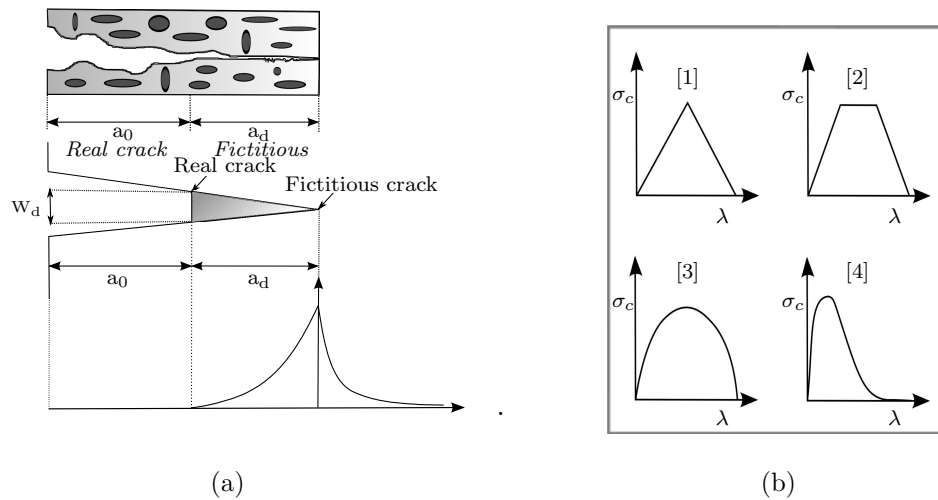


**Figure 2.4:** (a) Sketch of cohesive zone as the representation of an extended crack tip and (b) various forms of traction-separation law of CZM ([1] Bilinear [2] Trapezoidal [3] Polynomial [4] Exponential).

crack” applied in the cohesive zone exhibits an active field of interactive stress, where the phenomenological traction-separation law is motivated. Thus, the cohesive zone is considered as the representation of an extended crack tip.

As introduced in PARK & PAULINO (2011), the constitutive law of CZM can be developed based on either *nonpotential*-based or *potential*-based model. By using simple formulations, the nonpotential-based cohesive model is established, yet the consistency for arbitrary mixed-mode condition can not be ensured, dependent of separation paths. With regard to potential-based model, the CZM law is obtained from a potential function associated with the non-negative work for closed processes, hence, not only the consistency is fulfilled but also it is independent of path.

Form	Sketch	Application	References
Bilinear	Figure 2.4(b)[1]	pull-out or impact	GEUBELLE & BAYLOR (1998), CHANDRA ET AL. (2002), SONG ET AL. (2006)
Trapezoidal	Figure 2.4(b)[2]	crack growth	TVERGAARD & HUTCHINSON (1992), ALFANO ET AL. (2009)
Polynomial	Figure 2.4(b)[3]	particle-matrix decohesion	NEEDLEMAN (1987), FREED & BANKS-SILLS (2008)
Exponential	Figure 2.4(b)[4]	void nucleation	NEEDLEMAN (1990), XU & NEEDLEMAN (1993), ALFANO ET AL. (2009), TÁVARA ET AL. (2013)

**Table 2.1:** Summary of widely used traction-separation laws consisting of forms, applications and references.

Widely adopted traction-separation laws are displayed in Figure 2.4(b), e.g. *bilinear*, *trapezoidal*, *polynomial* and *exponential*. Among various forms of traction-separation law, the common feature is clearly concluded that initially the magnitude of the traction is increased as the separation of cohesive surfaces rises, and after reaching a critical peak value, the traction drops towards zero following various softening curves. For instance, GEUBELLE & BAYLOR (1998) adopted the bilinear form to simulate the spontaneous initiation and propagation of transverse matrix cracks and delamination fronts in thin composite plates subjected to low-velocity impact. The trapezoidal form was used in TVERGAARD & HUTCHINSON (1992) to calculate the crack growth initiation and the subsequent resistance in an elastic-plastic solid. NEEDLEMAN (1987) employed the exponential form to simulate the particle debonding in the metal matrices. In application to the pre-cracked bonded double cantilever beam specimen with mode I fracture, ALFANO ET AL. (2009) assessed whether or not the forms of the traction-separation law may have influences on numerical results, e.g. exponential, bilinear and trapezoidal. A short summary is displayed in Table 2.1, in which a limited number of applications as well as references of various forms of traction-separation law are outlined, see CHANDRA ET AL. (2002) and PARK & PAULINO (2011) for thorough reviews. Here, some additional features of CZM are as follows:

- CZM is capable of modeling not only a single crack tip, but also crack propagation,
- CZM allows additional constitutive relationships to be incorporated into its framework, such that it is able to account for other phenomena like contact and frictional sliding along fracture surface.

For a comprehensive insight into the CZM, its limitations are also underlined:

- No item defined for the interaction of constitutive laws between the bulk phase and the interface phase raises the difficulty in determining parameters of CZM through parameter identification compared with the experiment,
- CZM has problems solving not only too small-scale problem, such as nanoscale, but also mixed-mode fracture.

For getting more details of limitations of the CZM, the reader is referred e.g to PARK & PAULINO (2011), LI ET AL. (2012) and references therein.

### 2.5.2 Adopted CZM in this work

The goal of the present subsection is to focus on the employed CZM in the present work originating from TVERGAARD (2003) in order to describe the debonding between aggregates and HCP in concrete. Prior to the introduction of the nonlinear traction-separation law, an equivalent interface opening  $\lambda$  is defined as a function of the normal displacement jump  $\llbracket \mathbf{u} \rrbracket_n$  and tangential displacement jump  $\llbracket \mathbf{u} \rrbracket_{ti}$

$$\lambda = \sqrt{\langle \llbracket \mathbf{u} \rrbracket_n \rangle_+^2 + \sum_{i=1}^2 (\llbracket \mathbf{u} \rrbracket_{ti})^2} \quad , \quad (2.5.1)$$

where  $\langle \bullet \rangle_+$  indicates that only the positive displacement jump is considered. The equivalent traction  $\boldsymbol{\sigma}_c$  across the cohesive crack is given by

$$\boldsymbol{\sigma}_c(\lambda) = \begin{cases} K_p \lambda & ; \lambda < \lambda_0 \\ f_t \exp\left(-\frac{f_t(\lambda - \lambda_0)}{G_f}\right) & ; \text{otherwise} \end{cases}, \quad (2.5.2)$$

where  $f_t$  is the tensile strength,  $G_f$  is the fracture energy,  $K_p$  is the penalty stiffness and  $\lambda_0 = \frac{f_t}{K_p}$  denotes the elastic limit. The potential  $\Phi$  is expressed by

$$\Phi = \int_{\mathcal{B}_t} \boldsymbol{\sigma}_c(\lambda) d\lambda. \quad (2.5.3)$$

The traction across the cohesive crack satisfies the continuity condition

$$\mathbf{t}_c^+ = -\mathbf{t}_c^-, \quad (2.5.4)$$

where the superscripts  $(\bullet)^+$  and  $(\bullet)^-$  indicate the separate parts  $\partial\mathcal{B}_t^+$  and  $\partial\mathcal{B}_t^-$  respectively, as shown in Figure 2.3. The traction  $\mathbf{t}_c$  consists of the normal traction  $\mathbf{t}_{cn}$  and the tangential traction  $\mathbf{t}_{cti}$

$$\mathbf{t}_c = \begin{bmatrix} \mathbf{t}_{cn} \\ \mathbf{t}_{ct1} \\ \mathbf{t}_{ct2} \end{bmatrix}, \quad (2.5.5)$$

which are obtained through partial derivatives of the potential  $\Phi$  with respect to the normal displacement jump  $\|\mathbf{u}\|_n$  and the tangential displacement jump  $\|\mathbf{u}\|_{ti}$

$$\mathbf{t}_{cn} = \frac{\partial\Phi}{\partial\|\mathbf{u}\|_n} = \boldsymbol{\sigma}_c(\lambda) \frac{\|\mathbf{u}\|_n}{\lambda}, \quad \mathbf{t}_{cti} = \frac{\partial\Phi}{\partial\|\mathbf{u}\|_{ti}} = \boldsymbol{\sigma}_c(\lambda) \frac{\|\mathbf{u}\|_{ti}}{\lambda}, \quad (2.5.6)$$

where  $\lambda$  is assumed to be the maximum value of the equivalent strain during the loading history. In order to implement it in the FEM, the mechanical tangent material matrix  $\mathbb{C}_c^u$  is obtained by partial differentiations of the resulting traction with respect to the displacement jump

$$\mathbb{C}_c^u = \begin{bmatrix} \frac{\partial\mathbf{t}_{cn}}{\partial\|\mathbf{u}\|_n} & \frac{\partial\mathbf{t}_{cn}}{\partial\|\mathbf{u}\|_{t1}} & \frac{\partial\mathbf{t}_{cn}}{\partial\|\mathbf{u}\|_{t2}} \\ \frac{\partial\mathbf{t}_{ct1}}{\partial\|\mathbf{u}\|_n} & \frac{\partial\mathbf{t}_{ct1}}{\partial\|\mathbf{u}\|_{t1}} & \frac{\partial\mathbf{t}_{ct1}}{\partial\|\mathbf{u}\|_{t2}} \\ \frac{\partial\mathbf{t}_{ct2}}{\partial\|\mathbf{u}\|_n} & \frac{\partial\mathbf{t}_{ct2}}{\partial\|\mathbf{u}\|_{t1}} & \frac{\partial\mathbf{t}_{ct2}}{\partial\|\mathbf{u}\|_{t2}} \end{bmatrix}. \quad (2.5.7)$$

By using the chain rule, the components of the mechanical tangent stiffness matrix  $\mathbb{C}_c^u$  are given by

$$\begin{aligned}
\frac{\partial \mathbf{t}_{cn}}{\partial \|\mathbf{u}\|_n} &= \left[ \frac{\partial \boldsymbol{\sigma}_c}{\partial \lambda} - \frac{\boldsymbol{\sigma}_c}{\lambda} \right] \frac{\partial \lambda}{\partial \|\mathbf{u}\|_n} \frac{\|\mathbf{u}\|_n}{\lambda} + \frac{\boldsymbol{\sigma}_c}{\lambda} \\
\frac{\partial \mathbf{t}_{cn}}{\partial \|\mathbf{u}\|_{ti}} &= \left[ \frac{\partial \boldsymbol{\sigma}_c}{\partial \lambda} - \frac{\boldsymbol{\sigma}_c}{\lambda} \right] \frac{\partial \lambda}{\partial \|\mathbf{u}\|_{ti}} \frac{\|\mathbf{u}\|_n}{\lambda} \\
\frac{\partial \mathbf{t}_{cti}}{\partial \|\mathbf{u}\|_n} &= \left[ \frac{\partial \boldsymbol{\sigma}_c}{\partial \lambda} - \frac{\boldsymbol{\sigma}_c}{\lambda} \right] \frac{\partial \lambda}{\partial \|\mathbf{u}\|_n} \frac{\|\mathbf{u}\|_{ti}}{\lambda} \\
\frac{\partial \mathbf{t}_{cti}}{\partial \|\mathbf{u}\|_{tj}} &= \left[ \frac{\partial \boldsymbol{\sigma}_c}{\partial \lambda} - \frac{\boldsymbol{\sigma}_c}{\lambda} \right] \frac{\partial \lambda}{\partial \|\mathbf{u}\|_{tj}} \frac{\|\mathbf{u}\|_n}{\lambda} + \delta_{ij} \frac{\boldsymbol{\sigma}_c}{\lambda} ,
\end{aligned} \tag{2.5.8}$$

where  $\delta_{ij}$  is the KRONECKER delta symbol. The derivative of the equivalent interface traction  $\boldsymbol{\sigma}_c$  with respect to the equivalent interface opening  $\lambda$  is expressed by

$$\frac{\partial \boldsymbol{\sigma}_c}{\partial \lambda} = \begin{cases} K_p & ; < \lambda_0 \\ -\frac{f_t^2}{G_f} \exp\left(-\frac{f_t(\lambda-\lambda_0)}{G_f}\right) & ; \text{otherwise} \end{cases} , \tag{2.5.9}$$

Moreover, derivatives of the equivalent interface opening  $\lambda$  with respect to the displacement jump are given by

$$\frac{\partial \lambda}{\partial \|\mathbf{u}\|_n} = \frac{\|\mathbf{u}\|_n}{\lambda} , \quad \frac{\partial \lambda}{\partial \|\mathbf{u}\|_{cti}} = \frac{\|\mathbf{u}\|_{cti}}{\lambda} . \tag{2.5.10}$$

Note that the formulations mentioned above are applied to the case of the tension, with a positive interface opening in the normal direction. If the interface is subjected to the compressive load, by means of the penalty method in the context of contact mechanics, the normal interface compression pressure is formulated by

$$\mathbf{t}_{cn} = K_p \|\mathbf{u}\|_n , \tag{2.5.11}$$

where  $K_p$  is a penalty parameter, which can be interpreted as a spring stiffness. The penalty method allows for a small penetration of the crack faces, depending on the penalty parameter  $K_p$ . Clearly, a high penalty parameter yields a small penetration, but it also results in the ill-conditioned problem.

In compression, the mechanical tangent material matrix  $\mathbb{C}_c^{\mathbf{u}}$  is given by

$$\mathbb{C}_c^{\mathbf{u}} = \begin{bmatrix} K_p & 0 & 0 \\ 0 & \frac{\partial \mathbf{t}_{ct1}}{\partial \|\mathbf{u}\|_{t1}} & \frac{\partial \mathbf{t}_{ct1}}{\partial \|\mathbf{u}\|_{t2}} \\ 0 & \frac{\partial \mathbf{t}_{ct2}}{\partial \|\mathbf{u}\|_{t1}} & \frac{\partial \mathbf{t}_{ct2}}{\partial \|\mathbf{u}\|_{t2}} \end{bmatrix} , \tag{2.5.12}$$

where the components can be found in Equation (2.5.8).

Figure 2.5 illustrates the normal traction-opening and the tangential traction-opening, from which the physical meanings of  $f_t$  and  $G_f$  are indicated, e.g.  $f_t$  is the peak value

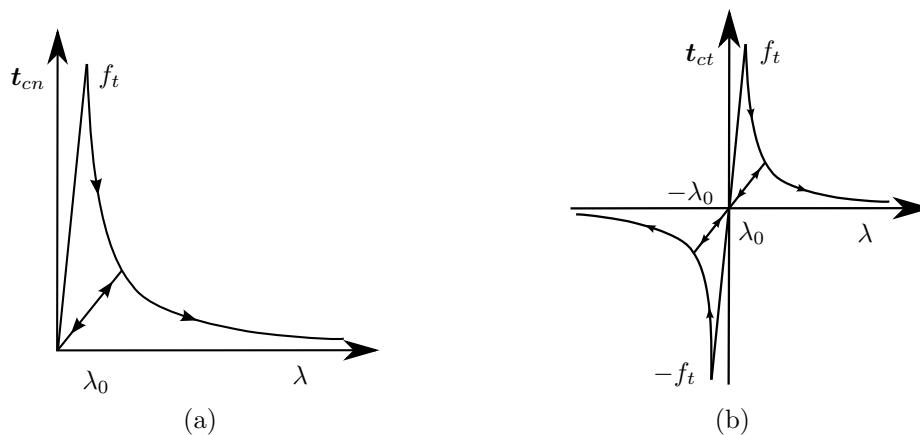


**Figure 2.5:** Traction-separation law including the irreversible damage in loading-unloading (a) normal traction-opening and (b) tangential traction-opening.

of the traction-separation law and  $G_f$  represents the area beneath the curve. Clearly, the magnitude of the traction rises as  $\lambda$  is increased initially, and if  $\lambda$  reaches a characteristic value  $\lambda_0$ , the traction starts decreasing towards zero. For a reliable CZM, the irreversible behavior in unloading has to be also taken into account, such that the standard CZM is extended with the description of damage, plasticity or combined damage-plasticity. In the present work, the extension of CZM with damage description is based on a single history parameter  $\lambda_m$ , representing the maximum equivalent interface opening during the loading history, as displayed in Figure 2.5. In this case, if the body is in loading,  $\lambda = \lambda_m$  and  $\dot{\lambda} \geq 0$ , and if it is in unloading,  $\lambda \leq \lambda_m$ . More advanced and well-established interface damage models can be found e.g. in ORTIZ & PANDOLFI (1999), ALFANO & SACCO (2006) and KOLLURI ET AL. (2014). Additionally, CZM is extended with combined damage-plasticity model, thereby depicting the influence of both crack tip damage and plasticity on fracture properties, see BIEL & STIGH (2010) and KOLLURI ET AL. (2014).

As indicated before,  $f_t$  and  $G_f$  are crucial parameters of CZM, hence, Figure 2.6 is concerned with the influence of tensile strength  $f_t$  and fracture energy  $G_f$  on the traction-separation law respectively. Clearly, as displayed in Figure 2.6, the larger  $f_t$  yields the higher peak cohesive stress, and the smaller  $G_f$  renders the steeper slope of the post-peak curve. Being aware of the influence of  $f_t$  and  $G_f$  on the traction-separation law in the analytical mode not only enhances the understanding on the theory of CZM, but also supports the implementation of the parameter identification in the computational analysis.

Figure 2.7 illustrates the normal traction and the tangential traction with functions of normal displacement jump and tangential displacement jump.

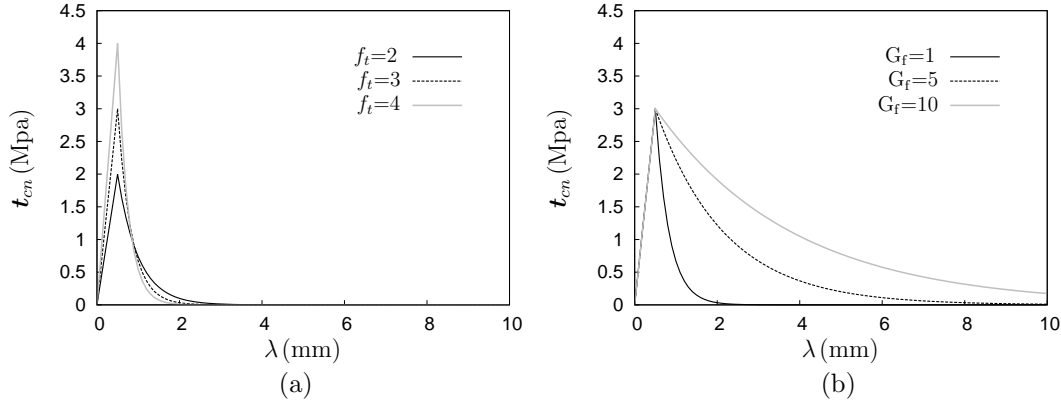


**Figure 2.6:** Traction-separation law affected by (a) tensile strength  $f_t$  (N/mm<sup>2</sup>) and (b) fracture energy  $G_f$  (N/mm).

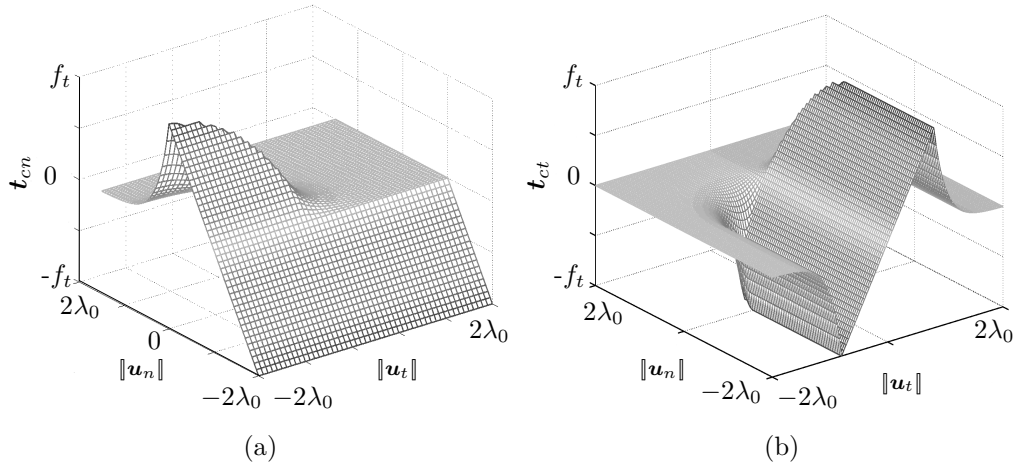


**Figure 2.7:** Traction-separation law (a) normal traction and (b) tangential traction, with functions of normal displacement jump and tangential displacement jump.

### 2.5.3 Thermal conduction across the interface

Ideally, when two dissimilar materials are assumed to be perfectly bonded, there is no temperature jump and no thermal flux jump cross the interface, namely thermally perfect interface, see DAHER & MAUGIN (1986). However, realistically the perfectly bonded interface does not exist, explained by either pre-existing microcracks at the interface or the debonding induced by the external load. Therefore, it motivates the investigation to the thermal conduction across the imperfect interface. According to the thermal property of the interface, the classification is concluded as follows:

- *Thermally perfect interface:* both the temperature and the heat flux across the interface are continuous.
- *Thermally imperfect interface:* either the temperature or the heat flux (or both)

across the interface are discontinuous.

(I) *Highly-conducting interface* (HC): the temperature across the interface is continuous, yet the jump of the normal heat flux exists, induced by the presence of the heat conduction along the interface. It can be identified as a very thin interface with high conductivity between two dissimilar bulk materials.

(II) *Lowly-conducting interface* (LC): it allows for the jump of the temperature across the interface, rather than the thermal flux, based on the KAPITZA's assumption of the thermal resistance.

(III) *General interface*: both the temperature and the normal heat flux across the interface are discontinuous. The governing equations of the general imperfect interface model are determined not only by material parameters characterizing the interface but also by parameters associated with the surrounding phases. However, derivations of constitutive laws in the HC model and the LC model are assumed to be independent of the material properties of the surrounding material phases.

Type	Temperature Jump	Flux Jump	References
Perfect	no	no	DAHER & MAUGIN (1986)
HC imperfect	no	yes	LIPTON (1997), YVONNET ET AL. (2008), LE-QUANG ET AL. (2010), JAVILI ET AL. (2013)
LC imperfect	yes	no	YVONNET ET AL. (2011), JAVILI ET AL. (2012), SAPORA & PAGGI (2014)
General imperfect	yes	yes	HASHIN (2001), BENVENISTE (2006), ÖZDEMİR ET AL. (2010), JAVILI ET AL. (2014)

**Table 2.2:** Summary of thermal conduction across the interface: perfect and imperfect.

A short summary to characterize the continuity or discontinuity of the temperature and the thermal flux among various thermal interface models can be found in Table 2.2. For more details of each thermal interface model, the reader is referred e.g. to LE-QUANG ET AL. (2010), JAVILI (2012), JAVILI ET AL. (2014) and references therein.

### Constitutive equation of thermal conduction across the interface

If the interface crack is induced, as illustrated in Figure 2.3, the temperature jump of two separated faces  $\partial\mathcal{B}_t^+$  and  $\partial\mathcal{B}_t^-$  is given by

$$\llbracket\theta\rrbracket = \theta^+ - \theta^- \quad . \quad (2.5.13)$$

Multiplying the thermal flux  $\mathbf{q}_c$  across the interface crack with an outward unit normal  $\mathbf{n}$  yields the normal component  $q_c$

$$q_c := \mathbf{q}_c \cdot \mathbf{n} \quad . \quad (2.5.14)$$

The continuity condition of the normal thermal flux  $q_c$  across the interface crack

$$q_c^+ = -q_c^- \quad . \quad (2.5.15)$$

has to be fulfilled. In the present work, the LC imperfect interface model listed in Table 2.2 is chosen. Therefore, the tangential components of the thermal flux along the interface crack are not taken into account. The constitutive law of thermal conduction across the interface crack is formulated by

$$q_c := -(1 - D_c^\theta)k_c \|\theta\| \quad . \quad (2.5.16)$$

Here,  $k_c$  is the thermal conductivity of the interface. Theoretically, the thermally perfect interface is supposed to have infinitely large  $k_c$ , however, a sufficiently large value is chosen instead during the numerical simulation, see Section 3.3.3 for more details.  $D_c^\theta$  ( $0 \leq D_c^\theta \leq 1.0$ ) is a thermal interface damage for illustrating the progressive thermal resistance due to interface crack, see the details in the following subsection. The thermal conduction across the interface crack relies on the contributions not only of the solid phase but also of the air, thus leading to

$$q_c := -\left((1 - D_\theta)k_c + k_a\right) \|\theta\| \quad , \quad (2.5.17)$$

where  $k_a$  is the thermal conductivity of the air. Note that the contribution of the air could be neglected when the temperature of the surrounding bulk phase is less than 400 °C.

### Thermal interface damage

Over the past years, some previous work has already been conducted concerning the thermal resistance of the interface. For instance, WILLAM ET AL. (2004) addressed the nonlinear relationship between the convective heat transfer coefficient of the interface and the separation. ÖZDEMİR ET AL. (2010) defined a thermal damage variable with the ratio of the maximum equivalent interface opening and the crack equivalent interface opening. SAPORA & PAGGI (2014) adopted the KAPITZA's constant resistance model to formulate the relationship between the thermal flux and the normal gap across the cohesive interface.

In this work, an irreversible thermal interface damage variable  $D_c^\theta$  based on ÖZDEMİR ET AL. (2010) is expressed by

$$D_c^\theta = \frac{\lambda_m}{\lambda_{cr}} \quad . \quad (2.5.18)$$

Here, the maximum equivalent interface opening  $\lambda_m$  was introduced in Subsection 2.5.2 and the crack equivalent interface opening  $\lambda_{cr}$  is given by

$$\lambda_{cr} = \sqrt{\|\mathbf{u}\|_{n_{cr}}^2 + \sum_{i=1}^2 \|\mathbf{u}\|_{ti_{cr}}^2} \quad , \quad (2.5.19)$$

where  $\llbracket \mathbf{u} \rrbracket_{n\,cr}$  and  $\llbracket \mathbf{u} \rrbracket_{ti\,cr}$  are the normal interface opening and the tangential interface opening of the complete crack, where traction values are quite small, e.g.  $0.1f_t$  in the post-peak regime of the traction-separation curve in Figure 2.5. By using  $D_c^\theta$ , it establishes the fundamentals of mechanical-thermal cohesive coupling.

#### 2.5.4 Humidity diffusion across the interface

Several studies have already been conducted to analyze the influence of cracks on the diffusivity of cement-based materials, e.g. SAMAHA & HOVER (1992), LOCOGE ET AL. (1992), WONG ET AL. (2009) and VASCONCELOS ET AL. (2011).

##### Constitutive equation of diffusion across the interface

As displayed in Figure 2.3, the jump of the humidity  $\llbracket s \rrbracket$  across two separate parts  $\partial\mathcal{B}_t^+$  and  $\partial\mathcal{B}_t^-$  is expressed by

$$\llbracket s \rrbracket = s^+ - s^- \quad . \quad (2.5.20)$$

Multiplying the diffusion flux  $\mathbf{j}_c$  across the interface crack with an outward unit normal  $\mathbf{n}$  leads to the normal component  $j_c$

$$j_c := \mathbf{j}_c \cdot \mathbf{n} \quad . \quad (2.5.21)$$

The continuity condition of the normal diffusion flux  $j_c$  has to be ensured

$$j_c^+ = -j_c^- \quad . \quad (2.5.22)$$

The constitutive law of the humidity diffusion cross the interface crack is formulated by

$$j_c := -(1 + M)d_c \llbracket s \rrbracket \quad , \quad (2.5.23)$$

where  $d_c$  is the diffusivity of the interface. In analogous to the thermal problem, the perfectly diffusion interface should have infinitely large  $d_c$ , yet a sufficiently large value is used during the numerical simulation. A scalar  $M$  is defined in order to comply with the experimental observation (JANG ET AL. (2011)) that the diffusivity of concrete rises as the crack width is increased.

##### Influence of the crack on diffusivity

JANG ET AL. (2011) adopted the steady-state migration test to measure the diffusivity of concrete as a function of crack width, see Figure 2.8(a) for the experimental data. It was also found that the diffusivity does not increase until the crack width is above the threshold value, around  $55\text{-}80\mu\text{m}$ . Then the experimental data in Figure 2.8(a) is simply replaced by a curve of  $M$  as a function of crack width, as seen in Figure 2.8(b). Above the threshold value,  $M$  starts to linearly increase with the crack width. Thus, the experimental observation mentioned above can be modeled by Equation (2.5.23) with the aid of  $M$ .

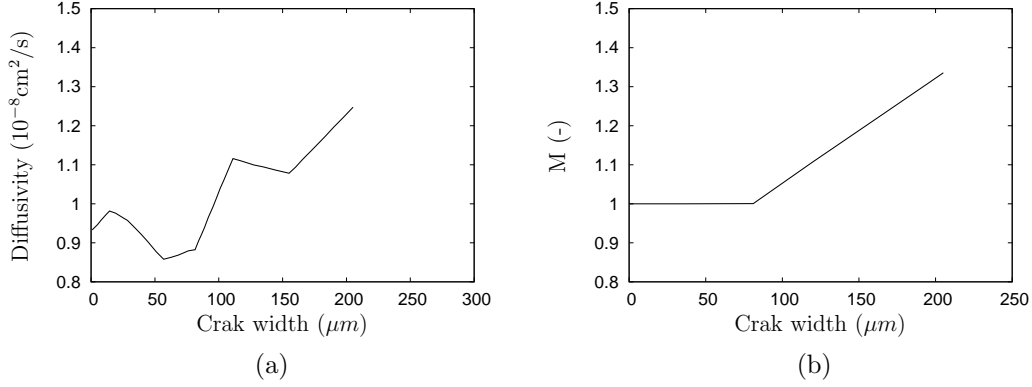


**Figure 2.8:** (a) Measured relationship between diffusivity and crack width (JANG ET AL. (2011)) and (b) artificially defined  $M$  as a function of crack width.

## 2.6 Weak forms of balance equations

The strong form of balance equations mentioned before, i.e. the balance of linear momentum in Equation (2.3.9), can not be solved analytically with arbitrary boundary conditions. For this reason, the weak form of the balance of linear momentum is formulated. The present section outlines the weak forms of balance equations in the context of mechanical, thermal and diffusion problems, including the components related to bulk and interface phases.

### 2.6.1 Weak form of balance of linear momentum

In the current configuration, a body  $\mathcal{B}_t$  is separated by a interface crack into two parts:  $\mathcal{B}_t^+$  and  $\mathcal{B}_t^-$ , see Figure 2.3. The weighted residual of the mechanical equilibrium in the bulk phase is obtained through multiplying the balance of linear momentum in Equation (2.3.9) with the continuously differentiable virtual displacement field  $\delta \mathbf{u}$ , also known as a mechanical test function  $\boldsymbol{\eta}^u$ , integrating over the entire domain  $\mathcal{B}_t$  and applying the divergence theorem as well as partial integration

$$\int_{\mathcal{B}_t} \boldsymbol{\sigma} : \text{grad} \boldsymbol{\eta}^u \, dv - \int_{\mathcal{B}_t} \mathbf{f} \cdot \boldsymbol{\eta}^u \, dv - \int_{\partial \mathcal{B}_t} \bar{\mathbf{t}} \cdot \boldsymbol{\eta}^u \, da = 0 \quad . \quad (2.6.1)$$

Incorporating the contribution of the interface phase yields

$$\begin{aligned} G^u(\mathbf{u}, \boldsymbol{\eta}^u) &= \underbrace{\int_{\mathcal{B}_t} \boldsymbol{\sigma} : \text{grad} \boldsymbol{\eta}^u \, dv - \int_{\mathcal{B}_t} \mathbf{f} \cdot \boldsymbol{\eta}^u \, dv - \int_{\partial \mathcal{B}_t} \bar{\mathbf{t}} \cdot \boldsymbol{\eta}^u \, da}_{G_b^u} \\ &+ \underbrace{\int_{\partial \mathcal{B}_t^+} \mathbf{t}_c^+ \cdot \boldsymbol{\eta}^{u^+} \, da + \int_{\partial \mathcal{B}_t^-} \mathbf{t}_c^- \cdot \boldsymbol{\eta}^{u^-} \, da}_{G_c^u} = 0 \quad , \end{aligned} \quad (2.6.2)$$

consisting of the term of the bulk phase  $G_b^u$  and the term of the interface phase  $G_c^u$ . If Equation (2.5.4) is also taken into account, it leads to

$$\begin{aligned} G^u(\mathbf{u}, \boldsymbol{\eta}^u) &= \underbrace{\int_{\mathcal{B}_t} \boldsymbol{\sigma} : \text{grad } \boldsymbol{\eta}^u \, dv - \int_{\mathcal{B}_t} \mathbf{f} \cdot \boldsymbol{\eta}^u \, dv - \int_{\partial \mathcal{B}_t} \bar{\mathbf{t}} \cdot \boldsymbol{\eta}^u \, da}_{G_b^u} \\ &+ \underbrace{\int_{\partial \mathcal{B}_t^+} \mathbf{t}_c^+ \cdot (\boldsymbol{\eta}^{u^+} - \boldsymbol{\eta}^{u^-}) \, da}_{G_c^u} = 0 \quad . \end{aligned} \quad (2.6.3)$$

The mechanical boundary conditions are given by

$$\mathbf{u} = \bar{\mathbf{u}} \text{ on } \partial \mathcal{B}_{tu} \quad , \quad \mathbf{t} = \bar{\mathbf{t}} \text{ on } \partial \mathcal{B}_{t\sigma} \quad , \quad (2.6.4)$$

where  $\partial \mathcal{B}_{tu}$  is the DIRICHLET boundary with prescribed displacements  $\bar{\mathbf{u}}$  and  $\partial \mathcal{B}_{t\sigma}$  is the NEUMANN boundary with prescribed tractions  $\bar{\mathbf{t}}$  with  $\partial \mathcal{B}_{tu} \cap \partial \mathcal{B}_{t\sigma} = \emptyset$ . Also, as mentioned above,  $\boldsymbol{\eta}^u$  has to fulfill  $\boldsymbol{\eta}^u = 0$  on  $\partial \mathcal{B}_{tu}$ .

Considering Equation (2.4.1), the weak form in Equation (2.6.3) can be written as

$$\begin{aligned} G^u(\mathbf{u}, \boldsymbol{\eta}^u) &= \underbrace{\int_{\mathcal{B}_t} (1 - D^u) \delta^u \boldsymbol{\epsilon} : \mathbb{C}_0 : \boldsymbol{\epsilon}^{\text{el}} \, dv - \int_{\mathcal{B}_t} \mathbf{f} \cdot \boldsymbol{\eta}^u \, dv - \int_{\partial \mathcal{B}_t} \bar{\mathbf{t}} \cdot \boldsymbol{\eta}^u \, da}_{G_b^u} \\ &+ \underbrace{\int_{\partial \mathcal{B}_t^+} \mathbf{t}^+ \cdot (\boldsymbol{\eta}^{u^+} - \boldsymbol{\eta}^{u^-}) \, da}_{G_c^u} = 0 \quad . \end{aligned} \quad (2.6.5)$$

with  $\delta^u \boldsymbol{\epsilon} := {}^{\text{sym}} \text{grad } \boldsymbol{\eta}^u = \frac{1}{2}(\text{grad } \boldsymbol{\eta}^u + \text{grad } \boldsymbol{\eta}^{uT})$ .

## 2.6.2 Weak form of balance of energy

The interface crack leads to the existence of the temperature jump  $\llbracket \theta \rrbracket$  across the interface, as seen in Figure 2.3. Prior to the analysis on the interface crack, the instationary thermal balance equation is utilized to describe the thermal conduction in the bulk phase, indicating that the temperature change in time equals the heat flux  $q_b$  through the surface of the body and the heat sources  $Q$  in the bulk phase of the body

$$\int_{\mathcal{B}_t} \rho c \dot{\theta} \, dv = - \int_{\partial \mathcal{B}_t} q_b \, da + \int_{\mathcal{B}_t} Q \, dv \quad , \quad (2.6.6)$$

where  $\rho$  is the density,  $c$  is the heat capacity. Multiplying the thermal flux  $\mathbf{q}_b$  in the bulk phase with an outward unit normal vector  $\mathbf{n}$  leads to the thermal flux  $q_b$  normal to the boundary

$$q_b := \mathbf{q}_b \cdot \mathbf{n} \quad , \quad (2.6.7)$$

where  $\mathbf{q}_b$  is obtained through the FOURIER's equation

$$\mathbf{q}_b := -k_b \text{grad} \theta, \quad (2.6.8)$$

indicating that the rate of flow of heat energy across the surface is proportional to the negative temperature gradient. As the balance equation is assumed to hold for any arbitrary balance domain, applying Equation (2.6.6) and the divergence theorem yields the local form in the bulk phase

$$\rho c \dot{\theta} = \text{div}(k_b \text{grad} \theta) \quad , \quad (2.6.9)$$

without consideration of the heat sources  $Q$ .

Multiplying the local form of energy balance in Equation (2.6.9) with a thermal test function  $\eta^\theta$  (or virtual temperature field  $\delta\theta$ ) and then using the divergence theorem and the FOURIER's equation yields the weak form of energy balance of the whole body

$$\begin{aligned} G^\theta(\theta, \eta^\theta) = & \underbrace{\int_{\mathcal{B}_t} \rho c \dot{\theta} \eta^\theta \, dv + \int_{\partial \mathcal{B}_t} q_b \eta^\theta \, da + \int_{\mathcal{B}_t} k_b \text{grad} \theta \cdot \text{grad} \eta^\theta \, dv}_{G_b^\theta} \\ & + \underbrace{\int_{\partial \mathcal{B}_t^+} q_c^+ \eta^{\theta^+} \, da + \int_{\partial \mathcal{B}_t^-} q_c^- \eta^{\theta^-} \, da}_{G_c^\theta} = 0 \quad , \end{aligned} \quad (2.6.10)$$

where  $G_b^\theta$  is the term of the bulk phase and  $G_c^\theta$  is the term of the interface phase. The thermal boundary conditions are written as

$$\theta = \bar{\theta} \quad \text{on} \quad \partial \mathcal{B}_{t\theta} \quad , \quad q = \bar{q} \quad \text{on} \quad \partial \mathcal{B}_{tq} \quad , \quad (2.6.11)$$

where  $\partial \mathcal{B}_{t\theta}$  is the DIRICHLET boundary with prescribed temperature  $\bar{\theta}$  and  $\partial \mathcal{B}_{tq}$  is the NEUMANN boundary with prescribed thermal flux  $\bar{q}$  with  $\partial \mathcal{B}_{t\theta} \cap \partial \mathcal{B}_{tq} = \emptyset$ . In addition,  $\eta^\theta$  has to fulfill  $\eta^\theta = 0$ , on  $\partial \mathcal{B}_{t\theta}$ . Applying Equation (2.5.15) to (2.6.10) leads to

$$\begin{aligned} G^\theta(\theta, \eta^\theta) = & \underbrace{\int_{\mathcal{B}_t} \rho c \dot{\theta} \eta^\theta \, dv + \int_{\partial \mathcal{B}_t} q_b \eta^\theta \, da + \int_{\mathcal{B}_t} k_b \text{grad} \theta \cdot \text{grad} \eta^\theta \, dv}_{G_b^\theta} \\ & + \underbrace{\int_{\partial \mathcal{B}_t^+} q_c^+ (\eta^{\theta^+} - \eta^{\theta^-}) \, da}_{G_c^\theta} = 0 \quad . \end{aligned} \quad (2.6.12)$$

### 2.6.3 Weak form of balance of mass

Analogous to thermal problem, in order to solve the problem of humidity diffusion in the bulk phase, the instationary diffusion balance equation is employed, which states that the humidity  $s$  change in time is equal to the diffusion flux  $j_b$  across the surface in the bulk phase

$$\int_{\mathcal{B}_t} \dot{s} \, dv = - \int_{\partial\mathcal{B}_t} j_b \, da \quad . \quad (2.6.13)$$

The diffusion flux  $j_b$  in the bulk phase normal to the boundary is obtained by multiplying  $\mathbf{j}_b$  with an outward unit normal vector  $\mathbf{n}$

$$j_b := \mathbf{j}_b \cdot \mathbf{n} \quad . \quad (2.6.14)$$

The diffusion flux  $\mathbf{j}_b$  in the bulk phase is obtained by using FICK's law

$$\mathbf{j}_b := -d_b \text{grad } s \quad , \quad (2.6.15)$$

where  $d_b$  is the diffusivity of the bulk phase.

The balance equation is assumed to be valid for every domain, such that the diffusion local form in the bulk phase is obtained by using Equation (2.6.13) and the divergence theorem

$$\dot{s} = \text{div}(d_b \text{grad } s) \quad . \quad (2.6.16)$$

The weak form of balance mass of the whole body consisting of the bulk phase part  $G_b^s$  and the interface phase part  $G_c^s$  is

$$\begin{aligned} G^s(s, \eta^s) &= \underbrace{\int_{\mathcal{B}_t} \dot{s} \, dv + \int_{\partial\mathcal{B}_t} j_b \eta^s \, da + \int_{\mathcal{B}_t} d_b \text{grad } s \cdot \text{grad } \eta^s \, dv}_{G_b^s} \\ &+ \underbrace{\int_{\partial\mathcal{B}_t^+} j_c^+ \eta^{s^+} \, da + \int_{\partial\mathcal{B}_t^-} j_c^- \eta^{s^-} \, da}_{G_c^s} = 0 \quad , \end{aligned} \quad (2.6.17)$$

where  $G_b^s$  is obtained by multiplying the diffusion local form in Equation (2.6.16) with a diffusion test function  $\eta^s$  (or virtual humidity field  $\delta s$ ) and then using the divergence theorem and the FICK's equation. Applying Equation (2.5.22) yields

$$\begin{aligned} G^s(s, \eta^s) &= \underbrace{\int_{\mathcal{B}_t} \dot{s} \, dv + \int_{\partial\mathcal{B}_t} j_b \eta^s \, da + \int_{\mathcal{B}_t} d_b \text{grad } s \cdot \text{grad } \eta^s \, dv}_{G_b^s} \\ &+ \underbrace{\int_{\partial\mathcal{B}_t^+} j_c^+ (\eta^{s^+} - \eta^{s^-}) \, da}_{G_c^s} = 0 \quad . \end{aligned} \quad (2.6.18)$$

The diffusion boundary conditions with  $\partial\mathcal{B}_{ts} \cap \partial\mathcal{B}_{tj} = \emptyset$  is satisfied

$$s = \bar{s} \quad \text{on } \partial\mathcal{B}_{ts} \quad , \quad j_b = \bar{j} \quad \text{on } \partial\mathcal{B}_{tj} \quad , \quad (2.6.19)$$

where  $\partial\mathcal{B}_{ts}$  is the DIRICHLET boundary with prescribed humidity  $\bar{s}$  and  $\partial\mathcal{B}_{tj}$  is the NEUMANN boundary  $\bar{j}$  with prescribed diffusion flux. In addition,  $\eta^s$  has to fulfill  $\eta^s = 0$ , on  $\partial\mathcal{B}_{ts}$ .



# Chapter 3

## Fundamentals of computational aspect

The physical process can be described by formulating partial differential equations (PDEs). However, analytical solutions can not be resolved for complex geometries or arbitrary boundary conditions, therefore, the FINITE ELEMENT METHOD (FEM) as being a robust and flexible approach, was developed in order to solve PDEs numerically. The following sections address the approach of solving three-dimensional mechanical, thermal, diffusion problems by using the FEM. For a comprehensive insight into the FEM, the reader is referred e.g. to BELYTSCHKO ET AL. (2000), ZIENKIEWICZ & TAYLOR (2005), WRIGGERS (2008) and HUGHES (2010).

### 3.1 Finite elements

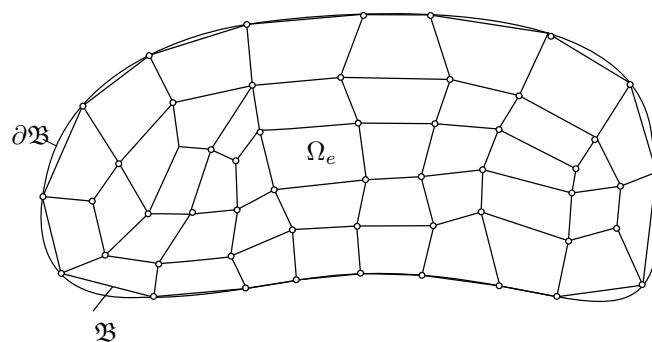


**Figure 3.1:** Approximation of the geometry by finite elements.

As displayed in Figure 3.1, the real geometry of the body  $\mathfrak{B}$  is approximated by finite elements through

$$\mathfrak{B} \approx \mathfrak{B}^h = \bigcup_{e=1}^{n_e} \Omega_e, m \quad (3.1.1)$$

with  $e$  is the element number,  $n_e$  is the total number of finite elements to approximate the body and  $\Omega_e$  is the volume of the element  $e$ .

### 3.1.1 Isoparametric concept

In the context of the FEM, the unknown functions, e.g. the displacement vector, temperature and humidity, can be expressed by using the nodal values of that element and proper shape functions. Taking the displacement vector as an example, the actual displacement  $\mathbf{u}$  and the virtual displacement  $\delta\mathbf{u}$  at point  $\mathbf{x}$  within an element are approximated by the nodal displacement  $\hat{\mathbf{u}}$  and iso-parametric shape functions  $N_I(\boldsymbol{\xi})$

$$\mathbf{u} \approx \sum_{I=1}^{n_p} N_I(\boldsymbol{\xi}) \hat{\mathbf{u}}_I, \quad \delta\mathbf{u} \approx \sum_{I=1}^{n_p} N_I(\boldsymbol{\xi}) \delta\hat{\mathbf{u}}_I, \quad (3.1.2)$$

where  $n_p$  is the number of element nodes and shape functions  $N_I(\boldsymbol{\xi})$  are piecewise-smooth polynomials, see WRIGGERS (2008).

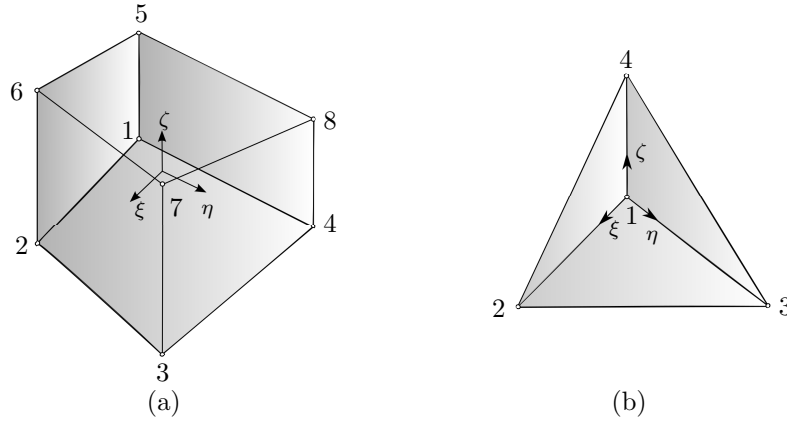


**Figure 3.2:** Isoparametric reference elements (a) three-dimensional brick element and (b) three-dimensional tetrahedral element.

For the three-dimensional brick element with eight nodes shown in Figure 3.2, trilinear shape functions are given by

$$N_I(\boldsymbol{\xi}) = \frac{1}{8}(1 + \xi_I \xi)(1 + \eta_I \eta)(1 + \zeta_I \zeta), \quad (I = 1, \dots, 8), \quad (-1 \leq \xi, \eta, \zeta \leq +1), \quad (3.1.3)$$

where  $\xi_I, \eta_I$ , and  $\zeta_I$  are the nodal coordinates of the reference element. In terms of the three-dimensional tetrahedral element with four nodes, the shape functions are written as

$$N_1 = 1 - \xi - \eta - \zeta, \quad N_2 = \xi, \quad N_3 = \eta, \quad N_4 = \zeta \quad (-1 \leq \xi, \eta, \zeta \leq +1). \quad (3.1.4)$$

The isoparametric framework is established to connect the reference element  $\Omega_{\square}$ , to an arbitrarily shaped element in the initial configuration  $\Omega_0$  or the current configuration

$\Omega_t$ , see Figure 3.3. Approximating the geometry of an element with the same shape functions as the unknown functions is the fundamentals of the isoparametric approach

$$\mathbf{X} = \sum_{I=1}^{n_p} N_I(\boldsymbol{\xi}) \mathbf{X}_I \quad , \quad \mathbf{x} \approx \sum_{I=1}^{n_p} N_I(\boldsymbol{\xi}) \mathbf{x}_I \quad . \quad (3.1.5)$$

for the initial and current configuration respectively.

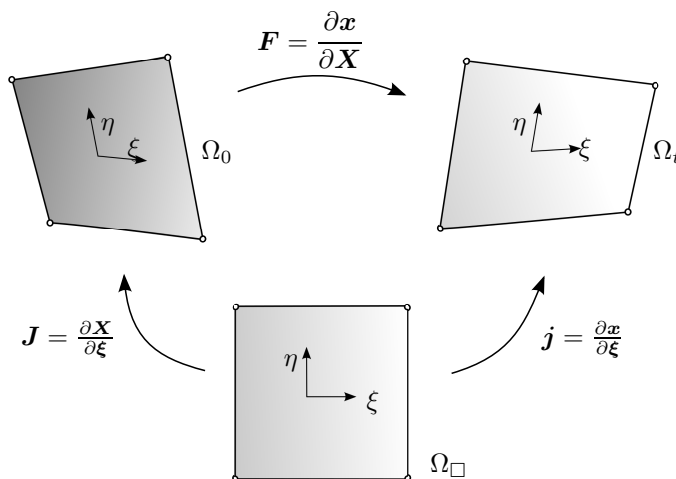


**Figure 3.3:** Isoparametric mapping applied to a rectangular element.

As displayed in Figure 3.3, the mapping between elements in the reference, initial and current configurations  $\Omega_0$ ,  $\Omega_t$  and  $\Omega_{\square}$  respectively, is written as

$$\mathbf{J} = \frac{\partial \mathbf{X}}{\partial \boldsymbol{\xi}} = \sum_{I=1}^{n_p} \mathbf{X}_I \otimes \frac{\partial N_I}{\partial \boldsymbol{\xi}} \quad , \quad \mathbf{j} = \frac{\partial \mathbf{x}}{\partial \boldsymbol{\xi}} = \sum_{I=1}^{n_p} \mathbf{x}_I \otimes \frac{\partial N_I}{\partial \boldsymbol{\xi}} \quad . \quad (3.1.6)$$

Here,  $\mathbf{J}$  and  $\mathbf{j}$  denote the JACOBI matrix in the initial and current configuration.

### 3.1.2 Solution strategies

Due to nonlinear behavior of the weak forms mentioned in Section 2.6, the NEWTON-RAPHSON approach is applied to solve the nonlinearity, see WRIGGERS (2008). However, if the approximation to the solution is far from the radius of convergence, the NEWTON-RAPHSON approach fails. Hence, the LINE-SEARCH and the ARC-LENGTH approaches are developed for solving some special problems. For getting more details of solution strategies in the FEM, the reader is referred e.g. to CRISFIELD (1992), ZIENKIEWICZ & TAYLOR (2000), WRIGGERS (2008) and references therein.

#### Newton-Raphson approach

The NEWTON-RAPHSON approach is an efficient and reliable approach to solve nonlinear equations. For mechanical problem, the linearized form of Equation (2.6.5) can

be written as

$$\begin{aligned} G_{n+1}^{\mathbf{u}}({}^m\mathbf{u}) &= G_n^{\mathbf{u}}({}^m\mathbf{u}) + \overline{D}^m G^{\mathbf{u}} \Delta \mathbf{u} \\ 0 &\stackrel{!}{=} G_n^{\mathbf{u}}({}^m\mathbf{u}) + \overline{D}^m G^{\mathbf{u}} \Delta \mathbf{u} \quad , \end{aligned} \quad (3.1.7)$$

such that

$$G_n^{\mathbf{u}}({}^m\mathbf{u}) = -\overline{D}^m G^{\mathbf{u}} \Delta \mathbf{u} \quad , \quad (3.1.8)$$

in which  ${}^m(\bullet)$  represents the current iteration and  $(\bullet)_n$  indicates the time step which is updated using a discrete time increment  $\Delta t$

$$t_{n+1} := t_n + \Delta t \quad . \quad (3.1.9)$$

The linearization  $\overline{D}^m G^{\mathbf{u}} \Delta \mathbf{u}$  refers to the GATEAUX derivative at  ${}^m\mathbf{u}$  in direction  $\Delta \mathbf{u}$

$$\overline{D}^m G^{\mathbf{u}} \Delta \mathbf{u} := \frac{\partial G_n({}^m\mathbf{u})}{\partial {}^m\mathbf{u}} \cdot \Delta \mathbf{u} \quad , \quad (3.1.10)$$

As long as  $|G_n^{\mathbf{u}}({}^m\mathbf{u})| \leq \text{TOL}$ , the displacement vector is updated.

$${}^{m+1}\mathbf{u} = {}^m\mathbf{u} + \Delta \mathbf{u} \quad . \quad (3.1.11)$$

The aforementioned NEWTON-RAPHSON approach can also be applicable to thermal and diffusion problems in a straightforward manner. The advantage of the NEWTON-RAPHSON iteration is its quadratic convergence rate. However, the tangent matrix has to be computed at each iteration step, making the computation very costly. In order to surmount this weakness, the quasi-NEWTON method is developed, where the tangent matrix is computed approximately from the known deformation states of the previous iterations, see WRIGGERS (2008) for more details.

### Line-search approach

The LINE SEARCH approach was developed by CRISFIELD (CRISFIELD (1992)) in conjunction with the NEWTON-RAPHSON approach to solve highly nonlinear finite element equations. Within this approach, an optimum line search parameter  $a$  ( $0 \leq a \leq 1$ ) scaling the correction of the displacement vector  $\mathbf{u}$  in Equation (3.1.11) in each iteration step is defined by

$${}^{m+1}\mathbf{u} = {}^m\mathbf{u} + a\Delta \mathbf{u} \quad . \quad (3.1.12)$$

If  $a$  is equal to 1, it is recovered by the NEWTON-RAPHSON approach. Two main approaches which are based on the total potential and on the residuals determine the line search parameter  $a$ , see BATHE (1995) and NOCEDAL & WRIGHT (2006) for more details.

### Arc-length approach

Figure 3.4 illustrates two load-displacement relationships involving limit point: snap-through and snap-back. For instance, the buckling of shallow arches could result in the snap-through, and the snap-back could be induced in the debonding example of

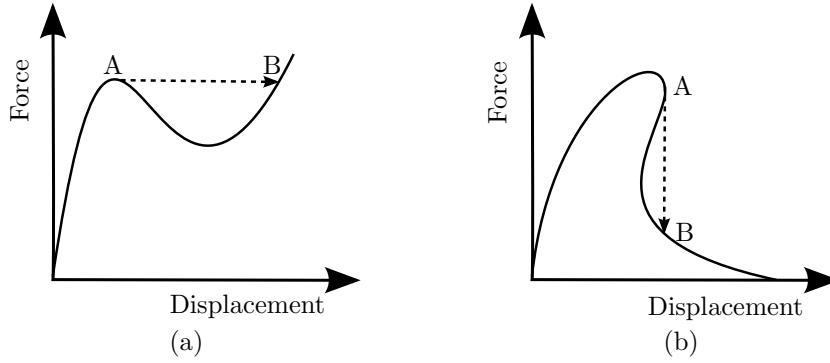


**Figure 3.4:** (a) snap-through and (b) snap-back.

the unit cell with a large sphere, see Subsection 5.2.2. If the structure is under load control, an unstable dynamic response is observed at the limit point, which follows a path from A to B, namely the snap-through, as seen in Figure 3.4(a). However, the response is stable under displacement control. For snap-back, an unstable dynamic response occurs under either load or displacement control, see Figure 3.4(b).

Limit points can not be passed through the NEWTON-RAPHSON iteration. Therefore, the ARC-LENGTH approach was developed by RIKS (1975) to enable solutions to pass through the limit points. Within this approach, both the load and displacement are unknowns and solved simultaneously. The incremental load is determined by a constraint equation as a function of the nodal displacement and the load factor. Furthermore, the NEWTON-RAPHSON equilibrium iterations converge along an “ARC”, thus preventing divergence when the slope of the load-displacement becomes zero or negative. Note that the constraint equation has to be ensured at each iteration step. More details about the ARC-LENGTH approach can be found in e.g. CRISFIELD ET AL. (1997), WRIGGERS (2008) and HUGHES (2010).

### 3.1.3 Numerical integration

Analytical approaches are not able to integrate the discretized weak forms, which will be introduced in the following sections. Here, an efficient so-called GAUSS integration scheme is used. An arbitrary function  $f_r$ , which is continuous, differentiable and sufficiently smooth in the domain  $\omega_t$ , is first mapped onto a reference domain  $\Omega_\square$  with the aid of the JACOBIAN. The resulting integration approximated by a sum over all quadrature points  $n_{gp}$  with  $f_r$  evaluated at these points and then multiplied with a weighting function  $\omega_{gp}$  yields

$$\int_{\Omega_t} f_r \, dv = \int_{\Omega_\square} f_r \det \mathbf{j} \, dv_\square \approx \sum_{gp=1}^{n_{gp}} f_r(\boldsymbol{\xi}_{np}) \omega_{gp} \det \mathbf{j}_{gp} \quad . \quad (3.1.13)$$

### 3.1.4 Coupling

As mentioned before, the concrete is generally split into bulk phase and interface phase. For each phase, the coupling framework has to be established and solved by using the FEM, where the tangent element stiffness matrix and the element residual vector in the context of mechanical, thermal and diffusion problems are derived. In order to solve the coupled problem, a staggered approach is adopted, see ZOHDI (2004) and ERBTS & DÜSTER (2012). Staggering usually has the disadvantage of being a small time step restriction in view of its explicit nature. However, it has a significantly simpler algorithmic structure compared to implicit scheme due to sequential solution of the coupled system of field equations.

As long as the local tangent element stiffness matrix and the local element residual vector are determined, it is crucial to assemble them to form the global tangent stiffness matrix and the global residual vector. The approach of managing local and global equations numbers within a finite element problem can be found e.g. in WRIGGERS (2008), HUGHES (2010) and references therein.

## 3.2 Discretized weak forms of balance equations of bulk phase

The section is concerned with the approach of discretizing weak forms of balance equations of bulk phase, in the context of mechanical, thermal and diffusion problems respectively. Inserting discretized field variables, e.g.  $\eta^u$ ,  $\eta^\theta$  and  $\eta^s$  ( $\delta\mathbf{u}$ ,  $\delta\theta$  and  $\delta s$ ), into weak forms of balance equations and applying the isoparametric mapping given in Equation (3.1.6) yields discretized weak forms of balance equations.

### 3.2.1 Mechanical problem

The NEWTON-RAPHSON approach is applied for solving the nonlinear mechanical problem. From the numerical point of view, the mechanical tangent element stiffness  $\mathbf{K}_{be}^u$  and the mechanical element residual  $\mathbf{r}_{be}^u$  have to be constructed, where  $\mathbf{K}_{be}^u$  is obtained by using a consistent linearization of  $G_b^u$  with respect to  $\mathbf{u}$  while the material tangent moduli is evaluated. For elasticity, the mechanical material tensor of the bulk phase  $\mathbb{C}_{bn+1}^u$  is given by

$$\mathbb{C}_{bn+1}^u := \frac{\partial \boldsymbol{\sigma}_{n+1}}{\partial \boldsymbol{\epsilon}_{n+1}^{\text{el}}} \quad , \quad (3.2.1)$$

without any internal variables. In terms of inelastic problem, as the elastic strain  $\boldsymbol{\epsilon}_{n+1}^{\text{el}}$  may be unknown, a tangent moduli  $\mathbb{C}_{bn+1}^u$  is formulated with the aid of  $\boldsymbol{\epsilon}_{n+1}$  by

$$\mathbb{C}_{bn+1}^u := \frac{\partial \boldsymbol{\sigma}_{n+1}}{\partial \boldsymbol{\epsilon}_{n+1}} \quad . \quad (3.2.2)$$

As described before, a visco-plastic model combined with an isotropic damage is defined for HCP, thus, a trial strain  $\boldsymbol{\epsilon}^{\text{trial}}$

$$\boldsymbol{\epsilon}^{\text{trial}} := \boldsymbol{\epsilon}_{n+1} - \boldsymbol{\epsilon}_n^{\text{pl}} \quad , \quad (3.2.3)$$

enables the tangent moduli  $\mathbb{C}_{bn+1}^u$  to be also written as

$$\mathbb{C}_{bn+1}^u := \frac{\partial \boldsymbol{\sigma}_{n+1}}{\partial \boldsymbol{\epsilon}^{\text{trial}}} : \frac{\partial \boldsymbol{\epsilon}^{\text{trial}}}{\partial \boldsymbol{\epsilon}_{n+1}} \quad . \quad (3.2.4)$$

The consistent linearization  $\overline{\mathbb{D}^m \mathbb{G}^u} \Delta \mathbf{u}$  of  $G_b^u$  in Equation (2.6.2) with respect to  $\mathbf{u}$  results in

$$\overline{\mathbb{D}^m \mathbb{G}^u} \Delta \mathbf{u} = \sum_{I=1}^{n_p} \sum_{J=1}^{n_p} \hat{\boldsymbol{\eta}}_I^{\mathbf{u}T} \int_{\Omega_t} \mathbf{B}_{bI}^{\mathbf{u}T} \mathbb{C}_b^u \mathbf{B}_{bJ}^u \, dv \Delta \hat{\mathbf{u}}_J \quad . \quad (3.2.5)$$

Then the mechanical element stiffness matrix  $\mathbf{K}_{be}^u$  is defined by

$$\mathbf{K}_{be}^u = \sum_{I=1}^{n_p} \sum_{J=1}^{n_p} \int_{\Omega_t} \mathbf{B}_{bI}^{\mathbf{u}T} \mathbb{C}_b^u \mathbf{B}_{bJ}^u \, dv \quad . \quad (3.2.6)$$

Here,  $\mathbf{B}_{bI}^u$  in the three-dimensional case with the formulation of

$$\mathbf{B}_{bI}^u := \begin{bmatrix} N_{I,x} & 0 & 0 \\ 0 & N_{I,y} & 0 \\ 0 & 0 & N_{I,z} \\ N_{I,y} & N_{I,x} & 0 \\ N_{I,z} & 0 & N_{I,x} \\ 0 & N_{I,z} & N_{I,y} \end{bmatrix} \quad , \quad (3.2.7)$$

interpolates the gradient of the mechanical displacement  $\mathbf{u}$  and the mechanical test function  $\boldsymbol{\eta}^u$

$$\boldsymbol{\epsilon} \approx \sum_{I=1}^{n_p} \mathbf{B}_{bI}^u \hat{\mathbf{u}}_I \quad , \quad \delta^u \boldsymbol{\epsilon} \approx \sum_{I=1}^{n_p} \mathbf{B}_{bI}^u \hat{\boldsymbol{\eta}}_I^u \quad . \quad (3.2.8)$$

Applying the discretization of  $G_b^u$  yields the mechanical element residual  $\mathbf{r}_{be}^u$

$$\mathbf{r}_{be}^u = \int_{\Omega_t} \delta^u \boldsymbol{\epsilon} : \boldsymbol{\sigma} \, dv \approx \sum_{I=1}^{n_p} \sum_{J=1}^{n_p} \int_{\mathcal{B}_t} \mathbf{B}_{bI}^{\mathbf{u}T} \boldsymbol{\sigma} \, dv \quad . \quad (3.2.9)$$

More details about the consistent linearization can be found in HAIN (2007).

### Visco-plasticity combined with damage

A visco-plastic model of the classical PERZYNA-type combined with an isotropic damage defined in the HCP was introduced in Subsection 2.4.2, which needs a *radial return mapping* approach to evaluate the evolution of the plastic strain in Equation (2.4.20) and the damage in Equation (2.4.21). The overall strain can be split into

$$\boldsymbol{\epsilon} := \boldsymbol{\epsilon}^{\text{el}} + \boldsymbol{\epsilon}^{\text{pl}} \quad , \quad (3.2.10)$$

without consideration of the thermal strain  $\boldsymbol{\epsilon}^\theta$  and the ASR-induced expansion strain  $\boldsymbol{\epsilon}^s$ . Applying Equations (3.2.10), (2.4.20) and (2.4.21), it addresses

$$\begin{aligned}\boldsymbol{\sigma}_{n+1} &= (1 - D_{n+1}^u)[\kappa \operatorname{tr}\boldsymbol{\epsilon}_{n+1}^{\text{el}} + 2\mu \operatorname{dev}\boldsymbol{\epsilon}_{n+1}^{\text{el}}] \\ &= (1 - D_{n+1}^u)[\kappa \operatorname{tr}(\boldsymbol{\epsilon}_{n+1} - \boldsymbol{\epsilon}_{n+1}^{\text{el}})\mathbf{1} + 2\mu \operatorname{dev}(\boldsymbol{\epsilon}_{n+1} - \boldsymbol{\epsilon}_{n+1}^{\text{el}} - \boldsymbol{\epsilon}_{n+1}^\theta)] \\ &= (1 - D_{n+1}^u)[\kappa \operatorname{tr}\boldsymbol{\epsilon}_{n+1}\mathbf{1} - \kappa \operatorname{tr}\boldsymbol{\epsilon}_{n+1}^{\text{pl}}\mathbf{1} + 2\mu \operatorname{dev}\boldsymbol{\epsilon}_{n+1} - 2\mu \operatorname{dev}\boldsymbol{\epsilon}_{n+1}^{\text{pl}}],\end{aligned}\quad (3.2.11)$$

with  $\Delta\lambda := \frac{\Delta t}{\eta}\phi^+$ . Then trial strain  $\boldsymbol{\epsilon}^{\text{trial}}$  and the trial stress  $\boldsymbol{\sigma}^{\text{trial}}$  are given by

$$\begin{aligned}\boldsymbol{\epsilon}^{\text{trial}} &:= \boldsymbol{\epsilon}_{n+1} - \boldsymbol{\epsilon}_n^{\text{pl}} \\ \boldsymbol{\sigma}^{\text{trial}} &:= (1 - D_n^u)[\kappa \operatorname{tr}\boldsymbol{\epsilon}^{\text{trial}}\mathbf{1} + 2\mu \operatorname{dev}\boldsymbol{\epsilon}^{\text{trial}}] \quad .\end{aligned}\quad (3.2.12)$$

Here, the stress can be split into

$$\boldsymbol{\sigma}_{n+1} := \boldsymbol{\sigma}^{\text{trial}} + \boldsymbol{\sigma}^{\text{add}} \quad , \quad (3.2.13)$$

where the additional stress  $\boldsymbol{\sigma}^{\text{add}}$  is defined by

$$\boldsymbol{\sigma}^{\text{add}} := -(1 - D_n^u)2\mu\Delta\lambda\mathbf{n} - \Delta\chi \frac{\partial S^u}{\partial Y} \left[ \kappa \operatorname{tr}\boldsymbol{\epsilon}^{\text{trial}}\mathbf{1} + 2\mu \operatorname{dev}\boldsymbol{\epsilon}^{\text{trial}} - 2\mu\Delta\lambda\mathbf{n} \right] , \quad (3.2.14)$$

with a generalized normal  $\mathbf{n}$

$$\mathbf{n} := \frac{\partial f}{\partial \boldsymbol{\sigma}} \quad , \quad \mathbf{n} = \frac{\operatorname{dev}\boldsymbol{\sigma}}{\|\operatorname{dev}\boldsymbol{\sigma}\|} \quad . \quad (3.2.15)$$

By using the increment  $\Delta\lambda$  or  $\Delta\chi$ , the trial strain  $\boldsymbol{\epsilon}^{\text{trial}}$  and the trial stress  $\boldsymbol{\sigma}^{\text{trial}}$  can be evaluated within the *radial return mapping* procedure

$$\begin{aligned}\frac{\eta}{\Delta t}\Delta\lambda - \phi^+ &\stackrel{!}{=} 0 \\ \frac{\eta}{\Delta t}\Delta\lambda - (f^{\text{trial}} + f^{\text{add}})^k &= 0 \quad ,\end{aligned}\quad (3.2.16)$$

in which the additional yield surface  $f^{\text{add}}$  is defined by

$$\begin{aligned}f^{\text{add}} &= \|\operatorname{dev}\boldsymbol{\sigma}^{\text{add}}\| \\ &= -(1 - D_n^u)2\mu\Delta\lambda - \Delta\chi \frac{\partial S^u}{\partial Y} 2\mu\|\operatorname{dev}\boldsymbol{\epsilon}^{\text{trial}}\| + \Delta\chi \frac{\partial S^u}{\partial Y} 2\mu\Delta\lambda \quad .\end{aligned}\quad (3.2.17)$$

Applying Equation (3.2.16) and a quadratic penalty function  $\phi(f)$  with  $k = 1$  lead to

$$\Delta\lambda = \frac{f^{\text{trial}} - 2\mu \frac{\partial S^u}{\partial Y} \|\operatorname{dev}\boldsymbol{\epsilon}^{\text{trial}}\| \Delta\chi}{\frac{\eta}{\Delta t} + (1 - D_n^u)2\mu - \Delta\chi \frac{\partial S^u}{\partial Y} 2\mu} \quad . \quad (3.2.18)$$

If  $S^u \leq 0$  the increment vanishes  $\Delta\chi = 0$ , otherwise

$$\begin{aligned}
 S_{n+1}^u &\stackrel{!}{=} 0 \\
 &= g(\kappa_b) - D_{n+1}^u \\
 &= g(\kappa_b) - D_n^u - \Delta\chi \frac{\partial S^u}{\partial Y} \\
 &= S^{\text{trial}} - \Delta\chi \frac{\partial S^u}{\partial Y} .
 \end{aligned} \tag{3.2.19}$$

Employing Equations (2.4.7), (2.4.8), (2.4.20) and (2.4.21) yields the evolution of damage

$$\begin{aligned}
 D_{n+1}^u &= D_n^u + \Delta\chi \frac{\partial S^u}{\partial Y} = D_n^u + S^{\text{trial}} \\
 D_{n+1}^u &= g(\kappa_b) \alpha_t D^t + \alpha_c D^c .
 \end{aligned} \tag{3.2.20}$$

which finally yields the increment  $\Delta\lambda$

$$\Delta\lambda = \frac{f^{\text{trial}} - 2\mu S^{\text{trial}} \|\text{dev}\boldsymbol{\epsilon}^{\text{trial}}\|}{\frac{\eta}{\Delta t} + (1 - D_n^u)2\mu - 2\mu S^{\text{trial}}} , \tag{3.2.21}$$

evaluating

$$\boldsymbol{\epsilon}_{n+1}^{\text{pl}} = \boldsymbol{\epsilon}_n^{\text{pl}} + \Delta\lambda \mathbf{n} . \tag{3.2.22}$$

Using Equation (3.2.11), the stress is given by

$$\boldsymbol{\sigma}_{n+1} = (1 - D_{n+1}^u) \left[ \kappa \text{tr}\boldsymbol{\epsilon}^{\text{trial}} \mathbf{1} + 2\mu \text{dev}\boldsymbol{\epsilon}^{\text{trial}} - 2\mu \Delta\lambda \mathbf{n} \right] , \tag{3.2.23}$$

The mechanical consistent tangent moduli  $\mathbb{C}_b^u$  is obtained based on Equation (3.2.4) within the NEWTON-RAPHSON algorithm

$$\begin{aligned}
 \mathbb{C}_b^u &:= \frac{\partial \boldsymbol{\sigma}_{n+1}}{\partial \boldsymbol{\epsilon}^{\text{trial}}} \frac{\partial \boldsymbol{\epsilon}^{\text{trial}}}{\partial \boldsymbol{\epsilon}} \\
 \mathbb{C}_b^u &= \frac{\partial \boldsymbol{\sigma}^{\text{trial}}}{\partial \boldsymbol{\epsilon}^{\text{trial}}} + \frac{\partial \boldsymbol{\sigma}^{\text{add}}}{\partial \boldsymbol{\epsilon}^{\text{trial}}} ,
 \end{aligned} \tag{3.2.24}$$

which results in

$$\begin{aligned}
 \frac{\partial \boldsymbol{\sigma}^{\text{trial}}}{\partial \boldsymbol{\epsilon}^{\text{trial}}} &= (1 - D_n^u) \left[ \kappa \mathbf{1} \otimes \mathbf{1} + 2\mu \underline{\mathbb{P}} \right] \\
 \frac{\partial \boldsymbol{\sigma}^{\text{trial}}}{\partial \boldsymbol{\epsilon}^{\text{trial}}} &= -2\mu(1 - D_n^u) \mathbf{A} - \kappa S^{\text{trial}} \mathbf{1} \otimes \mathbf{1} - 2\mu S^{\text{trial}} \underline{\mathbb{P}} + 2\mu S^{\text{trial}} \mathbf{A} ,
 \end{aligned} \tag{3.2.25}$$

with the aid of Equations (3.2.12) and (3.2.13). Here,  $\underline{\mathbb{P}}$  is defined as a fourth order projection tensor  $\underline{\mathbb{P}} := \underline{\mathbf{1}} - \frac{1}{3} \mathbf{1} \otimes \mathbf{1}$  and  $\mathbf{A}$  denotes the abbreviation

$$\begin{aligned}
 \mathbf{A} &:= \frac{\partial}{\partial \boldsymbol{\epsilon}^{\text{trial}}} \left[ \text{dev}(\Delta\lambda) \right] \\
 \mathbf{A} &= \frac{\Delta\lambda}{\|\text{dev}\boldsymbol{\sigma}^{\text{trial}}\|} \frac{\partial \text{dev}\boldsymbol{\sigma}^{\text{trial}}}{\partial \boldsymbol{\epsilon}^{\text{trial}}} + \Delta\lambda \text{dev}\boldsymbol{\sigma}^{\text{trial}} \otimes \frac{\partial \|\text{dev}\boldsymbol{\epsilon}^{\text{trial}}\|^{-1}}{\partial \boldsymbol{\epsilon}^{\text{trial}}} + \mathbf{n} \otimes \frac{\partial \Delta\lambda}{\partial \boldsymbol{\epsilon}^{\text{trial}}} ,
 \end{aligned} \tag{3.2.26}$$

The tangent moduli of the effective constitutive equation is given by

$$\begin{aligned} \mathbb{C}_b^{\mathbf{u}} = & (1 - D_n^{\mathbf{u}}) \left[ \kappa \mathbf{1} \otimes \mathbf{1} + 2\mu \underline{\mathbb{P}} \right] - \kappa S^{\text{trial}} \mathbf{1} \otimes \mathbf{1} - 2\mu S^{\text{trial}} \underline{\mathbb{P}} \\ & - 2\mu (1 - D_n^{\mathbf{u}} - S^{\text{trial}}) \left[ \frac{\Delta \lambda}{\|\text{dev} \boldsymbol{\sigma}^{\text{trial}}\|} \right] 2\mu (1 - D_n^{\mathbf{u}}) \underline{\mathbb{P}} \\ & - \Delta \lambda \text{dev} \boldsymbol{\sigma}^{\text{trial}} \otimes \frac{2\mu (1 - D_n^{\mathbf{u}})}{\|\text{dev} \boldsymbol{\sigma}^{\text{trial}}\|^2} \mathbf{n} + \mathbf{n} \otimes \frac{1}{\frac{\eta}{\Delta t} + (1 - D_n^{\mathbf{u}}) 2\mu - 2\mu S^{\text{trial}}} \\ & \left( 2\mu (1 - D_n^{\mathbf{u}}) \frac{\text{dev} \boldsymbol{\epsilon}^{\text{trial}}}{\|\text{dev} \boldsymbol{\epsilon}^{\text{trial}}\|} - 2\mu S^{\text{trial}} \frac{\text{dev} \boldsymbol{\epsilon}^{\text{trial}}}{\|\text{dev} \boldsymbol{\epsilon}^{\text{trial}}\|} \right) \Big] . \end{aligned} \quad (3.2.27)$$

### 3.2.2 Thermal problem

For a numerical realization of the NEWTON-RAPHSON procedure for thermal problem, the thermal tangent element stiffness matrix  $\mathbf{K}_{be}^{\theta}$  and the thermal element residual  $\mathbf{r}_{be}^{\theta}$  are required, where  $\mathbf{K}_{be}^{\theta}$  is obtained by partial differentiation of  $G_b^{\theta}$  in Equation (2.6.10) with respect to  $\theta$ . First of all, by using an implicit BACKWARD EULER approach, the time derivative  $\dot{\bullet}$  is approximated as discretized time  $\bullet_n$

$$\dot{\bullet} \approx \frac{\bullet_{n+1} - \bullet_n}{\Delta t} . \quad (3.2.28)$$

The linearization  $\overline{\text{D}^m G^{\theta}} \Delta \theta$  of  $G_b^{\theta}$  in Equation (2.6.10) with respect to  $\theta$  is formulated by

$$\overline{\text{D}^m G^{\theta}} \Delta \theta \approx \sum_{I=1}^{n_p} \sum_{J=1}^{n_p} \hat{\eta}_I^{\theta} \left[ \int_{\Omega_t} \frac{\rho c}{\Delta t} N_I N_J \, dv + \int_{\Omega_t} k \mathbf{B}_{bJ}^{\theta} \mathbf{B}_{bI}^{\theta T} \, dv \right] \Delta \hat{\theta}_J . \quad (3.2.29)$$

HAIN (2007) provides more details of the linearization. The thermal tangent element stiffness matrix  $\mathbf{K}_{be}^{\theta}$  is given by

$$\mathbf{K}_{be}^{\theta} = \sum_{I=1}^{n_p} \sum_{J=1}^{n_p} \left( \int_{\Omega_t} \frac{\rho c}{\Delta t} N_I N_J \, dv + \int_{\Omega_t} k_b \mathbf{B}_{bJ}^{\theta} \mathbf{B}_{bI}^{\theta T} \, dv \right) . \quad (3.2.30)$$

where  $\mathbf{B}_b^{\theta}$  interpolates the gradient of the temperature  $\theta$  and the gradient of test function  $\eta^{\theta}$

$$\text{grad} \theta \approx \sum_{I=1}^{n_p} \mathbf{B}_{bI}^{\theta} \hat{\theta}_I , \quad \text{grad} \eta^{\theta} \approx \sum_{I=1}^{n_p} \mathbf{B}_{bI}^{\theta} \hat{\eta}_I^{\theta} , \quad (3.2.31)$$

with the form of

$$\mathbf{B}_{bI}^{\theta} := \left[ N_{I,x} \quad N_{I,y} \quad N_{I,z} \right]^T . \quad (3.2.32)$$

Based on the discretization of  $G_b^{\theta}$ , the thermal element residual is obtained through

$$\mathbf{r}_{be}^{\theta} = \sum_{I=1}^{n_p} \sum_{J=1}^{n_p} \int_{\Omega_t} \frac{\rho c}{\Delta t} N_J (\hat{\theta}_{n+1}^J - \hat{\theta}_n^J) N_I \, dv + \sum_{I=1}^{n_p} \sum_{J=1}^{n_p} \int_{\Omega_t} k_b \mathbf{B}_{bJ}^{\theta} \hat{\theta}_n^J \mathbf{B}_{bI}^{\theta T} \, dv . \quad (3.2.33)$$

including the instationary part given by the first term and the stationary part stated by the second term.

### 3.2.3 Diffusion problem

The implementation of the diffusion tangent element stiffness matrix  $\mathbf{K}_{be}^s$  and the diffusion element residual  $\mathbf{r}_{be}^s$  in the NEWTON-RAPHSON framework is analogous to the themral field. The linearization  $\overline{\mathbf{D}^m \mathbf{G}^s} \Delta s$  of  $G_b^s$  in Equation (2.6.17) with respect to  $s$  is given by

$$\overline{\mathbf{D}^m \mathbf{G}^s} \Delta s \approx \sum_{I=1}^{n_p} \sum_{J=1}^{n_p} \hat{\eta}_I^s \left[ \int_{\Omega_t} \frac{1}{\Delta t} N_I N_J \, dv + \int_{\Omega_t} d_b \mathbf{B}_{bJ}^s \mathbf{B}_{bI}^{sT} \, dv \right] \Delta \hat{s}_J \quad . \quad (3.2.34)$$

Based on above, the diffusion tangent element stiffness matrix  $\mathbf{K}_{be}^s$  can be written as

$$\mathbf{K}_{be}^s = \sum_{I=1}^{n_p} \sum_{J=1}^{n_p} \left( \int_{\Omega_t} \frac{N_I N_J}{\Delta t} \, dv + \int_{\Omega_t} d_b \mathbf{B}_{bJ}^s \mathbf{B}_{bI}^{sT} \, dv \right) \quad . \quad (3.2.35)$$

where  $\mathbf{B}_b^s$  interpolates the gradient of the humidity  $s$  and the gradient of the test function  $\eta^s$  through

$$\text{grad } s \approx \sum_{I=1}^{n_p} \mathbf{B}_{bI}^s \hat{s}_I \quad , \quad \text{grad } \eta^s \approx \sum_{I=1}^{n_p} \mathbf{B}_{bI}^s \hat{\eta}_I^s \quad (3.2.36)$$

and is defined in the three-dimensional case by

$$\mathbf{B}_{bI}^s := \left[ N_{I,x} \quad N_{I,y} \quad N_{I,z} \right]^T \quad . \quad (3.2.37)$$

The discretization of  $G_b^s$  results in the diffusion element residual

$$\mathbf{r}_{be}^s = \sum_{I=1}^{n_p} \sum_{J=1}^{n_p} \int_{\Omega_t} \frac{1}{\Delta t} N_J (\hat{s}_{n+1}^J - \hat{s}_n^J) N_I \, dv + \sum_{I=1}^{n_p} \sum_{J=1}^{n_p} \int_{\Omega_t} d_b \mathbf{B}_{bJ}^s \hat{s}_n^J \mathbf{B}_{eI}^{sT} \, dv \quad . \quad (3.2.38)$$

with the instationary part denoted by the first term and the stationary part stated by the second term.

## 3.3 Discretized weak forms of balance equations of interface phase

The present section is concerned with Discretized weak forms of balance equations of interface phase for mechanical, thermal and diffusion problems respectively.

### 3.3.1 Review of numerical fracture mechanics for concrete

Over the past 40 years, a considerable amount of contributions were made to investigate the fracture mechanics in a numerical manner, with particular applications to concrete. Thorough reviews on analytical fracture mechanics can be found e.g. in JANSSEN ET AL. (2004) and KUNDU (2008). However, the restriction that the analytical fracture mechanics is only motivated by simple microstructural geometries, enforces the development of the numerical fracture mechanics. Linear elastic fracture mechanics (LEFM) was employed to account for the failure in concrete, see SHAH & OUYANG (1992). If the nonlinear zone ahead of the crack tip is large compared to specimen dimension, the nonlinear fracture mechanics approach (NLFEM) has to be considered, see MURTHY ET AL. (2009). However, both approaches lead to the singularity problem near the crack tip which can be circumvented by a cohesive zone model (CZM) characterizing the failure by means of a phenomenological model rather than an exact physical description of the fracture process zone. Hence, it was widely applied to model the crack at the macroscale as well as at the mesoscale of concrete, see ECKARDT (2009), ELICES ET AL. (2009), IDIART ET AL. (2011) and SNOZZI ET AL. (2012). Later, the eXtended Finite Element Method (XFEM) was applied to model the crack propagation process in concrete, see GOLEWSKI ET AL. (2012) and ZHANG ET AL. (2013). XFEM was inspired by the partition of unity method (PUM) combined with the level-set method (LSM), avoiding the remeshing issue in crack applications. The combination of CZM with XFEM is able to predict the crack initiation and propagation along arbitrary paths, since the crack propagation is not tied to the element boundaries in a mesh, see UNGER ET AL. (2007). Moreover, the strong discontinuity approach (SDA) with enhanced assumed strains (EAS) are alternatives to simulate the crack propagation, see REESE (2007), where discontinuities in the displacement field can be traced realistically, allowing a non-geometrical representation of crack discontinuities. The discrete lattice model is a popular approach to analyze the crack model, taking into account the mesostructure of concrete, where the continuum is replaced by a system of discrete particles, see e.g. SCHLANGEN & MIER (1992), GRASSL & JIRÁSEK (2010), SNOZZI ET AL. (2011) and SNOZZI ET AL. (2012).

In addition to numerical fracture mechanics approaches mentioned above with applications to concrete, there are still other alternatives, such as Boundary Element Method (BEM), element-free Galerkin method, Partition of Unity Method (PUM), particle methods, Arbitrary Lagrangian-Eulerian Methods as well as phase field, which are not explained in this work. For comprehensive knowledge of various approaches, e.g. fundamentals, advantages, limitations as well as the interactions among various approaches, the reader is referred e.g. to ALIABADI & ROOKE (1991), MÜLLER-HOEPPE ET AL. (2009), RABCZUK (2012) and references therein.

### 3.3.2 Numerical implementation of CZM

The aim of the present subsection is to illustrate the implementation of CZM in the FEM framework. A six-node single cohesive element is constituted by two triangular

surfaces connecting the faces of tetrahedrons, see Figure 3.5 for illustrations. Note that the two triangular surfaces of the cohesive element lie together in the initial configuration, hence, the interface element has zero-thickness. Later it separates as the adjacent solid elements deform. The approach of yielding the zero-thickness interface elements between HCP and aggregates as the representation of the ITZ, will be explained in Subsection 5.2.1.

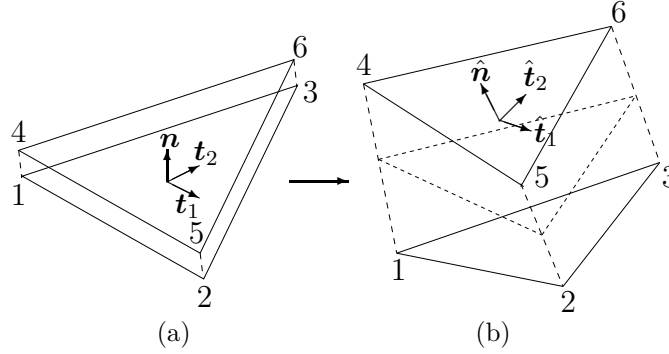


**Figure 3.5:** Single cohesive element (a) initial configuration with zero-thickness and (b) current configuration with the reference middle surface.

The nodal displacement vector  $\hat{\mathbf{u}}_c$  of one single cohesive element with six nodes in the global coordinate system are given by

$$\hat{\mathbf{u}}_c = (\hat{\mathbf{u}}_x^1 \ \hat{\mathbf{u}}_y^1 \ \hat{\mathbf{u}}_z^1, \dots, \hat{\mathbf{u}}_x^6 \ \hat{\mathbf{u}}_y^6 \ \hat{\mathbf{u}}_z^6)^T \quad . \quad (3.3.1)$$

The surface behavior of the CZM is formulated with respect to the reference middle surface, as displayed in Figure 3.5. Thus, the shape functions of the triangle reference element are introduced

$$N_1 = 1 - \xi - \eta, \quad N_2 = \xi, \quad N_3 = \eta, \quad (-1 \leq \xi, \eta \leq +1) \quad . \quad (3.3.2)$$

The displacement jump vector  $\llbracket \mathbf{u} \rrbracket$  across the cohesive interface in the global coordinate is formulated by

$$\llbracket \mathbf{u} \rrbracket = \mathbf{B}_c^u \hat{\mathbf{u}}_c \quad (3.3.3)$$

where  $\mathbf{B}_c^u$  is a  $3 \times 18$  matrix

$$\mathbf{B}_c^u = \begin{bmatrix} N_1 & 0 & 0 & \dots & N_3 & 0 & 0 & -N_1 & 0 & 0 & \dots & -N_3 & 0 & 0 \\ 0 & N_1 & 0 & \dots & 0 & N_3 & 0 & 0 & -N_1 & 0 & \dots & 0 & -N_3 & 0 \\ 0 & 0 & N_1 & \dots & 0 & 0 & N_3 & 0 & 0 & -N_1 & \dots & 0 & 0 & -N_3 \end{bmatrix} \quad (3.3.4)$$

Here, a  $3 \times 3$  rotation matrix  $\mathbf{R}$  transfers vectors from the global to the current local coordinate system

$$\mathbf{R} = \begin{pmatrix} \hat{\mathbf{n}} \\ \hat{\mathbf{t}}_1 \\ \hat{\mathbf{t}}_2 \end{pmatrix} \quad (3.3.5)$$

with three perpendicular components vectors  $\hat{\mathbf{n}}$ ,  $\hat{\mathbf{t}}_1$  and  $\hat{\mathbf{t}}_2$

$$\hat{\mathbf{n}} = \frac{1}{\left\| \frac{\partial \mathbf{x}}{\partial \xi} \times \frac{\partial \mathbf{x}}{\partial \eta} \right\|} \left( \frac{\partial \mathbf{x}}{\partial \xi} \times \frac{\partial \mathbf{x}}{\partial \eta} \right), \quad \hat{\mathbf{t}}_1 = \frac{1}{\left\| \frac{\partial \mathbf{x}}{\partial \xi} \right\|} \frac{\partial \mathbf{x}}{\partial \xi}, \quad \hat{\mathbf{t}}_2 = \hat{\mathbf{n}} \times \hat{\mathbf{t}}_1, \quad (3.3.6)$$

as displayed in Figure 3.5. The vector  $\hat{\mathbf{n}}$  is normal to the surface and  $\hat{\mathbf{t}}_1$  and  $\hat{\mathbf{t}}_2$  are tangential to the surface. Since the local coordinate system is established, the mechanical stiffness matrix of the cohesive element  $\mathbf{K}_{ce}^u$  is defined by

$$\mathbf{K}_{ce}^u = \sum_{I=1}^{n_p} \sum_{J=1}^{n_p} \int_{\Omega_t} \mathbf{B}_{cI}^{uT} \mathbf{R}^T \mathbb{C}_c^u \mathbf{R} \mathbf{B}_{cJ}^u dv, \quad (3.3.7)$$

where  $\mathbb{C}_c^u$  can be found in Equation (2.5.7) for the case of tension and in Equation (2.5.12) if compression is applied. The mechanical element residual  $\mathbf{r}_{ce}^u$  of the cohesive element is given by

$$\mathbf{r}_{ce}^u = \sum_{I=1}^{n_p} \sum_{J=1}^{n_p} \int_{\Omega_t} \mathbf{B}_{cI}^{uT} \mathbf{R}^T \mathbf{t}_c dv. \quad (3.3.8)$$

### Patch test of CZM

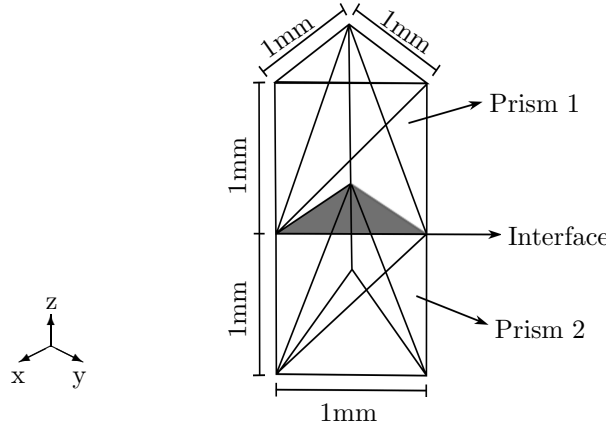


**Figure 3.6:** Geometry of patch test of CZM.

The following aim is to use a patch test for analyzing the behaviour of the CZM, see Figure 3.6 for illustration of the geometry with dimensions, which is constituted by two prisms comprised of three tetrahedral elements as well as a interface element with zero-thickness. Two prisms are assumed to behave elastically with identical YOUNG'S modulus and zero-thickness interface element is driven by CZM. The material properties of three components in the patch test are listed in Table 3.1.

Prescribing the tensile displacement boundary condition on the top surface in  $z$  direction and fixing the bottom surface in  $x$ ,  $y$  and  $z$  directions. This is called mode I, and the displacement in  $z$  direction and  $\sigma_{zz}$  of the patch test are displayed in Figure 3.7(a), from which the strong displacement jump across the interface and the uniform stress

Component	Property	Value
Prism 1	$E$	20000 (N/mm <sup>2</sup> )
Prism 1	$\nu$	0.0 (-)
Prism 2	$E$	20000 (N/mm <sup>2</sup> )
Prism 2	$\nu$	0.0 (-)
Interface	$f_t$	10.0 (N/mm <sup>2</sup> )
Interface	$G_f$	0.1 (N/mm)
Interface	$K_p$	500 (N/mm <sup>3</sup> )

**Table 3.1:** Mechanical parameters of the CZM patch test.

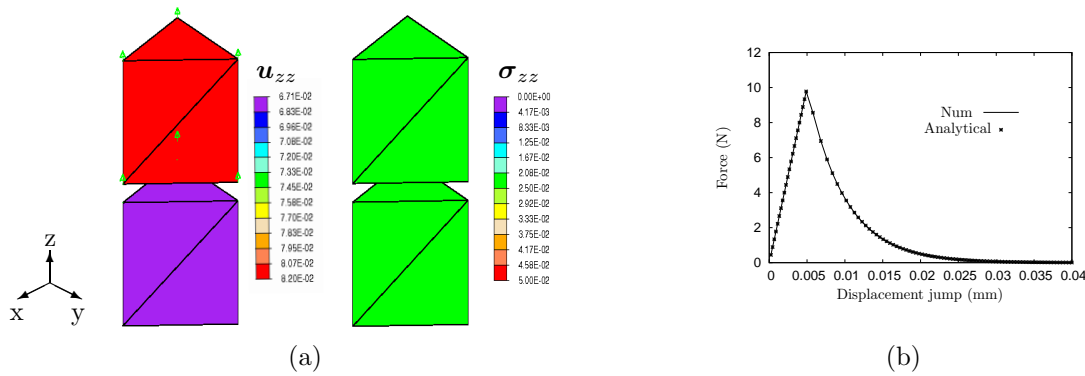


**Figure 3.7:** (a) Displacement in  $z$  direction and  $\sigma_{zz}$  of patch test in mode I and (b) comparison of analytical and numerical results in mode I.

in the two prisms are observed. The numerical force-displacement relationship on the upper surface coincides with the analytical traction-separation relationships of CZM as the displacement is increased, as can be seen in Figure 3.7(b).

### Numerical example of delamination

Delamination between composite layers, is one of the most common types of the failure in various materials, e.g. semiconductor (GOROLL & PUFALL (2012)), carbon-fibre composites (KOISSIN ET AL. (2013)). Figure 3.8 displays three different opening types according to the deformation of a crack. Mode I is the most important case for practical applications, which corresponds to a symmetric crack opening orthogonal to the local fracture surface. In mode II, the crack surfaces slide relatively to each other in the plane of the crack, thereby resulting in shear stresses in the concerning direction. In terms of mode III, the crack surfaces separate in the plane of the crack, parallel to the crack front.

The geometry of the delamination example is displayed in Figure 3.9, where interface elements with zero-thickness are inserted between two beams. In this example, two beams are assumed to behave elastically with the identical YOUNG's modulus. CZM motivates the interface elements, such that only the interface behavior is devoted to

Component	Property	Value
Upper beam	$E$	1000 (N/mm <sup>2</sup> )
Upper beam	$\nu$	0.0 (-)
Lower beam	$E$	1000 (N/mm <sup>2</sup> )
Lower beam	$\nu$	0.0 (-)
Interface	$f_t$	3.0 (N/mm <sup>2</sup> )
Interface	$G_f$	0.5 (N/mm)
Interface	$K_p$	3000 (N/mm <sup>3</sup> )

**Table 3.2:** Mechanical parameters of components for delamination example.

the failure of the beam structure, see Table 3.2 for the mechanical parameters of all components. Figure 3.10 present the VON-MISES stresses of the beam structure under boundary conditions of mode I, II and III respectively, as shown in Figure 3.8. Additionally, the macroscale displacement-force relationships of the beam structure under boundary conditions of mode I, II and III respectively are displayed in Figure 3.11. In Figure 3.11(a), the oscillation after the peak load is observed exists. Clearly, mesh refinement can alleviate the problem, see TURON ET AL. (2007) and NGUYEN & NGUYEN-XUAN (2013), however, the improvement is limited for some forms of traction-separation laws of CZM like bilinear. On the other hand, SCHELLEKENS & BORST (1993) used NEWTON-COTES integration scheme instead of GAUSS quadrature for integrating the tangent stiffness matrix and the internal forces vector of the

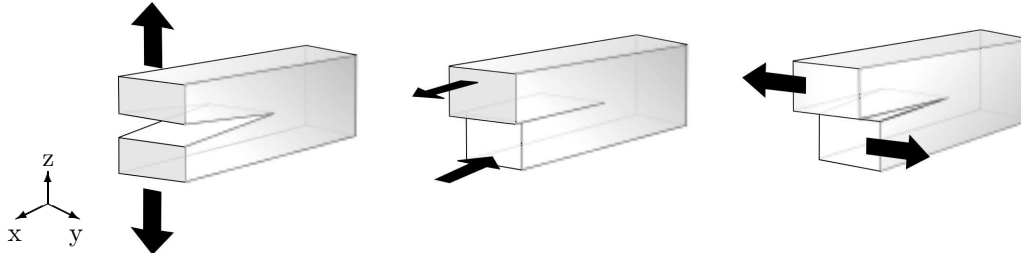


**Figure 3.8:** Different modes of fracture (a) mode I and (b) mode II and (c) mode III.

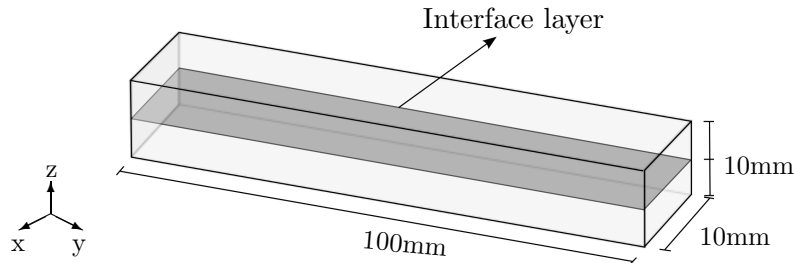


**Figure 3.9:** Geometric illustration of beam structure for delamination sample.

cohesive element if large stress gradients are present in the cohesive element, thus overcoming the problems of spurious oscillations. Moreover, as described in SAMIMI ET AL. (2011), the self-adaptive cohesive zone formulation is an efficient approach, enriching the displacement approximation along all four edges of quadrilateral interface elements located in the fracture process zone by adding bi-linear functions with mobile peaks as well as considering the process-driven positions of these peaks as additional degrees of freedom. Alternatively, the use of NUBRS and T-spline approaches were proven in NGUYEN & NGUYEN-XUAN (2013) and DIMITRI ET AL. (2014) to alleviate this problem successfully.

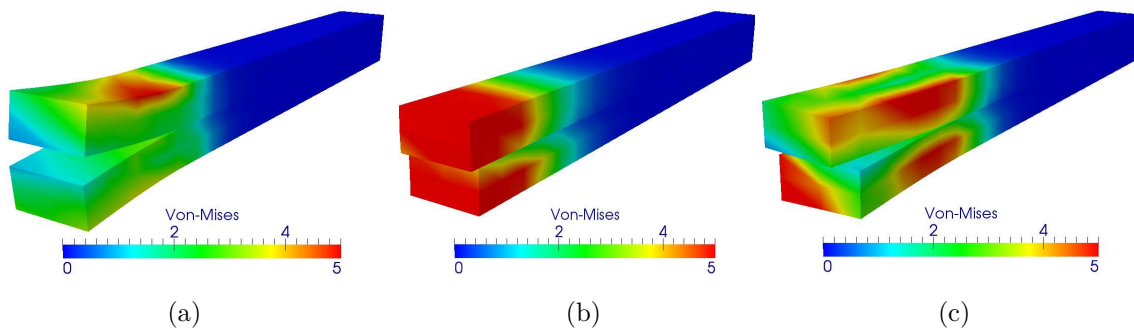


**Figure 3.10:** VON-MISES stresses (MPa) of beam structure in (a) mode I and (b) mode II and (c) mode III.

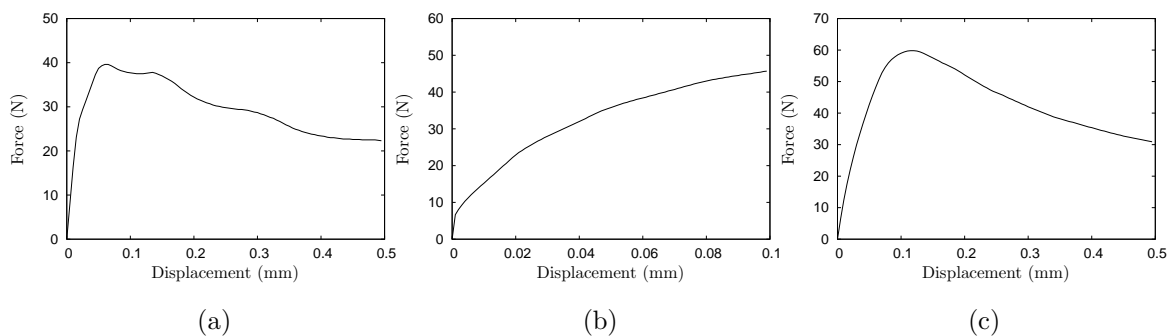


**Figure 3.11:** Macroscale displacement-force curve of beam structure in (a) mode I and (b) mode II and (c) mode III.

### 3.3.3 Thermal conduction across the interface in the FEM

To establish cohesive zone model together with a micromechanically motivated thermal flux-separation relation, the evolving thermal conduction across the crack interface has to be taken into account. In a single cohesive element, see Figure 3.5, the nodal

temperature vector is given by

$$\hat{\theta}_c = (\hat{\theta}_c^1, \hat{\theta}_c^2, \hat{\theta}_c^3, \hat{\theta}_c^4, \hat{\theta}_c^5, \hat{\theta}_c^6)^T . \quad (3.3.9)$$

The temperature jump across the interface is defined by

$$\llbracket \theta \rrbracket = \mathbf{B}_c^\theta \hat{\theta}_c , \quad (3.3.10)$$

with the aid of  $\mathbf{B}_c^\theta$

$$\mathbf{B}_c^\theta = [ N_1 \quad N_2 \quad N_3 \quad -N_1 \quad -N_2 \quad -N_3 ]^T . \quad (3.3.11)$$

where shape functions are introduced in Equation (3.3.2). Linearization of  $G_c^\theta$  in Equation (2.6.12) with respect to  $\theta$  leads to the thermal stiffness matrix of the interface phase  $\mathbf{K}_{ce}^\theta$

$$\mathbf{K}_{ce}^\theta = \sum_{I=1}^{n_p} \sum_{J=1}^{n_p} \int_{\Omega_t} \mathbf{B}_{cI}^{\theta T} (1 - D_c^\theta) k_c \mathbf{B}_{cJ}^\theta dv . \quad (3.3.12)$$

and the thermal element residual  $\mathbf{r}_{ce}^\theta$

$$\mathbf{r}_{ce}^\theta = \sum_{I=1}^{n_p} \sum_{J=1}^{n_p} \int_{\Omega_t} \mathbf{B}_{cI}^{\theta T} q_c dv , \quad (3.3.13)$$

where  $q_c$  is given in Equation (2.5.16).

### Patch test of thermal conduction across the interface

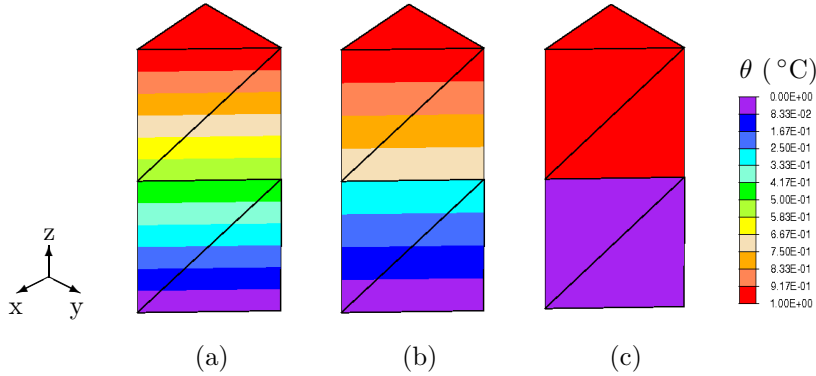


**Figure 3.12:** Temperature distribution in patch test with respect to different thermal conductivity of interface (a) 10000 (w/Mk) and (b) 1 (w/Mk) and (c) 0.01 (w/Mk).

The geometry of the thermal patch test across the interface is the identical to the pure mechanical one, see Figure 3.6. The thermal conductivities of both prisms are assumed to be 1.0 W/m.K. When the interface element with zero-thickness is utilized, no physical parameter can be defined for the thermal conductivity of the interface, therefore, a

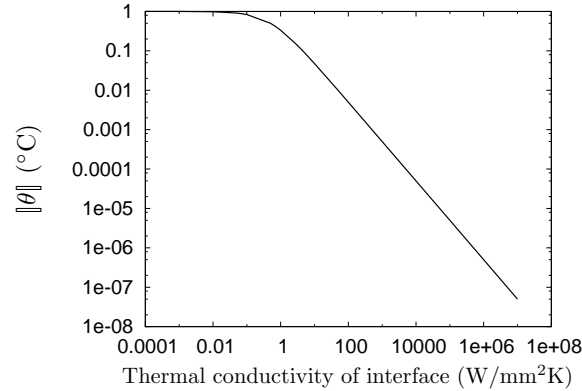


**Figure 3.13:** Temperature jump across the interface in patch test as a function of thermal conductivity of interface.

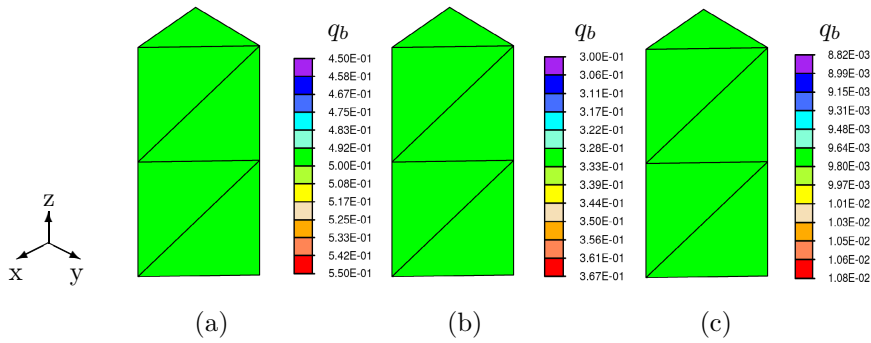


**Figure 3.14:** Thermal flux ( $\text{W}/\text{mm}^2$ ) in  $z$  direction in patch test with different thermal conductivity of interface (a) 10000 ( $\text{W}/\text{mm}^2\text{K}$ ) and (b) 1 ( $\text{W}/\text{mm}^2\text{K}$ ) and (c) 0.01 ( $\text{W}/\text{mm}^2\text{K}$ ).

penalty parameter originating from contact mechanics represents the thermal conductivity of the interface. In this case, the infinitely large penalty parameter results in the perfect thermal conduction across the interface. However, the infinitely large penalty number leads to the ill-conditioning of the stiffness matrix. Hence, a sufficiently large penalty number is chosen. Here, an artificial thermal conductivity of the interface is applied instead of  $(1 - D_c^\theta)k_c$  in Equation (3.3.12) in the numerical simulation, so as to solve the pure thermal conduction across the interface. Constant temperature of  $1.0^\circ\text{C}$  is prescribed on the top surface. Figure 3.12 illustrates the temperature distribution and Figure 3.13 illustrates the temperature jump  $\|\theta\|$  across the interface as the thermal conductivity of the interface or equivalently the penalty parameter is increased. It indicates that the infinitely large penalty parameter leads to the infinitely small temperature jump across the interface. Moreover, Figure 3.14 presents not only the existence of the uniform thermal flux  $\mathbf{q}_b$  of prisms in  $zz$  direction indicated by the LC interface model in Subsection (2.5.3) but the issue that the thermal flux  $\mathbf{q}_b$  is also reduced when the thermal conductivity of the interface is decreased.

### 3.3.4 Diffusion across the interface in the FEM

Similar to the case of thermal conduction across interface, the nodal humidity vector  $\hat{s}_c$  in the global coordinate system is written as

$$\hat{s}_c = (\hat{s}_c^1, \hat{s}_c^2, \hat{s}_c^3, \hat{s}_c^4, \hat{s}_c^5, \hat{s}_c^6)^T . \quad (3.3.14)$$

With the aid of  $\mathbf{B}_c^s$

$$\mathbf{B}_c^s = [ N_1 \quad N_2 \quad N_3 \quad -N_1 \quad -N_2 \quad -N_3 ]^T , \quad (3.3.15)$$

where shape functions are defined in Equation (3.3.2). The humidity diffusion across the interface can be defined as

$$\|s\| = \mathbf{B}_c^s \hat{s}_c . \quad (3.3.16)$$

The linearization of  $G_c^s$  in Equation (2.6.18) with respect to  $s$  yields the diffusion tangent element stiffness matrix  $\mathbf{K}_{ce}^s$

$$\mathbf{K}_{ce}^s = \sum_{I=1}^{n_p} \sum_{J=1}^{n_p} \int_{\Omega_t} \mathbf{B}_{cI}^{sT} (1 + M) d_c \mathbf{B}_{cJ}^s dv , \quad (3.3.17)$$

and the diffusion element residual  $\mathbf{r}_{ce}^s$

$$\mathbf{r}_{ce}^s = \sum_{I=1}^{n_p} \sum_{J=1}^{n_p} \int_{\Omega_t} \mathbf{B}_{cI}^{sT} j_c dv , \quad (3.3.18)$$

where  $j_c$  is given in Equation (2.5.23).

#### Patch test of diffusion across imperfect interface

As the diffusivity of aggregate is much lower than the one of HCP, a patch test imitating the case in concrete is established for the analysis of humidity diffusion across the interface. The diffusivities of prisms are set to be 1.0cm<sup>2</sup>/h and 0.01cm<sup>2</sup>/h. The constant humidity boundary condition is prescribed on the top surface. Concerning different diffusivity of interface, the humidity distribution are shown in Figure 3.15. Also, Figure 3.16 illustrates the humidity jump  $\|s\|$  as the diffusivity of interface rises, resembling the thermal conduction result in Figure 3.13 .

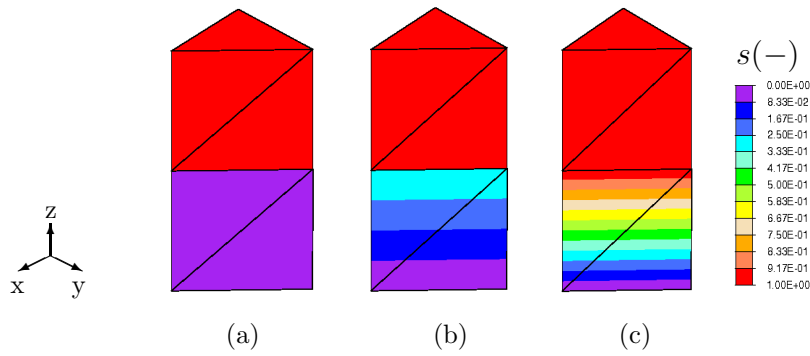


**Figure 3.15:** Humidity distribution in patch test with different diffusivity of interface element (a) 10000 (m/s) and (b) 1 (m/s) and (c) 0.01 (m/s).

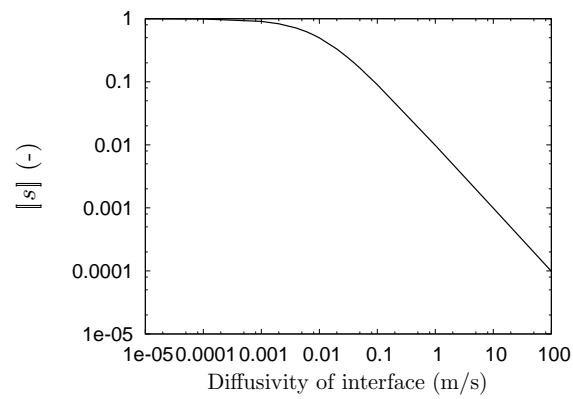


**Figure 3.16:** Humidity jump cross the interface as a function of diffusivity of the interface.



# Chapter 4

## Alkali-Silica Reaction

The existence of the chemical reaction between the alkali from the cement paste and the silica from aggregates in the concrete, namely alkali-silica reaction (ASR), was first pointed out by HOLDE in 1935, and then the harm of ASR to the concrete was found by STANTON in 1940. The hydraulic structure “Parker Dam” was first diagnosed to be affected by ASR in 1941. Later on, more concrete structures suffered from ASR were continuously reported in different countries, thereby raising demands for reliable approaches to reassess the extent of the reaction and to inhibit such reaction. In addition, since ASR is a long-term reaction, it is artificially accelerated in laboratories with high temperature and high humidity. As a consequence of the development of modern technologies, such as scanning electron microscope (SEM) and computed tomography (CT), it enables to visualize the ASR induced failure of the concrete at the lower scale. For instance, SEM images in Figure 4.1 display the ASR induced microcracks in two concrete specimens, which was conducted by BERNARDES at Universidade Estadual Paulista Júlio de Mesquita Filho in Brazil.

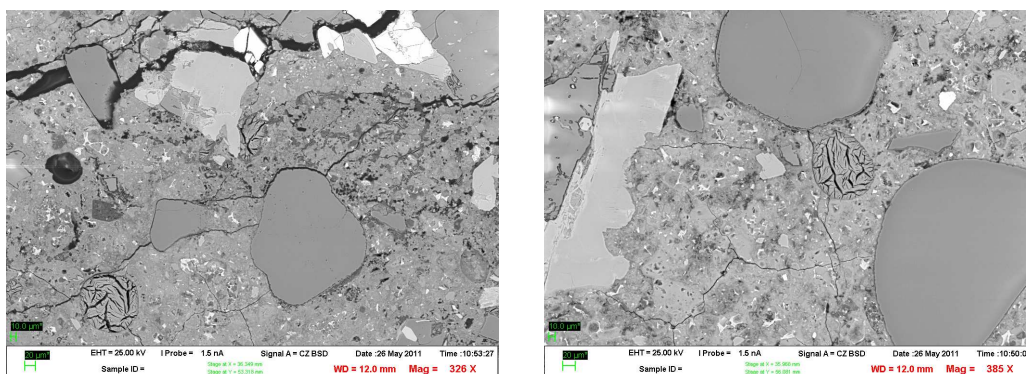


**Figure 4.1:** SEM images presenting microcracks in two concrete samples subjected to ASR (Universidade Estadual Paulista Júlio de Mesquita Filho, Brazil).

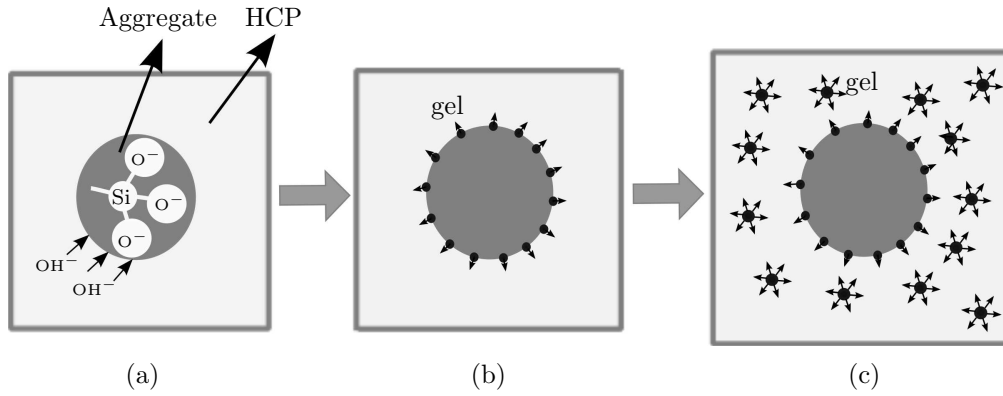
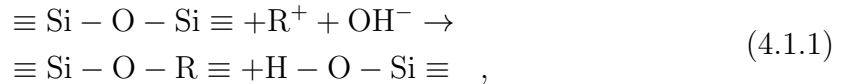


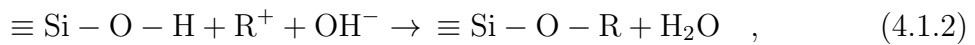
**Figure 4.2:** Overall chemical mechanism of ASR (a)  $\text{OH}^-$  from the pore solution in the cement paste attacks siloxane networks in aggregates (b) production of the amorphous gel (c) expansion of the gel in the presence of water.

## 4.1 Chemical mechanism of ASR

ASR, discovered in the 1940s, is a long-term chemical reaction and detrimental to the concrete structure. ASR is characterized by the breakdown of the siloxane bonds (Si-O) in poorly crystallized silica of aggregates, which is attacked by the hydroxyl ions  $\text{OH}^-$  in micropores from the cement paste. It leads to the formation of an amorphous alkali-silica gel, which swells in the presence of the water and exerts pressure on the surrounding material. Hence, it induces micro-and, eventually, macro-cracking of the structure, see ULM ET AL. (2000), BAŽANT & STEFFENS (2000) and LEMARCHAND ET AL. (2005). As illustrated in Figure 4.2, the complex mechanism of ASR can be generally summarized into two steps. In the first step, as shown in Figure 4.2(a), the attacks of hydroxyl ions break the siloxane networks of aggregates, thereby yielding the silicic acid



where  $\text{R}^+$  denotes alkali ions ( $\text{Na}^+$  and  $\text{K}^+$ ). Due to the characteristics of weak acid, the produced silicic acid immediately reacts with hydroxyl ions



producing the amorphous alkali-silica gel. As shown in Figures 4.2(b) and 4.2(c), the second step is comprised of the production of the gel and the expansion of the gel by absorption of free water



where  $n$  is the hydration number. The resulting expansion stress leads to the formation of the failure of the concrete. Overall, three factors are indispensable for ASR:

- alkali content from the pore solution in the cement paste,

- poorly crystallized silica in aggregates,
- moisture content.

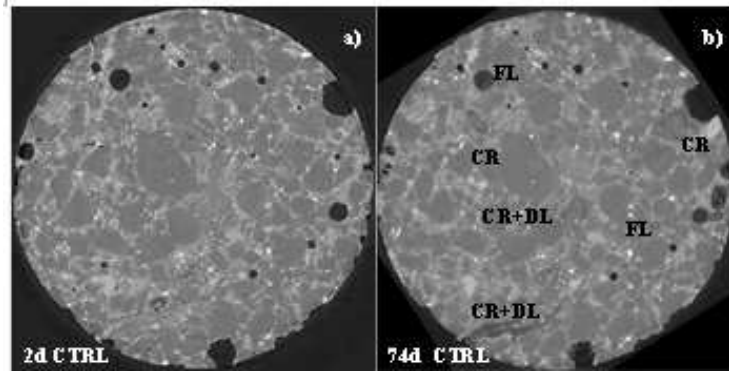


**Figure 4.3:** Two-dimensional micro-CT images of concrete sample suffered from ASR at 2 and 74 days (University of California, Berkeley, 2013).

For illustrative purpose, two- and three-dimensional micro-CT images obtained at University of California, Berkeley, are displayed in Figures 4.3 and 4.4, which offer a limpid manner to describe the ASR process in the concrete. For instance, Figure 4.3 illustrates two-dimensional images obtained for the same cross-section of the concrete sample suffered from ASR at 2 and 74 days respectively. As shown in Figure 4.3, no ASR occurred at 2 days, while it was observed at 74 days when reactive aggregates dissolved (indicated as DL), the neighbouring pores were filled with ASR gel (indicated as FL) and microcracks were also filled with ASR gel (indicated as CR+DL).

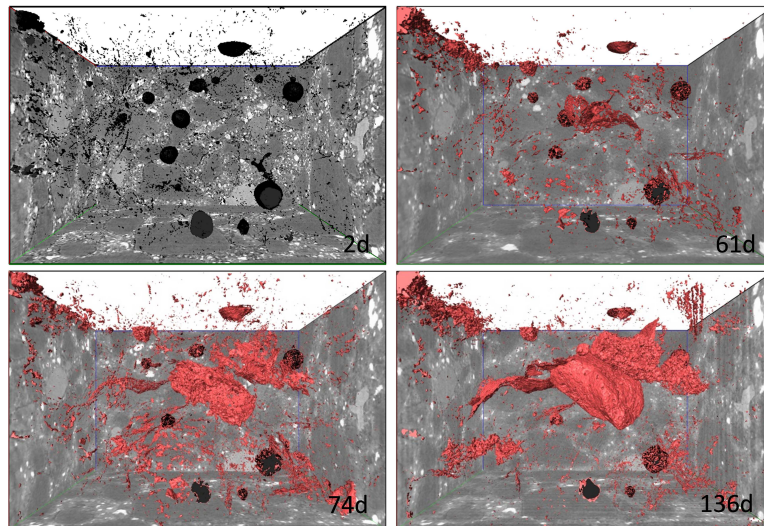


**Figure 4.4:** Three-dimensional micro-CT images of concrete sample suffered from ASR at 1, 61, 74 and 136 days (University of California, Berkeley, 2013).

The three-dimensional volume rendered images offer a better insight into the phenomenon of ASR, see Figure 4.4. At 2 days, one can observe the distribution of voids

as well as gaps due to entrained air. At 61 days, the phenomenon that voids were filled, aggregate dissolved and few cracks were formed in some defected aggregates, implies the existence of ASR. At 74 days and 136 days, the dissolution of aggregates turned stronger and cracks were propagated through the matrix, voids and some aggregates. The closely related values of grey scale between gaps, cracks and ASR gel yields the difficulty in the three-dimensional segmentation. Thus, some features seem to disappear on the image at 136 days.

### 4.1.1 Review of theoretical models of ASR

As mentioned before, two stages of the mechanism of ASR are summarized: the non-instantaneous dissolution of the silica in aggregates and the instantaneous swelling of the gel. During the dissolution stage, the hydroxyl ions  $\text{OH}^-$  from the pore solution in the HCP attack the amorphous or poorly crystalline silica in aggregates, thereby breaking the siloxane bonds of silanol groups (Si-O). The phenomenon of the dissolution occurring at the interface between aggregates and the pore solution in the HCP has already been well understood, see LEMARCHAND ET AL. (2005). At the second stage, due to the hydrophilic property, the gel swells in the presence of water and exerts pressures on the surrounding HCP, thus forming micro- and macro-cracking of the concrete structure, yet it is still a challenging topic to thoroughly explain this stage. However, a series of theoretical models have been developed to explain this mechanism from different points of view. For instance, a micromechanical approach accounting for *topochemical* and *through-solution* mechanisms was proposed by LEMARCHAND ET AL. (2005). In detail, the *topochemical* mechanism assumed that the gel was generated at sites of the dissolution of the silica, while *through-solution* mechanism proposed that the gel was produced in porous locations. As explained in MCGOWAN & VIVIAN (1952), a solid layer was formed on the surface of the aggregate to absorb the water from the pore solution in the HCP, and then the solid substance was transferred to the gel. MULTON ET AL. (2009) proposed that the gel was generated inside aggregates after alkali and hydroxyl ions diffused into aggregates and broke silanol bonds. Then, the gel permeated through the connected porous volume between aggregates and HCP, hence, the gel was maintained inside aggregates and generated. As pointed out by IDORN (2001), GARCIA-DIAZ ET AL. (2006) and ICHIKAWA & MIURA (2007), the aggregate was tightly packed by an insoluble rim, allowing the penetration of the alkaline solution, rather than the viscous alkali-silica gel. Similarly, HAHA ET AL. (2007) and DUNANT & SCRIVENER (2010) highlighted the predominant effect of the formation of the gel in aggregates, thereby resulting in the damage in aggregates themselves and subsequently in the surrounding cement paste. PONCE & BATIC (2006) addressed the overall conclusion that the different locations of the gel reported in HAHA ET AL. (2007), MULTON ET AL. (2009) and DUNANT & SCRIVENER (2010) can be explained by types of aggregates. The experiment in PONCE & BATIC (2006) captured that cracking patterns of ASR-affected concrete rely on the mineralogical nature of aggregates through petrographic examination with a stereobinocular and a polarizing microscope. It was also observed that aggregates such as opal and vitreous volcanic

rocks result in the formation of the gel at the interface between the aggregate and the cement paste, thus causing cracks in the cement paste. On the other hand, mixed mineralogy aggregates form cracks in both aggregates and cement paste. The general review of theoretical models concerning the formation site of the ASR gel is listed in Table 4.1.

Site of Gel	Reference	Description
Inside aggregates	IDORN (2001), GARCIA-DIAZ ET AL. (2006), HAHN (2006), ICHIKAWA & MIURA (2007), DUNANT & SCRIVENER (2010)	gel was formed inside aggregates, thus leading to the failure in aggregates themselves and subsequently in the surrounding cement paste
Thickness layer	MCGOWAN & VIVIAN (1952), MULTON ET AL. (2009)	gel permeated through the connected porous volume to form the gel layer with certain thickness in the vicinity of aggregates
Topomechanical	LEMARCHAND ET AL. (2005)	gel was generated at the interface between cement paste and aggregates, where hydroxyl ions from the pore solution in the cement paste attack the poorly silica networks in aggregates.
Through-solution	DRON & BRIVOT (1993), LEMARCHAND ET AL. (2005)	gel was formed in the porous space of cement paste

**Table 4.1:** General review of theoretical models of ASR concerning the formation site of the ASR gel.

#### 4.1.2 Review of numerical models of ASR

During the last decade, a considerable number of numerical models have been developed to predict the ASR induced failure at different length-scales of concrete. HUANG & PIETRUSZCZAK (1996) established the correlation between the expansion strain due to ASR and the mechanical degradation at the macroscale of the concrete, where the expansion strain had a similar formulation with the thermal dilation strain. An advanced thermo-chemo-mechanical model was developed by ULM ET AL. (2000) in the framework of BIOT's theory, where the concrete was conceived as a two-phase material including the expansive gel and the homogenized concrete skeleton. Moreover, the volumetric expansion of the gel was evaluated as a function of the reaction kinetics, which is influenced by the temperature. COMI ET AL. (2012) developed the model based on ULM ET AL. (2000), where not only temperature but also relative humidity contribute to the extent of the reaction. In addition, the investigation on ASR at the macroscale of the concrete was developed by BANGERT ET AL. (2004), where

the concrete was treated as a mixture of three superimposed constituents through the theory of porous media: skeleton, pore liquid and pore gas. The model was based on converting the mass of unreacted material into the mass of the reacted material in the skeleton. Various analytical models based on empirical equations were also developed to explain ASR at the mesoscale of the concrete, see BAŽANT & STEFFENS (2000) and MULTON ET AL. (2009). For instance, BAŽANT & STEFFENS (2000) proposed that the chemical reaction kinetics was related to the diffusion process of the reactants, leading to the subsequent fracture in the characteristic unit cell of the concrete modeled with one spherical glass particle. Detailed numerical models at the mesoscale were limited. COMBY-PEYROT ET AL. (2009) introduced a three-dimensional mesoscopic model, where aggregates were randomly distributed in the cement matrix. The damage in the cement matrix was caused by the isotropic dilatation phenomenon in the reactive aggregates induced by ASR. DUNANT (2009) and DUNANT & SCRIVENER (2010) proposed a two-dimensional finite element/extended finite element framework to qualitatively depict the ASR induced deterioration at the mesoscale of the concrete. The growing gel pockets defined in aggregates triggered the damage to them, where the geometry of gel swelling was represented by updating the enrichment function. ALNAGGAR ET AL. (2013) adopted the framework of the lattice discrete particle model (LDPM) to capture the ASR induced crack patterns at the mesoscale of the concrete. The expansion of the gel occurred at the level of each individual aggregate particle. Due to the lack of reliable microscale models and representations, no results have been found at the microscale of the concrete with applications to ASR. A general review of numerical models on ASR is described in Table 4.2. For more details, the reader is referred to HAHA ET AL. (2007), PAN ET AL. (2012) and references therein.

Length scale	Multiphysics	References	General Description
Macroscale	Mechanical	CHARLWOOD (1994), THOMPSON ET AL. (1994), PIETRUSZCZAK (1996), CAPRA & SELLIER (2003), HERRADOR ET AL. (2009)	Extensive work has been carried out to identify the expansion strain as a function of the stress tensor
Macroscale	Chemo-mechanical	LEGER ET AL. (1996), FARAGE ET AL. (2004), FAIRBAIRN ET AL. (2006), SAOUMA & PEROTTI (2006), MULTON ET AL. (2009)	A nonlinear relation between the expansion strain of concrete and the chemical extent was adopted to construct a model at the structural level
Macroscale	Hydro-thermo-chemo-mechanical	HUANG & PIETRUSZCZAK (1996), ULM ET AL. (2000), COMI ET AL. (2009), BANGERT ET AL. (2004), COMI ET AL. (2012), PESAVENTO ET AL. (2012)	Temperature and relative humidity contributed to the chemical extent of ASR and the expansion strain, leading to the failure of the concrete structure
Mesoscale	Chemo-mechanical	BAŽANT ET AL. (2000), SHIN (2009), DUNANT (2009), DUNANT & SCRIVENER (2010), CHARPIN & EHRLACHER (2012), COMBY-PEYROT ET AL. (2009)	Randomly distributed aggregates were embedded in the matrix to represent the mesoscale of the concrete. The formation and expansion of ASR gel were described at the level of each individual aggregate. Influences of aggregates on the expansion strain and the subsequent damage in the concrete were taken into account
Microscale	Hydro-thermo-chemo-mechanical	Current work	It initializes the analysis of ASR at the microscale of HCP and investigates the correlation between damage due to ASR and chemical extent. The extent is influenced by the temperature and the relative humidity. The ASR induced damage at the microscale is upscaled to the mesoscale via computational homogenization towards observable failure

**Table 4.2:** General review of numerical models of ASR.

ASR is a complex chemical reaction and its mechanisms at the material level are still in dispute. Some numerical models concerning ASR have already been successfully set up at the macro- and meso-scale of the concrete. The objective of the present work is to establish a multiscale computational framework for predicting ASR induced damage where, for the first time to the best knowledge of the authors'. The analysis on ASR is carried out at the microscale of the concrete and the ASR induced deterioration is upscaled to the mesoscale. The general scope of the study is as follows:

- to investigate the contribution of the chemical extent of ASR to the expansion strain of the gel at the micropore and the resulting deterioration of HCP,
- to obtain the correlation between the effective mesoscale damage due to ASR and the chemical extent through computational homogenization,
- to carry out hydro-thermo-chemo-mechanical coupling based on a staggered method at the mesoscale, where transient temperature and relative humidity are employed, thereby establishing a multiscale and multiphysics model to predict the failure due to ASR.

## 4.2 Kinetics of ASR

ASR can be specifically modeled as a two-stage process, involving the dissolution of the silica and the swelling of the gel. DRON & BRIVOT (1993) proposed that the dissolution stage can be described by a first-order kinetic law, which was widely adopted by LARIVE (1998), ULM ET AL. (2000), COMI ET AL. (2009), COMI ET AL. (2012). In addition, LARIVE (1998) verified the dependence of the chemical reaction kinetics on the temperature and the relative humidity.

### 4.2.1 Chemical reaction kinetics

The aforementioned first-order kinetics law can be expressed as

$$\tilde{t} \frac{d\xi}{dt} = 1 - \xi \quad , \quad (4.2.1)$$

where  $t$  is the time,  $\tilde{t}$  is the intrinsic time of the reaction and  $\xi \in [0, 1]$  is the chemical extent, measuring the progression of the reaction:  $\xi = 0$  is the beginning and  $\xi = 1$  is the end. For macroscopic experiments,  $\xi$  is defined by the ratio between the current expansion strain and the terminal one of the concrete specimen. An explicit equation of  $\tilde{t}$  was proposed in LARIVE (1998)

$$\tilde{t} = \tau_{ch} \frac{1 + \exp[-\tau_{lat}/\tau_{ch}]}{\xi + \exp[-\tau_{lat}/\tau_{ch}]} \quad , \quad (4.2.2)$$

where  $\tau_{lat}$  is the latency time and  $\tau_{ch}$  is the characteristic time, corresponding to the initiation and the development period of ASR respectively. LARIVE (1998) addressed that  $\tau_{lat}$  and  $\tau_{ch}$  rely on the temperature and the relative humidity. If only the temperature  $\theta$  is taken into account, the dependence was proposed in the form

$$\tau_{lat}(\theta) = \tau_{lat}(\theta_0) \exp[U_{lat}(1/\theta - 1/\theta_0)] \quad , \quad (4.2.3)$$

$$\tau_{ch}(\theta) = \tau_{ch}(\theta_0) \exp[U_{ch}(1/\theta - 1/\theta_0)] \quad , \quad (4.2.4)$$

where  $\theta_0 = 38^\circ\text{C}$  is the reference temperature, and  $U_{lat}$  and  $U_{th}$  are the ARRHENIUS activation energies ( $U_{ch} = 5400 \pm 500 \text{ K}$  and  $U_{lat} = 9400 \pm 500 \text{ K}$ , see ULM ET AL. (2000)). The explicit equation of the chemical extent  $\xi$  for the isothermal case is obtained by taking the integral of Equation (4.2.1):

$$\xi(t, \theta) = \frac{1 - \exp(-t/\tau_{ch}(\theta))}{1 + \exp(-t/\tau_{ch}(\theta) + \tau_{lat}(\theta)/\tau_{ch}(\theta))} \quad . \quad (4.2.5)$$

In Figure 4.5, the *S-shape* curve illustrates the chemical extent under constant temperature  $\theta = 25^\circ\text{C}$  with respect to days, where the regions and physical meanings of the latency time and the characteristic time are indicated. Overall, the *S-shape* curve represents three stages of ASR: initiation, reaction and exhaustion.

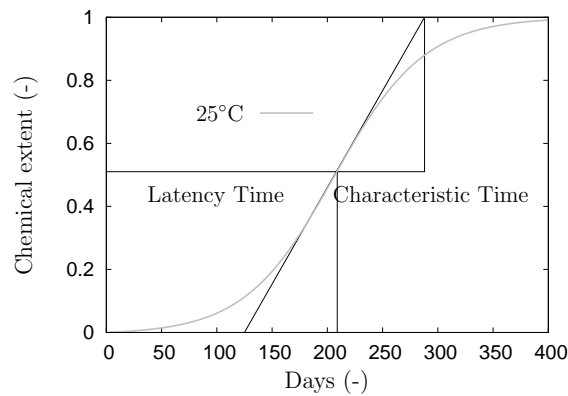


**Figure 4.5:** Latency time and characteristic time in the *S-shape* curve of chemical extent under constant temperature.

## 4.2.2 Influence of temperature on chemical extent

It is well understood that ASR is thermally activated, according to either the ARRHENIUS law or the experiment from LARIVE (1998), such that the higher the temperature is, the faster the reaction is. Studies associated with the influence of the temperature on the chemical extent  $\xi$  and the subsequent deterioration in the concrete have already been reported, see ULM ET AL. (2000) and COMI ET AL. (2012). Clearly, the chemical extent  $\xi$  as an irreversible internal variable can be calculated based on various temperature history inputs. Figure 4.6 present some examples of temperature variations with time and the calculated chemical extent.

## 4.2.3 Influence of relative humidity on chemical extent

As indicated in KURIHARA & KATAWAKI (1989) and NILSSON (1989), the influence of the relative humidity on ASR is another significant concern. Here, water has two main functions:

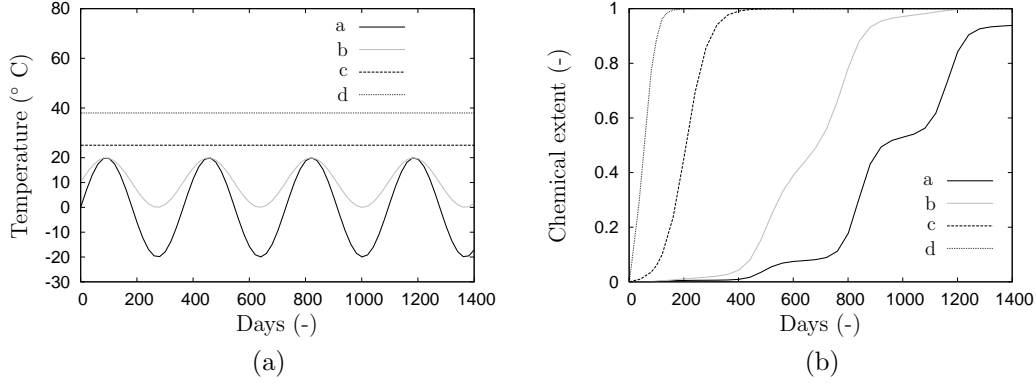


**Figure 4.6:** (a) Various temperature histories with respect to days and (b) the calculated chemical extent history under the imposed temperature variation.

- transport medium of the ionic species,
- reactant in the swelling of the amorphous gel.

KURIHARA & KATAWAKI (1989) and TOMOSAWA ET AL. (1989) have indicated that ASR can be inhibited if the relative humidity in the concrete is below certain threshold. NILSSON (1989) explained that there is no ASR induced degradation when the relative humidity drops below 0.8. LUDWIG (1989) stated that the threshold quantity of the relative humidity to initialize ASR is between 0.8 and 0.85 under a constant temperature of 20°C. Different threshold values found in the literature can be explained by different experimental conditions and mixtures of the concrete. The experimental data from LARIVE (1998) introduced the dependence of the latency time and the characteristic time on the relative humidity, see Figure 4.7, where the threshold value of relative humidity to activate the reaction is around 0.6. This observation is adopted in this contribution. LARIVE (1998) provided the experimental data of the latency time and the characteristic time with respect to saturation degree. Due to mechanisms of molecular absorption/desorption, capillary condensation, surface tension and disjoining pressure, a nonlinear relationship has been found between the saturation degree and the relative humidity, which is complexly affected by the temperature, see WU ET AL. (2012). In this work, the effects of absorption and desorption are not taken into account. Saturation degree is ideally replaced by the relative humidity. The discrete sampling data with respect to the relative humidity from LARIVE (1998) can be approximated by the continuous functions through

$$\tau_i(\theta, s) = \left( \tau_i(\theta_0, 1) + \frac{\tau_i(\theta_0, 0) - \tau_i(\theta_0, 1)}{1 + a_{1,i} \exp\left[-\frac{a_{2,i}(1-2s)}{s(1-s)}\right]} \right) \exp\left[U_i \left(\frac{1}{\theta} - \frac{1}{\theta_0}\right)\right], \quad i = (ch, lat) \quad , \quad (4.2.6)$$

where  $s$  is the relative humidity and subscribes  $i = (ch, lat)$  indicate the latency time and the characteristic time, respectively. In addition, 0 and 1 in the dependence of  $\tau_i$  represent the beginning and the end of the chemical reaction. The dependence of the chemical extent on the moisture content assumed in Equations (4.2.6) was first

proposed in COMI ET AL. (2012). Coefficients of approximations are listed in Table 4.3 and the corresponding curves in Figure 4.7.

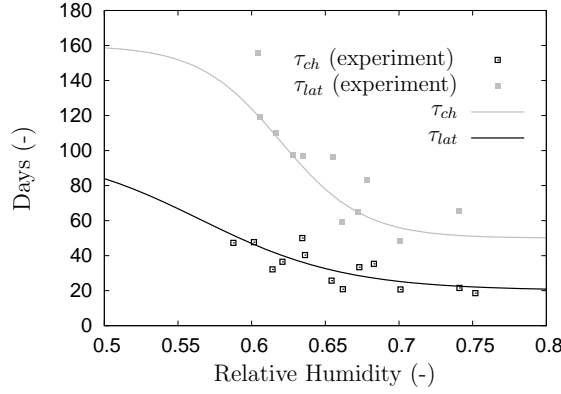


**Figure 4.7:** Experimental data from LARIVE (1998) and their approximations to take into account the effect of the relative humidity on the latency time and the characteristic time.

$i$	$\tau(\theta_0, 0)$ (Days)	$\tau(\theta_0, 1)$ (Days)	a1	a2
$t_{lat}$	160	50	20	-18.5222
$t_{ch}$	100	20	1	-10.52

**Table 4.3:** Coefficients of approximations to take into account the effect of the relative humidity on the latency time and the characteristic time.

Approximate curves in Figure 4.7 can be transferred into the expression of the chemical extent  $\xi$  in Equation (4.2.5), so that the effect of the relative humidity on ASR be incorporated into the present framework. In order to capture the irreversible characteristics of ASR while taking into account the effect of the relative humidity, Equations (4.2.5) and (4.2.6) are utilized to calculate the chemical extent  $\xi$ , where the relative humidity contributes to the latency time and the characteristic time through Equation (4.2.6). Subsequently, the obtained time quantities are adopted to calculate the chemical extent  $\xi$  through Equation (4.2.5). Examples of relative humidity histories with respect to days and the corresponding results for the chemical extent  $\xi$  are shown in Figure 4.8. Influences of the temperature and the relative humidity on the chemical extent  $\xi$  have so far been investigated separately. In order to involve both influences simultaneously, the combination of Equations (4.2.3), (4.2.4) and (4.2.6) are employed, see Figure 4.9, where the latency time and the characteristic time are functions of the temperature and the relative humidity. This establishes the basis of hydro-chemo-thermo coupling in the present work.

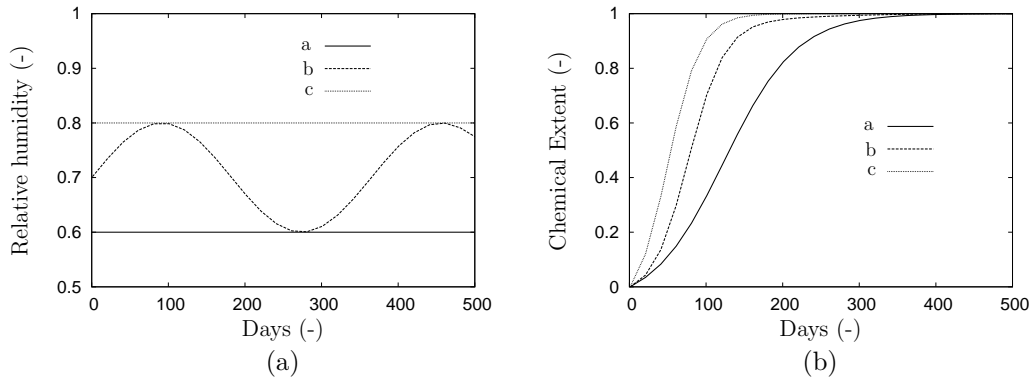


**Figure 4.8:** (a) Various relative humidity inputs with respect to days and (b) the corresponding chemical extent evolutions.

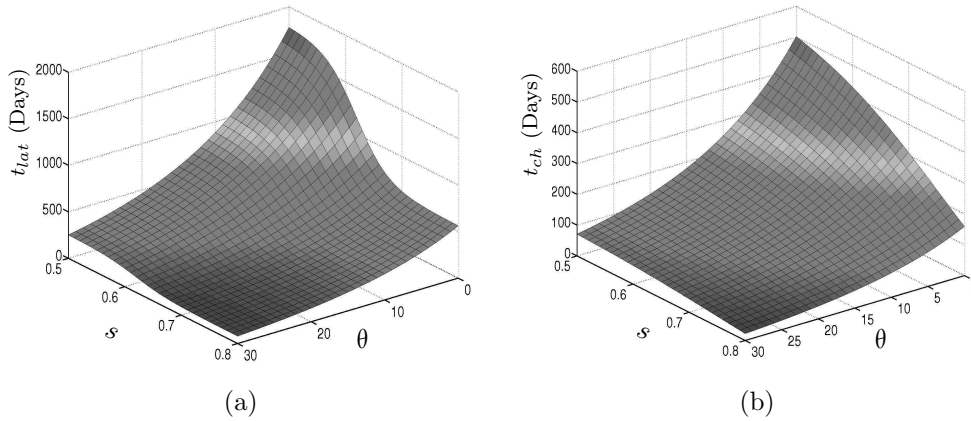


**Figure 4.9:** (a) The latency time and (b) the characteristic time, as functions of the temperature and the relative humidity.

#### 4.2.4 Fundamentals and assumptions

In the laboratory, the reaction is often accelerated by enforcing high temperature and large relative humidity, yet is still relatively slow. In Section 2.1, the obtained *S-shape* curve originating from Equation (4.2.5) captures two important stages of ASR: the initiation and the development periods, see LUDWIG (1989) and LEMARCHAND ET AL. (2005). The influences of the temperature and the relative humidity on the chemical extent are analyzed in Sections 4.2.2 and 4.2.3. It is noted that the observation that higher temperature and larger relative humidity cause larger expansion strain of the concrete specimen induced by ASR can be found in LUDWIG (1989) and LEMARCHAND ET AL. (2005), but this issue is not taken into account in this work. Previous work on the mechanisms of ASR was presented in Section 4.1.2. It is recalled that the ASR mechanism is not fully resolved. The objective of the present work is to initiate the investigation of the deterioration due to ASR at the microscale of HCP, and then to build the link between the microscale and the mesoscale of the concrete. Before moving further, some significant assumptions and simplifications need to be addressed:

- Despite the presence of several proposes regarding ASR is according to the experimental observation, the present work concentrates on the through-solution mechanism, see LEMARCHAND ET AL. (2005): gels are produced in micropores of HCP, and they exert pressure uniformly on the surrounding material,
- Gel rapidly fills up the micropore of HCP once ASR starts, yet exerting no pressure on the surrounding material at the beginning. In other words, the transition from the dissolution stage to the swelling stage is not modeled,
- The expansion strain of the gel at the microscale is defined by the product of the expansion coefficient of the gel and the chemical extent  $\xi$ . In addition, the expansion coefficient of the gel is assumed to remain permanent during the chemical reaction: it is independent of the temperature, relative humidity, time and position,
- The expansion induced by ASR at the micro and macroscale is assumed to be isotropic,
- The influences of reactivity types and the size of aggregates are not taken into account, see HAHA ET AL. (2007) and DUNANT & SCRIVENER (2010),
- Mild damage is considered,
- Scalar multiscale variables are typically projected as constants from the upper to the lower scales, as indicated in YU & FISH (2002) and TEMIZER & WRIGGERS (2010a). Complying with this observation, temperature and humidity mediated chemical extent variable is projected uniformly into the micropores of representative volume element (RVE) at the microscale of HCP. Hence, the analysis of the microscale does not require a full numerical coupling among all fields.

Based on assumptions mentioned above, a coupled hydro-thermo-chemo-mechanical simulation framework for the mesoscale of concrete will be developed in the remaining sections. For this purpose, each scale of concrete is treated next in an interactive fashion.



# Chapter 5

## Multiscale representation of concrete

The characteristics of low costs and recyclability render concrete with broad applications in the area of civil engineering, such as dams, roads, skyscrapers and among others. The concrete structures are subjected to various environmental attacks, e.g. frost (HAIN & WRIGGERS (2008a)), ASR (ULM ET AL. (2000)) as well as mechanical overload (DENARIÉ ET AL. (2006)), thereby leading to macrocracks and failure in concrete. The resulting problems can be explained by the variation or the deterioration of the underlying microstructure. For this reason, the development of a reliable analysis tool is motivated towards better understanding of inherent microstructure of concrete. However, highly heterogeneous microstructures at different length-scales of concrete raise difficulty in analyzing the performance of concrete. Specifically, at the *macroscale*, the concrete is treated as a homogeneous material. One scale lower, the *mesoscale*, includes a binding matrix, aggregates and pores with broad size distribution as well as interfacial zones (ITZ) between aggregates and the matrix. At the *microscale*, it constitutes the finest structural scale and is represented by the microstructure of HCP, consisting of hydration products, unhydrated residual clinker and micropores. For more details about the heterogeneity of concrete at different length-scales, the reader is referred to MEHTA & MONTEIRO (2001) and references therein.

Over the recent years, several multiscale models were developed to analyze the failure in concrete suffering from various attacks. HAIN & WRIGGERS (2008a) have evaluated the damage due to frost in the HCP using a finite element model that is based on the three-dimensional computer-tomography scans of HCP, and the obtained effective damage was upscaled to the next scale of concrete via a computational homogenization approach. CUSATIS & CEDOLIN (2007) developed an equivalent macroscopic cohesive law reflecting the meso-level failure mechanisms, where the investigation on the fracture behavior at the lower scale was carried out through a lattice-type model. A coupled macro-meso-micro model was described by NGUYEN ET AL. (2012) to link the micro-diffusive damage and the macro-crack in concrete, by incorporating a cohesive zone model within an iterative FE<sup>2</sup> approach. ECKARDT & KÖNKE (2008) adopted the nonlocal damage model to present the initiation, propagation and coalescence of

microcracks at the mesoscale and subsequent formation of macroscopic cracks. In addition, the adaptive domain decomposition method was used to analyze the multiscale failure in concrete. GHOSH & CHAUDHURI (2013) developed a multiscale failure model for concrete, where the material far from the fracture process zone was described by the homogenized elastic model, while a nonlinear model was used in the fracture process zone. The fracture at the mesoscale was modeled by CZM in the context of an enriched partition of unity meshfree method. IDIART ET AL. (2011) focused on the external sulfate attack on the concrete specimen at the meso-level, where zero-thickness interface elements with fracture-based constitutive laws were adopted. Moreover, the influence of discrete cracks on the transport of ions was explicitly taken into account.

This section starts from the introduction to approaches of generating randomly distributed aggregates embedded in the homogenized HCP as well as zero-thickness interface elements between aggregates and HCP representing the ITZ. Then it addresses the microstructure of the HCP obtained from micro-CT scan as well as the constitutive law of each component in the HCP. This section ends up with an example illustrating the ASR induced damage in the HCP.

## 5.1 Mesoscale of concrete

Figure 5.1 presents the scanning electron microscope (SEM) image of the cross-section of a concrete sample, from which the HCP and aggregates are clearly observable. However, the thickness of the ITZ is quite small, such that the distinction between ITZ and HCP has to be identified through SEM with higher resolution. To emphasize the significance of the ITZ, an individual section will be constructed to provide more details of the microstructure of the ITZ in Subsection 5.2.

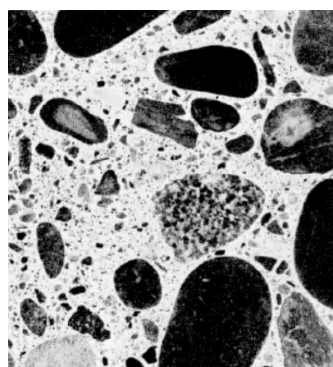


**Figure 5.1:** SEM image of the cross-section of a concrete specimen (MEHTA & MONTEIRO (1993)).

As compared to HCP, aggregates predominantly determine the unit weight, stiffness and stability of concrete. According to the size, aggregates can be generally classified into two categories: *fine* and *coarse*. Aggregates with radius less than 4.75 mm, are

generally referred to as *fine*, like sands. The converse are defined as *coarse* aggregates, e.g. gravel, natural rock and slags, see MEHTA & MONTEIRO (2001). Albeit the dominant volume fraction in concrete, aggregates are commonly considered as inert fillers due to stable microstructures. Conversely, by the existence of the diffusion of components in the porous microstructure of the HCP, it leads to chemical reactions and variations of its microstructure.

### 5.1.1 Representation of mesoscale

A significant task is to generate the mesoscale representation of concrete, which directly determines the accuracy and reliability of the numerical simulation. In Figure 5.2, some commonly adopted shapes of aggregates are displayed, and the distinction of shapes can be explained by the type of aggregates from the perspective of manufacturing process. Aggregates with spherical shape were adopted e.g. in WRIGGERS & MOFTAH (2006), COMBY-PEYROT ET AL. (2009) and SNOZZI ET AL. (2012). As an extension of the spherical case, HÄFNER ET AL. (2006) developed aggregates with elliptical shape, where various elliptical shapes were generated by varying parameters of ellipsoid functions. Clearly, aggregates with polygonal shape, generated by means of DELAUNAY tessellation, yield more accurate approximations of crushed aggregates, see WANG ET AL. (1999) and CAROL ET AL. (2001). However, the potential strong stress concentrations at the sharp edges are of significant concern during numerical simulations.

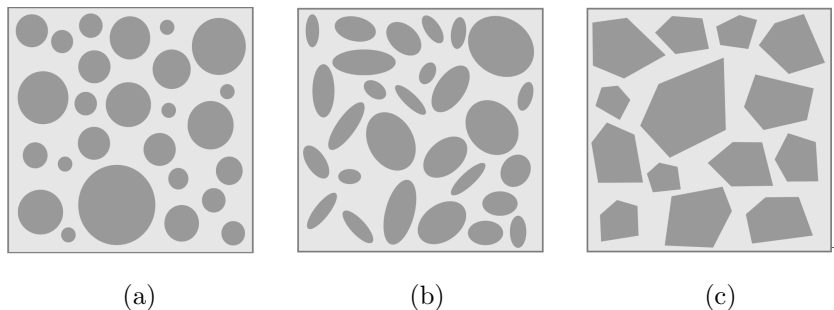


**Figure 5.2:** Commonly adopted shapes of aggregates embedded in the homogenized HCP (a) Sphere and (b) Ellipse and (c) Polygon.

In this subsection, various approaches to realistically generate the mesoscale representation of concrete are addressed, e.g. *divide-and-place* approach, *distinct element* approach and *take-and-place* approach. In the context of *divide-and-fill* approach, the whole domain is first divided into small domains, and then the resulting small domains are filled with aggregates. However, the generation of large three dimensional microstructures can be cumbersome, as pointed out in SCHUTTER & TAERWE (1993). With regard to the *distinct element* approach, the chosen aggregates are randomly placed in a vertical direction onto the previously deposited aggregates cluster, see MOFTAH (2005). In case of being in contact, the subsequent roll and slide of

aggregates in order to obtain more stable positions is also allowed. This approach is applicable to the case when more fine aggregates need to be generated. However, the sophisticated algorithm raises diffusivity in implementing it. The details of the *take-and-place* approach will be introduced in Subsection 5.1.2. As a consequence of the development of computer technology and non-destructive imaging device like CT, it yields the digital image output, presenting the material heterogeneity of concrete, see HAIN & WRIGGERS (2008a) and MAIN (2010). Among all approaches mentioned above, clearly the geometry obtained from CT provides the best approximation of the real concrete, however, the computational cost in the numerical simulation is giant.

### 5.1.2 Take-and-place approach

As described in WRIGGERS & MOFTAH (2006), the *take-and-place* approach employed in the present work to generate aggregates with spherical shapes embedded in the homogenized HCP, can be generally divided into two processes: *take* and *place*, see Table 5.1 for the general algorithm and WRIGGERS & MOFTAH (2006) for more details. The size of aggregates are obtained from a sieve size curve displayed in Figure 5.3 which is a certain aggregate size distribution yielding the optimal density and resembles the original concrete itself. Figure 5.4 illustrates examples with different volume fractions of aggregates embedded in the homogenized HCP.

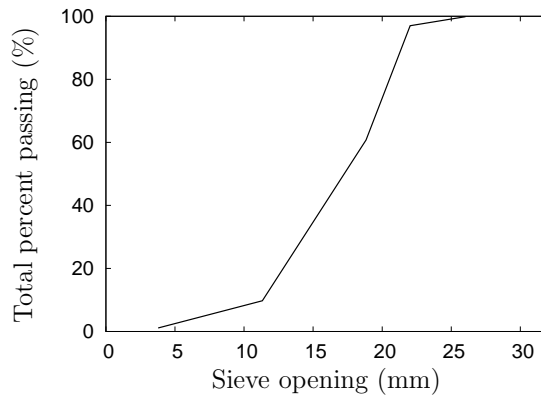


**Figure 5.3:** Aggregate size distribution curve.

### 5.1.3 Discretization technique

The construction of the mesh determines the quality with which the microstructures are resolved and thereby influences the accuracy of numerical simulations. The heterogeneity of the material causes difficulty in meshing the three-dimensional microstructure. Figure 5.5(a)<sub>1</sub> and 5.5(a)<sub>2</sub> present two prevailing meshing approaches: *conforming* and *nonconforming*, see ZOHDİ & WRIGGERS (2005) for details. The meshing approach referred to as *conforming* allows boundaries of elements to coincide with boundaries

*Take-process*

1. Divide the sieve size curve of aggregates in Figure 5.3 into segments and define a random number  $\varsigma \in (0, 1)$  such that the size of the aggregate  $d = d_{s+1} + \varsigma(d_s - d_{s+1})$ , where  $d_s$  and  $d_{s+1}$  indicate the upper and lower size limit of the segment.
2. Calculate the volume of the generated aggregate and subtract it from the volume of aggregates within the segment.
3. Keep running step 2 until the volume of aggregates left to be generated is less than  $\frac{4}{3}\pi\left(\frac{d_{s+1}}{2}\right)^3$ . Then move to the next segment and run aforementioned steps again.

*Place-process*

1. Random number is defined for the position of aggregates to be placed in the HCP.
2. Check whether place-process conditions are completely satisfied. For example, the overlaps between aggregates or between aggregate and HCP boundary are not allowed. Furthermore, SCHLANGEN & MIER (1992) indicated that the thickness between two adjacent aggregates can not be smaller than  $0.1(d_1 + d_2)/2$ , where  $d_1$  and  $d_2$  are the size of two different aggregates.

**Table 5.1:** Algorithm of *take-and-place* approach to generate the mesoscale representation of concrete.

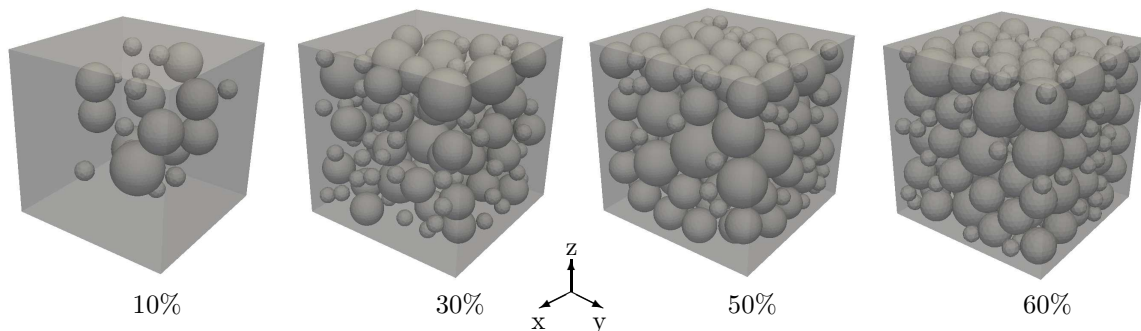


**Figure 5.4:** Mesoscale representations with different volume fractions of aggregates.

of the geometry, such that each element is assigned the material properties of either the matrix or the particle, see Figure 5.5(a)<sub>1</sub>. As compared to hexahedral element, the tetrahedral element is profitable for conforming meshing approach, thus circumventing the problem of strongly distorted elements, however, the generation of tetrahedral elements is a challenging task. Alternatively, nonconforming meshing approach with hexahedral elements offers the rapid mesh generation and yields less distorted elements, see Figure 5.5(a)<sub>2</sub>. Considering the *gauss point* method as a particular nonconforming meshing approach, with a focus on the interface elements between the matrix and the particle, it assigns particle properties to integration points that lie in the particle, and matrix properties to the remaining integration points, displayed in Figure 5.5(a)<sub>2</sub>, where integration points at interface elements are not shown. More associated details can be found in LÖHNERT (2004) and ZOHDI & WRIGGERS (2005). LÖHNERT (2004)

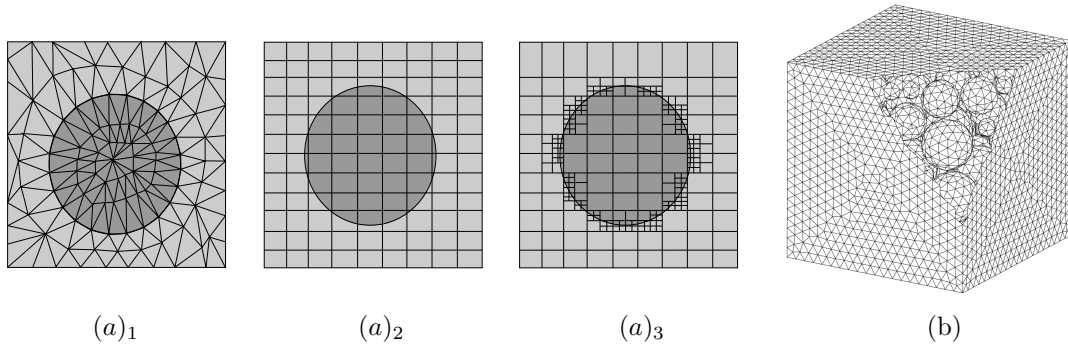


**Figure 5.5:**  $(a)_1$  Conforming meshing approach and  $(a)_2$  nonconforming meshing approach and  $(a)_3$  *hanging nodes* approach, (only cross-sections of three-dimensional geometry are displayed) and (b) discretization the mesoscale representation of concrete with the tetrahedral elements in the coarse mesh.

indicated that the jump in stiffness within the element still exists, thus leading to the problems of a kink in the displacement field and the mesh dependency. With an intention of solving this problem, the *hanging nodes* method was developed to adopt smaller elements close to the geometric boundaries to approximate the geometry, like a geometrically adaptive method, see Figure 5.5( $a_3$ ), such that one element is only assigned by one material property, see LÖHNERT (2004) for more details.

In this work, the mesostructure of concrete with the volume fraction of aggregates of 40% is generated. Then it is discretized through conforming meshing approach with tetrahedral elements in the automatic mesh generator CUBIT, see Figure 5.5(b) for the discretization example with coarse mesh. This approach forces boundaries of elements to coincide with boundaries of the geometry.

## 5.2 Interfacial transition zone between aggregates and HCP

As described in MASO (1996), ITZ is referred to as the particular region in the HCP with negligible thickness in the vicinity of aggregates. However, its property greatly differs from both the HCP and aggregates. Figure 5.6(a) presents the backscattered electron (BSE) image of concrete, where the aggregate is on the left and the white line indicates the significant discrete boundary with the thickness of 20-50  $\mu\text{m}$  between the ITZ and the HCP. The weak property of the ITZ is explained by its microstructure with higher porosity, thereby resulting in the phenomenon that microcracks are preferentially initiated at the ITZ. Figure 5.6(b) presents fracture paths lying along the interface between the HCP and aggregates. Thus, lots of attention has been given to the investigation on the microstructure of the ITZ. MONTEIRO ET AL. (1985) and MASO (1996) hypothesized that there are two main components at the ITZ. First component is a thin layer of about 2-3  $\mu\text{m}$  and is formed due to any reaction between aggregates

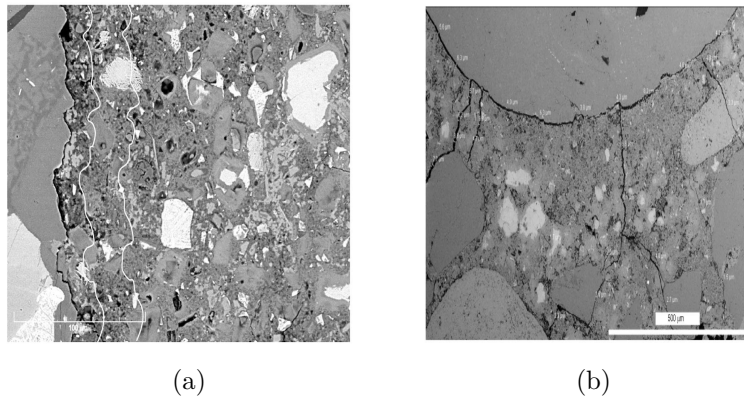


**Figure 5.6:** (a) BSE image of concrete (SCRIVENER ET AL. (2004)) and (b) microcracks lying along the interface between HCP and aggregate (WONG ET AL. (2009)).

and the HCP. Since aggregates affect the original packing of the HCP, another highly porous region of around  $50\mu\text{m}$  exists in the HCP. Also, it was concluded that the porosity of the microstructure of the ITZ can be reduced by lowering the water-cement ratio  $w_c$ . For more details about the microstructure of the ITZ, the reader is referred to MONTEIRO ET AL. (1985), MASO (1996) and references therein.

### 5.2.1 Zero-thickness interface element

The mesoscale representation of concrete discussed in Subsection 5.1.1 is comprised of randomly distributed aggregates and the homogenized HCP, without taking into account the ITZ. However, due to the significance of the ITZ, the next goal is to generate the representation of the ITZ. As described in Subsection 5.1.3, the conforming meshing approach was employed to discretize the mesostructure, such that boundaries of elements coincide with boundaries of the geometry. Concerning the thickness of the ITZ compared to the dimension of concrete, it is profitable to consider the ITZ as a layer with zero-thickness. Then interface elements with zero-thickness are inserted along all aggregate-HCP element boundaries for the representation of the ITZ. An algorithm for generating interface elements with zero-thickness is described in Figure 5.7 and Table 5.2. Figure 5.8 illustrates the undeformed interface elements between the HCP and aggregates.

The biggest challenge in applying CZM into the FEM is to resolve the displacement discontinuity, which can be overcome by using zero-thickness interface elements. DAY & POTTS (1994) addressed that the zero-thickness interface element is profitable for modeling the relative slip and opening/closing on predefined surfaces. However, during numerical simulations, zero-thickness elements may result in the ill-conditioning of the stiffness matrix and high stress gradients, when the stiffness of the zero-thickness element is 100 times greater than YOUNG's modulus of the surrounding phase.

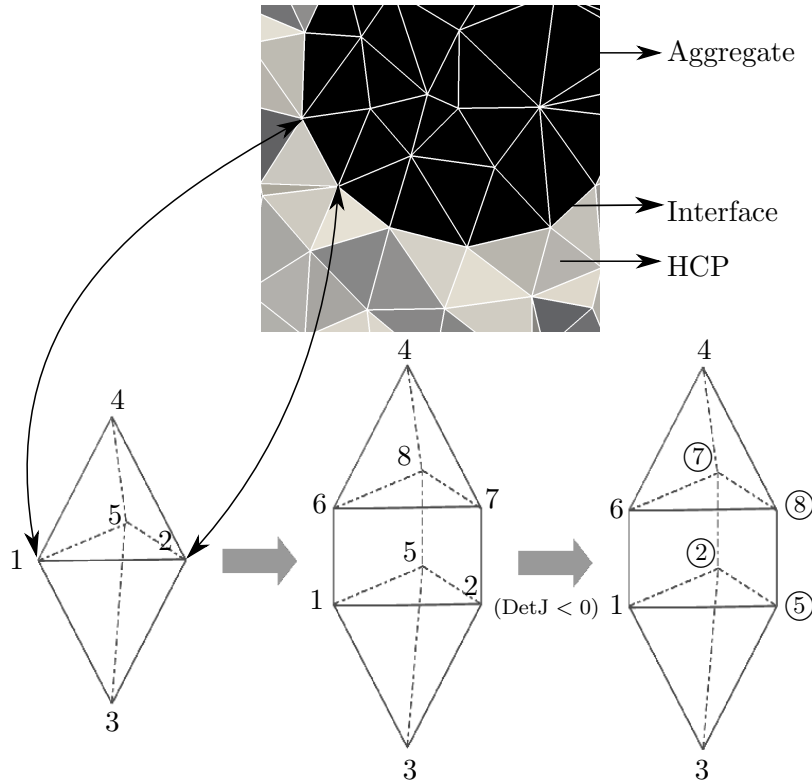


**Figure 5.7:** Generation of interface elements with zero-thickness between aggregates and the HCP for the representation of the ITZ.

- 
1. *Determine faces and nodes.* Determine contacting triangular faces of two adjacent tetrahedrons from the aggregate and the HCP and the nodal information of faces, see Figure 5.7, where one contacting face with nodes of  $(n_1, n_2, n_5)$  is shown.
  2. *Double nodes.* Double nodes on contacting faces e.g.  $(n_6, n_7, n_8)$  and replace original nodes on contacting faces from aggregate tetrahedrons with new doubled nodes, see Figure 5.7.
  3. *Establish interface element.* Use original nodes and doubled nodes to establish interface elements with zero-thickness, e.g.  $(n_1, n_2, n_5, n_6, n_7, n_8)$ .
  4. *Check  $Det(J)$ .* If  $Det(J)$  of interface elements is smaller than zero, change the consequence of nodes, e.g.  $(n_1, n_5, n_2, n_6, n_8, n_7)$ , as seen in Figure 5.7. Otherwise, keep the original consequence of nodes.
- 

**Table 5.2:** Algorithm for generating interface elements with zero-thickness between aggregates and the HCP.

## 5.2.2 Numerical example of unit cell

The next numerical example illustrates the behavior of the unit cell with zero-thickness interface. The unit cell is constructed by one sphere with the radius of 3 mm centrally

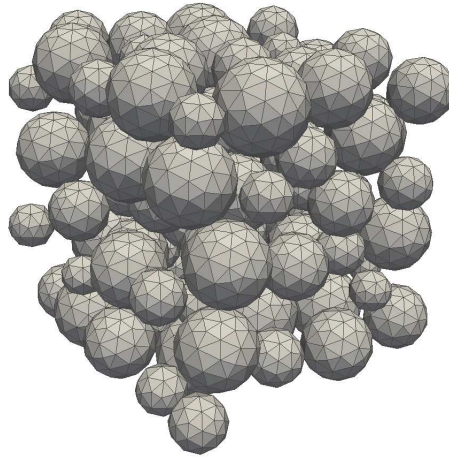


**Figure 5.8:** Undeformed interface elements.

located in the matrix with dimensions of  $10 \times 10 \times 10 \text{ mm}^3$  and zero-thickness interface elements are placed between the sphere and the matrix. During numerical simulations, the matrix and the sphere are assumed to behave elastically and interface elements are driven by CZM. The mechanical parameters of the unit cell example can be found in Table 5.3. Boundary conditions of tension, compression and shear are prescribed on the unit cell. Deformed configurations are displayed in Figure 5.9, where the white color indicate the debonding region. Furthermore, Figure 5.10 presents the stress  $\sigma_{zz}$  of the unit cell subjected to different boundary conditions mentioned above.

Component	Property	Value
Matrix	$E$	10000 (N/mm <sup>2</sup> )
Matrix	$\nu$	0.0 (-)
Sphere	$E$	70000 (N/mm <sup>2</sup> )
Sphere	$\nu$	0.0 (-)
Interface	$f_t$	4.0 (N/mm <sup>2</sup> )
Interface	$G_f$	0.005 (N/mm)
Interface	$K_p$	4000 (N/mm <sup>3</sup> )

**Table 5.3:** Mechanical parameters adopted in the numerical example of the unit cell.

Figure 5.11 demonstrates influences of parameters on the macroscale stress-strain relationship of the unit cell in uniaxial tension, e.g. tensile strength  $f_t$ , fracture energy  $G_f$  and YOUNG's modulus of the sphere. Among those curves, the common procedure from perfectly bonded, partially debonded to completely debonded is captured, where perfectly bonded is conducted by the case of no interface elements between the sphere and the matrix, and completely bonded is achieved when aggregates are replaced by

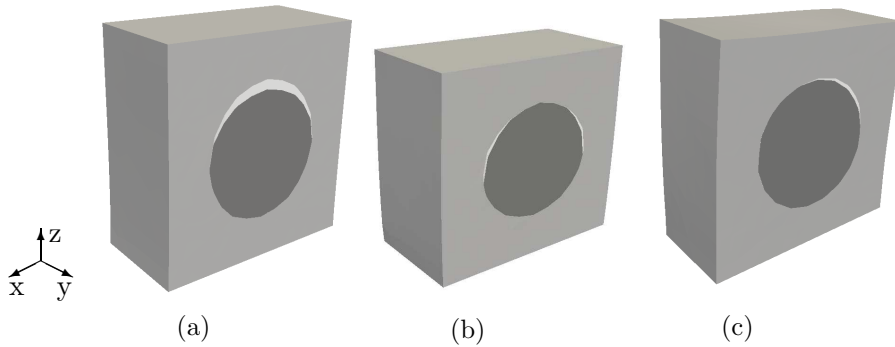


**Figure 5.9:** Deformations of the unit cell under various boundary conditions (a) tension and (b) compression and (c) shear (white color indicates the debonding region).

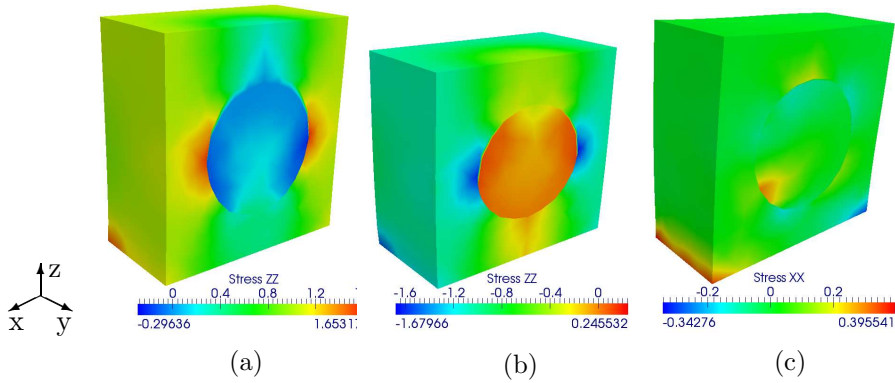


**Figure 5.10:** Stress  $\sigma_{zz}$  (MPa) of the unit cell under various boundary conditions (a) tension and (b) compression and (c) shear.

voids, see the solid curve and the curve with the label of *Voids* in Figure 5.11(a). Also, it indicates that larger tensile strength  $f_t$  requires larger load to initialize the debonding between the matrix and the sphere. For different fracture energy  $G_f$ , Figure 5.11(b) describes that debondings occur under the identical tensile load, yet following different softening curves. According to the influence of YOUNG's modulus of the sphere demonstrated in Figure 5.11(c), the stiffer sphere needs less tensile load to induce the debonding between the matrix and the sphere.

As an extension of numerical examples mentioned above, the effect of the sphere size is investigated, as shown in Figure 5.12 for illustration of different radius of the sphere. In addition to the radius of the sphere, the identical mechanical parameters of three samples are adopted. Figure 5.13 illustrates macroscale stress-strain relationships with respect to varying radius of the sphere in uniaxial tension. It can be clearly observed that the peak stress, prior to softening, is directly proportional to the radius of the sphere. Similarly, PETCH (1953) indicated that the strength linearly increases with

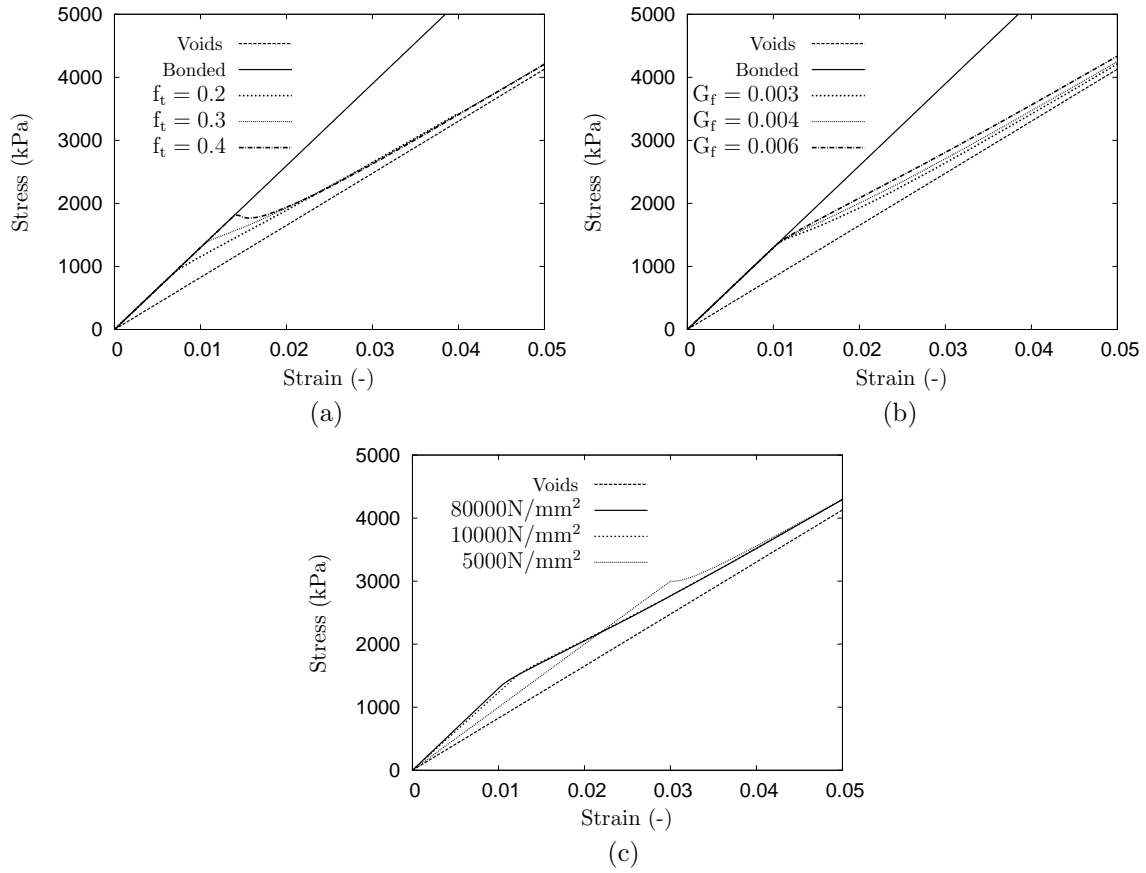


**Figure 5.11:** Macroscale stress-strain relationship of the unit cell in uniaxial tension influenced by various parameters (a) fracture energy and (b) tensile energy and (c) YOUNG’S modulus of sphere.

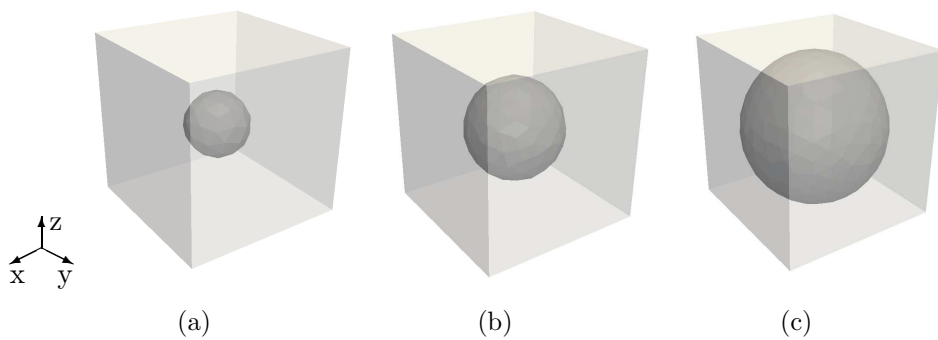


**Figure 5.12:** Increasing the radius  $r$  of the sphere in the unit cell (a)  $r=2$  mm and (b)  $r=3$  mm and (c)  $r=4.5$  mm.

the inverse square root of the particle size, as applicable to polycrystalline and fine reinforced materials. Furthermore, in Figure 5.13, the phenomena of a transition from snap-through to snap-back instability is also observed in the post-peak response as the

radius of the sphere is increased. By the existence of the snap-back, a simple displacement control is no longer profitable, and hence, an arc-length approach is adopted to overcome the snap-back problem, see Subsection 3.1.2 for more details. Also, the hardening behavior is captured when the radius of the sphere is reduced to a small value. As such, it is concluded that the size of the sphere influences not only the strength of the material, but also the stability of the interface crack.

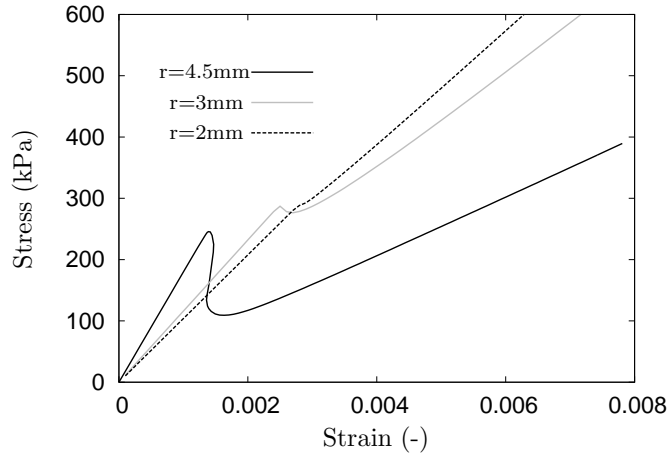


**Figure 5.13:** Macroscale stress-strain relationship of the unit cell with varying radius of the sphere in uniaxial tension.

### 5.3 Microscale of hardened cement paste

HCP, as a finely pulverized material, develops the binding property during the hydration process. In the cement, the cauterization above the temperature of sintering yields  $3\text{CaO} \cdot \text{SiO}_2$  (C3S) and  $2\text{CaO} \cdot \text{SiO}_2$  (C2S). With an purpose of accelerating the reaction,  $\text{Al}_2\text{O}_3$  and  $\text{Fe}_2\text{O}_3$  are added, such that by-products  $3\text{CaO} \cdot \text{Al}_2\text{O}_3$  (C3A) and  $4\text{CaO} \cdot \text{Al}_2\text{O}_3 \cdot \text{Fe}_2\text{O}_3$  (C4AF) are also generated. However, the phases of C3S, C2S, C4AF, and C3AF are intermediates, and in the presence of the water, the exothermic chemical-physical processes are initialized to yield the hydration product including calcium-silicate-hydrate (CSH) and calcium hydroxide (CH). Ultimately, hydration product, unhydrated residual klinker and micropores consist of the microstructure of the HCP. For more details of the hydration process in the cement paste, the reader is referred to MEHTA & MONTEIRO (2001) and references therein. In the theory of POWERS (1962), the fractional volume of pores  $c_p$  and of unhydrated residual clinker  $c_u$  are given by

$$c_p = \frac{w_c - 0.36h_d}{w_c + 0.32}, \quad c_u = \frac{0.32(1 - h_d)}{w_c + 0.32}, \quad (5.3.1)$$

where  $w_c$  is the water-cement ratio and  $h_d$  is the hydration degree.

### 5.3.1 Representation of hardened cement paste

Over the past 20 years, several computer modeling packages were developed to simulate the formation processes of the microstructure of the HCP. For instance, in CEMHYD3D, developed at National Institute of Standards and Technology (NIST) in the U.S, the microstructure of the HCP is divided into topological, geometrical, and physical uniform cells by using a cellular-automata approach, see BENTZ (2000). The state of each cell at new time step in the formation process relies on its state at old time step, the states of next-neighbors and a random part. Owing to random-based rule, it distributes the parts very evenly and has no capability to capture the accumulations of pores, as described in HAIN (2007). HYMOSTRUC3D model was developed at Delft University of Technology in Netherlands, for the simulation of the reaction process and of the formation of the microstructure in the hydrating Portland cement. Within this package, the cement particles are modeled as digitized spheres randomly distributed in the domain, and the hydrating cement grains are simulated as growing spheres. As the cement hydrates, the cement grains gradually dissolve and a porous layer of hydration products is formed around the grain, see YE ET AL. (2003) for more details. The introduction to another similar so-called MIC package developed at École Polytechnique Fédérale de Lausanne (EPFL) in Switzerland is described in BISHNOI & SCRIVENER (2009).

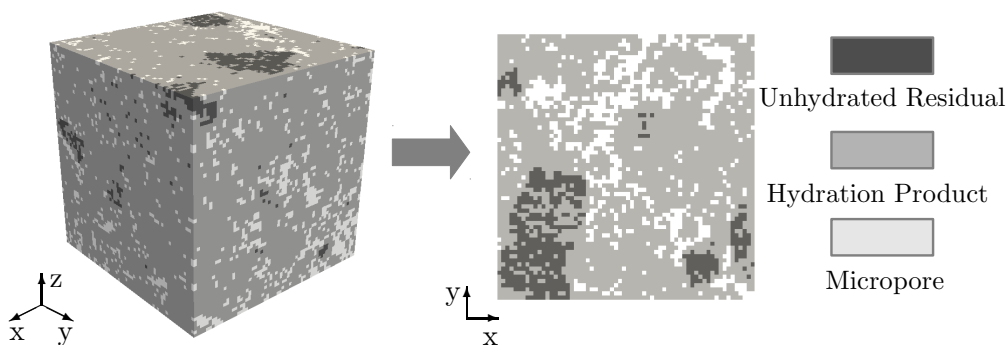


**Figure 5.14:** Three- and two-dimensional representations of HCP transferred from micro-CT-scan of HCP.

As an alternative to approaches mentioned above, CT is a non-destructive evaluation technique for producing three-dimensional images of a specimen through X-ray, enabling to obtain the microstructure of the material and subsequently analyze the mechanical behavior through numerical simulations. In the present work, a cement specimen of length  $1750\ \mu\text{m}$  was used to obtain the microstructural geometry of HCP through three-dimensional micro-CT scans with a resolution of  $1\ \mu\text{m}$  per voxel dimension. Due to this underlying voxel data structure, the natural element to use within the finite element method to discretize the microstructure is an 8-node brick where each element is assigned to a single material phase. This choice allows a straightforward transition from the micro-CT scan data to the numerical analysis stage, see HAIN

(2007) and HAIN & WRIGGERS (2008b). Three- and two-dimensional representations of HCP are displayed in Figure 5.14, where the gray parts are hydration products, while white parts are micropores and black parts are unhydrated residual clinker. The volume fraction of hydration products is 84%, the one of micropores is 14% and the one of unhydrated is 2%. Although hydration products have the dominant volume fraction in HCP, the micropore phase with a lower volume fraction also plays a significant role in the performance of HCP. Note that as the resolution of the micro-CT scans is  $1 \mu m$ , it only provides an approximation of the microstructural geometry, not being able to capture the micropores whose diameters are less than  $1 \mu m$ .

### 5.3.2 Constitutive equation of each component in HCP

The present section introduces constitutive equations for three components in the HCP as well as for the ASR gel only existing in micropores of the HCP.

#### 5.3.3 Solid phase

Among other continuum damage models which can depict the failure of the HCP, the simplified constitutive model developed in HAIN & WRIGGERS (2008a) and HAIN & WRIGGERS (2008b) is employed in this work where damage was constrained to the hydration products because of its high volume fraction in the HCP. Within this simplified model, the mechanical strain  $\epsilon^u$  is comprised of an elastic strain  $\epsilon^{el}$  and a crack strain  $\epsilon^{cr}$

$$\epsilon^u := \epsilon^{el} + \epsilon^{cr} \quad . \quad (5.3.2)$$

The stress  $\sigma$  is split into the volumetric and deviatoric part in a classical manner

$$\sigma := C_{vol} \kappa_h \operatorname{tr} \epsilon^{el} \mathbf{1} + C_{iso} 2\mu_h \operatorname{dev} \epsilon^{el} \quad , \quad (5.3.3)$$

where  $C_{vol} \in [0; 1]$  and  $C_{iso} \in [0; 1]$  control the remaining stiffness of the volumetric and the deviatoric part.  $\kappa_h$  and  $\mu_h$  are the bulk modulus and shear modulus of the hydration product. The occurrence of the damage is induced by the volumetric deformations, such as the expansion of the gel. The update of damage works as follows: if  $|\operatorname{vol} \epsilon^{el}| \geq \alpha$  at the initial loading stage,  $C_{vol} \approx 0$  and  $C_{iso} = \beta_{iso}$ . When  $|\operatorname{vol} \epsilon^{el}| \leq \alpha$  during the unloading process,  $C_{vol} = \beta_{vol}$  and  $C_{iso} = \beta_{iso}$ . When the material is loaded again and if  $|\operatorname{vol} \epsilon^{el}| \geq \gamma\alpha$ ,  $C_{vol} \approx 0$  and  $C_{iso} = \beta_{iso}$ . More details of this algorithm can be found in HAIN (2007) and HAIN & WRIGGERS (2008b) from which the damage parameters, determined through experimental results, are adopted:  $[\alpha, \beta_{iso}, \beta_{vol}, \gamma] = [0.004, 0.05, 0.01, 0.50]$ . The unhydrated residual klinker is assumed to behave elastically. The undamaged mechanical properties of hydration product and unhydrated residual klinker in HCP are listed in Table 5.4.

#### 5.3.4 Gel in micropores of HCP

The deterioration of concrete resulting from ASR is induced by the expansion of the gel. Hence, the mechanical properties of the gel play a central role. The gel has a

Part	$E$ (N/mm <sup>2</sup> )	$\nu$ (-)	$\kappa$ (N/mm <sup>2</sup> )
Unhydrated residual clinker	132,700 [1]	0.30 [1]	-
Hydration product	24,000 [1]	0.24 [1]	-
Gel	-	0.49997 [2]	25,000 [3]

**Table 5.4:** Mechanical properties of components in the HCP ( [1] for (HAIN & WRIGGERS (2008b)), [2] for DUNANT (2009) and [3] for PHAIR ET AL. (2005))

complex structure that depends on the composition of HCP and on the types of the aggregates. Moreover, due to its unstable chemical characteristics, the experimental determination of the gel properties is challenging. The observation that the gel is chemically similar to calcium-silicate-hydrate (C-S-H) enables it to be conceived as a nearly incompressible material with a Poisson's ratio of 0.49997, see DUNANT (2009).

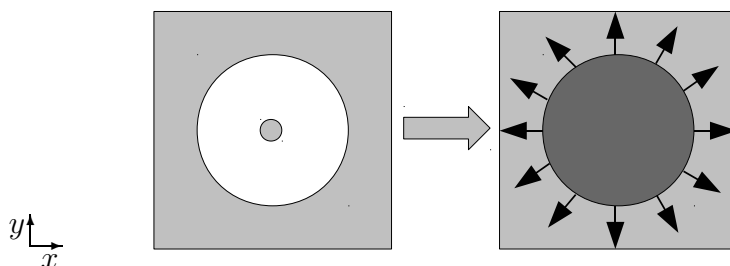


**Figure 5.15:** Swelling of gel induced by ASR exerts isotropic pressure to surrounding matrix.

Standard finite elements cannot appropriately handle incompressibility due to volumetric locking. Higher-order interpolations may suffer less from this problem, but the displacement solution is still of low order accuracy, see BOERNER & WRIGGERS (2008), WRIGGERS (2008) and MÜLLER-HOEPPE ET AL. (2009). In this work, the classical Q1P0 method is employed where the displacement and pressure are the primary unknowns. The hydrostatic pressure  $P_g$  induced by the expansion of the gel in the micropores (see Figure 5.15) is expressed by

$$P_g := \kappa_g (\text{tr} \epsilon - A) = \kappa_g \text{tr} \epsilon - \kappa_g \beta \xi \quad . \quad (5.3.4)$$

where  $A = \beta \xi$  denotes the expansion strain of the gel,  $\beta$  presents the expansion coefficient of the gel,  $\xi$  is the chemical extent and  $\kappa_g$  is the bulk modulus of the gel. As assumed before, the expansion strain of the gel  $A$  is proportional to the chemical extent  $\xi$ . The mechanical properties of the gel are listed in Table 5.4.

### 5.3.5 ASR induced damage in HCP

Not only the difficulty in conducting the experiment at such small scale but also unstable chemical property of the gel yields that the expansion coefficient of the gel  $\beta$  is still

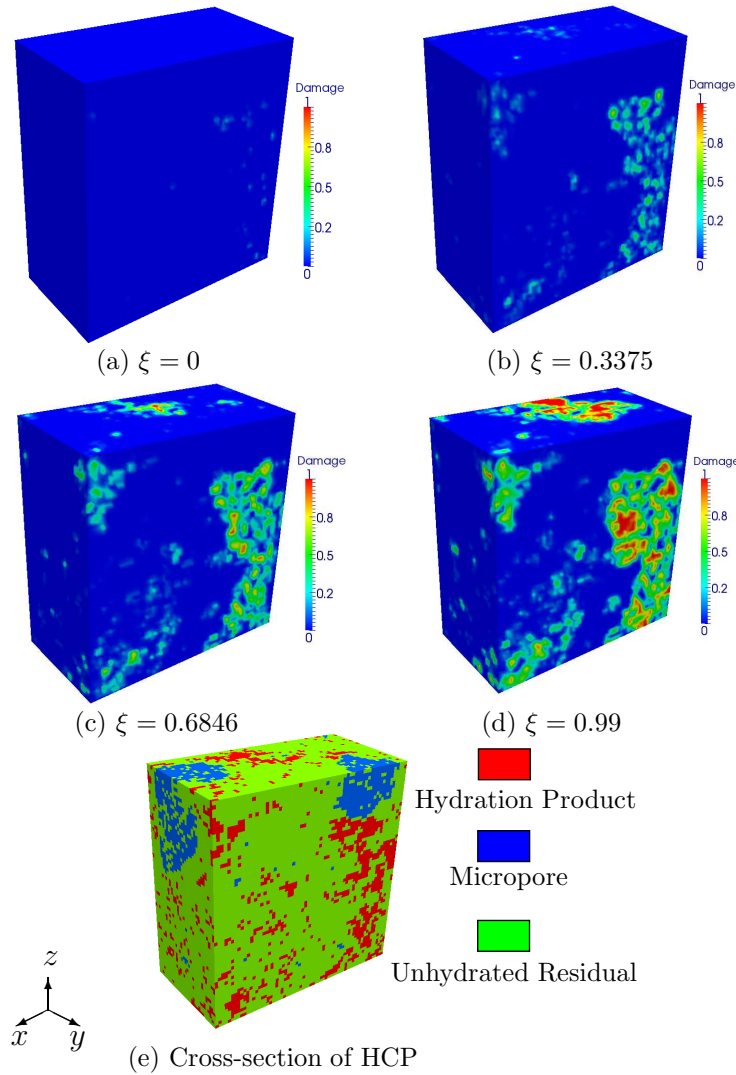


**Figure 5.16:** (a)-(d) ASR induced damage distribution on a cross-section of HCP with various chemical extent  $\xi$  and (e) material distribution on cross-section.

unknown. In Subsection 6.3.4, two-step homogenization approach, namely multiple parameter identifications, is employed to obtain  $\beta$ . Here, an example with  $\beta$  of 0.002 is implemented, with the combination of the damage model defined in the hydration products, where the stress-free boundary conditions are prescribed on the HCP, such that only the expansion of the gel contributes to the damage in HCP. The distribution and evolution of the ASR induced damage in HCP with respect to different extent  $\xi$  are illustrated in Figure 5.16, where the damage occurs in the hydration products in the vicinity of micropores triggered by the expansion of the gel in micropores. Ultimately, the coalescence of the microscale damage leads to the formation of the macroscale failure in concrete.

# Chapter 6

## Computational homogenization to ASR damage

### 6.1 Introduction

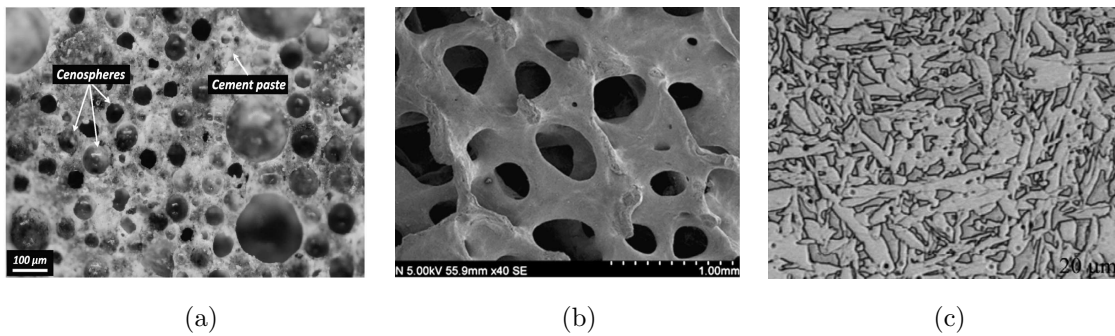


**Figure 6.1:** (a) Optical microscope image of fiber-reinforced ultra lightweight cement composites with cenospheres (WANG ET AL. (2013)) and (b) SEM image of scaffold from bovine cancellous bone (BI ET AL. (2010)) and (c) microstructure of low-carbon high-strength steel weld metal (WAN ET AL. (2012)).

The determinations of physical properties of materials from laboratory experiments, e.g. YOUNG's modulus, thermal conductivity and diffusivity, rely on the assumption that materials are homogeneous. However, as a matter of fact, most materials are heterogeneous at one or another scale, where physical properties vary throughout their microstructures. For this reason, the significance of a close view at microstructures of materials is favourable to be highlighted. For instance, Figure 6.1(a) presents an optical microscope image of fiber-reinforced ultra lightweight cement composites with cenospheres, in order to enhance the thermal resistance and reduce the mass density. Figure 6.1(b) illustrates the SEM image of the scaffold from bovine cancellous bone with porous structures, as applicable to calcination, lyophilization, chemical treatment and supercritical CO<sub>2</sub>. The microstructure of the low-carbon high-strength steel weld metal obtained through electron backscattered diffraction analysis is displayed in Figure 6.1(c), where inclusions, repeated nucleation as well as fixed orientation relationships

of acicular ferrite grains are observed. It is of great interest to determine the effective or macroscale properties of materials from the knowledge of constitutive laws of heterogeneous components and their volume fractions. One efficient approach referred to as *homogenization* was developed in the late 19th century, through which the heterogeneous material is replaced by the homogeneous material, see Figure 6.2.

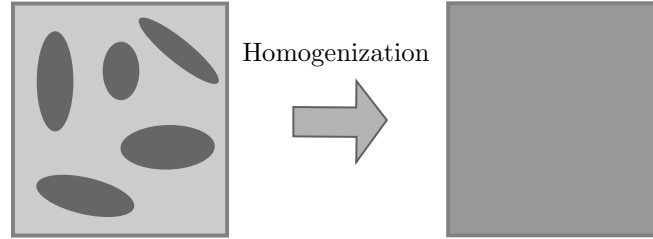


**Figure 6.2:** Heterogeneous material replaced by homogeneous material.

The current section starts from the introduction to the analytical homogenization, and then it focuses on the fundamental aspects of computational homogenization in the context of mechanical, thermal and diffusion problems as well as the subsequent application to the microstructure of the HCP. In the end, it concerns the way of obtaining the effective damage of the HCP induced by ASR as a function of chemical extent  $\xi$ .

## 6.2 Analytical homogenization

VOIGT (1889) and REUSS (1929) developed pioneering theories of analytical homogenization by employing simple approximations for the effective material properties of inhomogeneous linear elastic materials. In the context of VOIGT bound, the effective modulus is obtained relying on the assumption of the uniform strain field in the microstructure, however, the local non-equilibrium leads to the kinetically inadmissible problem for a general arbitrary microstructure. Thus, the effective modulus in the VOIGT bound is determined by the volume average of the material tensor

$$\mathbb{C}_{\text{VOIGT}}^{\text{eff}} = \langle \mathbb{C} \rangle \quad , \quad (6.2.1)$$

with the definition

$$\langle \bullet \rangle = \frac{1}{|v|} \int_{\mathcal{B}_t} \bullet \, dv \quad , \quad (6.2.2)$$

where  $v$  is the analysis volume. Conversely, the constant stress field in the microstructure was assumed in the REUSS bound, thereby resulting in the kinematically inadmissible problem due to the imperfect bonding in the material. As a consequence, the effective compliance is determined by the volume average of the compliance tensor

$$\mathbb{C}_{\text{REUSS}}^{\text{eff}} = \langle \mathbb{C}^{-1} \rangle^{-1} \quad . \quad (6.2.3)$$

Albeit imperfect assumptions in the VOIGT and REUSS bounds, HILL (1952) has proven that the real effective material tensor is located within the bounds

$$\mathbb{C}_{\text{VOIGT}}^{\text{eff}} \leq \mathbb{C}^{\text{eff}} \leq \mathbb{C}_{\text{REUSS}}^{\text{eff}} \quad . \quad (6.2.4)$$

The broad bounds from VOIGT and REUSS justify the need of developing alternatives for tight bounds. For instance, the asymptotic HASHIN-SHTRIKMAN bound (HASHIN (1963)) based on variational principles, offers the tightest bound for the general isotropic material without restrictions to the geometry of the microstructure, while it is limited to a theoretical infinite size of the representative volume element. An alternative approximation of effective material properties for an ellipsoidal inclusion within an infinite domain in the case of linear elasticity was developed by ESHELBY (1957), where the stress and the strain in the inclusion are uniform, implicitly depending on the ESHELBY's tensor which describes the geometry of the inclusion. Also, it is crucial to identify the analytical localization tensor by using various simplifications of the microstructure. For example, the DILUTE method accounts for no interactions between inclusions, thereby offering reasonable estimates for the case with small fractional volumes. The drawback existing in the DILUTE method can be overcome by initiating an iterative homogenization, see KANAUN & LEVIN (2008). Furthermore, the assumption of the weak interactions between inclusions for the approximation was proposed in the MORI-TANAKA method, see MORI & TANAKA (1973).

## 6.3 Computational homogenization

The limitation that analytical estimates are only motivated by simple microstructural geometries, is devoted to the need of developing the computational homogenization approach. Specifically, computational homogenization has been developed to provide arbitrarily refinable bounds and is widely used in the multi-scale analysis for heterogeneous materials. The fundamental underlying methodology of computational homogenization is to characterize the macroscopic behavior of the heterogeneous material by approximately identifying a statistically representative volume element (RVE), which is a sample from the heterogeneous material when it is small enough compared to the macrostructural dimensions, yet it includes sufficient statistical information about the microstructure so as to accurately represent the response that the heterogeneous material exhibits on the macroscale. Without this method, the computation cost is giant, since one has to directly solve the fine scale representation of the whole domain, including all heterogeneities.

As pointed out in ZOHDI & WRIGGERS (2005), boundary conditions applied for computational homogenization have to fulfill the HILL's criterion. For mechanical problem, the satisfaction of the HILL's criterion indicates the energy dissipation is preserved while making the transition from the microscale to the macroscale. Table 6.1 presents a summary of widely employed boundary conditions for computational homogenization in the context of mechanical, thermal and diffusion problems respectively, as well as

their corresponding HILL's criteria in general. An ordering of the macroscopic elastic property obtained via homogenization under pure displacement and pure traction boundary conditions was clearly proven by HUET (1990), later extended to periodic boundary condition, see HAZANOV & HUET (1994).

Field	HILL's criterion	Type of Boundary Conditions (BCs)
Mechanical	$\langle \boldsymbol{\sigma} \cdot \boldsymbol{\epsilon} \rangle = \langle \boldsymbol{\sigma} \rangle \cdot \langle \boldsymbol{\epsilon} \rangle$	Linear displacement BCs, uniform traction BCs and mechanical periodic BCs
Thermal	$-\langle \mathbf{q} \cdot \nabla \theta \rangle = -\langle \mathbf{q} \rangle \cdot \langle \nabla \theta \rangle$	Linear temperature BCs, uniform normal thermal flux BCs and thermal periodic BCs
Diffusion	$-\langle \mathbf{j} \cdot \nabla s \rangle = -\langle \mathbf{j} \rangle \cdot \langle \nabla s \rangle$	Linear humidity BCs, uniform normal diffusion flux BCs and diffusion periodic BCs

**Table 6.1:** A summary of widely employed BCs for computational homogenization for mechanical, thermal and diffusion problems.

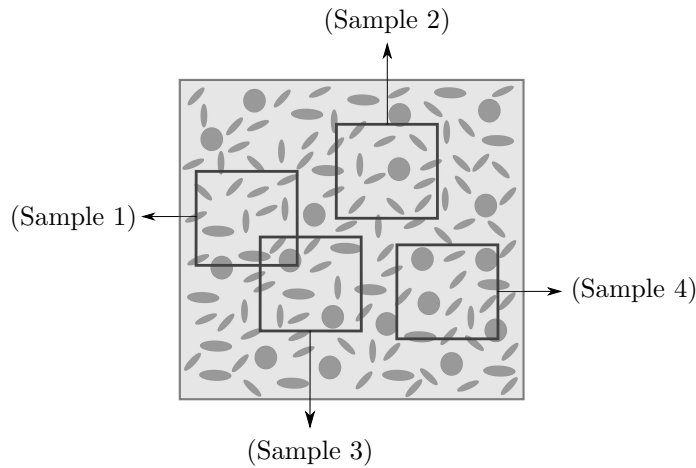


**Figure 6.3:** Four statistical samples obtained from the microstructure of the material.

Theoretically, it is desirable to choose an RVE including entirely realistic information of the microstructure, such that the obtained effective response is independent of the type of boundary conditions, yet the computational cost is high. As such, realistically the sample slightly smaller than the ideal RVE is chosen. By using a sufficient number of samples, randomly obtained from the microstructure, it is capable of overcoming the bias in the estimation due to different boundary conditions, see Figure 6.3. The specific details can be found e.g. in KANIT ET AL. (2003), ZOHDI & WRIGGERS (2005) and references therein.

### 6.3.1 Computational thermal homogenization

During the past 20 years, the computational homogenization approach has been applied for thermal problem. For instance, ASAKUMA ET AL. (2004) calculated the effective

thermal conductivity of the metal hydride bed. It was also applied to open-cell metallic foams by LASCHET ET AL. (2009). ZHANG ET AL. (2011a) obtained the effective thermal conductivity of the granular assemblies based on the discrete element method. In addition, a second-order thermal homogenization framework with higher-order fluxes was proposed by TEMIZER & WRIGGERS (2010b) to capture absolute size effects when the RVE size is not sufficiently small compared to a representative macrostructural length scale. The goal of the present section is to apply the computational thermal homogenization approach to identify the macroscopic thermal conductivity of the HCP, with consideration of the effect of the relative humidity in micropores.

### Theorem

FOURIER's law in Equation (2.6.8) is assumed to be valid for each component in the HCP. Note that the subscripts in Equation (2.6.8) are removed in this section in order to explain the general theorem for thermal homogenization. Table 6.2 describes three widely adopted boundary conditions for thermal homogenization, e.g. linear temperature BCs, uniform normal thermal flux BCs as well as thermal periodic BCs, which have to fulfill the HILL's criterion in order to support it on physical grounds. Appendix A presents the proof through the theorems of averaged thermal dissipation and the thermal dissipation of the average. Note that the average dissipation is prescribed concerning the temperature gradient and the normal flux only for a perfectly bonded material with  $\llbracket \theta \rrbracket = 0$ , see ROSEN & HASHIN (1970) and TORQUATO (2002) for more details.

- 
1. *Linear temperature BCs:*  $\theta = \mathbf{G}_0 \cdot \mathbf{x}$  on  $\partial\mathcal{B}_t$ , with the coordinates  $\mathbf{x}$  of the boundary and  $\langle \nabla \theta \rangle = \mathbf{G}_0$ .
  2. *Uniform normal thermal flux BCs:*  $q = \mathbf{Q}_0 \cdot \mathbf{n}$ , with  $q = \mathbf{q} \cdot \mathbf{n}$  and  $\langle \mathbf{q} \rangle = \mathbf{Q}_0$ .
  3. *Thermal periodic BCs:*  $\theta^+ - \theta^- = \mathbf{G}_0 \cdot (\mathbf{x}^+ - \mathbf{x}^-)$  (periodicity of the temperature) and  $q^+ = -q^-$  (anti-periodicity of the normal thermal flux) with  $\langle \mathbf{q} \rangle = \mathbf{Q}_0$ .
- 

**Table 6.2:** Three widely used boundary conditions for computational thermal homogenization.

In the context of thermal homogenization procedure, effective thermal conductivity  $\bar{k}$  is determined by minimizing a least-square function

$$\Pi := [\langle \mathbf{q} \rangle - \mathbf{q}^*(\langle \nabla \theta \rangle)]^2 \rightarrow \min, \quad (6.3.1)$$

where an effective constitutive equation for isotropic thermal conduction is given by

$$\mathbf{q}^*(\langle \nabla \theta \rangle) := -\bar{k} \langle \nabla \theta \rangle, \quad (6.3.2)$$

with thermal flux  $\mathbf{q} = (q_1, q_2, q_3)^T$ . Differentiation of Equation (6.3.1) with respect to  $\bar{k}$  yields

$$\frac{d\Pi}{d\bar{k}} \stackrel{!}{=} 0, \quad (6.3.3)$$

such that the isotropic effective thermal conductivity is obtained through

$$\bar{k} = -\frac{\langle \mathbf{q} \rangle_1 \langle \nabla \theta \rangle_1 + \langle \mathbf{q} \rangle_2 \langle \nabla \theta \rangle_2 + \langle \mathbf{q} \rangle_3 \langle \nabla \theta \rangle_3}{\langle \nabla \theta \rangle_1^2 + \langle \nabla \theta \rangle_2^2 + \langle \nabla \theta \rangle_3^2} . \quad (6.3.4)$$

### Comparison between numerical results and experiment

Material	Thermal conductivity (W/mK)
Hydration product	1.015 (WU ET AL. (2012))
Unhydrated clinker	1.55 (BENTZ (2007))
Micropore	0.604 (BENTZ (2007))

**Table 6.3:** Thermal conductivity of components in HCP.

As mentioned before, identifying an adequate RVE determines the accuracy and reliability of computational thermal homogenization. The RVE with the size of  $64^3 \mu m^3$  in the HCP was verified to satisfy the requirement of the HILL's criterion, see HAIN & WRIGGERS (2008b). The linear temperature boundary condition, illustrated in Table 6.2, is employed to initialize the thermal homogenization for determining the effective thermal conductivity of the HCP, where all the nodes lying on the boundary surface of the RVE are imposed based on the constant tensor  $\mathbf{G}_0$ . Then 8000 randomly selected RVEs of  $64^3 \mu m^3$  from the microstructure of the HCP are carried out, where the thermal conductivity of components in the HCP are listed in Table 6.3. Table 6.4 shows the mean value and the standard deviation of 8000 statistical tests. In Figure 6.4(a), one can observe that the probability density of 8000 statistical tests is very close to the GAUSSIAN distribution.

Mean value (W/mK)	Standard deviation (W/mK)
0.9568	0.0257

**Table 6.4:** Mean value and standard deviation of 8000 statistical tests for computational thermal conductivity in HCP

Figure 6.4(b) displays the comparison between the computed mean value of 8000 statistical tests and the experimental data from BENTZ (2007), where a thermal constants analyzer, including a variety of transient plane source probes connected to a computerized control unit, was used to measure the thermal conductivity of the cement paste as a function of the hydration degree at  $20^\circ C$ . All cement pastes were prepared using Cement and Concrete Reference Laboratory (CCRL) cement proficiency sample with  $w_c=0.4$  and over saturated condition. In Figure 6.4(b), one can observe that the hydration degree has a minor effect on the measured thermal conductivity and the computed values with the hydration degree of 0.945 are generally in the same region

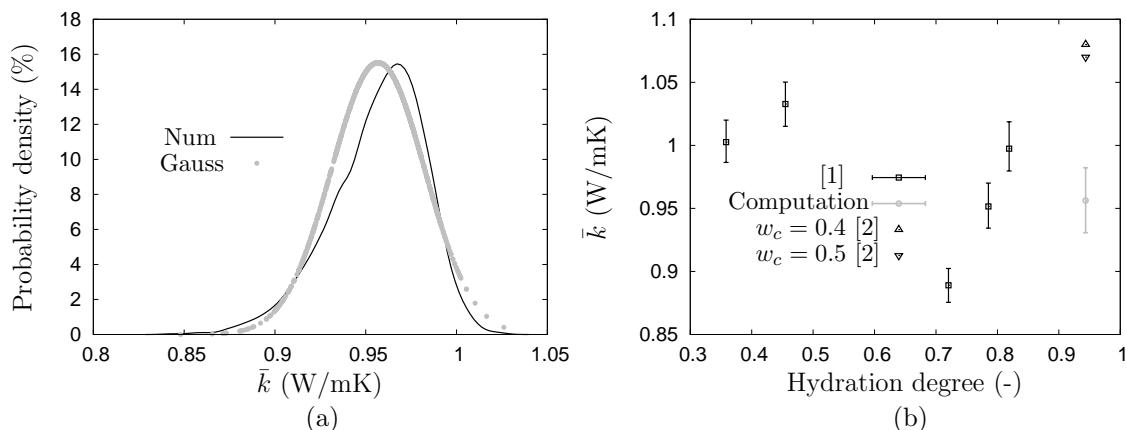


**Figure 6.4:** (a) 8000 statistical tests distribution and GAUSSIAN distribution (b) computed effective thermal conductivity of HCP and experimental data of cement paste (BENTZ (2007) [1] and ABDELALIM ET AL. (2007) [2]).

with the experimental data from BENTZ (2007), particularly when the factor of the standard deviation is considered. The computed values from Table 6.4 underestimate the experimental data from ABDELALIM ET AL. (2007), which used the photoacoustic technique to measure the effective thermal conductivity of the HCP with  $w_c=0.4$  and 0.5, after the fresh cement paste was cured for one month under room temperature. It is known that the pore width gets larger as the  $w_c$  increases, thus leading to the lower thermal conductivity, see ABDELALIM ET AL. (2007), as triangles in Figure 6.4(b) indicate. Since the type of HCP in the numerical simulation is different from the one in ABDELALIM ET AL. (2007), it is a possible reason why the computed results underestimate the experiment data. Furthermore, the thermal conductivity of the HCP is also sensitive to the water content in pores, as will be investigated next. Nevertheless, all computational results are of the same order of magnitude with experimental observations.

### Effect of humidity in micropores on thermal conductivity of HCP

JEON (2003) pointed out the influence of the water content in micropores on the thermal conductivity of the HCP, hence, it is crucial to take into account the role of the water content in the computational thermal homogenization. Assuming that the micropore is simply considered as a mixture of the water and the gaseous phase of the air, the thermal conductivity of the micropore  $K_{\text{pore}}^m$  can be determined by a modification of the REUSS-VOIGT type estimates, namely the LICHTENECKER's equation (PAVLÍK ET AL. (2009))

$$k_{\text{pore}}^m = V_{\text{air}} k_{\text{air}}^m + V_{\text{water}} k_{\text{water}}^m \quad , \quad (6.3.5)$$

where the superscript  $m \in [-1, 1]$  is the mode parameter, indicating the range from the REUSS bound with  $m = -1$  to the VOIGT bound with  $m = 1$ .  $V_{\text{air}}$  and  $V_{\text{water}}$  are the volume fractions of the air and the water in micropores.  $k_{\text{air}}$  and  $k_{\text{water}}$  are thermal

conductivity of the air and the water, listed in Table 6.5.

Material	Thermal conductivity (W/mK)
Water	0.604 (BENTZ (2007))
Air	0.025 (CARSON ET AL. (2004))

**Table 6.5:** Thermal conductivity of components in micropore.

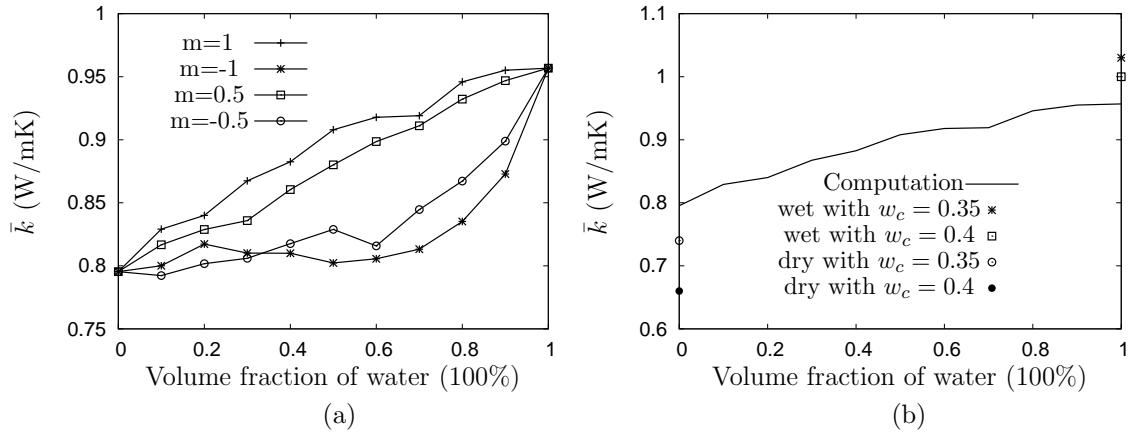


**Figure 6.5:** (a) Effective thermal conductivity of 150 statistical RVEs of HCP as a function of the volume fraction of the water content in micropores and (b) comparison between the computed effective thermal conductivity considering water effect and experimental results (JEON (2003)).

The values of (1.0, -1.0, 0.5, -0.5) for  $m$  in Equation (6.3.5) are selected respectively and for each value of  $m$ , 150 statistical samples are chosen for computational thermal homogenization, such that the effect of the water content in micropores is taken into account, see Figure 6.5(a) for the computed results. Also, Figure 6.5(b) illustrates the comparison between the computed results for  $m = 1$  and the experimental data from JEON (2003). In this experiment, two-linear-parallel-probe (TLPP) method was used to determine the thermal conductivity of the HCP with  $w_c=0.35$  and 0.4 under dry and wet conditions respectively. Two probes were inserted into two parallel holes drilled in the specimen, where one probe was used as a heating source and the other as a temperature sensor. It was also assumed that the volume fraction of the water in the pore is 0% for the dry condition and 100% for the wet condition. This never occurs in reality, since hydrostatic pressure enables the release of the trapped air from the pores and the hygroscopic range of saturation is up to 97%. Additionally, capillary saturation and micropores with the radius smaller than  $1\mu m$  are neglected. All reasons mentioned above can seemingly explain the difference between experimental data and computed values. Unfortunately, experimental data on the thermal conductivity of cement paste between a dry state and a wet state is not available.

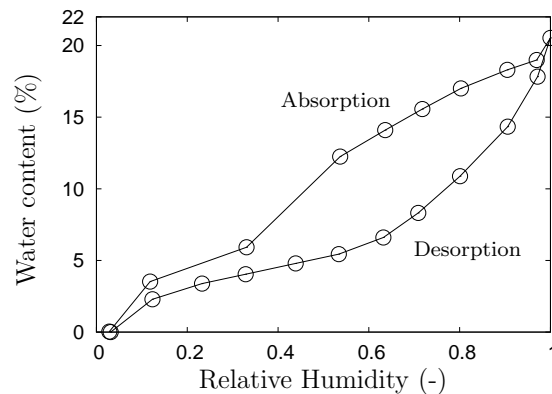


**Figure 6.6:** Isothermal absorption-desorption (BAROGHEL-BOUNY (2007)).

Mechanisms of the absorption and the desorption are very common in the porous material, where a substance is absorbed or released by another substance. The isothermal desorption and absorption curves for HCP with  $w_c=0.45$  from BAROGHEL-BOUNY (2007) are illustrated in Figure 6.6, which can be clarified by physical mechanisms, e.g. molecular absorption/desorption, capillary condensation, surface tension and disjoining pressure, see BAROGHEL-BOUNY (2007). In the experiment from BAROGHEL-BOUNY (2007), the saturated salt solution method was used where the specimens were kept in the sealed cells under constant temperature. Here, the relative humidity was kept constant by means of a saturated salt solution and the specimens were subjected to step-by-step desorption and subsequent absorption processes. Furthermore, various physically-based models have been developed to account for absorption/desorption isotherms, in order to understand the physics of confined systems and to predict their behavior, see BAROGHEL-BOUNY (2007) and ROUGELOT ET AL. (2009). Water content of the HCP under the same relative humidity is higher at desorption isotherm than the one at absorption isotherm, which is explained by the fact that the physical and chemical structures of cement paste are changed due to partial collapse of pure structure during first drying.

The relative saturation degree is defined as the current water content by the saturated water content in Figure 6.6, which has the same physical meaning as the volume fraction of the water used in previous computation steps. One can map the numerical curve in Figure 6.5(b) from the volume fraction of the water to the relative humidity through isothermal absorption curve, as the relative humidity is widely applied in the chemical reaction models. Therefore, the mean value and the standard deviation of 150 statistical tests as a function of the relative humidity are obtained, see Figure 6.7, and the approximations are obtained via

$$\bar{k}(s)^{\text{med}} = \sum_{i=0}^3 a_i^{\text{med}} s^i, \quad \bar{k}(s)^{\text{dev}} = \sum_{i=0}^3 a_i^{\text{dev}} s^i, \quad (6.3.6)$$

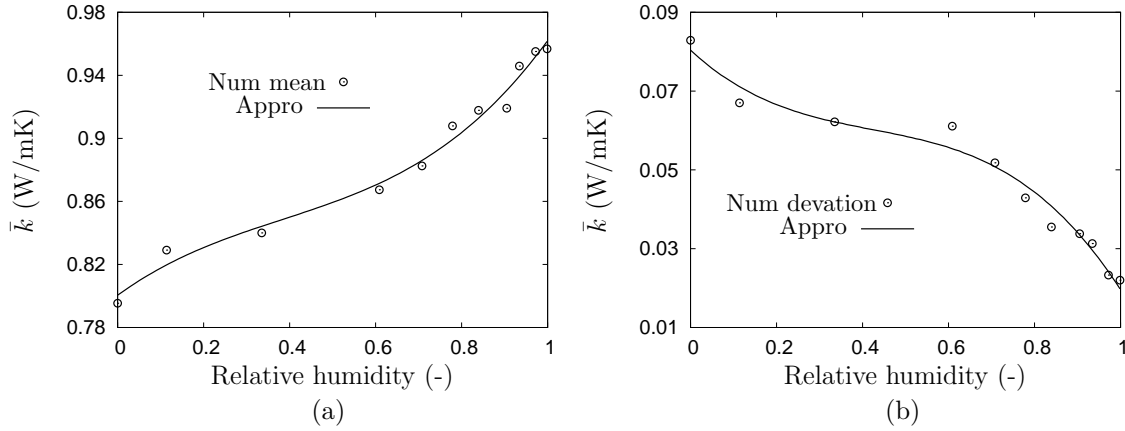


**Figure 6.7:** Approximations of (a) mean value and (b) standard deviation, of effective thermal conductivity of HCP with  $m = 1$  as a function of relative humidity of water in micropore.

where  $a_i^{\text{med}}$  and  $a_i^{\text{dev}}$  are approximation coefficients of the mean value and the standard deviation listed in Table 6.6. As a consequence, one can directly upscale the effect of relative humidity in the microscale to the mesoscale.

i	0	1	2	3
$a_i^{\text{med}}$	0.80050	0.1985	-0.2860	0.2491
$a_i^{\text{dev}}$	0.0804	-0.1008	0.1886	-0.1486

**Table 6.6:** Coefficients of approximation for effective thermal conductivity of HCP as a function of relative humidity.

### 6.3.2 Window method

There are, however, cases where a direct application of the widely used boundary conditions (BCs) listed in Table 6.1 may be unfavorable. For instance, when soft phases or voids are present in the vicinity of the boundary, pure traction and periodic type BCs may cause overly deformed meshes that are numerically undesirable, see MIEHE & KOCH (2002). In fact, these BCs are simply not applicable when voids intersect the boundary of the analysis domain. This leaves pure displacement type BCs as an option. These, on the other hand, can significantly overestimate the macroscopic stiffness for a given microstructural sample, see ZOHDI & WRIGGERS (2005). A remedy to these problems is to embed the sample into a frame of a homogeneous material following similar ideas from analytical approaches. This *window method* was proposed in BABUŠKA ET AL. (1999), where the window frame material was chosen as the matrix, see Figure 6.8, also presenting an example of the RVE of the HCP embedded in the window frame. Average stresses and strains were monitored in the entire extended domain and

hence a correction factor was introduced in order to alleviate the effect of the frame. The idea was later employed in HAIN & WRIGGERS (2008b) where the frame material was represented by the average stiffness of the microstructural constituents while still monitoring average quantities in the sample only. Finally, this approach was further developed towards a SELF-CONSISTENT model in KRABBENHØFT ET AL. (2008) wherein the frame material was iteratively updated until it matched the macroscopic response obtained from the sample. See also DÜSTER ET AL. (2012) for an application to three-dimensional cellular microstructures as well as where the frame material is representative of the original heterogeneous medium.

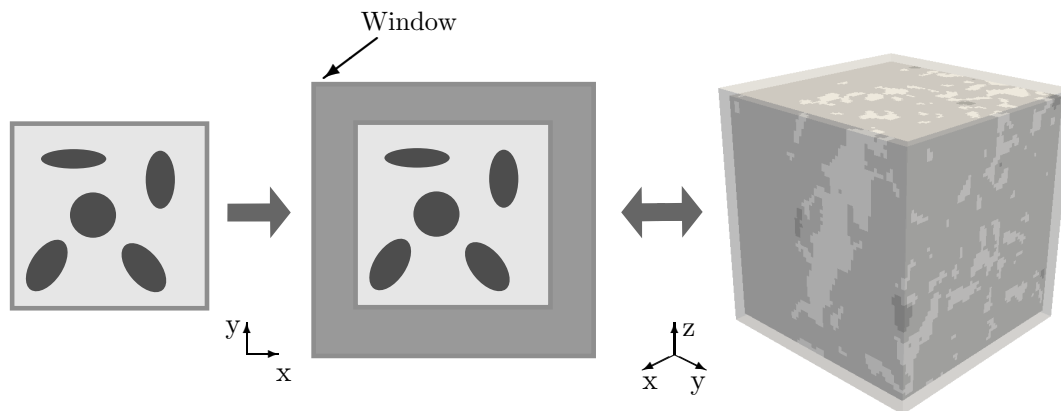


**Figure 6.8:** Window frame and a three-dimensional representation of an HCP sample from micro-CT scan with 64 voxels per direction embedded in a window.

Experience with the window method indicates that it delivers faster convergence of the macroscopic response with respect to BCs of pure displacement or traction type as the microstructural sample size is increased, a procedure that is necessary to assess the statistical representativeness of the sample. The variational background for this observed optimal convergence behavior of the homogenization results with the window method can be found in TEMIZER ET AL. (2013). The emphasis is on the effects of employing frames with finite width since the case of an infinite surrounding frame medium corresponds to the classical SELF-CONSISTENT scheme. A detailed overview of SELF-CONSISTENT methods is given in KANAUN & LEVIN (2008) and a recent discussion of their generalizations in BENVENISTE (2008). These methods have classically been applied to particulate- or fiber-reinforced composites, although extensions to more complicated heterogeneous media such as polycrystals have also been pursued, see JIANG & WENG (2004). Presently, no restrictions are imposed on the microstructural geometry however the presentation is limited to linear thermal conduction. The same variational principles apply to other physical phenomena within a linear framework in a straightforward fashion, in particular to diffusion or elasticity. An extension to the analysis of the overall electromagnetics response of heterogeneous media does not follow from this presentation yet it is expected to be realizable with additional effort in view of the applicability of classical micromechanics techniques to this physical regime,

see [BENVENISTE & MILTON \(2011\)](#).

### Augmented ordering relationship

Let  $\bar{k}_{LT}$ ,  $\bar{k}_{UF}$ ,  $\bar{k}_{PR}$  denote the homogenized thermal conductivities under linear temperature BCs, uniform normal thermal flux BCs and thermal periodic BCs obtained using the window method respectively. Without the frame, it is well-known ([HAZANOV & HUET \(1994\)](#)) that the ordering relationship

$$\bar{k}_{UF}^{(0)} \leq \bar{k}_{PR}^{(0)} \leq \bar{k}_{LT}^{(0)} \quad , \quad (6.3.7)$$

holds, where the superscript  $(\bullet)^{(0)}$  is used to denote that there is no frame and  $a \leq b$  means  $b - a$  is positive semi-definite. On the other hand, it will be shown that the window method subject to self-consistency delivers the augmented ordering relationship

$$\bar{k}_{UF}^{(0)} \leq \bar{k}_{UF} \leq \bar{k}_{PR} \leq \bar{k}_{LT} \leq \bar{k}_{LT}^{(0)} \quad . \quad (6.3.8)$$

Now, a signature of a statistically representative microstructural sample is that its response is independent of the boundary conditions imposed. Therefore, the gap between  $\bar{k}_{UF}^{(0)}$  and  $\bar{k}_{LT}^{(0)}$  is an indication of how well the sample represents the desired homogenized response. Increasing sample size typically results in a diminishing gap. When the gap is sufficiently small, the sample is deemed representative for computational purposes. Since it is undesirable to use very large samples, the practical significance of the augmented ordering relationship becomes apparent. The window method delivers results that always fall between the two alternative BC results and therefore, similar to periodic BCs, one expects it to deliver faster convergence with increasing sample size. In this sense, the window method provides a tighter control over the sample size such that it is eventually possible to use a smaller sample compared to the situation without a frame, assuming linear temperature BCs or uniform normal thermal flux BCs are of concern. Where  $\bar{k}_{PR}^{(0)}$  falls in Equation (6.3.8) will be commented upon.

The width of the frame appears to be a free variable and this was of concern in the original work of [BABUŠKA ET AL. \(1999\)](#) as well. Numerically, it is expected that choosing the frame width is similar to choosing the sample size—for a given sample size, one observes that  $\bar{k}$  saturates to a limit with increasing frame width. This expectation is based on the well-known self-consistent scheme, where the frame is essentially an infinite surrounding medium, which delivers a unique response independent of whether linear temperature BCs or uniform normal thermal flux BCs are employed ([NEMAT-NASSER & HORI \(1999\)](#)). In fact, one can show that the augmented ordering complemented by increasing frame width delivers a monotonic closure of the gap between linear temperature BCs and uniform normal thermal flux BCs results:

$$\bar{k}_{UF}^{(0)} \leq \bar{k}_{UF}^{(1)} \leq \bar{k}_{UF}^{(2)} \leq \dots \leq \bar{k}_W \leq \dots \leq \bar{k}_{LT}^{(0)} \leq \bar{k}_{LT}^{(1)} \leq \bar{k}_{LT}^{(2)} \quad . \quad (6.3.9)$$

Here, increasing superscript indicates the results obtained under increasing frame width and  $\bar{k}_W$  is the limit of the window method which corresponds the classical self-consistent

scheme. The thorough derivations based on variational theories about the augmented ordering relationship mentioned above can be found in WU ET AL. (2012). Although the presentation was pursued in a thermal context, the underlying variational basis is applicable to linear elasticity and diffusion in a straightforward manner.

The next objective is to demonstrate the observations of the earlier discussions through computations on two types of three-dimensional microstructures: (i) periodic microstructures where a unit cell corresponds to a sphere embedded in a matrix, and (ii) random microstructures which are obtained through the CT-scan of hardened cement paste, see Figure 6.8.

### Periodic media

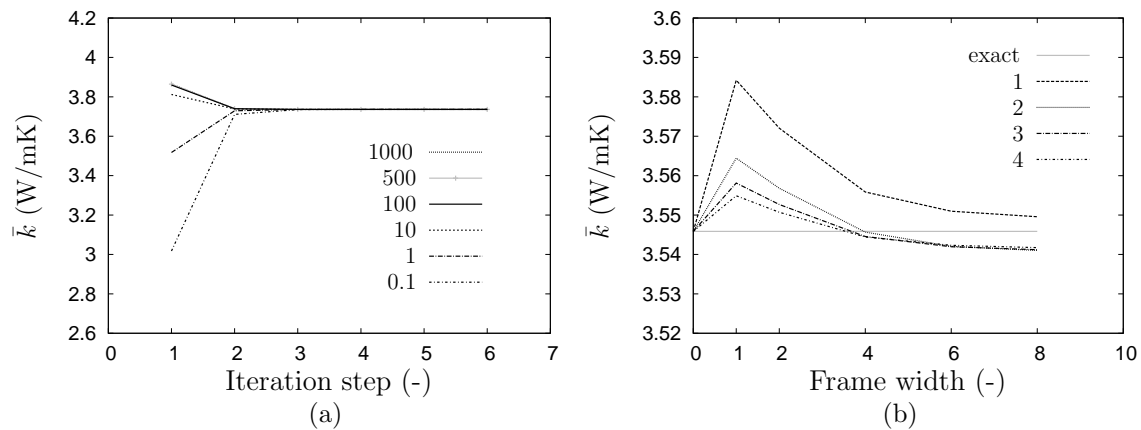


**Figure 6.9:** (a) Iterations under thermal periodic BCs with respect to various initial thermal conductivities  $k$  (W/mK) assigned to the frame of 1 unit around a unit cell and (b) influence of the frame width and number of unit cells per direction on the macroscopic thermal conductivity under PR-BCs. Self-consistency is ensured.

For investigations in the periodic setting, the unit cell width is set to 10 units while the diameter of the sphere is 9 units, corresponding to a volume fraction of approximately 0.38. The thermal conductivity of the sphere is 500 W/mK and the one of the matrix is 1 W/mK. The unit cell is embedded within a homogeneous frame and various BCs are directly prescribed on the frame to investigate the influence of the window method on the macroscopic response. The number of SELF-CONSISTENCY iterations vary depending on the conductivity initially assigned to the frame material but is typically less than four as summarized in Figure 6.9(a). The influence of the width of the frame is also illustrated in Figure 6.9(b) based on thermal periodic BCs, where it is observed that the results obtained with a frame converge to a limit with increasing frame width. In this periodic setting, it is also observed that this limit is very close to the exact result that is obtained with thermal periodic BCs directly on the unit cell. Clearly, for a given frame width, increasing the number of unit cells in the periodic sample also

drives the results closer to the exact result as expected, which is also shown in Figure 6.10(a) for the three types of BCs without a frame as well as with a fixed frame width of 4 units. Finally, the results of Equations (6.3.8) and (6.3.9) are also demonstrated in Figure 6.10(b), where strict ordering among different BCs as well as their convergence to a common limit with increasing frame width are observed.

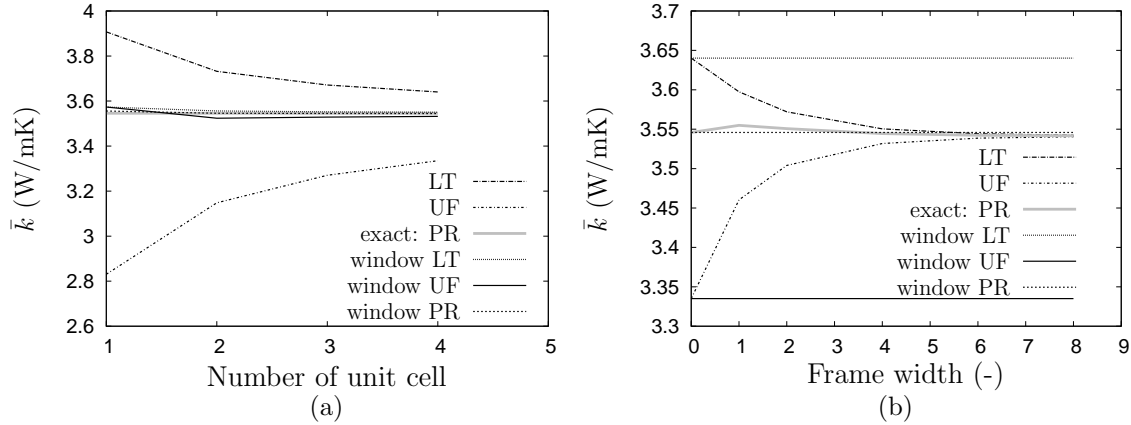


**Figure 6.10:** (a) Comparison of the macroscopic response with and without a frame (fixed width at 1 unit) under different BCs and increasing number of unit cells per spatial direction of the sample and (b) the influence of the frame width under different BCs with four unit cells per direction.

## Random media

As an application to random media, HCP is considered. The microstructure originates from a micro-CT scan although the assigned conductivities are artificial. The representation of an HCP sample embedded in a frame is illustrated in Figure 6.8, which is comprised of the unhydrated residual klinker, hydration product, micropores and window frame, referring to Subsection 5.3 for the volume fractions of the components in the HCP. The thermal conductivity of the klinker is set to 100 W/mK while the others are set to 1 W/mK. In presenting the results, a single quantity  $\bar{k}$  is monitored assuming macroscopic isotropy. This assumption is only satisfied for sufficiently large samples and therefore leads to some deviation from the predicted ordering relations for smaller sample sizes, the size referring to the number of voxels per spatial direction of the sample. This is observed in Figure 6.8 on a sample with 20 voxels per direction. Nevertheless, the response under different BCs approach each other with increasing frame width can be found in Figure 6.11(a). In order to obtain a statistically representative sample, larger CT-scans have to be employed. To alleviate randomness effects, 150 samples are tested per sample size. If no frame is used, it is observed that the linear temperature BCs and thermal periodic BCs results are close to each other but they remain significantly far away from uniform normal thermal flux BCs predictions, see Figure 6.11(b). This large gap casts a doubt on the quality of the macroscopic

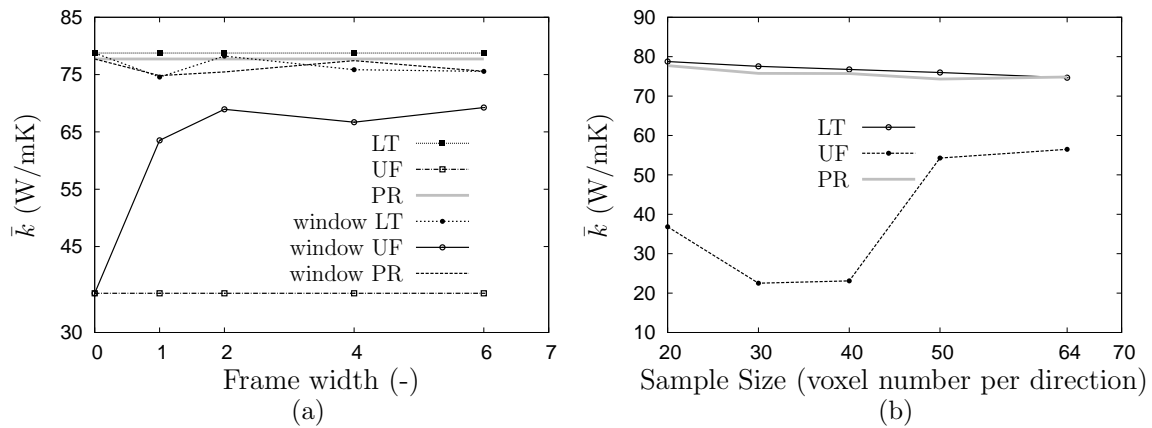


**Figure 6.11:** (a) The effect of the frame width on a single sample with 20 voxels per direction subjected to different BCs and (b) the effect of the sample size is demonstrated without a frame. 150 samples are tested and the results are averaged to alleviate randomness effects.

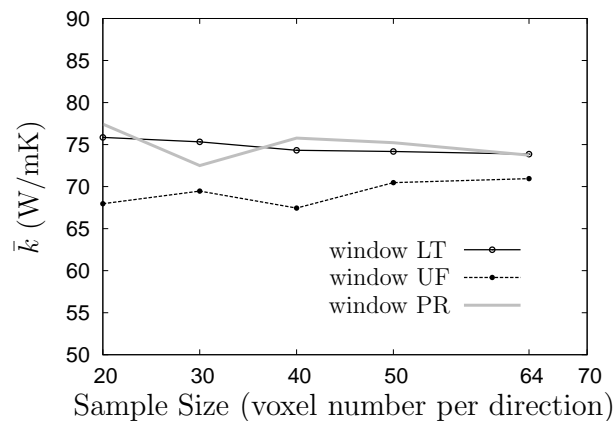


**Figure 6.12:** The effect of the sample size is demonstrated with a frame. 150 samples are tested.

predictions since the types of BCs should not affect the response of a statistically representative sample. When the same computations are carried out with a window, it is observed that the gap is small even at small sample sizes, see Figure 6.12. Consequently, one can state with confidence that the macroscopic conductivity is in the range of 70 to 75 W/mK. Considering that the frame width is only 4 units and that only two iterations were sufficient to ensure self-consistency, the additional cost of using the window method is negligible with this observed advantage. This advantage translates into a tighter control over the sample size when analyzing randomly heterogeneous media.

### 6.3.3 Computational diffusion homogenization

Also, computational homogenization approach was widely applied for diffusion problem. For example, the effective diffusivity of the stratum corneum via diffusion homogenization was obtained in RIM ET AL. (2007), which is the outermost layer of the skin, acting as a barrier membrane against the penetration of molecules into and out of the body. KRABBENHØFT ET AL. (2008) calculated the effective diffusivity of the HCP through computational homogenization approach, where the microstructure of the HCP was obtained from three-dimensional CT images. NILENIUS ET AL. (In press) applied the computational homogenization approach to the three-dimensional mesoscale of concrete, consisting of cement paste, aggregates and ITZ, where ITZ anisotropy was taken into account, thus leading to the dependence of the diffusivity tensor on the normal of the aggregate surface.

#### Theorem

FICK's law in Equation (2.6.15) is also assumed to be valid for each component of the HCP. Table 6.7 displayed three widely adopted boundary conditions for diffusion homogenization, e.g. linear humidity BCs, uniform normal diffusion flux BCs as well as diffusion periodic BCs. These BCs are proven to ensure the HILL's criterion through average humidity gradient and average diffusion flux theorems, see Appendix A for more details, which is only valid for the perfectly bonded material with  $\llbracket s \rrbracket = 0$ .

- 
1. *Linear humidity BCs:*  $s = \mathbf{W}_0 \cdot \mathbf{x}$  on  $\partial\mathcal{B}_t$ , with the coordinates  $\mathbf{x}$  of the boundary and  $\langle \nabla s \rangle = \mathbf{W}_0$ .
  2. *Uniform normal diffusion flux BCs:*  $j = \mathbf{J}_0 \cdot \mathbf{n}$ , with  $j := \mathbf{j} \cdot \mathbf{n}$  and  $\langle \mathbf{j} \rangle = \mathbf{J}_0$ .
  3. *Diffusion periodic BCs:*  $s^+ - s^- = \mathbf{W}_0 \cdot (\mathbf{x}^+ - \mathbf{x}^-)$  (periodicity of the humidity) and  $j^+ = -j^-$  (anti-periodicity of the diffusion normal flux) with  $\langle \mathbf{j} \rangle = \mathbf{J}_0$ .
- 

**Table 6.7:** Three widely used boundary conditions for computational diffusion homogenization.

In terms of the procedure of computational diffusion homogenization, effective diffusivity  $\bar{d}$  for the isotropic case is determined by minimizing a least-square function

$$II := [\langle \mathbf{j} \rangle - \mathbf{j}^*(\langle \nabla s \rangle)]^2 \rightarrow \min \quad . \quad (6.3.10)$$

in which the effective constitutive equation for diffusion is defined by

$$\mathbf{j}^*(\langle \nabla s \rangle) = -\bar{d} \langle \nabla s \rangle \quad . \quad (6.3.11)$$

with diffusion flux  $\mathbf{j} = (j_1, j_2, j_3)^T$ . Differentiation of Equation (6.3.10) with respect to  $\bar{d}$  leads to

$$\frac{dII}{d\bar{d}} \stackrel{!}{=} 0 \quad . \quad (6.3.12)$$

Thus, the isotropic effective diffusivity is obtained through

$$\bar{d} = -\frac{\langle \mathbf{j} \rangle_1 \langle \nabla s \rangle_1 + \langle \mathbf{j} \rangle_2 \langle \nabla s \rangle_2 + \langle \mathbf{j} \rangle_3 \langle \nabla s \rangle_3}{\langle \nabla s \rangle_1^2 + \langle \nabla s \rangle_2^2 + \langle \nabla s \rangle_3^2}. \quad (6.3.13)$$

### Comparison between numerical results and experiment

The effect of the temperature on the diffusivity of cement paste has been proven through experiments e.g. in HANCOX (1968), JOOSS & REINHARDT (2002) and PAVILÍK & ČERNÝ (2012). It justifies the need of incorporating the effect of the temperature into diffusion homogenization for determining the effective diffusivity of HCP. MILLS (1973) provided the experimental discrete data reflecting the dependence of the diffusivity of micropore  $d_p$  in the HCP on the temperature, see Figure 6.13(a). It is approximated by one polynomial curve, which is introduced in Table 6.8.

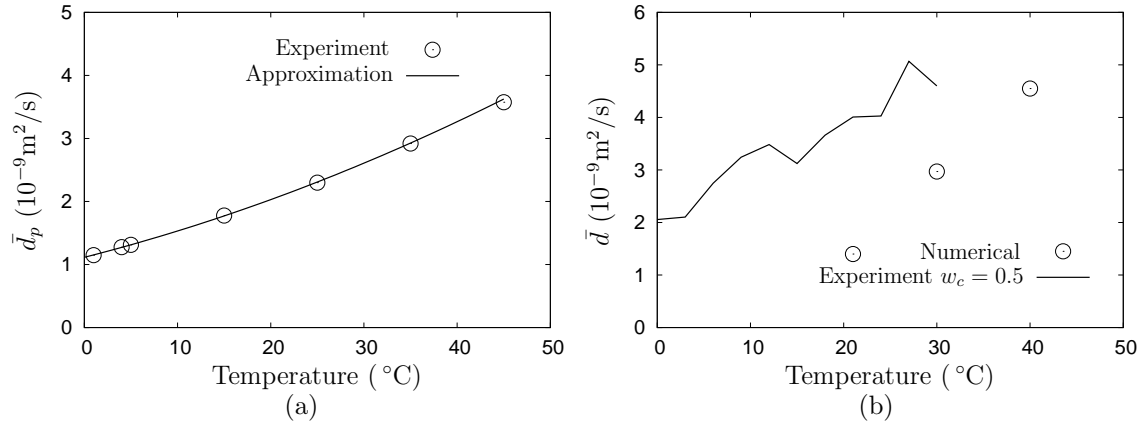


**Figure 6.13:** (a) Diffusivity of micropore affected by temperature from experiment (MILLS (1973)) and the approximation and (b) comparison between computed effective diffusivity of HCP and experiment (HANCOX (1968)).

Material	Diffusivity ( $10^{-9} \text{m}^2/\text{s}$ )
Hydration product	0.015 (ZHANG ET AL. (2011b))
Unhydrated clinker	0.0 (ZHANG ET AL. (2011b))
Micropore	$D_p = 1.1141 + 0.0378\theta + 0.0004\theta^2$ (Figure 6.13(a) )

**Table 6.8:** Diffusivity of components in HCP. Diffusivity of the micropore depends on temperature.

150 statistical RVEs of  $64^3 \mu\text{m}^3$  from the microstructure of HCP are chosen for diffusion homogenization under linear humidity boundary condition, see Figure 6.13(b) for the computed effective diffusivity. The mean value and the standard deviation of 150 statistical tests as a function of the temperature are approximated via

$$\bar{d}(\theta)^{\text{med}} = \sum_{i=0}^3 a_i^{\text{med}} \theta^i \quad , \quad \bar{d}(\theta)^{\text{dev}} = \sum_{i=0}^3 a_i^{\text{dev}} \theta^i \quad , \quad (6.3.14)$$

where  $a_i^{\text{med}}$  and  $a_i^{\text{dev}}$  are approximation coefficients of the mean value and the standard deviation, which are listed in Table 6.9.

i	0	1	2	3
$a_i^{\text{med}}$	0.20050	0.05	-0.20	0.241
$a_i^{\text{dev}}$	0.104	0.102	0.166	-0.486

**Table 6.9:** Coefficients of approximation of effective diffusivity of HCP as a function of temperature.

The obtained nonlinear correlation between the effective diffusivity of HCP and the humidity in micropores can be upscaled to the next length-scale. The comparison between the computed results and the experiment (HANCOX (1968)) is displayed in Figure 6.13(b). In the experiment, the drying of the cement paste specimens with  $w_c = 0.5$  has placed in an air stream of velocity  $10 \text{ cms}^{-1}$ , in the temperature range  $21\text{-}40^\circ\text{C}$ , and at mean temperatures between  $38.5$  and  $85^\circ\text{C}$ . Clearly, the numerical results overestimate the experimental data, which can be explained by the different cement paste specimens,  $w_c$  and experimental conditions. Nevertheless, the results are observed to be of the same order of magnitude.

### 6.3.4 Computational mechanical homogenization

In the linear elastic regime, computational homogenization scheme is well-established, see TORQUATO (2002), ZOHDI & WRIGGERS (2005) and references therein. The effective material matrix  $\bar{\mathbb{C}}$  is introduced to map the volume average of strain and the volume average of stress with the assumption of isotropy

$$\langle \boldsymbol{\sigma} \rangle = \bar{\mathbb{C}} : \langle \boldsymbol{\epsilon} \rangle \quad . \quad (6.3.15)$$

In the nonlinear elastic regime, the existing problems of non-uniqueness of the solution at finite deformations and the non-invertability of the stress-strain relation leads to the need of more efforts on the investigations, e.g. isotropic damage with finite deformation (LÖHNERT (2004)), anisotropic finite elastoplasticity (MIEHE & SCHOTTE (2007)) and crystal plasticity (LEHMANN (2013)).

Three widely adopted boundary conditions for mechanical homogenization are illustrated in Table 6.10, e.g linear displacement BCs, uniform normal traction BCs as well as mechanical periodic BCs. Appendix A provides the specific proof of the satisfaction of the HILL's criterion of these boundary conditions through theorems of average strain gradient and average stress for the perfectly bonded material with  $\|\mathbf{u}\| = 0$ .

- 
1. *Linear displacement BCs:*  $\mathbf{u} = \boldsymbol{\epsilon}_0 \cdot \mathbf{x}$  on  $\partial\mathcal{B}_t$ , with the coordinates  $\mathbf{x}$  of the boundary and  $\langle \boldsymbol{\epsilon} \rangle = \boldsymbol{\epsilon}_0$ .
  2. *Uniform normal traction BCs:*  $\mathbf{t} = \boldsymbol{\sigma}_0 \cdot \mathbf{n}$ , with  $\mathbf{t} := \boldsymbol{\sigma} \cdot \mathbf{n}$  and  $\langle \boldsymbol{\sigma} \rangle = \boldsymbol{\sigma}_0$ .
  3. *Mechanical periodic BCs:*  $\mathbf{u}^+ - \mathbf{u}^- = \boldsymbol{\epsilon}_0 \cdot (\mathbf{x}^+ - \mathbf{x}^-)$  (periodicity of the displacement) and  $\mathbf{t}^+ = -\mathbf{t}^-$  (anti-periodicity of the normal traction with  $\langle \boldsymbol{\epsilon} \rangle = \boldsymbol{\epsilon}_0$ ).
- 

**Table 6.10:** Three widely used boundary conditions for computational mechanical homogenization.

### Determination of ASR induced effective damage

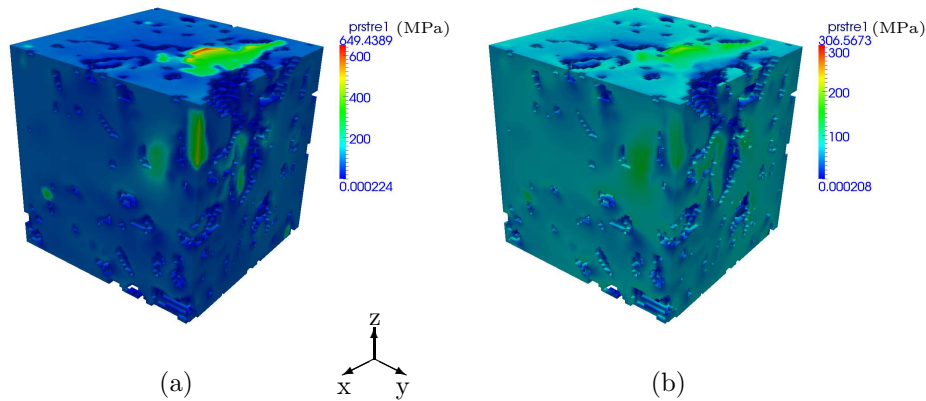


**Figure 6.14:** (a) Without the window method (micropores are not shown) and (b) with the window method (micropores and window are not shown).

The motivation of this subsection is to obtain the effective damage induced by ASR from the the microscale through homogenization approach, where the combination of displacement BCs and window method is prescribed, such that the resulting effective damage can be applied to the next length-scale. The widow width of  $4\mu m$  is adopted in this work, see HAIN & WRIGGERS (2008b), and the distinctions of principle stress in the RVE of HCP with and without window frame under displacement BCs of the same quantity are respectively shown in Figure 6.14.

Once the size of the RVE and width of the window are determined, computational homogenization is carried out to obtain the effective chemical damage  $D^c$ . It is determined through the volume average of the isotropic damage variable defined in Subsection 5.3.3, which is triggered by the expansion of the gel. It is computed by imposing a zero average strain on the famed sample. The expansion coefficient of the gel at the microscale is still unknown, so that some reasonable values are tested to demonstrate the effective damage with respect to days, see Figure 6.15(a), where the adopted correlation between chemical extent and days originates from Figure 4.5. Note that the accumulated plastic strain in the RVE due to gel expansion is much smaller than the total strain, see Figure

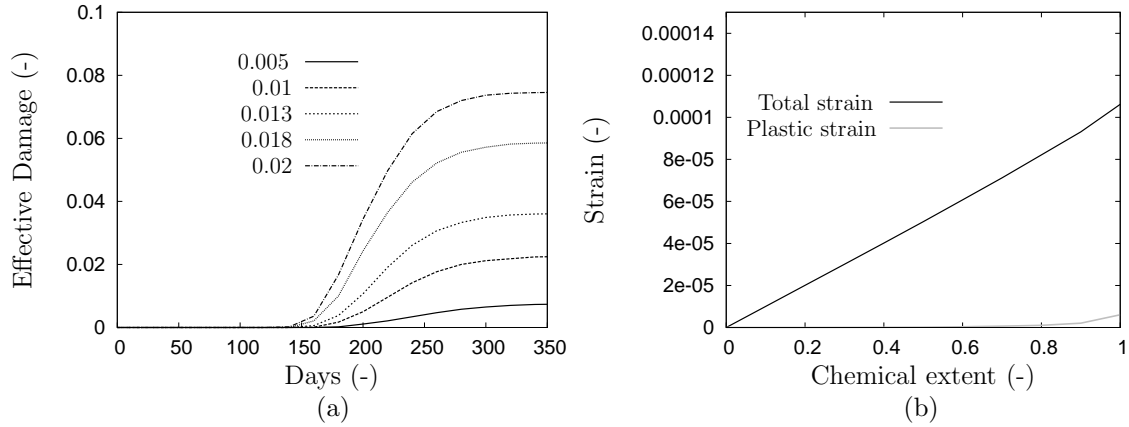


**Figure 6.15:** (a) Effective damage of RVE in HCP with different expansion coefficients of the gel with respect to days and (b) total strain and plastic strain of HCP under stress-free BCs.

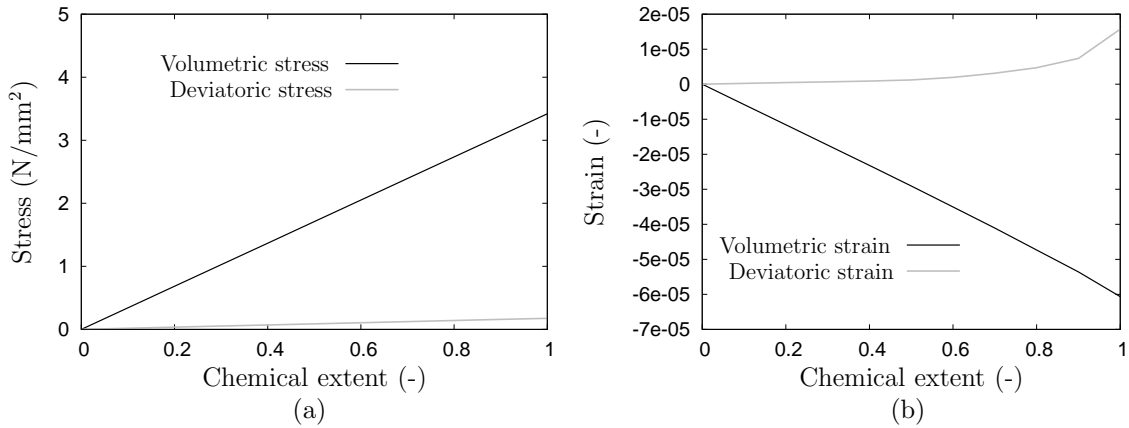


**Figure 6.16:** (a) Average volumetric and deviatoric stress under strain-free BCs and (b) average volumetric and deviatoric strain under stress-free BCs on HCP.

6.15(b). Accordingly, it is reasonable to assume that the microscale plasticity mechanisms do not significantly affect the mesoscale mechanical damage. This conclusion is expected since the chemical damage is predominantly due to gel expansion, which induces mostly volumetric strain and stress throughout the HCP. Figure 6.16 display a comparison of the average volumetric and deviatoric stresses in the microstructure under strain-free BCs as well as a comparison of the average volumetric and deviatoric strains under stress-free BCs. The deviatoric portions are responsible for plasticity and they are seen to be much smaller than the volumetric ones. With the ability to upscale the ASR induced damage, the overall homogenized mesoscale response is sought next.

### Two-step homogenization framework for parameter identification

The chemically unstable characteristics of the gel poses challenges in experimentally measuring its mechanical properties. Alternatively,  $FE^2$ -based homogenization can be utilized to obtain parameters at the microscale which are not easily measured through experiment, see SCHMIDT ET AL. (2012) for a recent example. In the context of  $FE^2$ , a coupled micro-macro simulation is carried out without the need for formulating an explicit homogenized formulation. If the resulting macroscopic mechanical behavior of the structure coincides with the experimental data, the parameters chosen at the microscale are deemed satisfactory, see YU & FISH (2002) and SCHMIDT ET AL. (2012). In the present study, this method is not applicable due to its prohibitive computational cost. Instead, a two-step homogenization procedure is applied in a reverse manner based on the explicit homogenized mechanical response of HCP, with the goal of obtaining the expansion coefficient of the gel at the microscale, see Figure 6.17.

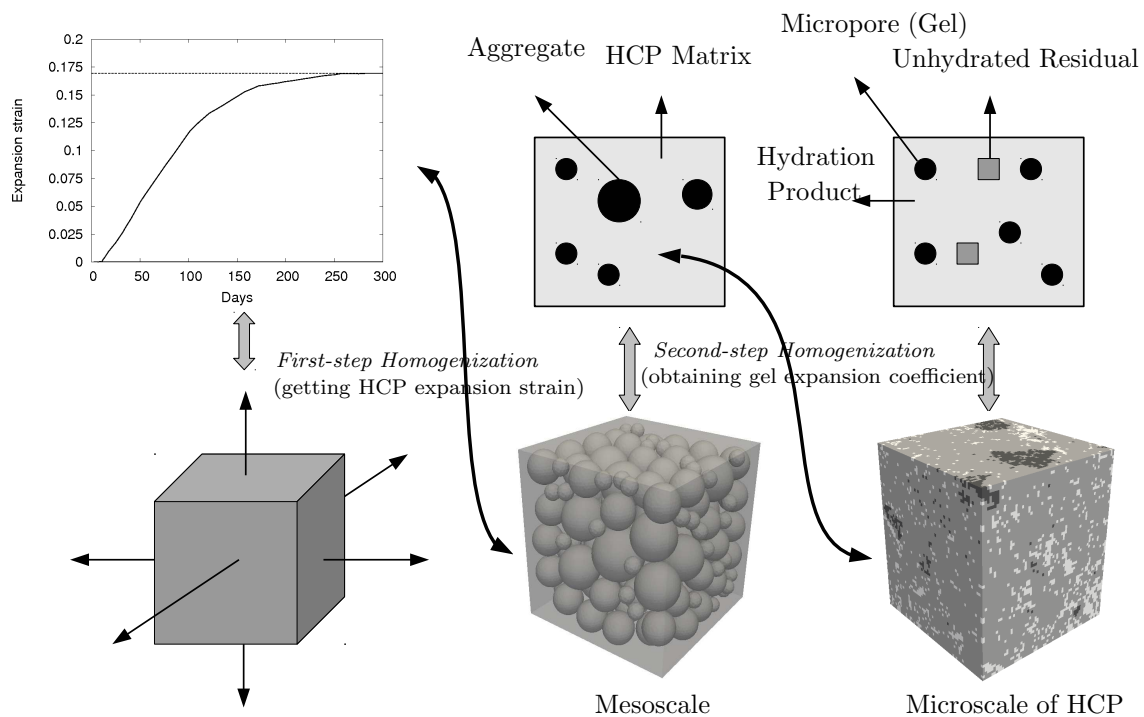


**Figure 6.17:** Framework of two-step homogenization for parameter identification: link between concrete and HCP, and link between HCP and micropores.

#### First step homogenization: HCP expansion strain determination

Experimentally, it is observed that the dimensions of a concrete specimen suffering from ASR increase due to the swelling of the constituents, see SMAOUI ET AL. (2004). The ASR induced volumetric expansion strain of the concrete specimen under stress-free conditions with respect to days is illustrated in Figures 6.17 and 6.18. The hypothesis

of the swelling mechanism in ASR employed in this work is that all gels are evenly produced and swell at the micropores of HCP. Consequently, the ASR induced expansion occurs in the HCP matrix of the mesoscale, rather than in the aggregates, thereby contributing to the macroscopic expansion of concrete. In the context of numerical implementation, an additional term for the expansion strain due to ASR is incorporated into the inelastic constitutive equation of HCP described in Subsection 2.4.1 and 2.4.2, thus presenting that the concrete is suffering from ASR internally:

$$\boldsymbol{\sigma} = (1 - D^u) \mathbb{C}_0 (\boldsymbol{\epsilon} - \boldsymbol{\epsilon}^{\text{pl}} - M_p \mathbf{1}) \quad , \quad (6.3.16)$$

where  $M_p$  denotes the ASR induced expansion strain in the HCP. The objective of the first step homogenization is to determine the value of  $M_p$ , so that the effective volumetric expansion strain of concrete through computational homogenization approach only triggered by the expansion mechanism of ASR can coincide with the experimental data in Figure 6.18. The experiment from Figure 6.18 was carried out under stress-free condition. Presently, the stress-free state is generated through strain-control to prescribe BCs for homogenization. The hypothesis that the gel retains permanent characteristics throughout the process renders it feasible to only concentrate on fitting the final expansion strain as a simplified case, see the straight line in Figure 6.18, where the chemical extent  $\xi$  is considered to be 1. The constant strain tensor  $\boldsymbol{\epsilon}_0$  defined by final volumetric expansion strain in Figure 6.18 is applied to impose displacement BCs for homogenization through  $\mathbf{u} = \boldsymbol{\epsilon}_0 \cdot \mathbf{x}$  on  $\partial\mathcal{B}_t$ , where  $\mathbf{x}$  is the coordinates of nodes on  $\partial\mathcal{B}_t$ .  $M_p$  is sought, until the hydrostatic stress of concrete equals to zero at the end of the reaction. This method is also adopted in the second step of homogenization.

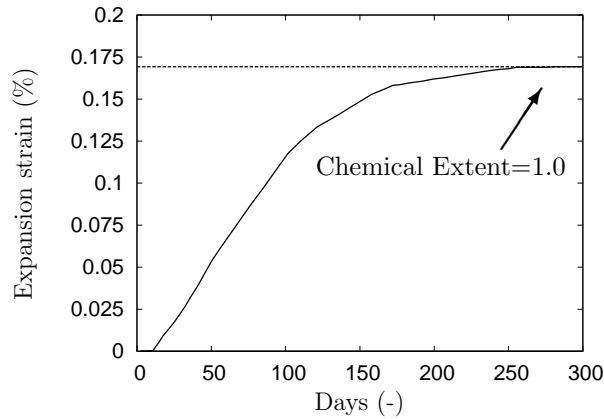


**Figure 6.18:** Volumetric strain due to ASR in the concrete specimen under stress-free condition (SMAOUI ET AL. (2004)).

### Second step homogenization: gel expansion coefficient determination

The second step of homogenization is to downscale to the microscale of HCP for determining the expansion coefficient of the gel. In this work, it is assumed that the swelling

of the gel occurs at the micropores of HCP, which results in the expansion of the HCP matrix and therefore of concrete. The expansion strain of the gel is modeled as proportional to the chemical extent  $\xi$ :  $A = \beta\xi$ , where  $A$  is the expansion strain of the gel, and  $\beta$  is the microscale expansion coefficient of the gel, independent of time according to earlier assumptions. The homogenization procedure explained in Subsection 6.3.4 is applied on the RVE of HCP with a window frame, where the  $M_p$  obtained from the first step homogenization prescribes displacement BCs for homogenization, thus inducing stress-free conditions. The step also concentrates on the end of the reaction, where the chemical extent is equal to 1.  $\beta = 0.0025$  is found to deliver negligible hydrostatic stress at the end of the reaction. Performing stress-free BCs through strain-control BCs for homogenization at the micro and mesoscale keeps the consistency in comparison to the expansion experiment implemented under stress-free BCs in Figure 6.18.

The deterioration due to ASR from the microscale is not taken into account at the first step homogenization, see Equation (6.3.16). However, it possibly affects the mechanical property and the subsequent expansion behavior of the concrete specimen. Its effect is investigated as follows. The obtained expansion coefficient  $\beta$  is adopted to calculate the effective damage of HCP due to ASR through homogenization approach with respect to extent, where strain-free BCs are prescribed. The chemical effective damage is incorporated into the inelastic constitutive equation of HCP to run the first step of homogenization again. The next task is to evaluate whether the change of the old  $M_p$  and the new  $M_p$  can be neglected. If not, it is necessary to carry out the second step of homogenization with the new  $M_p$  again. Iterations are carried out until the change of  $M_p$  from one step to the next step is small enough. The algorithm is summarized in Table 6.11.

### Statistical analysis associated with homogenization

The approximate RVE used in previous computation is only a randomly chosen sample from a much larger micro-CT scan of HCP. Hence, it is indispensable to carry out statistical tests to address the effect of randomness. For this purpose, 30 randomly obtained RVEs from a micro-CT scan are tested. The resulting effective damage due to the expansion of the gel with respect to days and chemical extent are shown in Figure 6.19, respectively. The corresponding mean value and standard deviation of the effective damage are calculated as a function of the chemical extent, see points in Figure 6.20, via the polynomial expansions

$$D^c(\xi)^{\text{med}} = \sum_{i=0}^3 e_i^{\text{med}} \xi^i \quad , \quad D^c(\xi)^{\text{std}} = \sum_{i=0}^3 e_i^{\text{std}} \xi^i \quad . \quad (6.3.17)$$

The coefficients of approximation are listed in Table 6.12. This correlation between effective damage due to ASR the chemical extent can be directly upscaled to HCP at the mesoscale of concrete. Since the chemical extent has been projected as a constant

1. *First step homogenization:* The extra term  $M_p$  as the expansion strain of HCP due to ASR is incorporated into the nonlinear constitutive equation of HCP at the mesoscale, see Subsection 2.4.1 and 2.4.2.
  - a. *Initial Step:*  $\boldsymbol{\sigma} = (1 - D^u)\mathbb{C}_0(\boldsymbol{\epsilon} - \boldsymbol{\epsilon}^{pl} - \mathbb{C}_0\mathbf{1})$ .
  - b. *Other steps:*  $\boldsymbol{\sigma} = (1 - D^u - D^c)\mathbb{C}_0(\boldsymbol{\epsilon} - \boldsymbol{\epsilon}^{pl} - M_p\mathbf{1})$ .
 Run homogenization at the mesoscale, where  $\boldsymbol{\epsilon}_0$  from Figure 6.18 is adopted to impose linear displacement BCs. The expansion strain  $M_p$  of HCP at the end of the reaction is obtained until the hydrostatic of concrete equals to 0.
2. *Second step homogenization:* Run homogenization in the RVE of HCP, where the obtained  $M_p$  from the first step homogenization is adopted to prescribe displacement BCs. The expansion strain of the gel  $A$  is acquired until the hydrostatic stress of HCP at the end of reaction is equal to 0. Thus the expansion coefficient of the gel  $\beta$  is obtained through  $A = \beta\xi$ , since  $\xi$  equals to 1.
3. *Upscale damage:* Run homogenization with the obtained  $\beta$  in the RVE of HCP under strain-free BCs to calculate the effective ASR induced damage  $D^c$  of HCP with respect to extent.
4. *Check.* Apply the sum of the damage from mechanical loading and chemical part to the constitutive equation of HCP at the mesoscale and run step 1 again.
  - a. If the change of  $M_p^{\text{old}}$  and  $M_p^{\text{new}}$  is small enough, stop computation.
  - b. If not, implement the step 2 again to get the new  $\beta$ . Then carry out the step 3 and step 4 again, until the change of  $M_p$  from one step to the next step is small enough.

**Table 6.11:** Algorithm of two-step homogenization to obtain the expansion of the gel at the microscale.

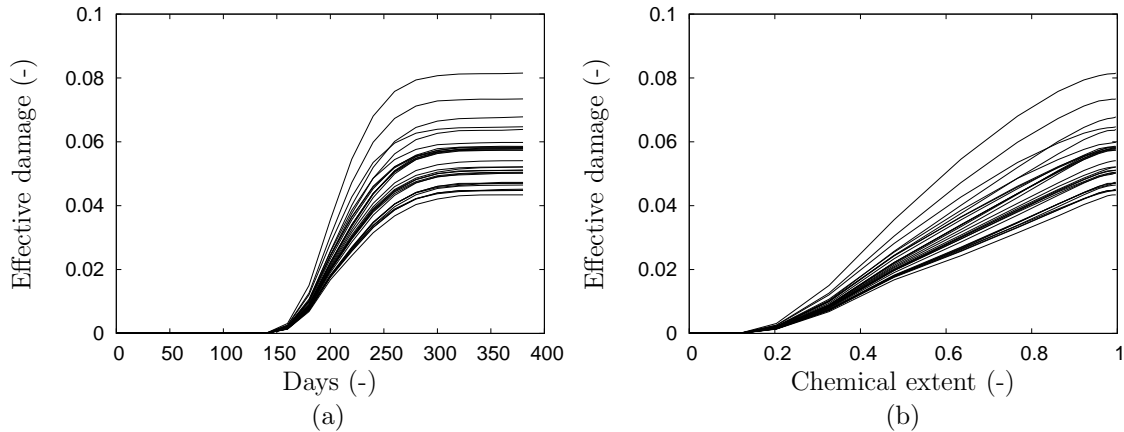


**Figure 6.19:** Effective ASR induced damage with respect to (a) days and (b) extent  $\xi$ , for 30 statistical tests.

to the RVE, hydro-thermo-mechanical (remember) coupling does not manifest itself at this scale. In order to reflect the observations that ASR is activated when the threshold of relative humidity is achieved, see Subsection 4.2.3, and that ASR induced damage

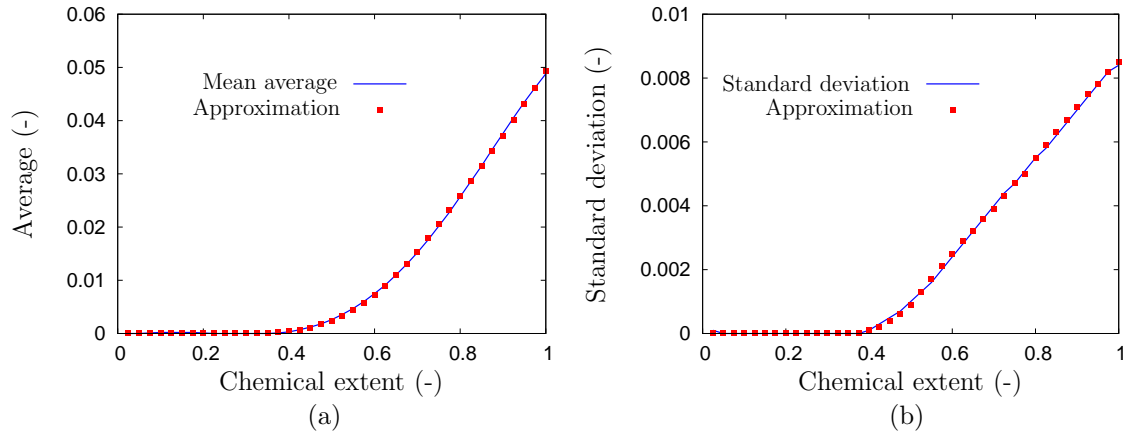


**Figure 6.20:** Approximations of (a) mean average and (b) standard deviation, of effective damage of statistical tests.

i	0	1	2	3
$e_i^{\text{med}}$	0.0809	-0.1737	0.1284	-0.0016
$e_i^{\text{std}}$	0.0344	-0.0581	0.0295	-0.0002

**Table 6.12:** Approximation coefficients of mean value and standard deviation of effective damage of statistical tests with respect to chemical extent.

occurs at the mesoscale after the chemical extent reaches to 0.3, see Figure 6.20, full coupling needs to be addressed at the mesoscale.



# Chapter 7

## Computational simulation of effects of the ITZ

Assuming the domain  $\mathcal{B}_t$  with an interface layer between the sub-domains  $\mathcal{B}_t^+$  and  $\mathcal{B}_t^-$ , namely ITZ between aggregates and HCP in concrete, boundary conditions with respect to mechanical, thermal and diffusion problems are prescribed on the surface of the boundary, see Figure 2.3. The microstructure of ITZ with higher porosity leads to its weak mechanical property. In this sense, at a relatively low stress level, ITZ may fail, rather than HCP or aggregates, therefore, it is crucial to concern the role of ITZ in the multiscale numerical simulation of concrete. For instance, in order to obtain a better estimation of the elastic modulus of concrete, not only the cement paste and aggregates, but also ITZ have already been considered in the numerical simulation, see RAMESH ET AL. (1996) and NADEAU (2003) for two-dimensional and LEE & PARK (2008) for three-dimensional cases. Furthermore, interface elements with zero-thickness are generated between HCP and aggregates as representatives of ITZ at the mesoscale of concrete, which is explicitly motivated by CZM allowing for the nonlinear behavior like debonding. This approach was widely utilized e.g. in CAROL ET AL. (2001), HÄFNER ET AL. (2006), ECKARDT & KÖNKE (2008), SNOZZI ET AL. (2011) and SNOZZI ET AL. (2012), accounting for the influence of ITZ on macroscale performance of concrete in terms of various types of load, e.g. static tension and compression as well as dynamic tension and compression.

In addition to the analysis of ITZ from a mechanical point of view, the present work also concerns the effects of the resulting debonding at the ITZ on the thermal conduction and humidity diffusion across the crack, see Figure 2.3 for the framework of displacement jump  $\llbracket \mathbf{u} \rrbracket$ , temperature jump  $\llbracket \theta \rrbracket$  and humidity jump  $\llbracket s \rrbracket$  across the crack. WILLAM ET AL. (2004) developed the thermo-mechanical cohesive model in interface elements with zero-thickness between aggregate and cement paste in concrete exposed to high temperature. In the interface elements, mechanical damage, thermal damage as well as their interactions were defined, with the purpose of reflecting the thermal resistance by the existence of the displacement jump at the interface. Furthermore, if the separated bodies tend to contact under external force, the thermal conduction flows through the contacting asperities of the rough surface. Hence, ZAVARISE ET AL.

(1992) proposed a model to conduct a modified penalty formulation with a contact law based on a thermo-plastic microscopic contact model, while taking into account the effect of roughness in the simulation. Also, more applications can be found in, e.g. polymer (ÖZDEMİR ET AL. (2010)), solders in electronics chip packages subjected to active power cycling (BENABOU ET AL. (2013)) and photovoltaics (SAPORA & PAGGI (2014)).

As compared to the thermal problem, more investigations concerning the influences of the crack or debonding on the diffusivity of concrete were conducted through not only analytical but also numerical approaches. As described in GÉRARD & MARCHAND (2000), an analytical approach was proposed to explain how the traversing cracks affect the diffusion properties of ions in the saturated concrete. However, for the sake of simplicity, cracks were assumed to be evenly distributed on a one- or two-dimensional grid with uniform size. From a numerical point of view, KAMALI-BERNARD & BERNARD (2009) developed a three-dimensional tool to investigate the influence of the tensile loading on the diffusivity of the mortar of  $w_c = 0.4$  with the aid of a numerical platform called MuMoCC (Multi-scale Modelling of Computational Concrete). The microstructure of the mortar was generated in CEMHYD3D and then the resulting voxelized images were transferred to ABAQUS, therefore, the diffusivity at different strains could be estimated. BENTZ ET AL. (2013) conducted two-dimensional simulations to estimate the influences of the cracking on the diffusivity of hydrating cement pastes, but a single crack located directly above the steel reinforcement was assumed.

By now, a majority of previous works are concerned with either mechanical-diffusion or mechanical-thermal coupling at the ITZ of concrete, which motivates the establishment of mechanical-thermal-diffusion cohesive zone model in the present work, thereby offering the overall investigations on the ITZ in concrete. Section 7.1 implements the influences of various parameters on the macroscale mechanical behavior of concrete, consisting of tensile strength, fracture energy, specimen size as well as random distribution of aggregates. Also, a scalar damage parameter is defined in interface elements in order to quantify how much they debond in tension and compression respectively. In the following, a mechanical-thermal-diffusion cohesive zone model based on a staggered approach is established, such that the influences of the debonding at the ITZ on the thermal conduction and humidity diffusion across the cohesive crack can be numerically depicted, see Section 7.3.

## 7.1 Numerical results in uniaxial tension

Before numerical simulations can be performed, it is crucial to review the mesostructure of concrete, constituting randomly distributed aggregates with a volume fraction of 40% embedded in the homogenized HCP with the dimension of  $100 \times 100 \times 100 \text{ mm}^3$  as well as zero-thickness interface elements exhibiting ITZ. Here, aggregates are assumed to behave elastically, MAZARS damage model (MAZARS & PIJAUDIER-CABOT (1989)) is

defined in the HCP and the interface elements are driven by CZM. In the following, various parameters are tested to investigate their influences on the macroscale behavior of concrete, including tensile strength, fracture energy, specimen size as well as random distribution of aggregates. Concerning the uniaxial tensile boundary condition, the lower surface of concrete is fixed and the displacement is prescribed at the upper surface in  $zz$  direction. The qualitative comparison of the stress in  $zz$  direction between perfectly bonded and imperfectly bonded are illustrated in Figure 7.1.

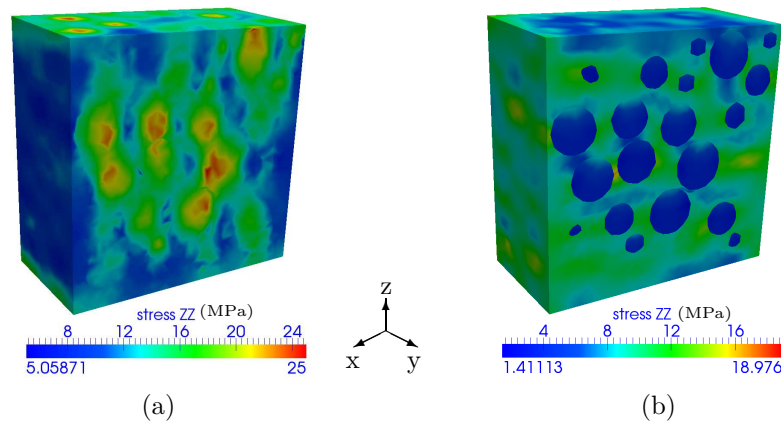


**Figure 7.1:** Stress in  $zz$  direction in uniaxial tension (a) perfectly bonded and (b) imperfectly bonded.

### 7.1.1 Damage distribution

MASO (1996) pointed out that a great amount of microcracks already exist at the ITZ in concrete without deformation. As indicated in VAN MIER & MAN (2009), when a uniaxial tensile load is applied to concrete, the resulting fracture behavior can be concluded with a three-stage process. The stable nucleation of microcracks is first initialized at the ITZ between HCP and aggregates in a distributed manner, and then these microcracks continue to grow and propagate as the tensile load increases. Finally, the coalescence of microcracks forms the unstable macrocracks, thus leading to the failure of concrete. Figure 7.2 presents the link of the computed damage distribution and macroscale stress-strain relationship of concrete in uniaxial tension. From it, it is observed that microcracks are developed first in a distributed manner, and then localize into only one or two competing macrocracks in a realistic fashion that the direction of the crack propagation is transverse to the direction of the load. Moreover, these microcracks coalesce to form macrocracks after the peak stress, thereby yielding the decrease of the ability of concrete to carry the load and the existence of failure in a strongly localized manner. For the tensile case, quite few energy is required for the initiation and growth of cracks, including pre-existing cracks at the ITZ and newly formed cracks in the matrix, characterizing the brittle property of concrete in tension.

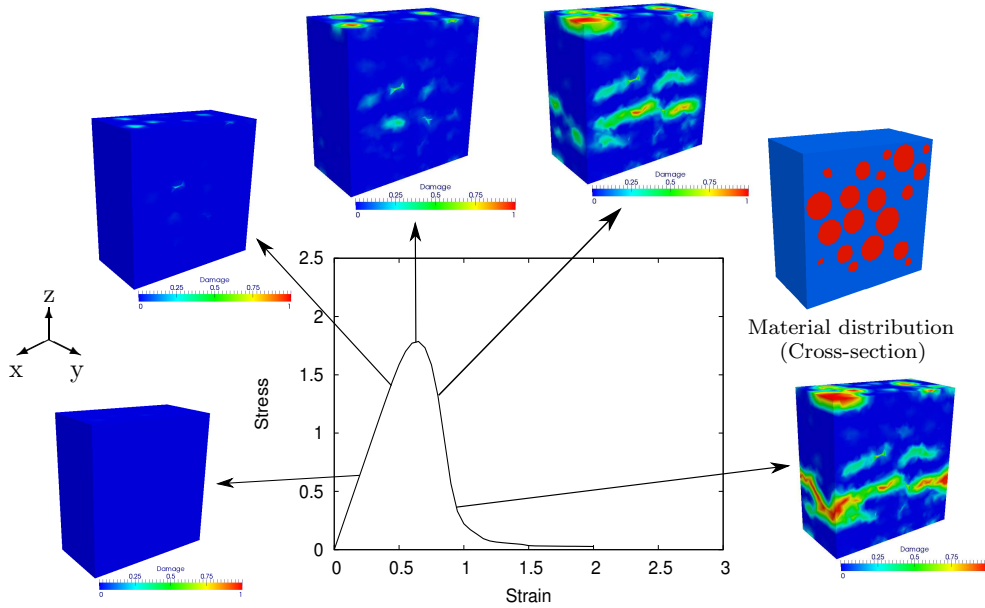


**Figure 7.2:** Distribution and evolution of damage with respect to different tensile load (from initiation, propagation and coalescence of microcracks).

### 7.1.2 Influence of parameters in CZM

With emphasis on the nonlinear phenomena only induced by the CZM, HCP is assumed to behave elastically. Figure 7.3 illustrates the influences of tensile strength  $f_t$  and fracture energy  $G_f$  on the macroscale stress-strain relationship of concrete in uniaxial tension. One can observe the common procedure from perfectly bonded to partially debonded, where the curves of perfectly bonded and completely debonded are obtained by the simulations of the mesostructure without interface elements between HCP and aggregates, as well as with aggregates replaced by voids respectively. Furthermore, the case of larger tensile strength requires a larger load to initialize the debonding between HCP and aggregates. For various fracture energy, it is observed that the debonding occurs under identical tensile load, yet following different debonding trends.

As an extension of the example implemented above, MAZARS damage model is applied in the HCP and the influence of tensile strength on the macroscale stress-strain relationship of concrete in uniaxial tension is displayed in Figure 7.4(a). Here, the LINE SEARCH approach in conjunction with the NEWTON-RAPHSON approach in Equation (3.1.12) with  $a = 0.8$  is utilized to solve the instability problem in the regime of the peak stress. From Figure 7.4(a), one can capture the difference between perfectly bonded and imperfectly bonded cases, yet they are getting closer when the tensile strength is decreased. MAZARS damage model used in the HCP, is capable of modeling the strain-softening failure with a negative slope of stress-strain curve. However, as it is a local damage model, the problem of the mesh dependency in the regime of softening is

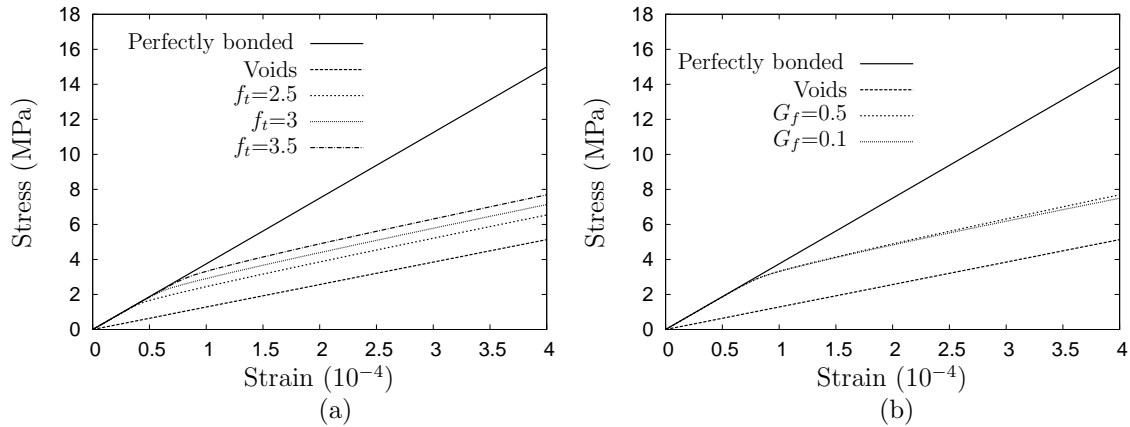


**Figure 7.3:** Influences of parameters in CZM on macroscale behavior of concrete with elastic HCP in uniaxial tension (a) tensile strength and (b) fracture energy.

induced. In order to prove it, a homogeneous material formulated by MAZARS damage model in terms of different mesh sizes are tested, see Figure 7.4(b) for the illustration of mesh dependency. Clearly, this problem becomes worse with an application to the heterogeneous material. From a mathematical point of view, the loss of ellipticity of the governing differential equations is induced by a negative tangent modulus, such that the boundary value problem becomes ill-posed. The local damage model leads to the strong localization of the damage in the weakened cross-section and pathological sensitivity of the numerical results to the element size. Applying a non-local damage model and a gradient damage approach overcomes the mesh dependency problem, see JIRÁSEK (2004) and PEERLINGS ET AL. (1998).

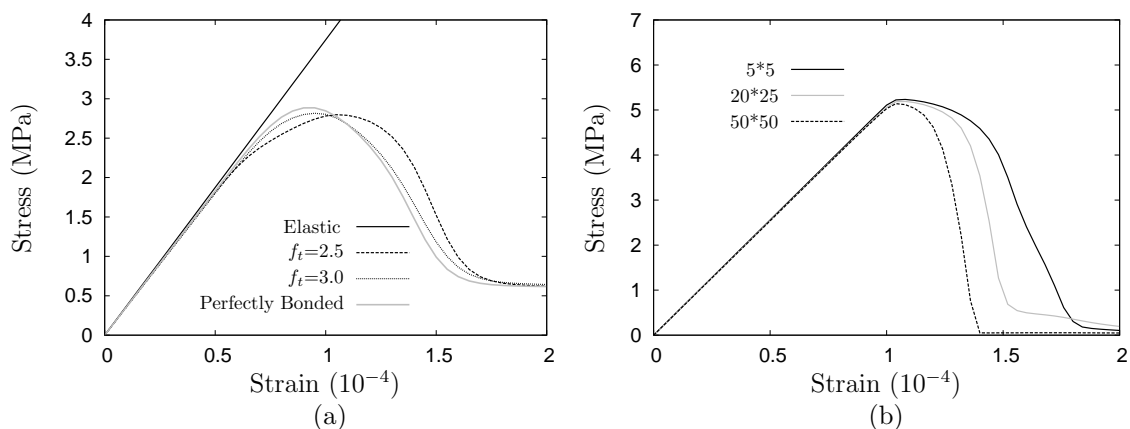


**Figure 7.4:** (a) Influence of tensile strength on macroscale stress-strain relationship of concrete with damage in HCP and (b) mesh size effect displaying the mesh dependency problem of local damage model.

### 7.1.3 Influence of specimen size

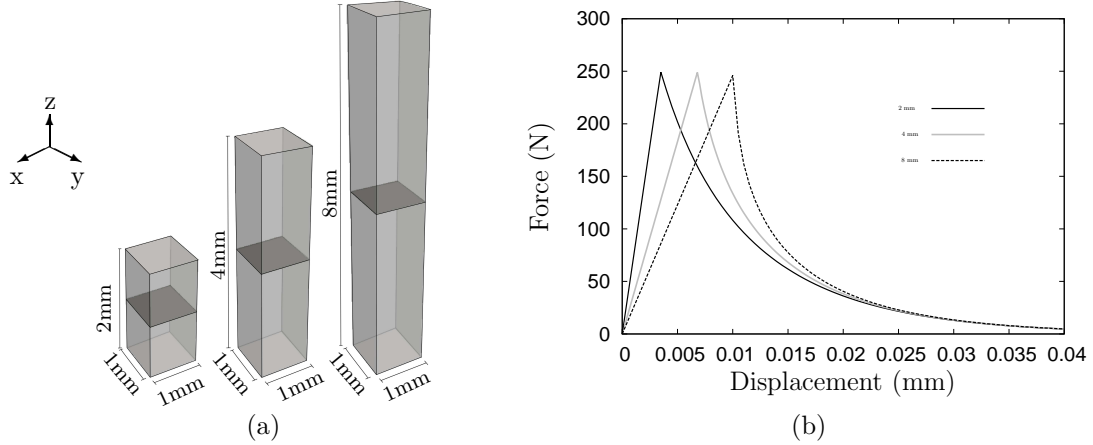


**Figure 7.5:** (a) Illustration of geometries with one-dimensional size scaling and (b) the resulting force-displacement relationship.

In the 16th century, LEONARDO DA VINCI and GALILEO GALILEI first pointed out an inverse relationship between the length and strength of concrete sample, thereby highlighting the durability issue in the civil engineering. Later, extensive investigations were conducted through the experiments (VAN VLIET & VAN MIER (2000)), phenomenological models (BAŽANT (1997)) as well as numerical approaches (VOŘECHOVSKÝ & SADILÉK (2008)). The aim of this section is to analyze the effect of the specimen size on the macroscale behavior of concrete. However, before that, simple numerical tests are carried out taking into account the effect of dimensions in relation to CZM, see Figure 7.5(a) for illustrations of geometries, where zero-thickness interface elements driven by CZM are inserted between two bricks with the identical elastic properties. Here, the dimension only increased in  $zz$  direction, is called one-dimensional size scaling, see MAIN (2010). In uniaxial tension, the macroscale force-displacement curves with respect to different lengths of the specimen are displayed in Figure 7.5(b), from which both macroscale tensile strength and macroscale fracture energy are independent of the length effect. However, as the length increases, the curve becomes steeper and the snap-back phenomena trends to occur. Note that all geometries in Figure 7.5(a) are discretized with a mesh of same size.

Over the past decades, a great amount of experiments were found to analyze the effects of the specimen size of concrete. For instance, the dependence of the macroscopic fracture energy of the quasi-brittle material like concrete on the specimen size was described, e.g in ADALLA & KARIHALOO (2004), CEDOLIN & CUSATIS (2008), BAŽANT & YU (2011) and TANG ET AL. (2012). However, only a few of them addressed how the macroscale fracture energy changes with the specimen size. On the other hand, VAN VLIET & VAN MIER (2000) observed that the macroscale tensile strength of concrete is reduced as the size increases in experiments. The well-known phenomenological size

effect law (SEL) depicting the variations of fracture energy as a function of specimen size was developed by BAŽANT, see BAŽANT (2000) and BAŽANT & YU (2009). From a numerical point of view, MAN & MIER (2008) directly transferred the results from X-ray scans of concrete into a three-dimensional lattice for constructing the mesoscale geometry of concrete, such that the real shapes of aggregates could be included into the lattice model, like oval-shaped or crushed aggregates. Then the 3-point bending tests based on a three-dimensional beam lattice model were conducted in order to analyze the effects of specimen size on the structural strength and fracture energy of concrete. More numerical contributions can be found e.g. in MIER & VLIET (2003), UNGER & ECKARDT (2011) and ELSANADEDY ET AL. (2012). All the efforts mentioned above address the conclusion that the size effect exists in concrete. However, various micromechanical mechanisms may contribute to the size effect, e.g. microcracks, process zone length relative to structural size, heterogeneity among others, see MIER & VLIET (2003).

Analyzing the size effect of concrete in a multiscale manner is the next aim, scaling the size of HCP in  $x$ ,  $y$  and  $z$  directions, yet the size and volume fraction of aggregates are not varied, see Figure 7.6, namely three-dimensional size scaling. The effects of the specimen size on the macroscale stress-strain relationship of concrete in uniaxial tension are displayed in Figure 7.7, where both MAZARS damage model and CZM are taken into account. Albeit the existence of the mesh-dependency problem due to the local damage model, it has minor influences on the peak stress, such that it is still feasible to capture that the peak stress is decreased with the enlargement of the specimen size. It qualitatively matches the observation from the experiment (VAN VLIET & VAN MIER (2000)) and computational work (UNGER & ECKARDT (2011)).

#### 7.1.4 Influence of random distribution of aggregates

The damage in the HCP of three concrete samples with different distributions of aggregates in uniaxial tension are displayed in Figure 7.8, where the localization zones of either one or two competing macrocracks are formed, explained by the shear forces

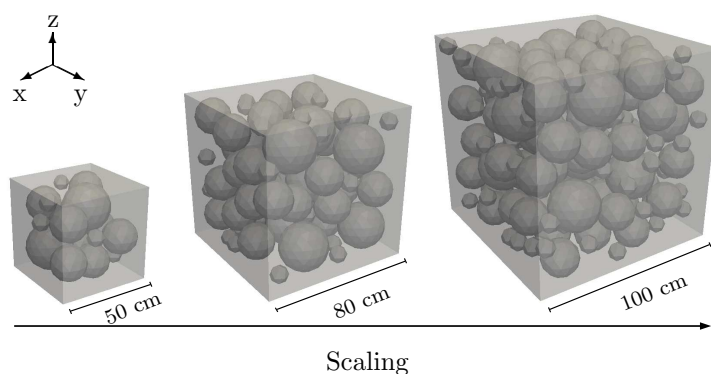


**Figure 7.6:** Three-dimensional size scaling of concrete.

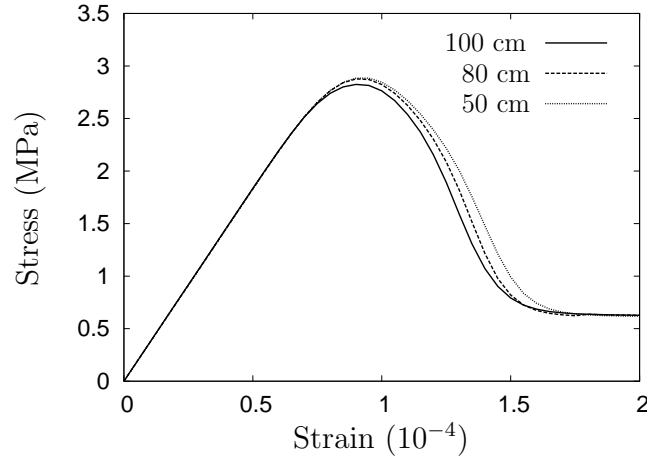


**Figure 7.7:** Macroscale stress-strain relationship of concrete affected by specimen size in uniaxial tension.

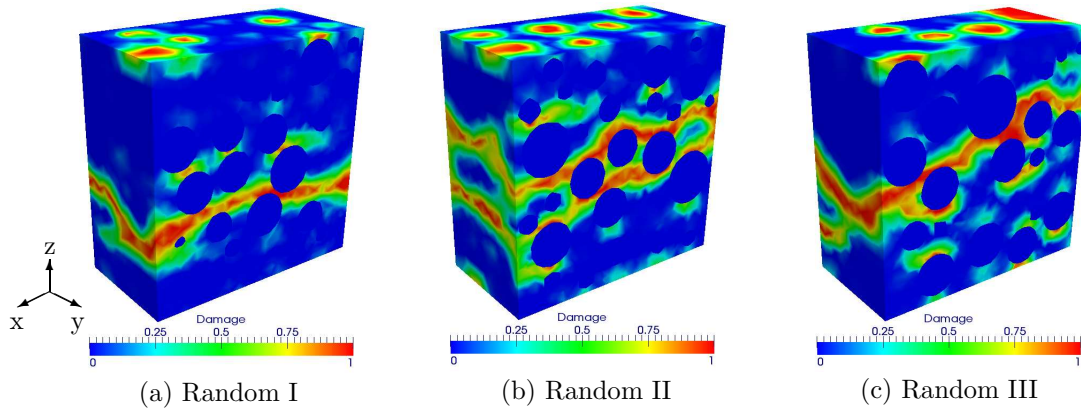


**Figure 7.8:** Damage in the HCP of three concrete samples with different distributions of aggregates in uniaxial tension.

relying on the distributions of aggregates. Figure 7.9 illustrate the macroscale stress-strain curves of three concrete samples in uniaxial tension, from that the macroscale tensile strength and fracture energy are less dependent on the distribution of aggregates. Therefore, it can be concluded that the statistical distribution of aggregates have a negligible effect on the overall mechanical performance of concrete.

### 7.1.5 Debonding interface damage in uniaxial tension

As indicated before, the prescribed tensile load may result in the debonding at the ITZ between HCP and aggregates. However, it is challenging to capture the interface failure due to its quasi-brittle property, without the aid of SEM. Alternatively, a debonding damage  $D_c^d$  is defined in the interface elements with the same formulation of thermal

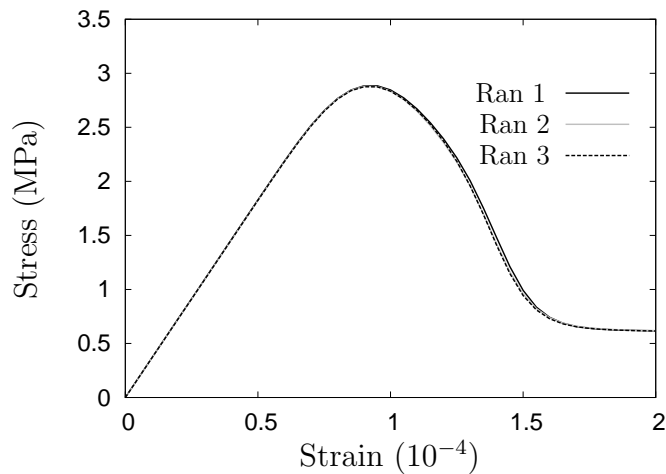


**Figure 7.9:** Macroscale stress-strain curves of three concrete samples with different distributions of aggregates in uniaxial tension.

interface damage  $D_c^\theta$  in Equation (2.5.18), quantifying the failure of the interface or how much the interface elements debond. Figure 7.10 displays the debonding damage  $D_c^d$  in the interface elements of three concrete samples with different distributions of aggregates in uniaxial tension, from which one can observe that the debonding interface damage  $D_c^d$  is initialized and then enhanced at the lower surfaces of aggregates as the tensile load increases. Moreover, the distributions of aggregates greatly affect the interface failure locally.

### 7.1.6 Parameter identification

The stress-strain curve from the experiment is measured relying on the assumption that the material is homogeneous, hence, by using conventional experiments in laboratories, it is challenging to obtain the material parameters defined in the constitutive laws of heterogeneous components at the lower scale of concrete, e.g. parameters in CZM and MAZARS's damage model. Alternatively, parameter identification is utilized with the approach of fitting the numerical results to the experimental data. The experimental set-up and data employed in HORDIJK (1992) are demonstrated in Figure 7.11, where the computed result of imperfectly bonded interface provides better approximation of the experimental data than the one of perfectly bonded interface. The material parameters of CZM and MAZARS damage model are listed in Table 7.1.

## 7.2 Numerical results in uniaxial compression

In concrete, the characteristics of heterogeneity lead to failure with more complex phenomena in compression than in tension, owing to splitting cracks, shear cracks and

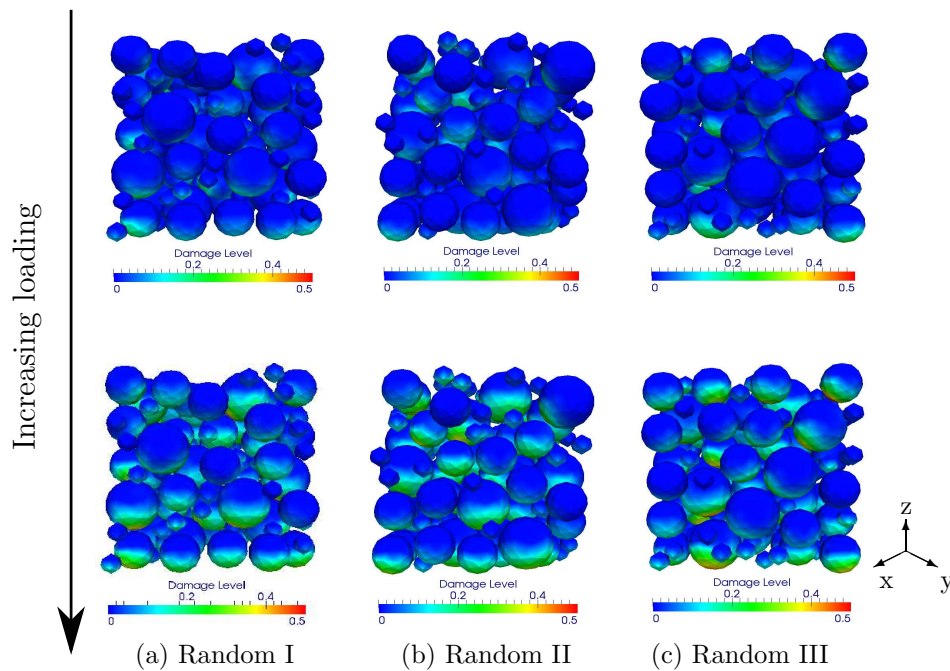


**Figure 7.10:** Debonding interface damage of three samples with different distributions of aggregates in increasing uniaxial tension.

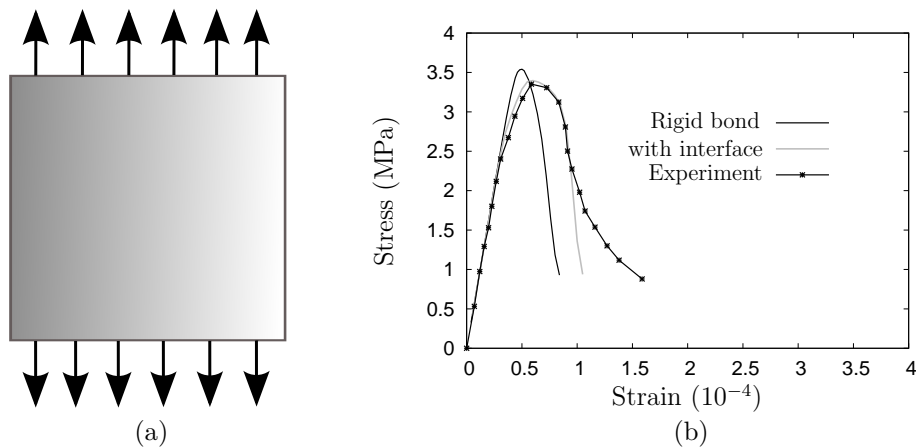


**Figure 7.11:** (a) Experimental set-up in uniaxial tension adopted in HORDIJK (1992) and (b) experimental data (HORDIJK (1992)) fitted by numerical results of perfectly bonded and imperfectly bonded interfaces.

others, see VONK (1993). For instance, READ & HEGEMIER (1984) indicated that shear cracks are formed through an array of “en echelon” splitting cracks. For this reason, a considerable number of contributions have already been made to analyze the mechanical behavior in compression from the view of experiments (MIER (1984)), theoretical models (STROEVEN (1973)) as well as numerical approaches (SNOZZI ET AL.

Parameter	$A_t$	$B_t$	$A_c$	$B_c$	$f_t$	$G_f$	$\kappa_0$
Value	1.0	10000	1.0	10000	3.4	0.1	0.0001

**Table 7.1:** Obtained material parameters in MAZARS damage model and CZM through parameter identification for tensile test.

(2012)).

When the concrete is imposed by uniaxial compressive boundary condition,  $\sigma_{zz}$  of perfectly bonded and imperfectly bonded are illustrated in Figure 7.12. Moreover, Figure 7.13 presents the macroscale stress-strain curves of concrete in uniaxial compression concerning the following cases, e.g. perfectly bonded with elastic matrix, perfectly bonded with damage matrix, imperfectly bonded with damage matrix and aggregates replaced by voids. In contrast to tensile tests, the significance of the interface is more apparent in compression. More energy is needed for the formation and extension of matrix cracks in compression than in tension. Therefore, concrete fails in a brittle manner in tension yet is relatively tough in compression.

Not only the imperfect failure surface but also local characteristics yield that MAZARS damage model is not able to correctly describe the failure of concrete in compression. Particularly for triaxial compression, it cannot be used at all. Assuming that the concrete is subjected to uniaxial load, the localization plane should be more or less parallel to the direction of compressive load or with inclined direction, caused by the combination of splitting and shear stresses due to heterogeneities, see STROEVEN (1973). Also, VONK (1993) addressed the influences of boundary conditions with or without horizontal constraint. Increasing the length of the specimen is proven to not be a remedy for obtaining the correct localization plane, see Figure 7.14.

Figure 7.15 displays the debonding interface damage of concrete in uniaxial compres-

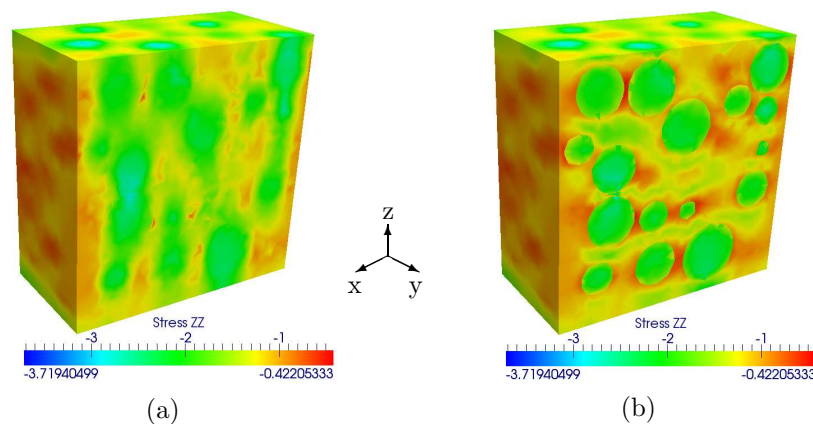


**Figure 7.12:**  $\sigma_{zz}$  (Mpa) in uniaxial compression (a) perfectly bonded and (b) imperfectly bonded.

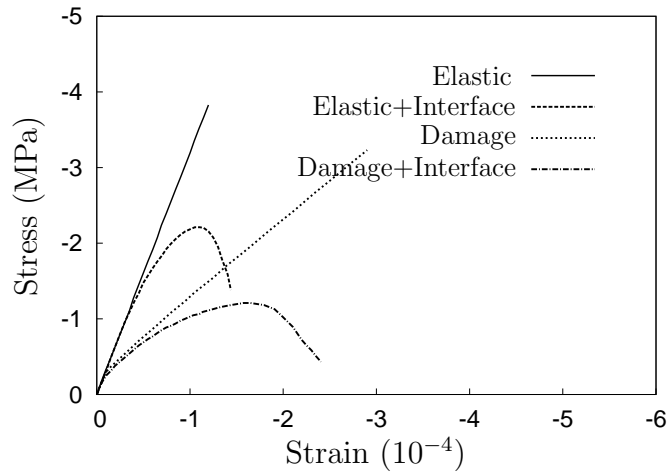


**Figure 7.13:** Macroscale stress-strain relationship of concrete in uniaxial compression.

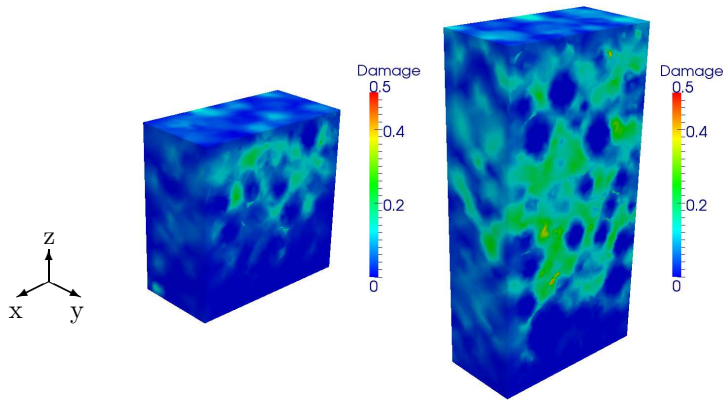


**Figure 7.14:** Damage distribution of concrete in uniaxial compression with dimensions of (a)  $100 \times 100 \times 100 \text{ mm}^3$  and (b)  $100 \times 100 \times 200 \text{ mm}^3$ , (clipped by plane).

sion, where one can observe the debonding is induced and then enhanced at the upper surface of aggregates as the load rises.

In this work, it is assumed that the tensile behavior of HCP is modeled by the MAZARS damage model. When it is under compressive load, MAZARS damage model combined with visco-plasticity model is employed for the description of the mechanical behavior. The parameters of visco-plasticity are obtained from HAIN (2007), see Table 7.2.

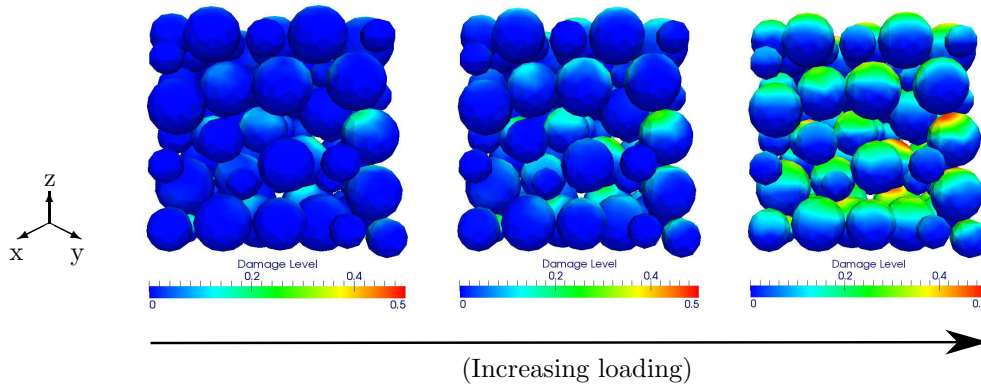


**Figure 7.15:** Debonding interface damage in increasing uniaxial compression.

Parameter	$k_f$	$\eta$	$\Delta t$
Value	48	8,240	0.0265

**Table 7.2:** Parameters in visco-plasticity model (HAIN (2007)).

## 7.3 Mechanical-thermal-diffusion coupling for the ITZ

As pointed out before, the debonding at the ITZ between HCP and aggregates could affect thermal conduction and humidity diffusion in concrete. In order to describe this phenomena, the traction-separation law in CZM combined with micromechanically motivated thermal flux-separation relation and diffusion flux-separation relation is established at interface elements.

### 7.3.1 Staggered method

The computational cost is huge for solving three-dimensional multiphysics problems. For this reason, a staggered method is utilized allowing to solve the fields sequentially, such that the size of the discretized problem is greatly reduced, see ZOHDI (2004). Within this method, each field is solved individually within the discretized time step, allowing the unknowns of the corresponding field to be active. As long as each field is solved, the corresponding unknowns are updated, which are employed for the next field. In the following, the time step is incremented and the procedures mentioned above are repeated. Usually staggering has the disadvantage of a small time step restriction in view of its explicit nature. However, it has a significantly simpler algorithmic structure compared to an implicit scheme due to the sequential solution of the coupled system of field equations, see ERBTS & DÜSTER (2012).

The next objectivity is to apply the staggered method to the concrete with an intention

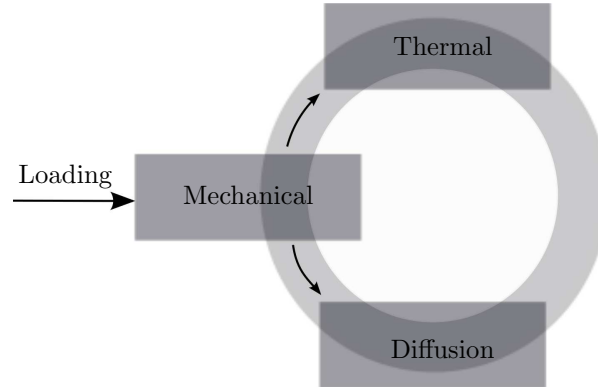


**Figure 7.16:** Framework of mechanical-thermal-diffusion coupling at interface.

1. *Mechanical field.* Assume components in the bulk phase to behave elastically and apply CZM introduced in Subsection (3.3.2) in the interface phase to model debonding between HCP and aggregates, for updating displacement  $\mathbf{u}^{n+1}$ .
2. *Thermal field.* Apply FOURIER's law in Equation (2.6.8) in the bulk phase and the relation of thermal flux  $q_c$  and temperature jump  $\llbracket \theta \rrbracket$  in Equation (2.5.16) in the interface phase, for updating temperature  $\theta^{n+1}$ .
3. *Diffusion field.* Use FICK's law in Equation (2.6.15) in the bulk phase and the relation of diffusion flux  $j_c$  and relative humidity jump  $\llbracket s \rrbracket$  in Equation (2.5.23) in the interface phase, for updating relative humidity  $s^{n+1}$ .
4. *Increase time step.* Update all the field variables and set the time step forward to go back to step 1.

**Table 7.3:** Algorithm of mechanical-thermal-diffusion coupling at interface based on staggered method.

Components	HCP	Aggregate	Interface
$E$ (N/mm <sup>2</sup> )	2300	7000	-
$\nu$ (-)	0.21	0.2	-
$f_t$ (N/mm <sup>2</sup> )	-	-	3.4
$G_f$ (N/mm)	-	-	0.1
$K_p$ (N/mm <sup>3</sup> )	-	-	50000
Thermal conductivity (W/mK)	0.9586	2.828	100
Diffusivity (cm <sup>2</sup> /h)	1.4e-3	0.04e-3	1

**Table 7.4:** Material parameters of components adopted for mechanical-thermal-diffusion coupling.

of presenting how the debonding at ITZ yields the temperature jump  $\|\theta\|$  and humidity jump  $\|s\|$  across the crack interface, and subsequently affects the thermal conduction and humidity diffusion in the bulk phase of concrete. The concrete is subjected to uniaxial tension combined with a constant temperature and relative humidity prescribed on the top surface of the concrete sample. The models of mechanical-thermal-diffusion coupling are established in not only the bulk phase but also in the interface phase. For the bulk phase, the interactions among fields are not taken into account, yet solving the fields sequentially based on a staggered approach, as well as HCP and aggregates are assumed to behave elastically. The framework of mechanical-thermal-diffusion coupling in the interface phase is displayed in Figure 7.16, where mechanical-thermal cohesive and mechanical-diffusion cohesive couplings are individually carried out with the aid of a staggered method, namely no interactions between thermal and diffusion fields. One can find the coupling algorithm in Table 7.3 and the material parameters in Table 7.4. As mentioned before, penalty parameters are defined for thermal conductivity and diffusivity of interface. The infinitely large penalty parameters yield the perfect thermal conduction and diffusion across the interface. However, realistically sufficiently large parameters are chosen explained by not only non-existence of a perfect interface but also convergence problems due to large penalty parameters from a numerical point of view, see Table 7.4.

### 7.3.2 Numerical thermal results

The debonding at the ITZ between HCP and aggregates induced by uniaxial tensile load yields the temperature jump  $\|\theta\|$  across the crack interface, thereby forming the thermal resistance along the interface and reduction of thermal flux in concrete, see Figure 7.17(a). The thermal interface damage is formed and then increased at the lower surface of aggregates as the tensile load rises, corresponding to the debonding interface damage, displayed in Figure 7.10. Thus, it results in the reduction of thermal conduction in the whole concrete sample, particularly with a great reduction in the regime where the interface elements strongly debond. If the concrete is subjected to uniaxial compression, one can obtain the thermal interface damage and the reduction of thermal conduction as well, see Figure 7.17(b).

### 7.3.3 Numerical diffusion results

Figure 7.18 illustrates no apparent influences of debonding on the diffusion flux of concrete, no matter how large the prescribed load is. It can be explained by the relative low diffusivity of aggregates in contrast to HCP, see Table 7.4. Hence, it forms the nature diffusion resistance between HCP and aggregates.

However, extensive experiments were conducted to present the phenomena that the diffusivity of concrete is increased as the crack width rises, see JEON (2003) and WONG ET AL. (2009), which could be explained by the existence of cracks throughout concrete, rather than only debonding between HCP and aggregates. Alternatively, assuming the diffusivity of aggregates to be identical to the one of HCP, the problem mentioned

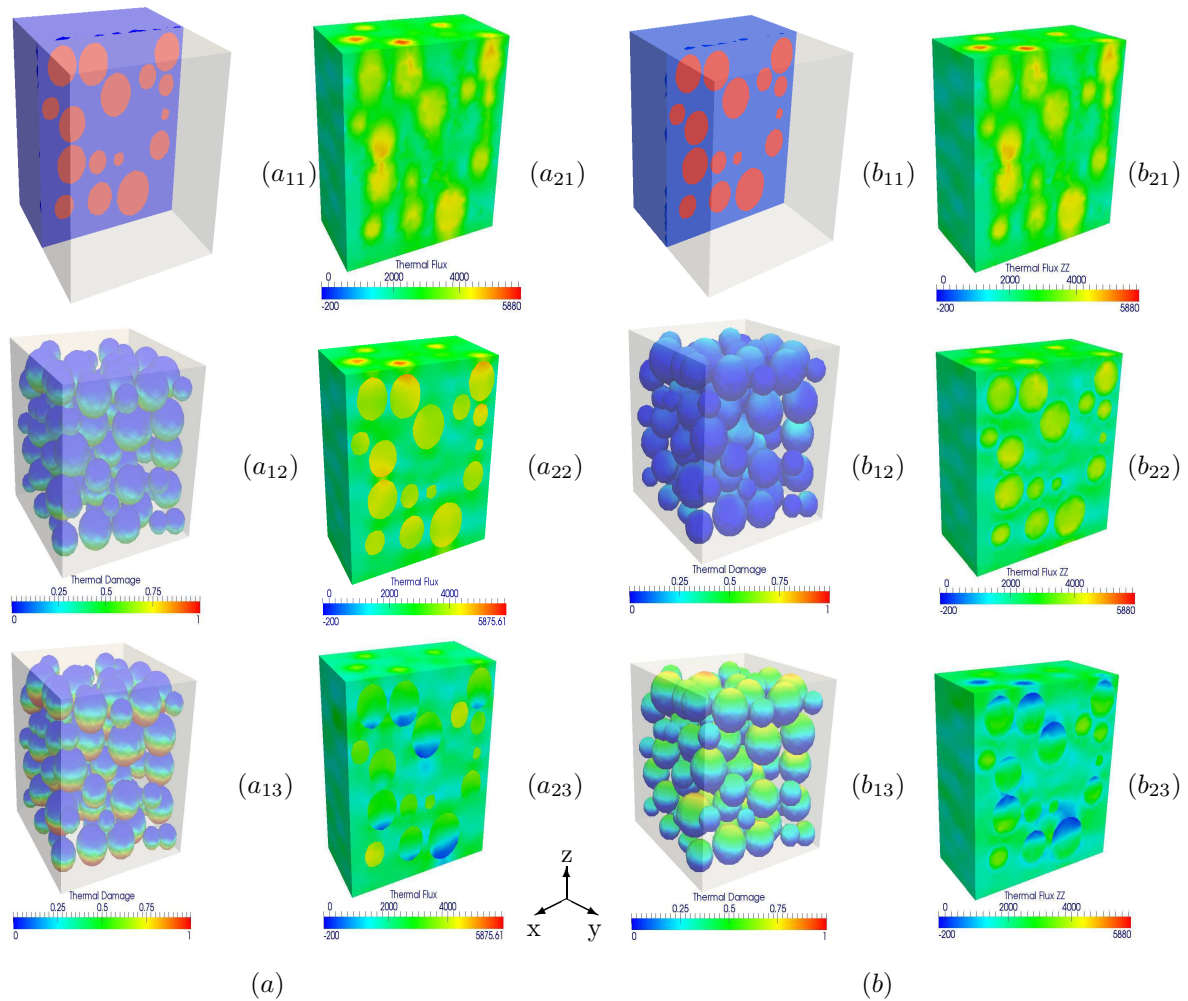


**Figure 7.17:** ( $a_{11}$ ) Material distribution of cross section and ( $a_{21}$ ) thermal flux of perfectly bonded and ( $a_{12}$ )-( $a_{13}$ ) thermal interface damage and ( $a_{22}$ )-( $a_{23}$ ) thermal flux of imperfectly bonded and ( $b_{11}$ ) material distribution of cross section and ( $b_{21}$ ) thermal flux of perfectly bonded and ( $b_{12}$ )-( $b_{13}$ ) thermal interface damage and ( $b_{22}$ )-( $b_{23}$ ) thermal flux of imperfectly bonded, ((a) in tension and (b) in compression, load is increased from upper to lower).

above is transferred to analyze the influence of crack on the diffusivity in homogenized HCP. When the relatively large tensile load is prescribed on concrete, the diffusion flux is increased, see Figure 7.19.

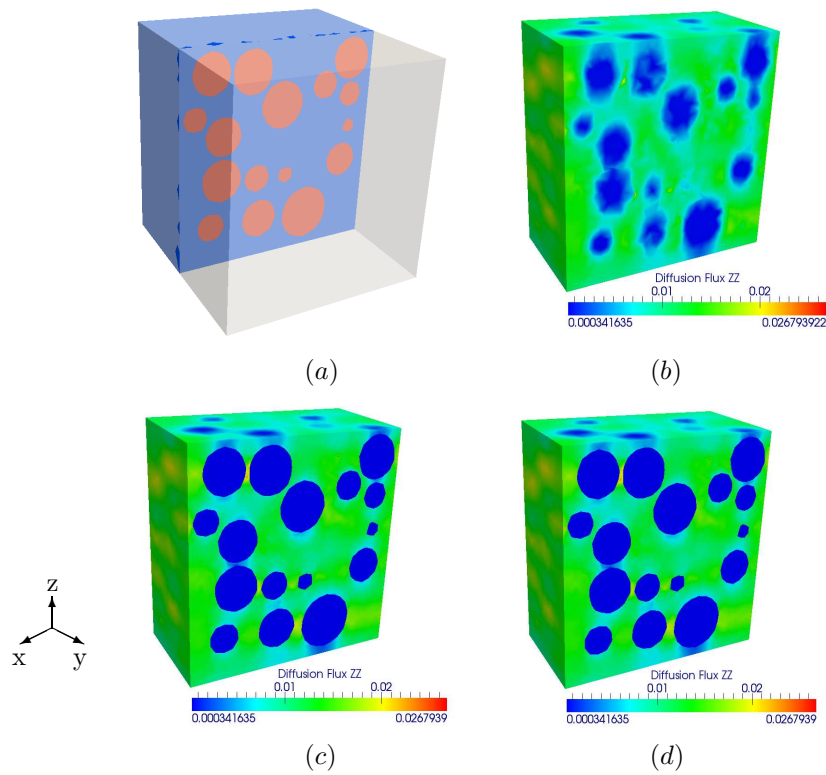


**Figure 7.18:** (a) Material distribution of cross-section and (b) diffusion flux of perfectly bonded and (c)-(d) diffusion flux of imperfectly bonded (uniaxial tensile load increases from left to right).

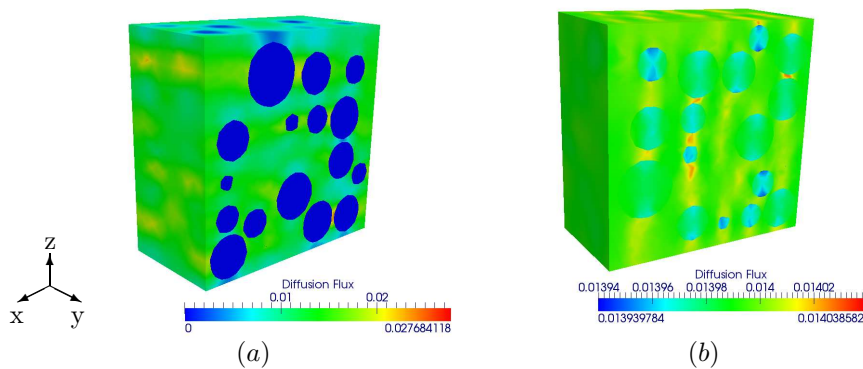


**Figure 7.19:** Diffusion flux of concrete subjected to (a) no load and (b) relatively large load.



# Chapter 8

## Multiscale Multiphysics Simulation Results

### 8.1 Introduction

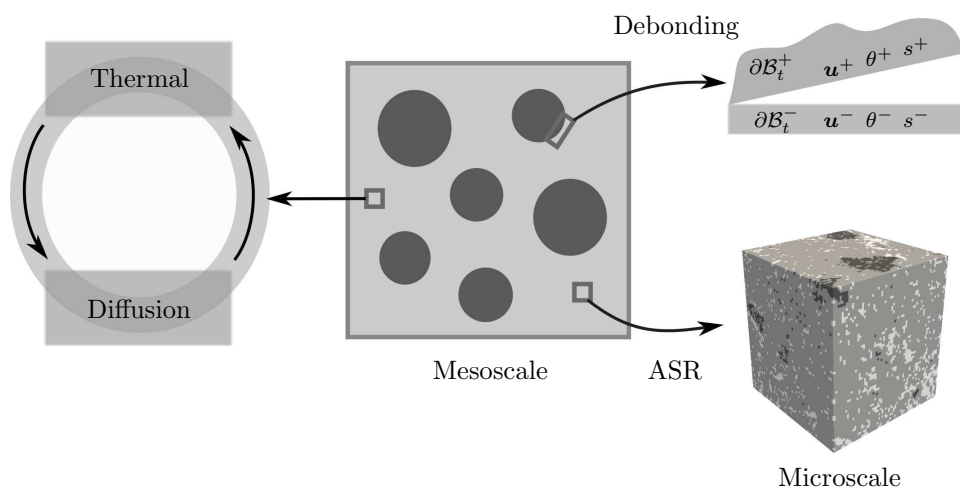


**Figure 8.1:** Framework of multiscale/multiphysics modeling in concrete.

Figure 8.1 demonstrates the framework of the multiscale/multiphysics model in concrete, constituting three main aspects: (I) *multiscale ASR*: by using instationary thermal conduction and diffusion equations, the mesoscopic local values of the transient temperature and relative humidity are obtained, which update the chemical extent  $\xi$  at the material point of mesoscale. The resulting chemical extent can directly determine the ASR induced damage at the microscale through the correlation between effective damage of HCP and chemical extent. The couple problem is solved at the mesoscale through a staggered method, yet it upscales the chemical damage from the microscale during the process. (II) *ITZ*: the debonding at the ITZ between HCP and aggregates induced by internal or external forces, yields the temperature jump and the humidity

jump across the interface crack. (III) *thermal and diffusion homogenization*: computational thermal homogenization and diffusion homogenization are applied for HCP for determining the effective thermal conductivity of HCP affected by humidity and the effective diffusivity of HCP affected by temperature. Such effects could be incorporated in to the modeling temperature and humidity mediated chemical extent induced by ASR.

The goal of the present section is to combine three aspects mentioned above, such that it provides a reliable multiscale multiphysics model to describe the induced failure in concrete. Assuming that the equilibrium for diffusion, thermal conduction and mechanical problems has already been obtained at time  $t_n$ , the procedure for searching for the solutions at time  $t_{n+1} = t_n + \delta t$  is described in Table 8.1.

- 
1. *Diffusion field*. Use the FICK's law in Equation (2.6.15) and the relationship between the effective diffusivity of HCP and temperature in Equation (6.3.14) in the bulk phase, and apply the relationship of diffusion flux  $j_c$  and relative humidity jump  $\llbracket s \rrbracket$  in Equation (2.5.23) in the interface phase, for updating relative humidity  $s^{n+1}$ .
  2. *Thermal field*. Employ the FOURIER's law in Equation (2.6.8) and the relationship between the effective conductivity of HCP and the humidity in Equation (6.3.6) in the bulk phase, and use the relationship of thermal flux  $q_c$  and temperature jump  $\llbracket \theta \rrbracket$  in Equation (2.5.16) in the interface phase, for updating temperature  $\theta^{n+1}$ .
  3. *Chemical extent*. Use  $s^{n+1}$  and  $\theta^{n+1}$  to update the chemical extent  $\xi^{n+1}$ , see Subsections 4.2.2 and 4.2.3. Then apply the obtained chemical extent  $\xi^{n+1}$  at the mesoscale to determine the ASR induced damage at the microscale, through the correlation between chemical extent and damage due to ASR, see Equation (6.3.17).
  4. *Mechanical field*. In the bulk phase, the sum of the mechanical damage  $D^u$  and the chemical damage  $D^c$  combined with a visco-plastic model of the classical PERZYNA-type is used to describe the nonlinear behavior of HCP and aggregates are assumed to behave elastically. For the interface phase, the debonding is modeled by the CZM introduced in Subsection 3.3.2.
  5. *Increase time step*. Update all the field variables and set the time step forward to go back to step 1.
- 

**Table 8.1:** Algorithm of multiscale/multiphysics modeling in concrete.

## 8.2 Numerical example

Two simple examples are tested in this section: (1) in uniaxial compression (2) in stress-free. Mechanical properties of components at the mesoscale of concrete can be found in Table 7.1 and 7.2 and 8.2. Thermal and diffusion properties of components are listed in Table 8.3.

In the first example, the constant temperature 20 °C and relative humidity 1.0 are prescribed on the top surface of the mesoscale representation of concrete. Furthermore,

Components	HCP	Aggregate	Interface
$E$ (N/mm <sup>2</sup> )	2300	7000	-
$\nu$ (-)	0.21	0.2	-
$f_t$ (N/mm <sup>2</sup> )	-	-	3.4
$G_f$ (N/mm)	-	-	0.1
$K_p$ (N/mm <sup>3</sup> )	-	-	50000

**Table 8.2:** Mechanical properties of components at the mesoscale of concrete.

Component	Capacity of heat	Thermal conductivity	Density	Diffusivity
HCP	1000J/kgK [1]	1.4W/mK [1]	2120kg/m <sup>3</sup> [1]	10 <sup>-10</sup> m <sup>2</sup> /s [2]
Aggregate	2600J/kgK [4]	2.828W/mK [6]	2600kg/m <sup>3</sup> [5]	1.85 × 10 <sup>-12</sup> m <sup>2</sup> /s [3]
Interface	-	100W/mK	-	10 <sup>-12</sup> m <sup>2</sup> /s

**Table 8.3:** Thermal and diffusion properties of components at the mesoscale of concrete ([1] HAIN (2007) [2] ZHANG ET AL. (2011b) [3] VASCONCELOS ET AL. (2011) [4] KODIDE (2010) [5] BULLETIN (1999) and [6] WU ET AL. (2012)).

the concrete is also under uniaxial compressive load. The multiscale simulation results predict the deterioration due to ASR in compression as shown in Figure 8.2, where the deterioration is constituted by the mechanical damage induced by external load and the chemical damage due to ASR.

In the second example, the concrete sample is immersed into a vessel full of water under the room temperature of 20 °C, as displayed in Figure 8.3. Thus, only relative humidity is controlled, and it is a widely adopted in the laboratory for analyzing ASR. Figure 8.4 illustrates the multiscale simulation results predict the deterioration due to ASR in stress-free. This example present that ASR is a relative show reaction and it only occurs in HCP. The evolution of the ASR induced damage follows the extent of reaction. In other words, the chemical extent of ASR determines in which region damage induced by ASR occurs more easily in concrete. Since the initial temperature and relative humidity are not taking into account in concrete, temperature and relative humidity mediated chemical extent evolves from lower to upper surface of concrete.

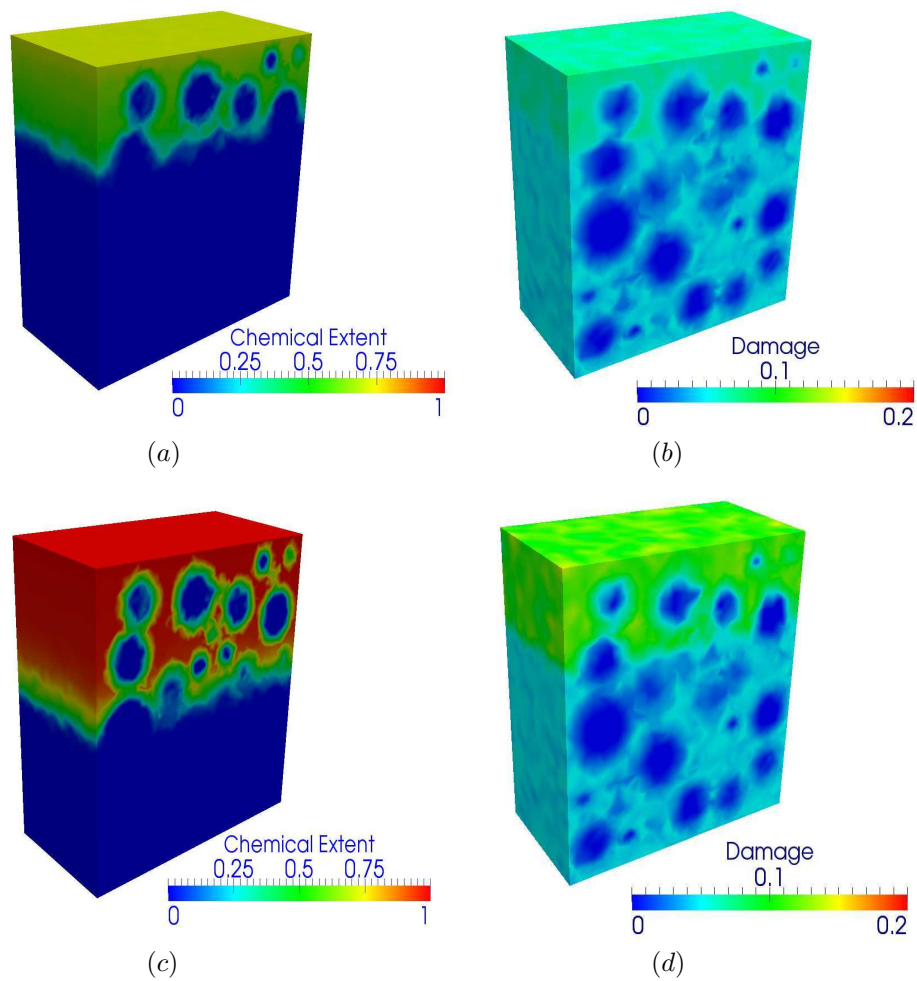


**Figure 8.2:** Deterioration prediction through multiscale/multiphysics model in uniaxial compression: (a) chemical extent in 50 days (b) damage in 50 days (c) chemical extent in 300 days (d) damage in 300 days.

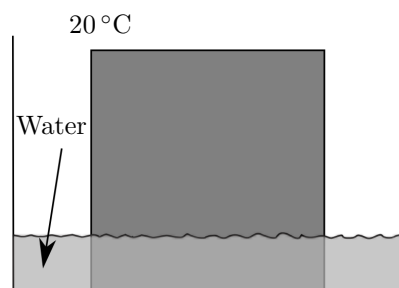


**Figure 8.3:** A concrete sample immersed into a vessel full of water.

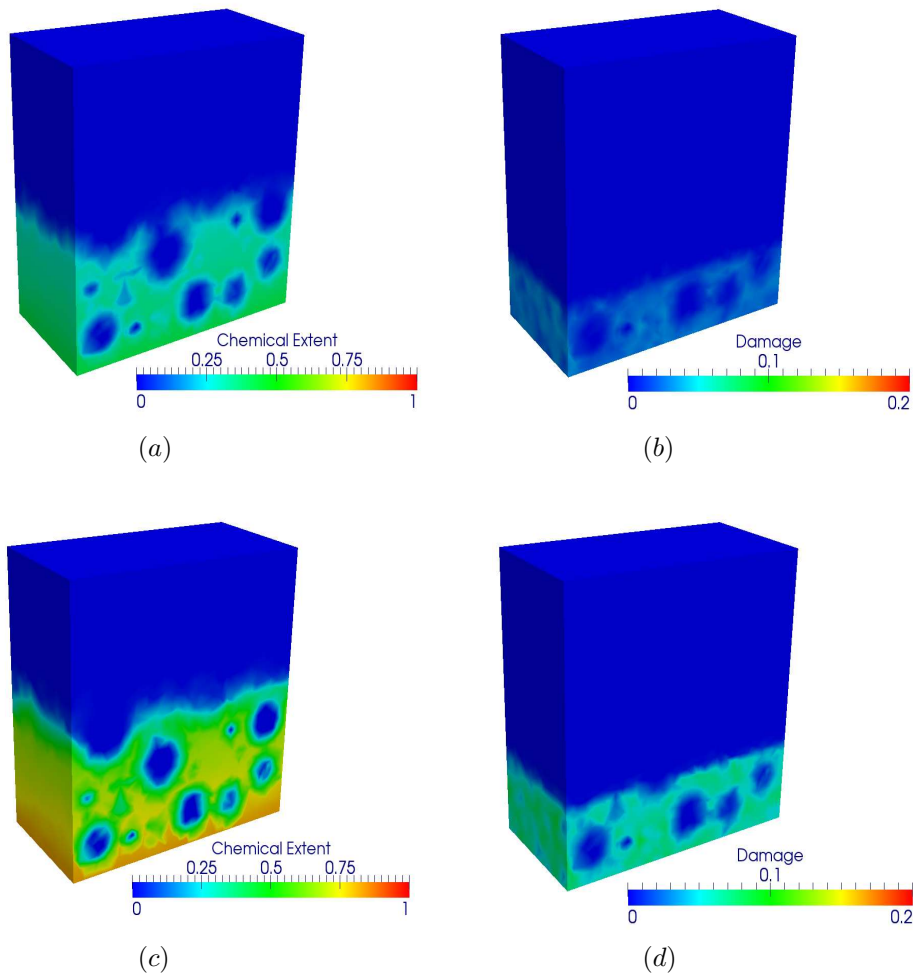


**Figure 8.4:** Deterioration prediction through multiscale/multiphysics model in stress-free: (a) chemical extent in 50 days (b) damage in 50 days (c) chemical extent in 300 days (d) damage in 300 days.



# Chapter 9

## Conclusions and outlook

This work established a reliable multiscale multiphysics model to analyze failure of concrete due to alkali-silica reaction (ASR) and to the weak properties of the interfacial transition zone (ITZ). The mesostructure of concrete consists of aggregates with a random distribution embedded in a homogenized hardened cement paste (HCP) as well as interface elements with zero-thickness as the representation of the ITZ. One scale lower, the microscale constitutes the finest structural scale and is represented by the microstructure of the HCP obtained from three-dimensional computed tomography (CT) scans, which is comprised of hydration products, unhydrated residual clinker and micropores.

Problems associated with ASR in concrete structures usually arise several years after construction. This work constructed a multiscale model to predict the deterioration due to ASR in concrete with the goal of accelerating the prediction of the extent of damage in comparison to experimental procedures. Starting from the assumption that the gels are evenly produced in micropores of the HCP and exert uniform pressure on the surrounding material, the expansion coefficient of the gel at the microscale was obtained through a two-step homogenization approach. Based on a correlation between the effective damage and the chemical extent, the simulation of ASR induced deterioration at the mesoscale was carried out through a coupled diffusion-thermal-chemical-mechanical framework in a staggered setting, yet upscaling the chemical damage quantity from the microscale during the process.

Computational thermal homogenization with statistical tests was applied to obtain the effective thermal conductivity of HCP, thus enabling to identify the macroscopic thermal conductivity of concrete efficiently. Taking into account the variation of water content in the micropores, a nonlinear relationship between the effective thermal conductivity of HCP and the volume fraction of water content in micropores was obtained, which was then mapped from the volume fraction of water content to the relative humidity through the isothermal curve of absorption. Analogous to the thermal field, applying computational diffusion homogenization with consideration of the effect of temperature resulted in a nonlinear relationship between the effective diffusivity of HCP and the temperature. This framework is inexpensive, fast, and not restricted

by space and time, compared with the conventional experimental approach. The resulting nonlinear relationships are of significant importance in modeling long term temperature-controlled chemical reactions in concrete like ASR.

The window method, where the microstructural sample is embedded into a frame of a homogeneous material, offered an alternative to classical boundary conditions in computational homogenization. Experience with the window method, which is essentially the self-consistent scheme but with a finite surrounding medium instead of an infinite one, indicates that it delivers faster convergence of the macroscopic response with respect to boundary conditions of pure essential or natural type as the microstructural sample size is increased to ensure statistical representativeness. In this work, the variational background for this observed optimal convergence behavior of the homogenization results with the window method is provided and the method is compared with periodic boundary conditions that it closely resembles.

The microstructure of the ITZ with higher porosity yields its weak mechanical properties. In this work, a cohesive zone model (CZM) was used to describe the debonding at the ITZ between HCP and aggregates. Also, the influence of various parameters on the macroscale mechanical behavior of concrete was analyzed. The investigated parameters were tensile strength, fracture energy, specimen size as well as random distribution of aggregates. A scalar interface damage parameter was defined in the interface elements in order to quantify how much they debond in tension and in compression respectively. Apart from the mechanical problem, the influence of the interface crack on the thermal conduction as well as humidity diffusion was also investigated. The traction-separation law in CZM combined with micromechanically motivated thermal flux-separation relation and diffusion flux-separation relation was established, thereby leading to the temperature jump  $\llbracket \theta \rrbracket$  and humidity jump  $\llbracket s \rrbracket$  across the cohesive crack. This study built the fundamentals of mechanical-thermal and mechanical-diffusion couplings in the interface elements.

This work was concluded with numerical examples combining ASR induced damage, nonlinear effective thermal conductivity affected by humidity and effective diffusivity as a function of temperature respectively, as well as a mechanical-thermal-diffusion cohesive model at the ITZ between aggregates and HCP. The developed framework offers a reliable multiscale model to investigate failure induced by ASR and weak property of the ITZ in concrete, which also can be applied to other closely related phenomena such as Delayed Ettringite Formation (DEF) (DIAMOND (2000) or Alkali-Carbonate Reaction (ACR) (XU ET AL. (2002)). As follows, possible extensions of the presented work are addressed:

- According to the review in Chapter 4, ASR is an extremely complex reaction in concrete and only one of various possible mechanisms has been adopted in this work, therefore, the multiscale model is limited in its ability to comprehensively predict failure caused by ASR. For this reason, a comparison between the numer-

ical simulations and experimental data has not been attempted. As indicated by HAAH (2006) and DUNANT & SCRIVENER (2010), cracking through aggregates induced by ASR is the predominant failure, see Figure 9.1. Thus, this mechanism has to be taken into account in future work.

- The limitation of MAZARS damage model adopted in this work, i.g. its inability to correctly depict the failure in compression, determines the need of developing a more suitable damage model, see PIGNATELLI ET AL. (2013) and KIM & AL-RUB (2011). Furthermore, in order to overcome the strong localization and the mesh dependency problem induced by local damage, either non-local damage or gradient damage approaches should be applied, see e.g. JIRÁSEK (2004) and PEERLINGS ET AL. (1998).
- CT scans of concrete providing the best approximation of the real concrete can replace the spherical aggregates employed in this work.

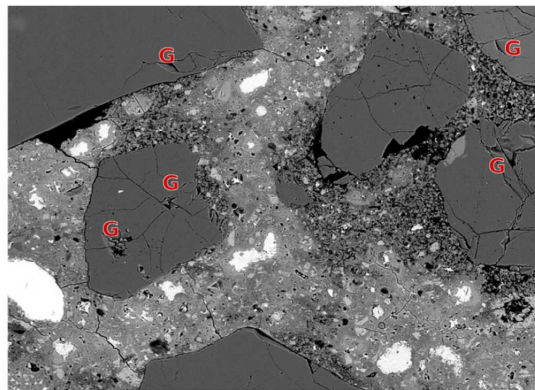


**Figure 9.1:** Concrete specimen subjected to ASR with cracks through aggregates observed at École Polytechnique Fédérale de Lausanne (EPFL), Switzerland.



# Appendix A

## Homogenization

### A.1 Mechanical homogenization

In order to apply a reliable mechanical homogenization, for a perfectly bonded material with  $\llbracket \mathbf{u} \rrbracket = 0$ , the prescribed boundary conditions have to fulfill the HILL's criterion

$$\langle \boldsymbol{\sigma} \cdot \boldsymbol{\epsilon} \rangle \stackrel{!}{=} \langle \boldsymbol{\sigma} \rangle \cdot \langle \boldsymbol{\epsilon} \rangle \quad , \quad (\text{A.1.1})$$

describing the equivalence of averaged mechanical dissipation and the mechanical dissipation of the averages. Therefore, the dissipation is preserved while making the transition from the microscale to the macroscale. By using algebraic operations, it gives

$$\begin{aligned} \langle \boldsymbol{\sigma} \cdot \boldsymbol{\epsilon} \rangle - \langle \boldsymbol{\sigma} \rangle \cdot \langle \boldsymbol{\epsilon} \rangle &= 0 \\ \left\langle (\boldsymbol{\sigma} - \langle \boldsymbol{\sigma} \rangle) \cdot (\boldsymbol{\epsilon} - \langle \boldsymbol{\epsilon} \rangle) \right\rangle &= 0 \\ \frac{1}{|v|} \int_{\mathcal{B}_t} (\boldsymbol{\sigma} - \langle \boldsymbol{\sigma} \rangle) \cdot (\boldsymbol{\epsilon} - \langle \boldsymbol{\epsilon} \rangle) \, dv &= 0 \quad . \end{aligned} \quad (\text{A.1.2})$$

#### A.1.1 Average strain theorem

The linear displacement boundary condition for mechanical homogenization is prescribed to the boundary of the body  $\partial\mathcal{B}_t$  with the aid of a constant strain tensor  $\boldsymbol{\epsilon}_0$

$$\mathbf{u} = \boldsymbol{\epsilon}_0 \cdot \mathbf{x} \quad \text{on} \quad \partial\mathcal{B}_t \quad . \quad (\text{A.1.3})$$

Considering  $\text{grad } \mathbf{u} = 1$  or  $\nabla \mathbf{x} = 1$ , the average of strain can be given by

$$\begin{aligned}
\langle \boldsymbol{\epsilon} \rangle &= \frac{1}{|v|} \int_{\mathcal{B}_t} \boldsymbol{\epsilon} \, dv \\
&= \frac{1}{|v|} \int_{\mathcal{B}_t} \text{sym} \text{grad } \mathbf{u} \, dv \\
&= \frac{1}{|v|} \int_{\partial \mathcal{B}_t} \text{sym}(\mathbf{u} \cdot \mathbf{n}) \, da \\
&= \frac{\boldsymbol{\epsilon}_0}{|v|} \int_{\partial \mathcal{B}_t} \text{sym}(\mathbf{x} \cdot \mathbf{n}) \, da \\
&= \frac{\boldsymbol{\epsilon}_0}{|v|} \int_{\mathcal{B}_t} \text{sym} \text{grad } \mathbf{x} \, dv \quad ,
\end{aligned} \tag{A.1.4}$$

leading to

$$\langle \boldsymbol{\epsilon} \rangle = \boldsymbol{\epsilon}_0 \quad , \tag{A.1.5}$$

where  $\text{sym}(\bullet)$  refers to the symmetrization with  $\text{sym}(\bullet) := \frac{1}{2}(\bullet + \bullet^T)$ . It proves that the HILL's criterion in Equation (A.1.2) is satisfied.

### A.1.2 Average stress theorem

For the average stress theorem, a constant tensor  $\boldsymbol{\sigma}_0$  is used to impose uniform traction boundary condition to the boundary of the body  $\partial \mathcal{B}_t$ .

$$\mathbf{t} = \boldsymbol{\sigma}_0 \cdot \mathbf{n} \quad \text{on } \partial \mathcal{B}_t \quad . \tag{A.1.6}$$

With consideration of the CAUCHY's theorem, the average of the stress can be written as

$$\begin{aligned}
\langle \boldsymbol{\sigma} \rangle &= \frac{1}{|v|} \int_{\mathcal{B}_t} \boldsymbol{\sigma} \, dv \\
&= \frac{1}{|v|} \int_{\mathcal{B}_t} (\boldsymbol{\sigma} + \mathbf{x} \otimes \text{div} \boldsymbol{\sigma}) \, dv \\
&= \frac{1}{|v|} \int_{\mathcal{B}_t} \text{div}(\mathbf{x} \otimes \boldsymbol{\sigma}) \, dv \\
&= \frac{1}{|v|} \int_{\partial \mathcal{B}_t} \mathbf{x} \otimes \boldsymbol{\sigma} \cdot \mathbf{n} \, da \\
&= \frac{1}{|v|} \int_{\partial \mathcal{B}_t} \mathbf{x} \otimes \mathbf{t} \, da \\
&= \frac{\boldsymbol{\sigma}_0}{|v|} \int_{\partial \mathcal{B}_t} \mathbf{x} \otimes \mathbf{n} \, da \\
&= \frac{\boldsymbol{\sigma}_0}{|v|} \int_{\mathcal{B}_t} \text{grad } \mathbf{x} \, dv \quad ,
\end{aligned} \tag{A.1.7}$$

which results in

$$\langle \boldsymbol{\sigma} \rangle = \boldsymbol{\sigma}_0 \quad , \tag{A.1.8}$$

such that the satisfaction of the HILL's criterion in Equation (A.1.2) has been proven.

## A.2 Thermal homogenization

In analogous to the mechanical problem, when the material is perfectly bonded with  $\llbracket \theta \rrbracket = 0$ , the prescribed boundary conditions for thermal homogenization have to satisfy the HILL's criterion

$$\langle \mathbf{q} \cdot \nabla \theta \rangle \stackrel{!}{=} \langle \mathbf{q} \rangle \cdot \langle \nabla \theta \rangle \quad , \quad (\text{A.2.1})$$

which also can be written as

$$\begin{aligned} \langle \mathbf{q} \cdot \nabla \theta \rangle - \langle \mathbf{q} \rangle \cdot \langle \nabla \theta \rangle &= 0 \\ \left\langle (\mathbf{q} - \langle \mathbf{q} \rangle) \cdot (\nabla \theta - \langle \nabla \theta \rangle) \right\rangle &= 0 \\ \frac{1}{|v|} \int_{\mathcal{B}_t} (\mathbf{q} - \langle \mathbf{q} \rangle) \cdot (\nabla \theta - \langle \nabla \theta \rangle) &= 0 \quad . \end{aligned} \quad (\text{A.2.2})$$

### A.2.1 Average temperature gradient theorem

The linear temperature boundary condition for thermal homogenization is given by

$$\theta = \mathbf{G}_0 \cdot \mathbf{x} \quad \text{on} \quad \partial \mathcal{B}_t \quad , \quad (\text{A.2.3})$$

using a constant  $\mathbf{G}_0$  on the boundary of the body. Applying the algebraic operation of the average  $\langle \nabla \theta \rangle$  results in

$$\begin{aligned} \langle \nabla \theta \rangle &= \frac{1}{|v|} \int_{\mathcal{B}_t} \nabla \theta \, dv \\ &= \frac{1}{|v|} \int_{\partial \mathcal{B}_t} \theta \mathbf{n} \, da \\ &= \frac{\mathbf{G}_0}{|v|} \int_{\partial \mathcal{B}_t} \mathbf{x} \mathbf{n} \, da \\ &= \frac{\mathbf{G}_0}{|v|} \int_{\mathcal{B}_t} \nabla \mathbf{x} \, dv \quad , \end{aligned} \quad (\text{A.2.4})$$

yielding

$$\langle \nabla \theta \rangle = \mathbf{G}_0 \quad . \quad (\text{A.2.5})$$

Thus, the HILL's criterion for thermal homogenization introduced in Equation (A.2.2) is satisfied trivially. Note that  $\text{grad} \bullet$  and  $\nabla \bullet$  are equivalent.

### A.2.2 Average thermal flux theorem

The uniform thermal flux boundary condition is prescribed through

$$\mathbf{n} \cdot \mathbf{q} := \mathbf{n} \cdot \mathbf{Q}_0 \quad \text{on} \quad \partial \mathcal{B}_t \quad , \quad (\text{A.2.6})$$

with the aid of a prescribed thermal flux constant  $\mathbf{Q}_0$  on the boundary of the body. The average  $\langle \mathbf{q} \rangle$  is given by

$$\begin{aligned}
\langle \mathbf{q} \rangle &= \frac{1}{|v|} \int_{\mathcal{B}_t} \mathbf{q} \, dv \\
&= \frac{1}{|v|} \int_{\mathcal{B}_t} (\mathbf{q} + \mathbf{x} \otimes \nabla \cdot \mathbf{q}) \, dv \\
&= \frac{1}{|v|} \int_{\mathcal{B}_t} \nabla \cdot (\mathbf{x} \otimes \mathbf{q}) \, dv \\
&= \frac{1}{|v|} \int_{\partial \mathcal{B}_t} \mathbf{x} \otimes \mathbf{q} \mathbf{n} \, da \\
&= \frac{\mathbf{Q}_0}{|v|} \int_{\partial \mathcal{B}_t} \mathbf{n} \otimes \mathbf{x} \, da \\
&= \frac{\mathbf{Q}_0}{|v|} \int_{\mathcal{B}_t} \nabla \mathbf{x} \, dv \quad ,
\end{aligned} \tag{A.2.7}$$

which leads to

$$\langle \mathbf{q} \rangle = \mathbf{Q}_0 \quad . \tag{A.2.8}$$

It proves that the HILL's criterion in Equation (A.2.2) is satisfied, when the uniform thermal flux boundary condition is used for thermal homogenization.

### A.3 Diffusion homogenization

For applying a reliable diffusion homogenization, when the material is perfectly bonded with  $\llbracket s \rrbracket = 0$ , the prescribed boundary conditions have to ensure the HILL's criterion

$$\langle \mathbf{j} \cdot \nabla s \rangle \stackrel{!}{=} \langle \mathbf{j} \rangle \cdot \langle \nabla s \rangle \quad . \tag{A.3.1}$$

By using algebraic operations, it gives

$$\begin{aligned}
\langle \mathbf{j} \cdot \nabla s \rangle - \langle \mathbf{j} \rangle \cdot \langle \nabla s \rangle &= 0 \\
\left\langle (\mathbf{j} - \langle \mathbf{j} \rangle) \cdot (\nabla s - \langle \nabla s \rangle) \right\rangle &= 0 \\
\frac{1}{|v|} \int_{\mathcal{B}_t} (\mathbf{j} - \langle \mathbf{j} \rangle) \cdot (\nabla s - \langle \nabla s \rangle) &= 0 \quad .
\end{aligned} \tag{A.3.2}$$

#### A.3.1 Average humidity gradient theorem

The linear humidity boundary condition for diffusion homogenization is given by

$$s = \mathbf{W}_0 \cdot \mathbf{x} \quad \text{on} \quad \partial \mathcal{B}_t \quad , \tag{A.3.3}$$

using a prescribed humidity constant  $\mathbf{W}_0$  on the boundary of the body. Algebraic operation of the average  $\langle \nabla s \rangle$  using  $\nabla \mathbf{x} = \mathbf{1}$  yields

$$\begin{aligned}
 \langle \nabla s \rangle &= \frac{1}{|v|} \int_{\mathcal{B}_t} \nabla s \, dv \\
 &= \frac{1}{|v|} \int_{\partial \mathcal{B}_t} s \mathbf{n} \, da \\
 &= \frac{\mathbf{W}_0}{|v|} \int_{\partial \mathcal{B}_t} \mathbf{x} \mathbf{n} \, da \\
 &= \frac{\mathbf{W}_0}{|v|} \int_{\mathcal{B}_t} \nabla \mathbf{x} \, dv \quad ,
 \end{aligned} \tag{A.3.4}$$

and

$$\langle \nabla s \rangle = \mathbf{W}_0 \quad . \tag{A.3.5}$$

Thus, the linear humidity boundary condition satisfies the HILL's criterion in Equation (A.3.2).

### A.3.2 Average diffusion flux theorem

The uniform diffusion flux boundary condition is prescribed by

$$\mathbf{n} \cdot \mathbf{j} := \mathbf{n} \cdot \mathbf{J}_0 \quad \text{on} \quad \partial \mathcal{B}_t \quad , \tag{A.3.6}$$

with the aid of a prescribed diffusion flux constant  $\mathbf{J}_0$  on the boundary. The average  $\langle \mathbf{j} \rangle$  is obtained through

$$\begin{aligned}
 \langle \mathbf{q} \rangle &= \frac{1}{|v|} \int_{\mathcal{B}_t} \mathbf{j} \, dv \\
 &= \frac{1}{|v|} \int_{\mathcal{B}_t} (\mathbf{j} + \mathbf{x} \otimes \nabla \cdot \mathbf{j}) \, dv \\
 &= \frac{1}{|v|} \int_{\mathcal{B}_t} \nabla \cdot (\mathbf{x} \otimes \mathbf{j}) \, dv \\
 &= \frac{1}{|v|} \int_{\partial \mathcal{B}_t} \mathbf{x} \otimes \mathbf{j} \mathbf{n} \, da \\
 &= \frac{\mathbf{J}_0}{|v|} \int_{\partial \mathcal{B}_t} \mathbf{n} \otimes \mathbf{x} \, da \\
 &= \frac{\mathbf{J}_0}{|v|} \int_{\mathcal{B}_t} \nabla \mathbf{x} \, dv \quad ,
 \end{aligned} \tag{A.3.7}$$

indicating that the HILL's criterion in Equation (A.3.2) is ensured, when the uniform diffusion flux boundary condition is used for diffusion homogenization.



# Bibliography

- ABDELALIM A., ABDALLAH S., EASAWI K., NEGM S. ET AL. Thermal properties of hydrated cement pastes studied by the photoacoustic technique. pages 1073–1080. Proceedings for 15th International conference on photoacoustic and photothermal phenomena (ICPPP15), Leuven, Belgium, 2007.
- ADALLA H.M. & KARIHALOO B.L. A method for constructing the bilinear tension softening diagram of concrete corresponding to its true fracture energy. *Magazine of Concrete Research*, 56 (2004): 597–604.
- ALFANO G. & SACCO E. Combining interface damage and friction in a cohesive-zone model. *International Journal for Numerical Methods in Engineering*, 68 (2006): 542–582.
- ALFANO M., FURGIUELE F., LEONARDI A., MALETTA C. ET AL. Mode I fracture of adhesive joints using tailored cohesive zone models. *International Journal of Fracture*, 157 (2009): 193–204.
- ALIABADI M.H. & ROOKE D.P. *Numerical Fracture Mechanics (Solid Mechanics and Its Applications)*. Wiley, 1991.
- ALNAGGAR M., CUSATIS G. & LUZIO G.D. Lattice discrete particle modeling (LDPM) of alkali silica reaction (ASR) deterioration of concrete structures. *Cement and Concrete Composites*, 41 (2013): 45–59.
- ASAKUMA Y., MIYAUCHI S., YAMAMOTO T., AOKI H. ET AL. Homogenization method for effective thermal conductivity of metal hydride bed. *International Journal of Hydrogen Energy*, 29 (2004): 209–216.
- BABUŠKA I., ANDERSSON B., SMITH P.J. & LEVIN K. Damage analysis of fiber composites part I. statistical analysis on fiber scale. *Computer Methods in Applied Mechanics and Engineering*, 172 (1999): 27–77.
- BADEL P., GODARD V. & LEBLOND J.B. Application of some anisotropic damage model to the prediction of the failure of some complex industrial concrete structure. *International Journal of Solids and Structures*, 44 (2007): 5848–5874.

- BANGERT F., KUHL D. & MESCHKE G. Chemo-hygro-mechanical modelling and numerical simulation of concrete deterioration caused by alkali-silica reaction. *International Journal for Numerical and Analytical Methods in Geomechanics*, 28 (2004): 689–714.
- BAROGHEL-BOUNY V. Water vapour sorption experiments on hardened cementitious materials: Part I: essential tool for analysis of hygral behaviour and its relation to pore structure. *Cement and Concrete Research*, 37 (2007): 414–437.
- BATHE K.J. *Finite Element Procedures*. Prentice Hall, 1995.
- BAŽANT Z.P. & STEFFENS A. Mathematical model for kinetics of alkali-silica reaction in concrete. *Cement and Concrete Research*, 30 (2000): 419–428.
- BAŽANT Z.P. & YU Q. Universal size effect law and effect of crack depth on quasi-brittle structure strength. *Journal of Engineering Mechanics*, 135 (2009): 78–84.
- BAŽANT Z.P. Scaling of quasibrittle fracture: asymptotic analysis. *International Journal of Fracture*, 83 (1997): 19–40.
- BAŽANT Z.P. Size effect. *International Journal and Solids and Structures*, 37 (2000): 69–80.
- BAŽANT Z.P. & YU Q. Effect testing of cohesive fracture parameters and nonuniqueness of work-of-fracture method. *Journal of Engineering Mechanics*, 137 (2011): 580–588.
- BAŽANT Z.P., ZI G. & MEYER C. Fracture mechanics of ASR in concretes with waste glass particles of different sizes. *Journal of Engineering Mechanics*, 126 (2000): 226–232.
- BELYTSCHKO T., LIU W.K. & MORAN B. *Nonlinear Finite Elements for Continua and Structures*. Wiley, 2000.
- BENABOU L., SUN Z. & DAHOO P.R. A thermo-mechanical cohesive zone model for solder joint lifetime prediction. *International Journal of Fatigue*, 49 (2013): 18–30.
- BENTZ D.P. *CEMHYD3D: A Three-Dimensional Cement Hydration and Microstructure Development Modelling Package. Version 2.0*. Ph.D. thesis, National Institute of Standards and Technology, Gaithersburg (2000).
- BENTZ D.P. Transient plane source measurements of the thermal properties of hydrating cement pastes. *Materials and Structures*, 40 (2007): 1073–1080.
- BENTZ D.P., GARBOCZI E.J., YANG L., MARTYS N. ET AL. Modeling of the influence of transverse cracking on chloride penetration into concrete. *Cement and Concrete Composites*, 38 (2013): 65–74.

- BENVENISTE Y. A general interface model for a three-dimensional curved thin anisotropic interphase between two anisotropic media. *Journal of the Mechanics and Physics of Solids*, 54 (2006): 708–734.
- BENVENISTE Y. Revisiting the generalized self-consistent scheme in composites: Clarification of some aspects and a new formulation. *Journal of the Mechanics and Physics of Solids*, 56 (2008): 2984–3002.
- BENVENISTE Y. & MILTON G.W. An effective medium theory for multi-phase matrix-based dielectric composites with randomly oriented ellipsoidal inclusions. *International Journal of Engineering Science*, 49 (2011): 2–16.
- BI L., LI D., LIU M., JIN J. ET AL. The influence of approaches for the purification of natural cancellous bone grafts: Morphology, microstructure, composition, strength and biocompatibility study. *Materials Letters*, 64 (2010): 2056–2059.
- BIEL A. & STIGH U. Damage and plasticity in adhesive layer: an experimental study. *International Journal of Fracture*, 165 (2010): 93–103.
- BISHNOI S. & SCRIVENER K.L.  $\mu ic$ : A new platform for modelling the hydration of cements. *Cement and Concrete Research*, 39 (2009): 266–274.
- BOERNER E.F.I. & WRIGGERS P. A macro-element for incompressible finite deformations based on a volume averaged deformation gradient. *Computational Mechanics*, 42 (2008): 407–416.
- BULLETIN A.C.I.E. Aggregates for concrete. *Farmington Hills, MI: American Concrete Institute*, E1-07 (1999).
- CAPRA B. & SELIER A. Orthotropic modelling of alkali-aggregate reaction in concrete structures: numerical simulations. *Mechanics of Materials*, 35 (2003): 817–830.
- CAROL I., LÓPEZ C.M. & ROA O. Micromechanical analysis of quasi-brittle materials using fracture-based interface elements. *International Journal for Numerical Methods in Engineering*, 52 (2001): 193–215.
- CARSON J.K., LOVATT S.J., TANNER D.J. & CLELAND A.C. Experimental measurements of the effective thermal conductivity of a pseudo-porous food analogue over a range of porosities and mean pore sizes. *Journal of Food Engineering*, 63 (2004): 87–95.
- CEDOLIN L. & CUSATIS G. Identification of concrete fracture parameters through size effect experiments. *Cement and Concrete Composites*, 30 (2008): 788–797.
- CHANDRA N., LI H., SHET C. & GHONEM H. Some issues in the application of cohesive zone models for metal-ceramic interfaces. *International Journal of Solids and Structures*, 39 (2002): 2878–2855.

- CHARLWOOD R.G. A review of alkali-aggregate reaction in hydro plants and dams. *International Journal on Hydropower and Dams*, 10 (1994): 73–80.
- CHARPIN L. & EHRLACHER A. A computational linear elastic fracture mechanics-based model for alkali-silica reaction. *Cement and Concrete Research*, 42 (2012): 613–625.
- CIARLET P. *Mathematical elasticity I: Three dimensional elasticity*. North-Holland, 1994.
- COMBY-PEYROT I., BERNARD F., BOUCHARD P.O., BAY F. ET AL. Development and validation of a 3D computational tool to describe concrete behaviour at mesoscale. Application to the alkali-silica reaction. *Computational Materials Science*, 46 (2009): 1163–1177.
- COMI C., FEDELE R. & PEREGO U. A chemo-thermo-damage model for the analysis of concrete dams affected by alkali-silica reaction. *Mechanics of Materials*, 41 (2009): 210–230.
- COMI C., KIRCHMAYR B. & PIGNATELLI R. Two-phase damage modeling of concrete affected by alkali-silica reaction under variable temperature and humidity conditions. *International Journal of Solids and Structures*, 49 (2012): 3367–3380.
- COMI C. & PEREGO U. Fracture energy based bi-dissipative damage model for concrete. *International Journal of Solids and Structures*, 38 (2001): 6427–6454.
- CRISFIELD M.A. *Non-linear Finite Element Analysis of Solids and Structures*. Wiley; Volume 2, 1992.
- CRISFIELD M.A., HELLWEG H.B. & DAVIES G.A.O. Failure analysis of composite structures using interface elements. pages 1–4. Proceedings for the NAFEMS Conference on Application of Finite Elements to Composite Materials, London, U.K, 1997.
- CUSATIS G. & CEDOLIN L. Two-scale study of concrete fracturing behavior. *Engineering Fracture Mechanics*, 74 (2007): 3–17.
- DAHER N. & MAUGIN G.A. The method of virtual power in continuum mechanics application to media presenting singular surfaces and interfaces. *Acta Mechanica*, 60 (1986): 217–240.
- DAY R.A. & POTTS D.M. Zero thickness interface elements-numerical stability and application. *International Journal for Numerical and Analytical Methods in Geomechanics*, 18 (1994): 689–708.
- DENARIÉ E., CÉCOT C. & HUET C. Characterization of creep and crack growth interactions in the fracture behavior of concrete. *Cement and Concrete Research*, 36 (2006): 571–575.

- DIAMOND S. The relevance of laboratory studies on delayed ettringite formation to DEF in field concretes. *Cement and Concrete Research*, 30 (2000): 1987–1991.
- DIMITRI R., LORENZIS L.D., WRIGGERS P. & ZAVARISE G. NURBS- and T-spline-based isogeometric cohesive zone modeling of interface debonding. *Computational Mechanics*, 0 (2014): 394–414.
- DRON R. & BRIVOT F. Thermodynamic and kinetic approach to the alkali-silica reaction. Part 2: experiment. *Cement and Concrete Research*, 23 (1993): 93–103.
- DUGDALE D.S. Yielding of steel sheets containing slits. *Journal of the Mechanics and Physics of Solids*, 8 (1960): 100–104.
- DUNANT C. *Experimental and modelling study of the alkali-silica-reaction in concrete*. Ph.D. thesis, École Polytechnique Fédérale de Lausanne, Lausanne, Switzerland (2009).
- DUNANT C.F. & SCRIVENER K.L. Micro-mechanical modelling of alkali-silica-reaction-induced degradation using the AMIE framework. *Cement and Concrete Research*, 40 (2010): 517–525.
- DÜSTER A., SEHLHORST H.G. & RANK E. Numerical homogenization of heterogeneous and cellular materials utilizing the finite cell method. *Computational Mechanics*, 50 (2012): 413–431.
- ECKARDT S. *Adaptive heterogeneous multiscale models for the nonlinear simulation of concrete*. Ph.D. thesis, Bauhaus-Universität Weimar, Weimar, Germany (2009).
- ECKARDT S. & KÖNKE C. Adaptive damage simulation of concrete using heterogeneous multiscale models. *Journal of Algorithms & Computational Technology*, 2 (2008): 275–297.
- ELICES M., ROCCO C. & ROSELLÓ C. Cohesive crack modelling of a simple concrete: Experimental and numerical results. *Engineering Fracture Mechanics*, 76 (2009): 1398–1410.
- ELSANADEDY H.M., AL-SALLOUM Y.A., ALSAYED S.H. & LQBAL R.A. Experimental and numerical investigation of size effects in FRP-wrapped concrete columns. *Construction and Building Materials*, 29 (2012): 56–72.
- ERBTS P. & DÜSTER A. Accelerated staggered coupling schemes for problems of thermoelasticity at finite strains. *Computers & Mathematics with Applications*, 64 (2012): 2408–2430.
- ESHELBY J.D. The determination of the elastic field of an ellipsoidal inclusion, and related problems. *Proceedings of the Royal Society of London*, 241(Series A) (1957): 376–396.

- FAIRBAIRN E.M.R., RIBEIRO F.L.B., LOPES L.E., TOLEDO-FILHO R.D. ET AL. Modelling the structural behaviour of a dam affected by alkali-silica reaction. *Communications in Numerical Methods in Engineering*, 22 (2006): 1–12.
- FARAGE M.C.R., ALVES J.L.D. & FAIRBAIRN E.M.R. Macroscopic model of concrete subjected to alkali-aggregate reaction. *Cement and Concrete Research*, 34 (2004): 495–505.
- FICHANT S., BORDERIE C.L. & PIJAUDIER-CABOT G. Isotropic and anisotropic descriptions of damage in concrete structures. *Mechanics of Cohesive-Frictional Materials*, 4 (1999): 339–359.
- FREED Y. & BANKS-SILLS L. A new cohesive zone model for mixed mode interface fracture in bimaterial. *Engineering Fracture Mechanics*, 75 (2008): 4583–4593.
- GARCIA-DIAZ E., RICHE J., BULTEEL D. & VERNET C. Mechanism of damage for the alkali-silica reaction. *Cement and Concrete Research*, 36 (2006): 395–400.
- GÉRARD B. & MARCHAND J. Influence of cracking on the diffusion properties of cement-based materials: Part I: Influence of continuous cracks on the steady-state regime. *Cement and Concrete Research*, 30 (2000): 37–43.
- GEUBELLE P.H. & BAYLOR J.S. Impact-induced delamination of composites: A 2D simulation. *Composites Part B: Engineering*, 29 (1998): 589–602.
- GHOSH A. & CHAUDHURI P. Computational modeling of fracture in concrete using a meshfree meso-macro-multiscale method. *Computational Materials Science*, 69 (2013): 204–215.
- GOLEWSKI G.L., GOLEWSKI P. & SADOWSKI T. Numerical modelling crack propagation under mode II fracture in plain concretes containing siliceous fly-ash additive using XFEM method. *Computational Materials Science*, 62 (2012): 75–78.
- GOROLL M. & PUFALL R. Determination of adhesion and delamination prediction for semiconductor packages by using grey scale correlation and cohesive zone modelling. *Microelectronics Reliability*, 52 (2012): 2289–2293.
- GRASSL P. & JIRÁSEK M. Meso-scale approach to modelling the fracture process zone of concrete subjected to uniaxial tension. *International Journal of Solids and Structures*, 47 (2010): 957–968.
- GURTIN M.E., FRIED E. & ANAND L. *The mechanics and thermodynamics of continua*. Cambridge University Press, 2010.
- HÄFNER S., ECKARDT S., LUTHER T. & KÖNKE C. Mesoscale modeling of concrete: Geometry and numerics. *Computers & Structures*, 84 (2006): 450–461.

- HABA M.B. *Mechanical effects of alkali silica reaction in concrete studied by SEM-image analysis*. Ph.D. thesis, École Polytechnique Fédérale de Lausanne, Lausanne, Switzerland (2006).
- HABA M.B., GALLUCCI E., GUIDOUM A. & SCRIVENER K.L. Relation of expansion due to alkali silica reaction to the degree of reaction measured by SEM image analysis. *Cement and Concrete Research*, 37 (2007): 1206–1214.
- HAIN M. *Computational homogenization of micro-structural damage due to frost in hardened cement paste*. Ph.D. thesis, Leibniz Universität Hannover, Hannover, Germany (2007).
- HAIN M. & WRIGGERS P. Computational homogenization of micro-structural damage due to frost in hardened cement paste. *Finite Elements in Analysis and Design*, 44 (2008a): 233–244.
- HAIN M. & WRIGGERS P. Numerical homogenization of hardened cement paste. *Computational Mechanics*, 42 (2008b): 197–212.
- HALM D. & DRAGON A. An anisotropic model of damage and frictional sliding for brittle materials. *European Journal of Mechanics-A/Solids*, 17 (1998): 439–460.
- HANCOX N.L. The role of moisture diffusion in the drying of cement paste under the influence of temperature gradients. *Journal of Physics D: Applied Physics*, 1 (1968): 1769–1777.
- HASHIN Z. A variational approach to the theory of the elastic behaviour of multiphase materials. *Journal of the Mechanics and Physics of Solids*, 11 (1963): 127–140.
- HASHIN Z. Thin interphase/imperfect interface in conduction. *Journal of Applied Physics*, 89 (2001): 2261–2267.
- HAUPT P. *Continuum mechanics and theory of materials*. Springer, 2002.
- HAZANOV S. & HUET C. Order relationships for boundary conditions effect in heterogeneous bodies smaller than the representative volume. *Journal of the Mechanics and Physics of Solids*, 42 (1994): 1995–2011.
- HERRADOR M.F., MARTÍNEZ-ABELLA F. & FERNÁNDEZ-GAGO R.D.H. Mechanical behavior model for ASR-affected dam concrete under service load: formulation and verification. *Materials and Structures*, 42 (2009): 201–212.
- HILL. The elastic behaviour of a crystalline aggregate. *Proceedings of the Royal Society of London*, 65(Series A) (1952): 349–354.
- HOLZAPFEL G. *Nonlinear solids mechanics*. Wiley, 2000.
- HORDIJK D.A. *Tensile and tensile fatigue behaviour of concrete; experiments, modelling and analyses*. HERON, vol 37. Stevin Laboratory and TNO Research, Delft, The Netherlands, 1992.

- HUANG M. & PIETRUSZCZAK S. Numerical analysis of concrete structures subjected to alkali-aggregate reaction. *Mechanics of Cohesive-Frictional Materials*, 1 (1996): 305–319.
- HUET C. Application of variational concepts to size effects in elastic heterogeneous bodies. *Journal of the Mechanics and Physics of Solids*, 38 (1990): 813–841.
- HUGHES T. *The Finite Element Method*. Dover, 2010.
- ICHIKAWA T. & MIURA M. Modified model of alkali-silica reaction. *Cement and Concrete Research*, 37 (2007): 1291–1297.
- IDIART A.E., LÓPEZ C.M. & CAROL I. Chemo-mechanical analysis of concrete cracking and degradation due to external sulfate attack: a meso-scale model. *Cement and Concrete Composites*, 33 (2011): 411–423.
- IDORN G.M. A discussion of the paper “Mathematical model for kinetics of alkali-silica reaction in concrete” by Zdenek P. Bazant and Alexander Steffens. *Cement and Concrete Research*, 31 (2001): 1109–1110.
- JANG S.Y., KIM B.S. & OH B.H. Effect of crack width on chloride diffusion coefficients of concrete by steady-state migration tests. *Cement and Concrete Research*, 41 (2011): 9–19.
- JANSSEN M., ZUIDEMA J. & WANHILL R.J.H. *Fundamentals of fracture mechanics*. Taylor & Francis, 2004.
- JAVILI A. *Thermomechanics of solids accounting for surfaces and interfaces*. Ph.D. thesis, Universität Erlangen-Nürnberg, Erlangen, Germany (2012).
- JAVILI A., KAESSMAIR S. & STEINMANN P. General imperfect interfaces. *Computer Methods in Applied Mechanics and Engineering*, 275 (2014): 76–97.
- JAVILI A., MCBRIDE A. & STEINMANN P. Numerical modelling of thermomechanical solids with mechanically energetic (generalised) Kapitza interfaces. *Computational Materials Science*, 65 (2012): 542–551.
- JAVILI A., MCBRIDE A. & STEINMANN P. Numerical modelling of thermomechanical solids with highly-conductive energetic interfaces. *International Journal for Numerical Methods in Engineering*, 93 (2013): 551–574.
- JEON S.E. *Analysis of concrete structures with hydration heat and differential shrinkage*. Ph.D. thesis, Korea Advanced Institute of Science and Technology, Daejeon, Korea (2003).
- JIANG B. & WENG G.J. A generalized self-consistent polycrystal model for the yield strength of nanocrystalline materials. *Journal of the Mechanics and Physics of Solids*, 52 (2004): 1125–1149.

- JIRÁSEK M. Non-local damage mechanics with application to concrete. *Revue Française de Génie Civil*, 8 (2004): 683–707.
- JOOSS M. & REINHARDT H.W. Permeability and diffusivity of concrete as function of temperature. *Cement and Concrete Research*, 32 (2002): 1497–1504.
- KAMALI-BERNARD S. & BERNARD F. Effect of tensile cracking on diffusivity of mortar: 3D numerical modelling. *Computational Materials Science*, 47 (2009): 178–185.
- KANAUN S.K. & LEVIN V. *Self-Consistent Methods for Composites-Vol. 1: Static Problems*. Springer, 2008.
- KANIT T., FOREST S., GALLIET I., MOUNOURY V. ET AL. Determination of the size of the representative volume element for random composites: statistical and numerical approach. *International Journal of Solids and Structures*, 40 (2003): 3647–3679.
- KARIHALOO B.L. & FU D. An isotropic damage model for plain concrete. *Engineering Fracture Mechanics*, 35 (1990): 205–209.
- KIM C.M. & AL-RUB R.K.A. Meso-scale computational modeling of the plastic-damage response of cementitious composites. *Cement and Concrete Research*, 41 (2011): 339–358.
- KODIDE U. *Thermal conductivity and its effects on the performance of Pcc pavements in MEPDG*. Ph.D. thesis, Louisiana State University, Baton Rouge, USA (2010).
- KOISSIN V., WARNET L.L. & AKKERMAN R. Delamination in carbon-fibre composites improved with in situ grown nanofibres. *Engineering Fracture Mechanics*, 101 (2013): 140–148.
- KOLLURI M., HOEFNAGELS J.P.M., VAN DOMMELSEN J.A.W. & GEERS M.G.D. Irreversible mixed mode interface delamination using a combined damage-plasticity cohesive zone enabling unloading. *International Journal of Fracture*, 185 (2014): 77–95.
- KRABBENHØFT K., HAIN M. & WRIGGERS P. *Computation of effective cement paste diffusivities from microtomographic images*. In V. Kompis (Ed.), *Composites with micro- and nano-structure: Computational modeling and experiments (pp.281-297)*. Berlin, Heidelberg, New York: Springer, 2008.
- KUNDU T. *Fundamentals of fracture mechanics*. Taylor & Francis, 2008.
- KURIHARA T. & KATAWAKI K. Effects of moisture control and inhibition on alkali silica reaction. pages 629–634. Proceedings for 8th International Conference on Alkali Aggregate Reaction in Concrete, Kyoto, Japan, 1989.

- LARIVE C. *Apports combinés de l'expérimentation et de la modélisation à la compréhension de l'alcali-réaction et de ses effets mécaniques*. Ph.D. thesis, Laboratoire Central des Ponts et Chaussées, Paris, France (1998).
- LASCHET G., SAUERHERING J., REUTER O., FEND T. ET AL. Effective permeability and thermal conductivity of open-cell metallic foams via homogenization on a microstructure model. *Computational Materials Science*, 45 (2009): 597–603.
- LE-QUANG H., BONNET G. & HE Q.C. Size-dependent Eshelby tensor fields and effective conductivity of composites made of anisotropic phases with highly conducting imperfect interfaces. *Physical Review B*, 81 (2010): 064 203.
- LEE K.M. & PARK J.H. A numerical model for elastic modulus of concrete considering interfacial transition zone. *Cement and Concrete Research*, 38 (2008): 396–402.
- LEGER P., COTÉ P. & TINAWI R. Finite element analysis of concrete swelling due to alkali-aggregate reactions in dams. *Computers & Structures*, 60 (1996): 601–611.
- LEHMANN E. *Computational homogenisation of polycrystalline elastoplastic microstructures at finite deformation*. Ph.D. thesis, Leibniz Universität Hannover, Hannover, Germany (2013).
- LEMARCHAND E., DORMIEUX L. & ULM F.J. Micromechanics investigation of expansive reactions in chemoelastic concrete. *Philosophical Transactions of the Royal Society. Mathematical, Physical, and Engineering Sciences*, 363 (2005): 2581–2602.
- LI S., THOULESS M.D., WAAS A.M., SCHROEDER J.A. ET AL. Use of a cohesive-zone model to analyze the fracture of a fiber-reinforced polymer-matrix composite. *Composites Science and Technology*, 65 (2005): 537–549.
- LI S.F., ZENG X.W., REN B., QIAN J. ET AL. An atomistic-based interphase zone model for crystalline solids. *Computer Methods in Applied Mechanics and Engineering*, 229-232 (2012): 87–109.
- LIPTON R. Variational methods, bounds, and size effects for composites with highly conducting interface. *Journal of the Mechanics and Physics of Solids*, 45 (1997): 361–384.
- LOCOGE P., MASSAT M., OLLIVIER J.P. & RICHEL C. Ion diffusion in microcracked concrete. *Cement Concrete Research*, 22 (1992): 431–438.
- LÖHNERT S. *Computational homogenization of microheterogeneous materials at finite strains including damage*. Ph.D. thesis, Leibniz Universität Hannover, Hannover, Germany (2004).
- LUDWIG U. Effects of environmental conditions on alkali-aggregate reaction and preventive measures. pages 583–596. Proceedings for 8th International Conference on Alkali Aggregate Reaction in Concrete, Kyoto, Japan, 1989.

- LUNDGREN K. Modeling the effect of corrosion on bond in reinforced concrete. *Magazine of Concrete Research*, 54 (2002): 165–173.
- MAIN H.K. *Analysis of 3D scale and size effects in numerical concrete*. Ph.D. thesis, Eidgenössische Technische Hochschule Zürich, Zürich, Switzerland (2010).
- MAN H.K. & MIER J.G.M.V. Size effect on strength and fracture energy for numerical concrete with realistic aggregate shapes. *International Journal of Fracture*, 154 (2008): 61–72.
- MASE G.E. & MASE G.T. *Continuum Mechanics for Engineers*. CRC Press, 1999.
- MASO J.C. *Interfacial transition zone in concrete*. Rilem Report 11, 1996.
- MAZARS J. A description of micro- and macroscale damage of concrete structures. *Engineering Fracture Mechanics*, 25 (1986): 729–737.
- MAZARS J. & PIJAUDIER-CABOT G. Continuum damage theory-application to concrete. *Journal of Engineering Mechanics*, 115 (1989): 345–365.
- MCGOWAN J.K. & VIVIAN H.E. Studies in cement-aggregate reaction: correlation between crack development and expansion of mortars. *Australian Journal of Applied Science*, 3 (1952): 228–232.
- MEHTA P.K. & MONTEIRO P.J.M. *Concrete: Microstructure, Properties, and Materials*. McGraw-Hill Professional, 1993.
- MEHTA P.K. & MONTEIRO P.J.M. *Concrete: Microstructure, Properties, and Materials*. McGraw-Hill Professional, 2001.
- MIEHE C. & KOCH A. Computational micro-to-macro transitions of discretized microstructures undergoing small strains. *Archive of Applied Mechanics*, 72 (2002): 300–317.
- MIEHE C. & SCHOTTE J. Anisotropic finite elastoplastic analysis of shells: simulation of earing in deep-drawing of single- and polycrystalline sheets by taylor-type micro-to-macro transitions. *Computer Methods in Applied Mechanics and Engineering*, 193 (2007): 25–57.
- VAN MIER J.G.M. & MAN H.K. Some notes on microcracking, softening, localization, and size effects. *International Journal of Damage Mechanics*, 18 (2009): 283–309.
- MIER J.G.M.V. *Strain-softening of concrete under multiaxial loading conditions*. Ph.D. thesis, Eindhoven University of Technology, Eindhoven, Netherlands (1984).
- MIER J.G.M.V. & VLIET M.R.A.V. Influence of microstructure of concrete on size/scale effects in tensile fracture. *Engineering Fracture Mechanics*, 70 (2003): 2281–2306.

- MILLS R. Self-diffusion in normal and heavy water in the range 1-45 degree. *The Journal of Physical Chemistry*, 77 (1973): 685–688.
- MOFTAH S.O. *Computational Homogenisation of Concrete*. Ph.D. thesis, Leibniz Universität Hannover, Hannover, Germany (2005).
- MONTEIRO P.J.M., MASO J.C. & OLLIVIER J.P. The aggregate-mortar interface. *Cement and Concrete Research*, 15 (1985): 953–958.
- MORI T. & TANAKA K. Average stress in matrix and average energy of materials with misfitting inclusions. *Acta Metall*, 21 (1973): 571–574.
- MÜLLER-HOEPPE D.S., LÖHNERT S. & WRIGGERS P. A finite deformation brick element with inhomogeneous mode enhancement. *International Journal for Numerical Methods in Engineering*, 78 (2009): 1164–1187.
- MULTON S., SELIER A. & CRY M. Chemo-mechanical modeling for prediction of alkali silica reaction (ASR) expansion. *Cement and Concrete Research*, 39 (2009): 490–500.
- MURTHY A.R.C., PALANI G.S. & IYER N.R. State-of-the-art review on fracture analysis of concrete structural components. *Sadhana*, 31 (2009): 345–367.
- NADEAU J.C. A multiscale model for effective moduli of concrete incorporating its water-cement ratio gradients, aggregate size distributions and entrapped voids. *Cement and Concrete Research*, 33 (2003): 103–402.
- NEEDLEMAN A. A continuum model for void nucleating by inclusion debonding. *Journal of Applied Mechanics*, 54 (1987): 525–531.
- NEEDLEMAN A. An analysis of tensile decohesion along an interface. *Journal of the Mechanics and Physics of Solids*, 38 (1990): 289–324.
- NEMAT-NASSER S. & HORI M. *Micromechanics: Overall properties of heterogeneous materials (Second Edition)*. Amsterdam: North-Holland, 1999.
- NGUYEN V.P. & NGUYEN-XUAN H. High-order b-splines based finite elements for delamination analysis of laminated composites. *Composite Structures*, 102 (2013): 261–275.
- NGUYEN V.P., STROEVEN M. & SLUYS L.J. Multiscale failure modeling of concrete: Micromechanical modeling, discontinuous homogenization and parallel computations. *Engineering Fracture Mechanics*, 201-204 (2012): 139–156.
- NILENIUS F., LARSSON F., LUNDGREN K. & PUNESSON K. Computational homogenization of diffusion in three-phase mesoscale concrete. *Computational Mechanics*, (In press).

- NILSSON L.O. Moisture effects on the alkali-silica reaction. pages 201–208. Proceedings for 6th International Conference on Alkali in Concrete, Copenhagen, 1989.
- NOCEDAL J. & WRIGHT S.J. *Numerical optimization*. In Mikosch, T. V., Resnick, S. I., and Robinson, S. M., editors, *Springer series in operations research and financial engineering*. Springer, 2nd edition, 2006.
- NOLL W. Die herleitung der grundgleichungen der thermomechanik der kontinua aus der statistischen mechanik. *Journal of Rational Mechanics and Analysis*, 4 (1955): 627–646.
- ORTIZ M. & PANDOLFI A. Finite deformation irreversible cohesive elements for three dimensional crack propagation analysis. *International Journal for Numerical Methods in Engineering*, 44 (1999): 1267–1282.
- ÖZDEMİR I., BREKELMANS W.A.M. & GEERS M.G.D. A thermo-mechanical cohesive zone model. *Journal of Computational Mechanics*, 46 (2010): 735–745.
- PAN J.W., FENG Y.T., WANG J.T., SUN Q.C. ET AL. Modeling of alkali-silica reaction in concrete: a review. *Frontiers of Structural and Civil Engineering*, 6 (2012): 1–18.
- PARK K. & PAULINO G.H. Cohesive zone models: A critical review of traction-separation relationships across fracture surfaces. *Applied Mechanics Reviews*, 64 (2011): 1–20.
- PAVILÍK Z. & ČERNÝ R. Determination of moisture diffusivity as a function of both moisture and temperature. *International Journal of Thermophysics*, 33 (2012): 1704–1714.
- PAVLÍK Z., VEJMEJKOVÁ E., FIALA L. & ČERNÝ R. Effect of moisture on thermal conductivity of lime-based composites. *International Journal of Thermophysics*, 30 (2009): 1999–2014.
- PEERLINGS R.H.J., DE BORST R., BREKELMANS W.A.M. & GEERS M.G.D. Gradient-enhanced damage modelling of concrete fracture. *Mechanics of Cohesive-frictional Materials*, 3 (1998): 323–342.
- PESAVENTO F., GAWIN D., WYRZYKOWSKI M., SCHREFLER B.A. ET AL. Modeling alkali-silica reaction in non-isothermal, partially saturated cement based materials. *Computer Methods in Applied Mechanics and Engineering*, 225-228 (2012): 95–115.
- PETCH N.J. The cleavage strength of polycrystals. *Journal of Iron and Steel Institute of London*, 173 (1953): 25–28.
- PHAIR J.W., TKACHEV S.N., MANGHNANI M.H. & LIVINGSTON R.A. Elastic and structural properties of alkaline-calcium silica hydrogels. *Journal of Materials Research*, 20 (2005): 344–349.

- PIETRUSZCZAK S. On the mechanical behaviour of concrete subjected to alkali-aggregate reaction. *Computers & Structures*, 58 (1996): 1093–1097.
- PIGNATELLI R., COMI C. & MONTEIRO P.J.M.Y. A coupled mechanical and chemical damage model for concrete affected by alkali-silica reaction. *Cement and Concrete Research*, 53 (2013): 196–210.
- PONCE J.M. & BATIC O.R. Different manifestations of the alkali-silica reaction in concrete according to the reaction kinetics of the reactive aggregate. *Cement and Concrete Research*, 36 (2006): 1148–1156.
- POWERS T.C. Physical properties of cement paste. *Proceedings of the Fourth International Symposium on the Chemistry of Cement; Paper V-1: Physical properties of cement paste*, 43 (1962): 577–613.
- RABCZUK T. Computational methods for fracture in brittle and quasi-brittle solids: State-of-the-Art review and future perspectives. *ISRN Applied Mathematics*, 2013 (2012): 1–38.
- RAMESH G., SOTELINO E.D. & CHEN W.F. Effect of transition zone on elastic moduli of concrete materials. *Cement and Concrete Research*, 26 (1996): 611–622.
- READ H.E. & HEGEMIER G.A. Strain softening of rock, soil and concrete—a review article. *Mechanics of Materials*, 3 (1984): 271–294.
- REDDY J.N. *An Introduction to Continuum Mechanics*. Cambridge University Press, 2008.
- REESE S.H. *Adaptive Methods for Continuous and Discontinuous Damage Modeling in Fracture Solids*. Ph.D. thesis, Leibniz Universität Hannover, Hannover, Germany (2007).
- REUSS A. Berechnung der Fließgrenze von Mischkristallen auf Grund der Plastizitätsbedingung für Einkristalle. *Zeitschrift für Angewandte Mathematik und Mechanik*, 9 (1929): 49–58.
- RIKS E. An incremental approach to the solution of snapping and buckling problems. *International Journal and Solids and Structures*, 15 (1975): 529–551.
- RIM J.E., PINSKY P.M. & v OSDOL W. Using the method of homogenization to calculate the effective diffusivity of the stratum corneum. *Journal of Membrane Science*, 293 (2007): 174–182.
- ROSEN B.W. & HASHIN Z. Effective thermal expansion coefficients and specific heats of composite materials. *International Journal of Engineering Science*, 8 (1970): 157–173.

- ROUGELOT T., SKOCZYLAS F. & BURLION N. Water desorption and shrinkage in mortars and cement pastes: experimental study and poromechanical model. *Cement Concrete Research*, 39 (2009): 36–44.
- SAMAHA H.R. & HOVER K.C. Influence of microcracking on the mass transport properties of concrete. *ACI Materials Journal*, 89 (1992): 416–424.
- SAMIMI M., DOMMELEN J.A.W.V. & GEERS M.G.D. A three-dimensional self-adaptive cohesive zone model for interfacial delamination. *Computer Methods in Applied Mechanics and Engineering*, 200 (2011): 3540–3553.
- SAOUMA V. & PEROTTI L. Constitutive model for alkali-aggregate reactions. *ACI Materials Journal*, 103 (2006): 194–202.
- SAPORA A. & PAGGI M. A coupled cohesive zone model for transient analysis of thermoelastic interface debonding. *Journal of Computational Mechanics*, 53 (2014): 845–857.
- SHELLEKENS J.C.J. & BORST R.D. On the numerical integration of interface elements. *International Journal Numerical Methods Engineering*, 36 (1993): 43–66.
- SCHLANGEN E. & MIER J.G.M.V. Simple lattice model for numerical simulation of fracture of concrete materials and structures. *Materials and Structures*, 25 (1992): 534–542.
- SCHMIDT U., MERGHEIM J. & STEINMANN P. Multiscale parameter identification. *International Journal for Multiscale Computational Engineering*, 10 (2012): 327–342.
- SCHUTTER G.D. & TAERWE L. Random particle model for concrete based on delaunay triangulation. *Materials and Structures*, 26 (1993): 67–73.
- SCRIVENER K.L., CRUMBIE A.K. & LAUGESEN P. The interfacial transition zone (ITZ) between cement paste and aggregate in concrete. *Interface Science*, 12 (2004): 411–421.
- SHAH S.P. & OUYANG C.S. Failure of concrete: fracture mechanics approach. *Anales de Mecánica de la Fractura*, 9 (1992): 352–375.
- SHIN J.H. *Modeling alkali-silica reaction using image analysis and finite element method*. Ph.D. thesis, University of Illinois at Urbana-Champaign, Urbana-Champaign, USA (2009).
- SICAT E., GONG F., UEDA T. & ZHANG D.W. Experimental investigation of the deformational behavior of the interfacial transition zone (ITZ) in concrete during freezing and thawing cycles. *Construction and Building Materials*, 65 (2014): 122–131.

- SMAOUI N., BÉRUBÉ M.A., FOURNIER B., BISSONNETTE B. ET AL. Evaluation of the expansion attained to date by concrete affected by alkali–silica reaction. Part I: experimental study. *Canadian Journal of Civil Engineering*, 31 (2004): 826–845.
- SNOZZI L., CABALLERO A. & MOLINARI J.F. Influence of the meso-structure in dynamic fracture simulation of concrete under tensile loading. *Cement and Concrete Research*, 41 (2011): 1130–1142.
- SNOZZI L., GATUINGT F. & MOLINARI J.F. A meso-mechanical model for concrete under dynamic tensile and compressive loading. *International Journal of Fracture*, 178 (2012): 179–194.
- SONG S.H., PAULINO G.H. & BUTTLAR W.G. A bilinear cohesive zone model tailored for fracture of asphalt concrete considering viscoelastic bulk material. *Engineering Fracture Mechanics*, 73 (2006): 2829–2848.
- STROEVEN P. *Some aspects of the micromechanics of concrete*. Ph.D. thesis, Delft University of Technology, Delft, Netherlands (1973).
- TANG W., LO Y. & CUI H. Size effect of waste compact disc shred on properties of concrete. *Advanced Materials Research*, 346 (2012): 40–46.
- TÁVARA L., MANTIĂ V., SALVADORI A., GRAY L.J. ET AL. Cohesive-zone-model formulation and implementation using the symmetric Galerkin boundary element method for homogeneous solids. *Computational Mechanics*, 51 (2013): 535–551.
- TEMIZER İ. & WRIGGERS P. Homogenization in finite thermoelasticity. *Journal of the Mechanics and Physics of Solids*, 59 (2010a): 344–372.
- TEMIZER İ. & WRIGGERS P. A micromechanically motivated higher-order continuum formulation of linear thermal conduction. *Zeitschrift für Angewandte Mathematik und Mechanik*, 90 (2010b): 768–782.
- TEMIZER İ. & WRIGGERS P. Homogenization in finite thermoelasticity. *Journal of the Mechanics and Physics of Solids*, 59 (2011): 344–372.
- TEMIZER İ., WU T. & WRIGGERS P. On the optimality of the window method in computational homogenization. *International Journal of Engineering Science*, 64 (2013): 66–73.
- THOMPSON G.A., CHARLWOOD R.G., STEELE R.R. & CURTIS D.D. Mactaquac generating station intake and spillway remedial measures. V. 1, Q-68, R.24, pages 73–80. Proceedings for 18th International Congress on Large Dams, Durban, South Africa, 1994.
- TOMOSAWA F., TAMURA K. & ABE M. Influence of water content of concrete on alkali-aggregate reaction. pages 881–885. Proceedings for 8th International Conference on Alkali Aggregate Reaction in Concrete, Kyoto, Japan, 1989.

- TORQUATO S. *Random Heterogeneous Materials: Microstructure and Macroscopic Properties*. Springer, Berlin Heidelberg New York, 2002.
- TOUMI B. & RESHEIDAT M. Influence of high temperatures on surface cracking of concrete studied by image scanning technique. *Jordan Journal of Civil Engineering*, 4 (2010): 155–163.
- TRUESDELL C. & NOLL W. *The non-linear field theories of the mechanics*. Springer, 1965.
- TRUESDELL C. & NOLL W. *The non-linear field theories of mechanics*. Springer-Verlag, Berlin, Heidelberg, New York, 3th edition, 2004.
- TURON A., DÁVILA C.G., CAMANHO P.P. & COSTA J. An engineering solution for mesh size effects in the simulation of delamination using cohesive zone models. *Engineering Fracture Mechanics*, 74 (2007): 1665–1682.
- TVERGAARD V. Cohesive zone representations of failure between elastic or rigid solids and ductile solids. *Engineering Fracture Mechanics*, 70 (2003): 1859–1868.
- TVERGAARD V. & HUTCHINSON J.W. The relation between crack growth resistance and fracture process parameters in elastic-plastic solids. *Journal of the Mechanics and Physics of Solids*, 40 (1992): 1377–1397.
- ULM F.J., COUSSY O., LI K.F. & LARIVE C. Thermo-chemo-mechanics of ASR expansion in concrete structures. *Journal of Engineering Mechanics*, 126 (2000): 233–242.
- UNGER J.F. & ECKARDT S. Multiscale modeling of concrete. *Archives of Computational Methods in Engineering*, 18 (2011): 341–393.
- UNGER J.F., ECKARDT S. & KÖNKE C. Modelling of cohesive crack growth in concrete structures with the extended finite element method. *Computer Methods in Applied Mechanics and Engineering*, 196 (2007): 4087–4100.
- VASCONCELOS K.L., BHASIN A., LITTLE D.N. & LYTTON R.L. Experimental measurement of water diffusion through fine aggregate mixtures. *Journal of Materials in Civil Engineering*, 23 (2011): 445–452.
- VAN VLIET M.R.A. & VAN MIER J.G.M. Experimental investigation of size effect in concrete and sandstone under uniaxial tension. *Engineering Fracture Mechanics*, 65 (2000): 165–188.
- VOIGT W. Über die Beziehung zwischen den beiden Elastizitätskonstanten isotroper Körper. *Wied. Ann.*, 38 (1889): 6429–6452.
- VONK R.A. A micromechanical investigation of softening of concrete loaded in compression. *Heron*, 38 (1993): 3–94.

- VOŘECHOVSKÝ M. & SADILÉK V. Computational modeling of size effects in concrete specimens under uniaxial tension. *International Journal of Fracture*, 154 (2008): 27–49.
- WAN X.L., WANG H.H., CHENG L. & WU K.M. The formation mechanisms of interlocked microstructures in low-carbon high-strength steel weld metals. *Materials Characterization*, 67 (2012): 41–51.
- WANG J.Y., CHIA K.S., LIEW J.Y.R. & ZHANG M.H. Flexural performance of fiber-reinforced ultra lightweight cement composites with low fiber content. *Cement and Concrete Composites*, 43 (2013): 39–47.
- WANG Z.M., KWAN A.K.H. & CHAN H.C. Mesoscopic study of concrete I: generation of random aggregate structure and finite element mesh. *Computers & Structures*, 70 (1999): 533–544.
- WILLAM K., RHEE I. & SHING B. Interface damage model for thermomechanical degradation of heterogeneous materials. *Computer Methods in Applied Mechanics and Engineering*, 193 (2004): 3327–3350.
- WONG H.S., ZOBEL M., BUENFELD N.R. & ZIMMERMAN R.W. Influence of the interfacial transition zone and microcracking on the diffusivity, permeability and sorptivity of cement-based materials after drying. *Magazine of Concrete Research*, 761 (2009): 571–589.
- WRIGGERS P. *Nonlinear finite element methods*. Springer, Berlin Heidelberg, 2008.
- WRIGGERS P. & MOFTAH S.O. Mesoscale models for concrete: Homogenisation and damage behaviour. *Finite Elements in Analysis and Design*, 42 (2006): 623–636.
- WU T., TEMIZER İ. & WRIGGERS P. Computational thermal homogenization of concrete. *Cement and Concrete Composites*, 35 (2012): 59–70.
- XU X.P. & NEEDLEMAN A. Void nucleating by inclusion debonding in a crystal matrix. *Modelling and Simulation in Materials Science and Engineering*, 1 (1993): 111–132.
- XU Z.Z., LAN X.H., DENG M. & TANG M.S. A new accelerated method for determining the potential alkali-carbonate reactivity. *Cement and Concrete Research*, 32 (2002): 851–857.
- YE G., VAN BREUGEL K. & FRAAIJ A.L.A. Three-dimensional microstructure analysis of numerically. *Cement and Concrete Research*, 33 (2003): 215–222.
- YU Q. & FISH J. Multiscale asymptotic homogenization for multiphysics problems with multiple spatial and temporal scales: a coupled thermo-viscoelastic example problem. *International Journal of Solids and Structures*, 39 (2002): 6429–6452.

- YVONNET J., HE Q.C. & TOULEMONDE C. Numerical modelling of the effective conductivities of composites with arbitrarily shaped inclusions and highly conducting interface. *Composites Science and Technology*, 68 (2008): 2818–2825.
- YVONNET J., HE Q.C., ZHU Q.Z. & SHAO J.F. A general and efficient computational procedure for modelling the Kapitza thermal resistance based on XFEM. *Composites Science and Technology*, 50 (2011): 1220–1224.
- ZAVARISE G., WRIGGERS P., STEIN E. & SCHREFLER B.A. A numerical model for thermomechanical contact based on microscopic interface laws. *International Journal for Numerical Methods in Engineering*, 35 (1992): 767–785.
- ZHANG H.W., ZHOU Q., XING H.L. & MUHLHAUS H. A DEM study on the effective thermal conductivity of granular assemblies. *Power Technology*, 1-3 (2011a): 172–183.
- ZHANG M.Z., GUANG Y. & VAN BREUGEL K. Microstructure-based modeling of water diffusivity in cement paste. *Construction and Building Materials*, 25 (2011b): 2046–2052.
- ZHANG S.R., WANG G.H. & YU X.R. Seismic cracking analysis of concrete gravity dams with initial cracks using the extended finite element method. *Engineering Structures*, 56 (2013): 528–543.
- ZHANG W.H. & CAI Y.Q. *Continuum damage mechanics and numerical applications*. Springer, 2010.
- ZIENKIEWICZ O. & TAYLOR R. *The finite element for solids and structural mechanics*. Elsevier Butterworth-Heinemann, 2005.
- ZIENKIEWICZ O.C. & TAYLOR R.L. *The Finite Element Method, Solids Mechanics*. Elsevier Butterworth-Heinemann, 2000.
- ZOHDI T.I. Modeling and simulation of a class of coupled thermo-chemo-mechanical processes in multiphase solids. *Computer Methods in Applied Mechanics and Engineering*, 193 (2004): 679–699.
- ZOHDI T.I. & WRIGGERS P. *Introduction to Computational Micromechanics*. Springer, Berlin Heidelberg New York, 2005.

## Curriculum vitae

### Curriculum vitae

Name: Tao Wu  
Date of Birth: 31. July 1984  
Place of Birth: Guixi, China  
Nationality: Chinese  
Marital status: Single

#### Education

2006 - 2009 Study of Computational Engineering,  
Rostock University, Rostock, Germany  
Major subject *Computational Electromagnetics* (M.Sc.)

2002 - 2006 Study of Electronics and Information Engineering,  
Wuhan University of Science and Engineering, China  
Major subject *Electronics and Information* (B.Sc.)

#### Occupation

09.2009 - 03.2014 Research assistant at the Institute of Continuum  
Mechanics, Leibniz Universität Hannover

#### Awards

2012 Award for Outstanding Self-financed Students Abroad  
of Chinese Government